Ollscoil na hÉireann, Corcaigh
National University of Ireland, Cork

ucc

Coláiste na hOllscoile Corcaigh, Éire
University College Cork, Ireland

Integrated Thin Film Magnetics in Advanced Organic Substrates

Thesis presented by

Declan Jordan, M.A.I, B.A.I, B.A

for the degree of

Doctor of Philosophy

Tyndall National Institute

Head of School: Prof. Jorge Oliveira

Supervisors: Dr. Paul McCloskey, Prof. Cian O' Mathúna

04-06-2021

Contents

List of Figures

List of Tables

Glossary

μmag Micromagnetic Modelling Activity Group

ACF Autocorrelation Function

AWGN Additive White Gaussian Noise

BMG Bulk Metallic Glasses

CIP Carbonyl-Iron Powder

CPU Central Processing Unit

CTE Coefficient of Thermal Expansion

CUDA Compute Unified Device Architecture

DFT Discrete Fourier Transform

DMH Dynamic Magnetic Hysteresis

DUT Device Under Test

DVFS Dynamic Voltage and Frequency Scaling

FEM Finite Element Model(ling)

FFT Fast Fourier Transform

FLOPS Floating Point Operations per Second

FMR Ferromagnetic Resonance

FOM Figure of Merit

FOMs Figures of Merit

FPC Ferrite Polymer Composite(s)

FPE Fokker Planck Equation

GFLOPS Giga Floating Point Operations per Second (FLOPS)

GPU Graphics Processing Unit

LLG Landau Lifshitz Gilbert

LTCC Low Temperature Co-Fired Ceramic

MEMS Micro-Electromechanical System

OOMMF Object Orientated MicroMagnetic Framework

OOP Object Oriented Programming

PI Polyimide

POL Point of Load

PVDF Polyvinylidene Fluoride

PwrSiP Power Supply in Package

PwrSoC Power Supply on Chip

SEM Scanning Electron Microscope

SMPS Switched Mode Power Supply

SMR Stochastic Magnetic Resonance

SMRA Stochastic Magnetic Resonance of Absorption

SRT Surface Roughness to Thickness Ratio

TST Transition State Theory

VHF Very High Frequency

VNA Vector Network Analyser

XRD X-Ray Diffraction

Acknowledgements

I would like to thank my family and friends for all their support throughout my PhD studentship and the writing of this thesis.

This Thesis was carried out in relation to a Texas Instruments industry project and an EU GaNonCMOS project. There were many individuals within Tyndall National Institute's Magnetic on Silicon team who contributed to this work. To my supervisors, Paul and Cian, I would like to thank them for their guidance and steadfastness along this journey. I would like to thank Ricky Anthony, Zahra Ghaferi, Liang Ye, and Guannan Wei for their role in the physical depositions of the various magnetic films.

Abstract

This thesis investigates the challenges of integrating thin film magnetics into advanced organic substrates for Power Supply in Package (PwrSiP) applications. The surface conditions of the substrate on which the thin films were deposited was found to play a critical role in terms of the magnetic performance and efficacy of the material used as the magnetic passive component. Whence, planarization of the underlying substrate, or a release process with which the magnetic core could be deposited, and later liberated from a polymer layer spun on smooth Si were developed in order to address the issue of surface roughness of the underlying substrate.

The released magnetic thin films were incorporated into advanced organic substrates by three methods, as follows: 1) the integration of the released magnetic core using wirebonds; 2) the embedding of the released magnetic material using a Flip-Chip approach; 3) fully embedding the released magnetic material between the prepreg layers in the PCB stack.

Finally, methods for the modelling and characterisation of the magnetisation dynamics of thin film magnetics were developed. The modelling of the magnetisation dynamics comprises two approaches: 1) development of software which enables large scale numeric modelling of the magnetic thin films using graphical processing units; 2) development of analytical models to characterise the magnetisation dynamics of magnetic thin films. Both the analytic and numeric methods were developed in order to characterise the issue of surface roughness in magnetic thin films, which was found to result in severely degraded magnetic performance. Furthermore, the thickness dependent multimodal behaviour of amorphous CZTB films spanning thickness 80nm – 500nm were investigated using Brown's continuous diffusion model of magnetic spins. It was found that there is a critical film thickness whereat there is a breakdown in the induced uniaxial anisotropy within the film, and hence, that thickness should be considered the maximum useful thickness of the material in ultra-low loss PwrSiP applications.

Chapter 1

Introduction

1.1 Introduction

The ongoing trend in electronic systems has been one of continuous miniaturisation of the electronic active and passive components, and of additional functionality required by the individual functional blocks in order to deliver increased processing capabilities [1]. The effects of this miniaturisation trend are most noticeable in the area of mobile phones and high performance computing. Indeed, the ever increasing processing capabilities has been achieved by the exponential increase in the number of functional blocks and processors used by these electronic products. This exponential increase in functionality has resulted in a proliferation of power rails required to effectively deliver power to these increasing complex systems. This poses a significant challenge for power management, especially in portable electronics which operate with a limited battery, to deliver the maximum operational battery charge time for the end-user.

A popular method for reducing the power consumption of multicore processors, and so increase battery longevity, is the use of Dynamic Voltage and Frequency Scaling (DVFS) [2–5]. This involves the rapid modulation of the supply voltage to the micro-processor based on the time-dependent particular demand. However the effectiveness of DVFS is determined by how fast the supply voltage can respond to the time dependent power requirement of the processor and hence DVFS is hampered by poor voltage transients which may arise due to unwanted parasitics. Thus there is a need to minimise the distance between the power supply module and the processor. Therefore, in order for the full benefits of DVFS, power supply modules must become ever more distributed and closer to the Point of Load (POL). A potential solution to this is the integration of the voltage regulator into a substrate forming a complete Power Supply in Package (PwrSiP) which can be local to the POL, cf Fig. 1.1.

As can been seen from Fig. 1.1 there is a move from systems being powered by a singular external power supply to a more discrete, or granular solution wherein the power supply is as close to the POL. However, traditionally the magnetic component of the voltage regulator have been bulky and act as a roadblock to an integrated granular power supply. There is significant

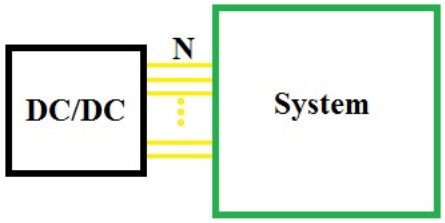

(a)

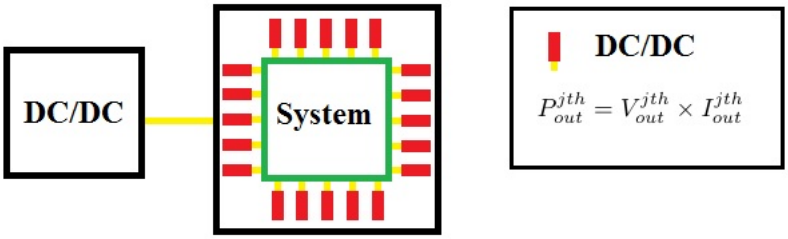

(b)

(c)

Figure 1.1: Illustration of PwrSiP. (a) High level illustration of system being powered by a single DC-DC converter with N distinct power rails. (b & c) High level illustration of power being delivered to a system by N DC-DC converters local to the system. Here the N DC-DC converters are *integrated* within the package and close to the POL. Image (b) presents the top-down view. Image (c) presents the cross-sectional view. Note here the term monolithic is used to refer to a single structure

activity in both research and academia for the integration of the magnetic component into the package. This typically involves the co-packaging of the semiconductor power die and the magnetic component, or by using the package as a substrate on which the semiconductor with an integrated magnetic component will be mounted. Note, the use of integrated magnetics on silicon**Si** for power delivery forms the interesting topic of Power Supply on Chip (PwrSoC). In the latter instance the solution provided by PwrSoC is embedded, or co-packaged forming a PwrSiP solution, whereas in the former the power die is co-packed with a discrete magnetic component. The main benefit of integrating the magnetic component into the package is that it can handle higher currents than its PwrSoC counterpart. The better current handling capabilities of package level integration arises due to the ease at which thicker copper traces can be electroplated in standard PCB manufacturing. Indeed package level integration of the magnetic component has been demonstrated to provide the high current and fast transient response required for a granular DVFS power supply [6–8]. Thus further integration of the magnetic passive components into the package substrate is seen as a critical requirement for the miniaturisation of the power supply module and the realisation of very high power densities required for future electronic devices [7, 9, 10].

A key enabling factor for the integration of magnetic passives into package is the ever increasing switching speed of the active MOSFET components in

the DC-DC converter [11]. The increased operating speed of the converter has facilitated a volumetric reduction in the amount of the magnetic passive components required in the converter, viz Faraday's law. This reduction in the size of the magnetic component has allowed researchers to either; 1) integrate the magnetic component directly onto the silicon power IC – forming a PwrSoC; or 2) incorporate the magnetic passive into the package housing the power IC – forming a PwrSiP. The integration of the magnetic component into the package, or onto the silicon IC, is a critical requirement for further miniaturisation of the power supply and the realisation of the very high power densities required by future electronic devices [12–14].

There are several magnetic material candidates to be used as the energy storage component in the converter. The ideal "soft" magnetic material would exhibit; 1) high magnetisation saturation; 2) low coercivity; 3) a large anisotropy field; 4) high magnetic susceptibility ($\approx$ permeability); and 5) large resistivity. Whilst ferrite materials have the large resistivity required to stymie eddy current formation within the core, their inherently low magnetisation saturation results in increasing hysteresis loss with increasing frequency – Snoek's law [15]. This makes them a poor choice for the magnetic passive components in DC-DC converters as they would have to employ methods to circumvent Snoek's relation. This typically involves drastically reducing the permeability of the material [16–18] in order to stave off high frequency hysteretic losses. Soft thin film magnetics (such as NiFe,

CoZrTaB, CoZrO, CoZrTa, etc...) on the other hand, simultaneously exhibit the desired magnetic properties 1- 4. However, the main drawback of such materials is that they are highly conductive as compared to ferrites. Whence, efforts must be taken to prevent large eddy formations within them. The prevention of eddy current formation is achieved through the limitation of the thin films thickness to be less than one "skin-depth" of the material at the desired operating frequency. Thus the thickness of the film is restricted by Eq. 1.1.1

$$\delta = \sqrt{\frac{2\rho}{\omega\mu}}. \tag{1.1.1}$$

Here ρ is the resistivity of the material, ω is the frequency of the applied magnetic field, and μ is the permeability of the material. As can be seen from Eq. 1.1.1, the thickness of the magnetic film must be reduced with increasing frequency. However, on decreasing the thickness of the film, the effects of the boundary conditions on magnetic performance become more prevalent.

In the next section the key technology trends and drivers for the integration of magnetic passives into package is discussed.

1.2 Technology Trends & Drivers

The realisation of a fully integrated PwrSiP is enabled by the ever increasing switching speeds of the control switches used in the power supply module. This increase in the active component switching frequency reduces the

amount of the passive storage component needed for power modules. Hence, the magnetic passive component can be incorporated into the substrate, on which the power die can later be mounted, and a plastic mould used to form a fully integrated PwrSiP. The miniaturisation trend enabled by increasing switching frequencies of the DC-DC converter has resulted in the reduction of the amount of passives needed has resulted in a decrease in the overall size of power supply modules leading to higher power densities, cf Fig. 1.2. This is a very tractable solution for applications which have very limited free space on the PCB and which require the power supply to be near the POL. Indeed, several PwrSiP products exist from companies, such as "Cypress Semiconductor Corporation", "Enpirion", "Texas Instruments".

There are several key technologies by which the magnetic component of the power supply are being fully integrated into the package. They are as follows: 1) Embedded bulk ferrite in the PCB substrate; 2) ferrite particles dispersed in a polymer matrix which is then integrated into package; 3) ferrite tapes incorporated into Low Temperature Co-Fired Ceramic (LTCC) stacks; and 4) integrated thin film magnetics. These various magnetic integration methods are fully discussed in Section 2.1 of the next chapter. In order to illustrate potentially useful magnetic materials for future PwrSiP applications the power density vs switching frequency of DC-DC converters using various magnetic materials is plotted, cf Fig. 1.3. It is evident from this figure that integrated thin film magnetics, which have already been realised in PwrSoC, exhibit the

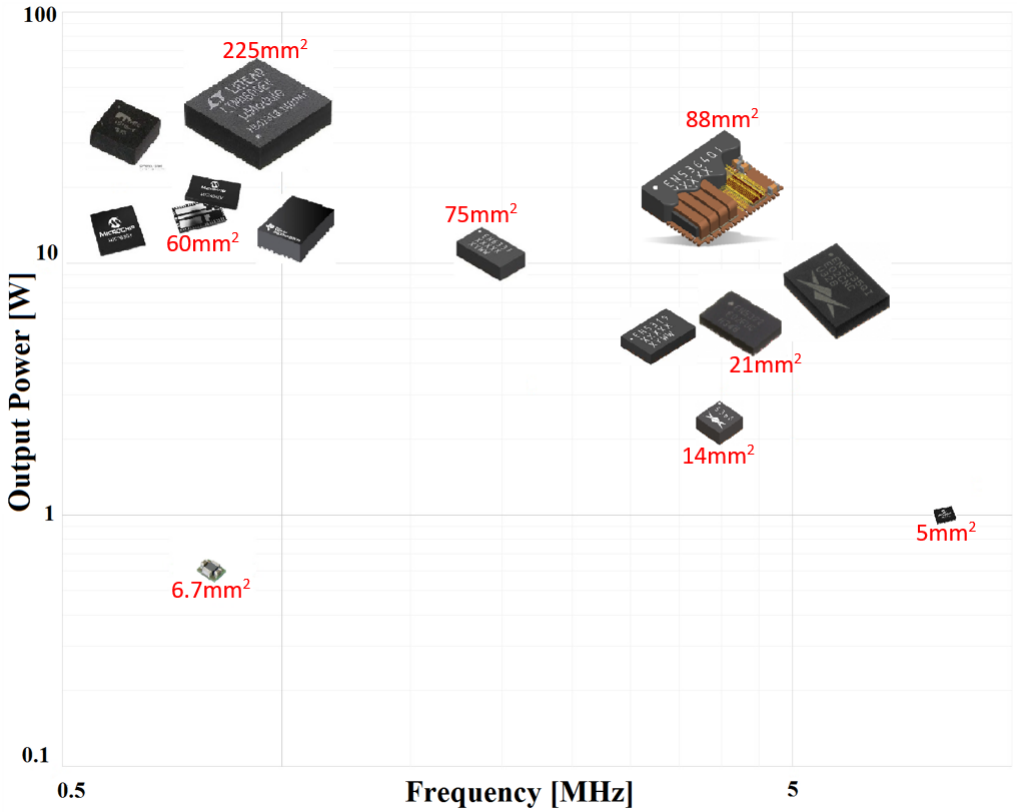

Figure 1.2: Concept evolution of PwrSiP. Figure illustrates the trend of reduced power module footprint with increasing frequency. See Table 1.1 for details.

high power densities in the 10s of MHz frequency range desired for future PwrSiP applications [19–22]. Moreover, such integrated magnetics on silicon have been incorporated by several researchers into package and demonstrated in DC-DC converters, forming a complete PwrSiP [23, 24].

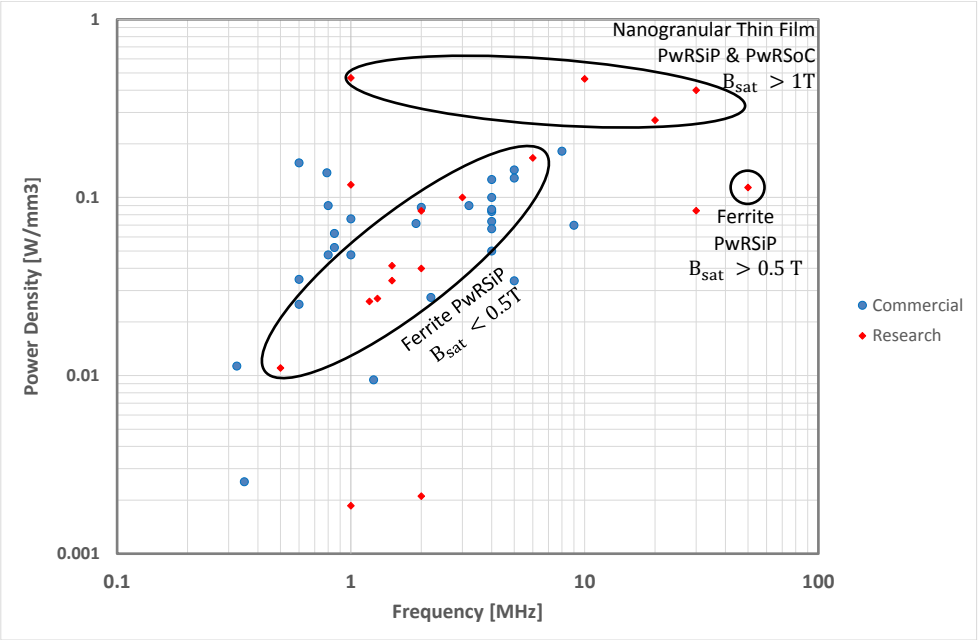

Figure 1.3: Power Density of DC-DC converters for PwrSiP & PwrSoC. Note the three groupings illustrate the importance of B_{sat} in terms of the power density and operating frequency of the device. See Table 1.1 for details.

[a]This is *only* the inductor power density and not the power density of the DC-DC converter.

[b]This is the efficiency the authors predict if the component was used in a DC-DC converter.

DC-DC converters for PwrSiP & PwrSoC (Commercial)								
Frequency [MHz]	Volume [mm^3]	Footprint [mm^2]	Package Type/ Magnetic Material	Power Density [W/mm^3]	Efficiency	Component Id/ Author	Institution	Year
0.85	630	225	LGA	0.0063	90.5	LTM4601	Linear Technology	-
0.85	630	225	LGA	0.0052	87	LTM4600	Linear Technology	-
0.8	630	225	LGA	0.0048	93	LTM4606	Linear Technology	-
1.25	634.5	225	LGA	0.009	80	LTM4614	Linear Technology	-
0.325	292	103.5	LGA	0.0113	87	LTM8022	Linear Technology	-
0.6	192	64	QFN	0.1562	90	MIC45116	Microchip Technology Inc.	2016
0.79	120	60	QFN	0.1375	82	MIC45404	Microchip Technology Inc.	2015
0.6	432	144	QFN	0.0347	91	MIC28303	Microchip Technology Inc.	2017
8	5.5	5	HJDFN	0.1818	80	MIC33030	Microchip Technology Inc.	2018
1	264	88	QFN	0.0758	92	EN2342QI	Enpirion Inc.	2019
2	150	60	QFN	0.088	91	EN6340QI	Enpirion Inc.	2018
1.9	138.75	75	QFN	0.0714	92	EN6337QI	Enpirion Inc.	2019
5	290.45	157	QFN	0.0341	88	EN5335QI	Enpirion Inc.	2019
4	90	50	QFN	0.0778	88	EN5322QI	Enpirion Inc.	2019
4	44	40	QFN	0.1261	87	EP53F8QI	Enpirion Inc.	2019
3.2	55	50	QFN	0.09	90	EN5319QI	Enpirion Inc.	2018
5	23.1	21	QFN	0.1429	87	EP53A7xQI	Enpirion Inc.	2019
4	39.6	36	QFN	0.0833	85	EN5311QI	Enpirion Inc.	2019
2.2	120.25	65	QFN	0.0274	92	EN6310QI	Enpirion Inc.	2018
4	30.8	28	QFN	0.0857	85	EP5388QI	Enpirion Inc.	2019
4	39.6	36	QFN	0.0667	87	EP53x2QI Family	Enpirion Inc.	2018
4	23.1	21	QFN	0.1	85	EP5368QI	Enpirion Inc.	2019
5	15.4	14	QFN	0.1286	90	EP5357xUI	Enpirion Inc.	2019
4	39.6	36	QFN	0.05	88	EP53x2QI Family	Enpirion Inc.	2018
9	18.9	21	μQFN	0.07	87	EP5348UI	Enpirion Inc.	2019
1	277.2	99	BQFN	0.0476	92	TPS84410	Texas Instruments	2018
0.8	7.4	6.67	MicroSiP	0.09	93	TPS82740x	Texas Instruments	2014
0.6	787.5	225	QFN	0.0251	90	ISL8204M	Intersil	2014
0.35	1960	196	-	0.0025	91	BR300	Sanken	2013
DC-DC converters for PwrSiP & PwrSoC (Research)								
1.3	784	2195.2	NiCuZn	0.0758	85	Lee [25]	Virginia Polytechnic Institute and State University	2010
1.5	1406.2	158	ESL-40011	0.0341	85	Gilham [26]	Virginia Tech	2012
1.5	870	150	Senfoliage	0.0412	87	Su [7]	Virginia Tech	2013
1.2	230	69	FeSiAl	0.0261	-	Cao, [27]	Hanyang University	2014
1	504	126	Senfoliage	0.1179	-	Hou [28]	Virginia Polytechnic and State University	2015
2	450.4	132.48	NiCuZn	0.04	-	Zhang [29]	Virginia Polytechnic Institute and State University	2014
2	1188	330	MnZn	0.002	-	Perrin [30]	Univ. Lyon	2016
1	10.24	10.24	FeBSiC	0.4689	77	Endo [24]	Tohoku University	2015
1	1076.4	414	Ferroxcube ER-9.5	0.0019	-	Sun [31]	Virginia Tech	2016
30	7.12	8.9	NiFe	0.0843	70	Wang [23]	Tyndall National Institute	2010
50	7.92	9	ZnFe	0.1136	74	Yanagihara [32]	Tokyo Institute of Technology	2015
3	1.215	5.76	NiZn	0.1	70	Sugahara [33]	Fuji Electric Company	2012
6	5.4	9	NiZn	0.1667	74	Wang [22]	University of Florida	2010
0.5	5984	2200	MnZn	0.011	66	Chen [34]	Jiaotong University	2007
20	12.15	13.5	-	0.2716	-	Zhang [19]	Enpirion Inc.	2012
2	15	25	NiZn	0.084	-	Mikura [35]	Kyocera Corporation	2006
30	0.4	1	CoZrO	0.4[a]	-	Qiu [36]	Dartmouth College	2012
10	5	12.474	CoZrO	0.5833[a]	88[b]	Prabhakaran [37]	Dartmouth College	2003
4	10.28	31.36	MnZn	0.5833	-	Dang [21]	The University of Alabama	2014

Table 1.1: Electrical characteristics of DC-DC converters for PwrSiP & PwrSoC applications.

As can be seen from Fig. 1.3, ferrite inductors, used as the magnetic component in low power (Watts < 5) PwrSoC applications, have severely diminishing power densities at higher frequencies. This is due to the poorer hysteresis losses of ferrites in the MHz frequency range. The reason ferrites have significantly higher hysteresis losses is due to the frequency dependent deterioration in their magnetic permeability, which stems from their much lower magnetic saturation field (typically 0.3T $\sim$ 0.6T) as compared to that of soft thin film magnetics (typically 1T $\sim$ 2.5T). This effect arises because there is a linear relationship between the product of the permeability and the resonance frequency of the material, and the magnetic field at which it saturates. This relationship is given in eq. 1.2.1. In Eq. 1.2.1 μ is the permeability, ω_0 is the ferromagnetic resonance frequency, and B_s is the field at which the material saturates.

$$\mu\omega_0 \propto B_s \tag{1.2.1}$$

Hence, extending the frequency response of ferrites results in a decrease in the magnetic permeability and loss in performance. Typically the high frequency performance of ferrites is extended by milling the ferrite material into fine particles and dispersing them in a polymer to form a composite (see Section 2.1).

The relatively high hysteresis losses of ferrites can be modelled using the Steinmetz equation, eq. 1.2.2

$$P_d = k f^{\alpha} B^{\beta} \tag{1.2.2}$$

Here P_d is the power loss density of the core, and k, α, and β are parameters which are selected to best fit the core loss data. Typical values for α and β for MnZn ferrites are 1 - 2, and 2 – 3, respectively [38]. Thus the core loss density of ferrites is heavily influenced by the amplitude of the magnetic field. One way to mitigate the high frequency losses of ferrites is therefore to limit the amplitude of the applied magnetic field in the core to be a small fraction of their saturation. Indeed, in the very low applied field limit ($B < 10$ mT) ferrites can effectively operate in the 10s of MHz frequency range [39]. However, this drastically reduces the power density of the storage passive component as the magnetic field energy density (E_d) is proportional to the square amplitude of the magnetic field, see eq. 1.2.3.

$$E_d = \frac{B^2}{2\mu} \tag{1.2.3}$$

Considering eqs. 1.2.2 and 1.2.3 it is evident that magnetic thin films operating in the Very High Frequency (VHF) range can have power densities significantly higher than that of their ferrite counterparts owing to the fact

that they do not have to limit the amplitude of the driving field in order to stave off high frequency losses. This males magnetic thin films a tractable solution for PwrSiP applications which require high power density at MHz switching speeds. This trade-off between the magnitude of the magnetic field, switching frequency, energy density, and power loss density, are entirely determined by the Steinmetz parameters α and β (see Eq. 1.2.4).

$$\frac{E_D}{P_D} = \left(\frac{1}{2\mu k f^{\alpha}}\right)\frac{B^2}{B^{\beta}} \tag{1.2.4}$$

In Fig. 1.4 the output power of DC-DC converters with integrated magnetics against the switching speed is plotted. There is a clear trend that the output power of DC-DC converters using ferrites rapidly decreases as the switching frequency increases. This is a direct consequence of the inability of ferrites to effectively handle large energy densities in the VHF range without an exponential increase in loss density. However DC-DC converters which utilise soft thin film magnetics have been well demonstrated to provide power for low power applications in the VHF frequency range.

[c]The National Microelectronics Research Centre would later become Tyndall National Institute.

Integrated Magnetics for PwrSiP & PwrSoC						
Frequency [MHz]	Power [W]	Material	Deposition	Author	Institution	Year
30	1.8	NiFe	Electroplated	Wang [23]	Tyndall National Institute	2010
8	0.9	NiFe	Electroplated	Wang [40]	Tyndall National Institute	2008
80	1.6	NiFe	Electroplated	Feeney [41]	Tyndall National Institute	2015
20	1.8	NiFe	Electroplated	Feeney [42]	Tyndall National Institute	2014
2.2	2	NiFe	Electroplated	Park [43]	Georgia Institute of Technology	2004
40	0.48	NiFe	Electroplated	Wang [44]	Tyndall National Institute	2013
1	1.65	NiFe	Electroplated	Ludwig [45]	National Microelectronics Research Centre[c]	2003
20	0.225	NiFe	Electroplated	Meere [46]	Tyndall National Institute	2009
2	0.4	NiFe	Electroplated	Brunet [47]	National Microelectronic Research Center[c]	2002
6	0.25	NiFe	Electroplated	Iyengar [48]	University of Cincinnati	1999
5	5	NiFe	Electroplated	Galle [49]	Georgia Institute of Technology	2007
7.5	3.5	NiFe	Electroplated	O'Donnell [50]	National Microelectronic Research Center[c]	2004
5	1.5	NiFe	RF Magnetron Sputtering	Yun [51]	Hoseo University	2004
5	0.5	NiFe	Electroplated	Musunuri [52]	University of Illinois	2005
20	0.6	NiFe	Electroplated	O'Donnell [53]	Tyndall National Institute	2008
2	5	MnZn	-	Perrin [30]	Univ. Lyon	2016
4	6	MnZn	-	Dang [21]	The University of Alabama	2014
0.5	66	MnZn	-	Chen [34]	Jiaotong University	2007
0.35	275	MnZn	-	Gong [6]	Jiaotong University	2008
1	2	MnZn	-	Sun [54]	Virginia Tech	2017
0.35	125	MnZn	-	Fujiwara [55]	Matsushita Electric Works	1998
0.5	10	MnZn	-	Pernia [56]	Universidad de Oviedo	2004
1	4	MnZn	Ferrite Polymer Composite(s) (FPC)	Kowase [57]	Shinshu University	2005
1.3	24	MnZn	LTCC	Ball [58]	Virginia Polytechnic Institute and State University	2008
1	3.3	NiZn	Embedded	Sun [31]	Virginia Tech	2016
3	0.72	NiZn	Ferrite Substrate	Sugahara [33]	Fuji Electric Company	2012
5	18	NiZn	LTCC	Li [59]	Virginia Polytechnic Institute and State University	2011
6	0.45	NiZn	FPC	Wang [22]	University of Florida	2010
0.36	00	NiZn	FPC	Cheng [60]	The Hong Kong Polytechnic University	2011
2	1.26	NiZn	LTCC	Mikura [35]	Kyocera Corporation	2006

Table 1.2: Comparison of integrated magnetics for PwrSiP versus PwrSoC.

Integrated Magnetics for PwrSiP & PwrSoC (*continued*)						
Frequency [MHz]	Power [W]	Material	Deposition	Author	Institution	Year
8.3	30	CoZrO	Sputtered	Harburg [61]	Dartmouth	2013
5	14.4	CoZrO	Sputtered	Prabhakaran [62]	Dartmouth	2005
30	10	CoZrO	Magnetron Sputtered	Qiu [36]	Dartmouth	2012
100	3.3	CoZrO	Magnetron Sputtered	Yao [63]	Dartmouth	2012
10	2.31	CoZrO	Reactive Sputtered	Prabhakaran [37]	Dartmouth	2003
1.3	59.4	NiCuZn	LTCC	Lim [25]	Virginia Polytechnic Institute and State University	2010
1.5	22	NiCuZn	LTCC	Zhang [29]	Virginia Polytechnic Institute and State University	2014
4	2.2	NiCuZn	LTCC	Lim [64]	Virginia Polytechnic Institute and State University	2008
1	1.32	NiCuZn	LTCC	Moon [65]	Hanyang University	2005
1.2	36	FeSiAl	Polymer Compound	Cao [27]	Hanyang University	2014
1.2	2	FeSiAl	Polymer Compound	Lim [66]	Hanyang University	2018
1	4.8	FeBSiC	Polymer Compound	Endo [24]	Tohoku University	2015
1.8	1.5	FeBN	RF Magnetron Sputtered	Kim [67]	Tohoku University	2002
1.2	1.05	FeTaN	Reactive Sputtered	Kim [68]	Hong-Ik University	2001
18	3.3	FeCo	Electroplated	Liakopoulos [20]	Enpiron Inc	2012
10	6.5	CoNiFe	Electroplated	Kim [69]	Georgia Institute of Technology	2015
1.84	0.515	CoFeNi	Melt Spun	Moazenzadeh [70]	University of Freiburg	2014
1	30	CoNiFe	Electroplated	Kelly [71]	NUI Galway	2007
40	0.9	ZnFe	FPC	Hagita [32]	SHINKO Electric Industries	2015
1.5	48	Ferrite	LTCC	Li [26]	Virginia Tech	2012
1.5	36	Ferrite	Flake Composite	Su [7]	Virginia Tech	2013
1	24	Ferrite	FPC	Hou [28]	Virginia Polytechnic and State University	2015
1	18	Ferrite	LTCC	Huang [72]	Northeastern University	2016
5	2	Ferrite	FPC	Jia [73]	University of Central Florida	2010
20	0.855	Ferrite	-	Zhang [19]	Enpirion, Inc	2012
5	94	Ferrite	FPC	Tang [74]	City University of Hong Kong	2001
70	0.6	Ferrite	-	Chia [75]	National Chung Hsing University	2014

Table 1.2: Comparison of integrated magnetics for PwrSiP versus PwrSoC (*continued*).

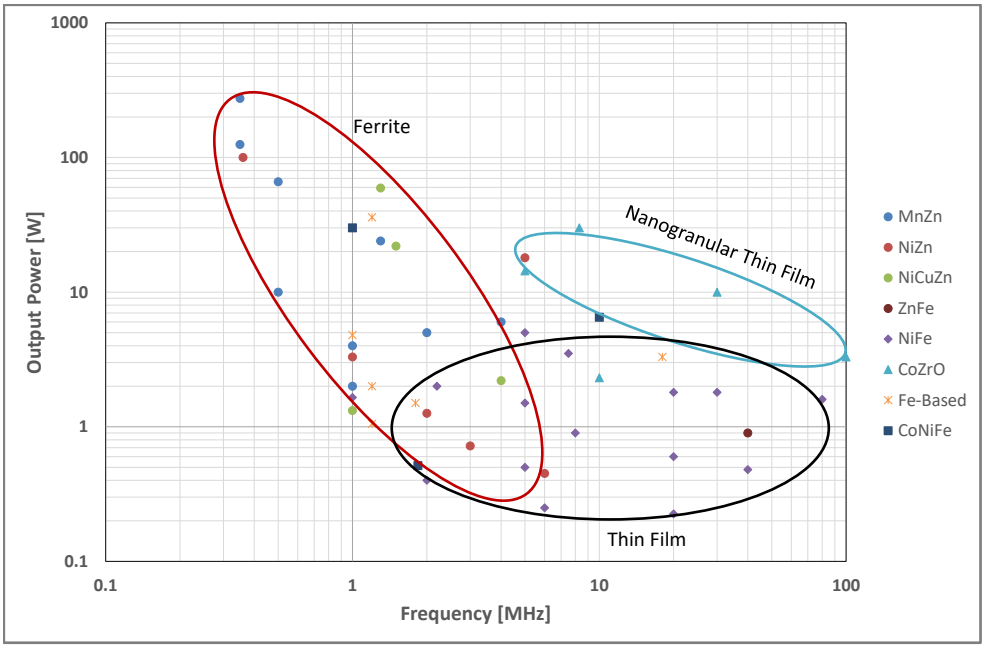

Figure 1.4: Comparison of integrated magnetics for PwrSiP versus PwrSoC. See Table 1.2 for details.

Thus it is clear that thin film magnetics are an ideal candidate for future PwrSiP applications, as they exhibit the excellent soft magnetic properties required in order to continue the trend of device miniaturisation. It is therefore useful to consider the exact manufacturing techniques used to realise integrated magnetics in PwrSiP. There are several manufacturing processes by which the magnetic component of the voltage regulator is being integrated into substrates for the purpose of PwrSiP. The main methods for integrating the magnetic component are as follows: 1) Embedding Bulk ferrite cores into

the Prepreg of the PCB; 2) Dispersing fine ferrite powders into a polymer, or epoxy, and then using standard screen printing technologies; 3) Incorporating ferrite tapes into the Low Temperature Co-Fired Ceramic manufacturing process; 4) Integrating Thin Film Magnetics into PCB via electroplating, embedding, or using wirebonds. While this thesis outlines the fabrication methods associated with the creation of integrated magnetics utilizing methods 1 - 3, our main focus is the detailed investigation of the experimental and theoretical aspects of method 4.

1.3 Executive Summary of Research & Thesis Outline

This section provides the reader with an outline of the structure of this Thesis and an overview of the major ideas presented therein.

Chapter 2 reviews existing technologies for the integration of magnetic materials used in PwrSiP applications. The strengths and weakness of those technologies are discussed along with benchmarking and performance analysis. Whence, chapter 2 serves as context for integrated thin film magnetics in advanced organic substrates for PwrSiP applications.

Chapter 3 outlines the experimental fabrication procedure used for the deposition of the magnetic thin films. During experiment it was observed that

the magnetic efficacy of films deposited on the PCB substrate was inferior to those deposited on Si. The surface roughness of the PCB substrate was determined to be the issue. Indeed, the Surface Roughness to Thickness Ratio (SRT) ratio of the thin film was determined to be a key limiting factor for their successful use in PwrSiP applications. Two processes were developed[a] in order to address this issue. The first approach sought to planarise the underlying PCB substrate through the application of a planarising polymer agent. The second approach developed a release process through which magnetic thin films deposited on silicon could be liberated, and then integrated into a PwrSiP application.

Chapter 4 pertains to the manufacture of the integrated magnetic inductor structures which utilised the released magnetic thin films. There were three generations of inductor considered in this work. The first generation used a PCB substrate and wirebonds to integrate the magnetic core [76]. The second generation used a "Flip-Chip" method to embed the magnetic core between two PCBs [77]. The third generation approach fully embedded the magnetic core within the prepreg layers of the PCB stack. This was by far the most complex approach and required the industry partnership with AT&S in order to do the embedding.

[a]There are other individuals within Tyndall National Institute's Magnetic on Silicon team who contributed to these development processes. They are rightly acknowledged as contributing authors on the relevant publications which stem from this thesis.

Chapter 5 pertains to the numeric and analytical models developed to characterise the magnetic thin films. As found in chapter 3, the surface roughness had a major influence in the magnetisation dynamics of the thin films. Two approaches were adopted in order to model this influence, one numeric, the other, analytic.

The numeric modelling approach used Object Oriented Programming (OOP) to create magnetic objects with inherent magnetic properties. This approach was conceptually very simple. First, the *continuous* surface of the magnetic thin film was approximated by a *discrete* mesh. Then the Gaussian distribution was mapped onto that mesh in order the surface roughness. Hence, the mean of the Gaussian determined the films thickness, and the roughness was modelled through the variance of the Gaussian. The simulator was deployed on a Graphics Processing Unit (GPU) using Compute Unified Device Architecture (CUDA) libraries in order to reduce simulation runtime. The simulator was verified against Micromagnetic Modelling Activity Group (μmag) standard problem #4.

The analytic modelling approach used Brown's continuous diffusion model of magnetic spins to treat the issue of surface roughness, and film thickness, in the magnetisation dynamics of magnetic thin films. Historically Brown's diffusion model was developed in order to understand the role of thermal fluctuations in the magnetisation dynamics of single domain magnetic parti-

cles. Brown's model was adapted to treat the issue of surface roughness as both surface roughness and thermal fluctuations shared identical statistical properties, namely both are sources of zero mean Additive White Gaussian Noise (AWGN).

Furthermore, Brown's model was later adapted to characterise the thickness dependent degradation of the induced in-plane uniaxial anisotropy in amorphous CZTB thin films spanning 80nm to 500nm thicknesses.

Chapter 6 provides a summary of the key findings of our work, and discussion on future works required. Further, this chapter lists the publications which stem from this thesis, and the conferences attended during the course of my PhD studentship.

Bibliography

[1] C. Ó. Mathúna, N. Wang, S. Kulkarni, and S. Roy, "Review of integrated magnetics for power supply on chip (pwrsoc)," *IEEE Transactions on Power Electronics*, vol. 27, no. 11, pp. 4799–4816, 2012.

[2] S. Eyerman and L. Eeckhout, "Fine-grained dvfs using on-chip regulators," *ACM Transactions on Architecture and Code Optimization (TACO)*, vol. 8, no. 1, p. 1, 2011.

[3] C. Isci, A. Buyuktosunoglu, C.-Y. Cher, P. Bose, and M. Martonosi, "An analysis of efficient multi-core global power management policies: Maximizing performance for a given power budget," in *Proceedings of the 39th annual IEEE/ACM international symposium on microarchitecture*, pp. 347–358, IEEE Computer Society, 2006.

[4] Q. Wu, P. Juang, M. Martonosi, and D. W. Clark, "Voltage and frequency control with adaptive reaction time in multiple-clock-domain processors," in *11th International Symposium on High-Performance Computer Architecture*, pp. 178–189, IEEE, 2005.

[5] W. Kim, M. S. Gupta, G.-Y. Wei, and D. Brooks, "System level analysis of fast, per-core dvfs using on-chip switching regulators," in *2008 IEEE 14th International Symposium on High Performance Computer Architecture*, pp. 123–134, IEEE, 2008.

[6] Z. Gong, Q. Chen, X. Yang, B. Yuan, W. Feng, and Z. Wang, "Design of high power density dc-dc converter based on embedded passive substrate," in *2008 IEEE Power Electronics Specialists Conference*, pp. 273–277, IEEE, 2008.

[7] Y. Su, W. Zhang, Q. Li, F. C. Lee, and M. Mu, "High frequency integrated point of load (pol) module with pcb embedded inductor substrate," in *2013 IEEE Energy Conversion Congress and Exposition*, pp. 1243–1250, IEEE, 2013.

[8] Y. Su, D. Hou, F. C. Lee, and Q. Li, "Low profile coupled inductor substrate with fast transient response," in *2015 IEEE Applied Power Electronics Conference and Exposition (APEC)*, pp. 1161–1168, IEEE, 2015.

[9] J. Popovic and J. Ferreira, "Converter concepts to increase the integration level," *IEEE transactions on power electronics*, vol. 20, no. 3, pp. 558–565, 2005.

[10] J. Popovic and J. Ferreira, "An approach to deal with packaging in

power electronics," *IEEE Transactions on Power Electronics*, vol. 20, no. 3, pp. 550–557, 2005.

[11] C. . Mathúna, N. Wang, S. Kulkarni, and S. Roy, "Review of integrated magnetics for power supply on chip (pwrsoc)," *IEEE Transactions on Power Electronics*, vol. 27, no. 11, pp. 4799–4816, 2012.

[12] J. Popovic and J. Ferreira, "An approach to deal with packaging in power electronics," *IEEE Transactions on Power Electronics*, vol. 20, no. 3, pp. 550–557, 2005.

[13] J. Popovic and J. Ferreira, "Converter concepts to increase the integration level," *IEEE transactions on power electronics*, vol. 20, no. 3, pp. 558–565, 2005.

[14] Z. Gong, Q. Chen, X. Yang, B. Yuan, W. Feng, and Z. Wang, "Design of high power density dc-dc converter based on embedded passive substrate," in *2008 IEEE Power Electronics Specialists Conference*, pp. 273–277, IEEE.

[15] J. M. Coey10, *Magnetism and magnetic materials*. Cambridge university press, 2010.

[16] Y. Sugawa, K. Ishidate, M. Sonehara, and T. Sato, "Carbonyl-iron/epoxy composite magnetic core for planar power inductor used in package-level power grid," *IEEE Transactions on Magnetics*, vol. 49, no. 7, pp. 4172–4175, 2013.

[17] S. Yan, L. Dong, Z. Chen, X. Wang, and Z. Feng, "The effect of the microstructure on the dc-bias superposition characteristic of nicuzn ferrite," *Journal of Magnetism and Magnetic Materials*, vol. 353, pp. 47–50, 2014.

[18] H.-I. Hsiang and J.-L. Wu, "Copper-rich phase segregation effects on the magnetic properties and dc-bias-superposition characteristic of nicuzn ferrites," *Journal of Magnetism and Magnetic Materials*, vol. 374, pp. 367–371, 2015.

[19] W. Zhang, M. A. Wilkowski, J. Weld, and A. Lotfi, "A 20mhz monolithic dc-dc converter manufactured with the first commercially viable silicon magnetics technology," in *Proceedings of The 7th International Power Electronics and Motion Control Conference*, vol. 1, pp. 705–712, IEEE, 2012.

[20] T. Liakopoulos, A. Panda, M. Wilkowski, A. Lotfi, K. Tan, L. Zhang, C. Lai, and D. Chen, "Introducing fca, a new alloy for power systems on a chip and wafer level magnetic applications," in *2012 13th International Conference on Electronic Packaging Technology & High Density Packaging*, pp. 949–954, IEEE, 2012.

[21] Z. Dang and J. A. A. Qahouq, "On-chip coupled power inductor for switching power converters," in *2014 IEEE Applied Power Electronics Conference and Exposition-APEC 2014*, pp. 2854–2859, IEEE, 2014.

[22] M. Wang, J. Li, K. D. Ngo, and H. Xie, "A novel integrated power inductor in silicon substrate for ultra-compact power supplies," in *2010 Twenty-Fifth Annual IEEE Applied Power Electronics Conference and Exposition (APEC)*, pp. 2036–2041, IEEE, 2010.

[23] N. Wang, J. Hannon, R. Foley, K. McCarthy, T. O'Donnell, K. Rodgers, F. Waldron, and C. Ó. Mathúna, "Integrated magnetics on silicon for power supply in package (psip) and power supply on chip (pwrsoc)," in *3rd Electronics System Integration Technology Conference ESTC*, pp. 1–6, IEEE, 2010.

[24] Y. Endo, H. Sato, T. Miyazaki, M. Yamaguchi, H. Kamada, M. Takahashi, M. Sakamoto, S. Maita, N. Kato, Y. Yorozu, *et al.*, "Study on the electric performances of planar inductor with fe-system magnetic flake composite integrated for sip dc-to-dc converter applications," *IEEE Transactions on Magnetics*, vol. 51, no. 11, pp. 1–4, 2015.

[25] M. H. F. Lim, J. D. van Wyk, and F. C. Lee, "Hybrid integration of a low-voltage, high-current power supply buck converter with an ltcc substrate inductor," *IEEE Transactions on Power Electronics*, vol. 25, no. 9, pp. 2287–2298, 2010.

[26] Q. Li, Y. Dong, F. C. Lee, and D. J. Gilham, "High-density low-profile coupled inductor design for integrated point-of-load converters," *IEEE Transactions on Power Electronics*, vol. 28, no. 1, pp. 547–554, 2012.

[27] G. Cao, H.-J. Kim, S.-T. Lim, G.-S. Han, *et al.*, "An embedded inductor using sendust powder composite films for step-up dc–dc converter," *IEEE Transactions on Magnetics*, vol. 50, no. 11, pp. 1–4, 2014.

[28] D. Hou, Y. Su, Q. Li, and F. C. Lee, "Improving the efficiency and dynamics of 3d integrated pol," in *2015 IEEE Applied Power Electronics Conference and Exposition (APEC)*, pp. 140–145, IEEE, 2015.

[29] W. Zhang, Y. Su, M. Mu, D. J. Gilham, Q. Li, and F. C. Lee, "High-density integration of high-frequency high-current point-of-load (pol) modules with planar inductors," *IEEE transactions on Power Electronics*, vol. 30, no. 3, pp. 1421–1431, 2014.

[30] R. Perrin, B. Allard, C. Buttay, N. Quentin, W. Zhang, R. Burgos, D. Boroyevic, P. Preciat, and D. Martineau, "2 mhz high-density integrated power supply for gate driver in high-temperature applications," in *2016 IEEE Applied Power Electronics Conference and Exposition (APEC)*, pp. 524–528, IEEE, 2016.

[31] B. Sun, R. Burgos, D. Boroyevich, R. Perrin, C. Buttay, B. Allard, N. Quentin, and M. Ali, "Two comparison-alternative high temperature pcb-embedded transformer designs for a 2 w gate driver power supply," in *2016 IEEE Energy Conversion Congress and Exposition (ECCE)*, pp. 1–7, IEEE, 2016.

[32] K. Hagita, Y. Yazaki, Y. Kondo, M. Sonehara, T. Sato, T. Fujii,

K. Kobayashi, S. Nakazawa, H. Shimizu, T. Watanabe, *et al.*, "Cmos switch buck dc-dc converter fabricated in organic interposer with embedded zn-fe ferrite core inductor," *Journal of the Magnetics Society of Japan*, p. 1501R002, 2015.

[33] S. Sugahara, K. Yamada, M. Edo, T. Sato, and K. Yamasawa, "90% high efficiency and 100-w/cm high power density integrated dc-dc converter for cellular phones," *IEEE transactions on power electronics*, vol. 28, no. 4, pp. 1994–2004, 2012.

[34] Q. Chen, Z. Gong, X. Yang, Z. Wang, and L. Zhang, "Design considerations for passive substrate with ferrite materials embedded in printed circuit board (pcb)," in *2007 IEEE Power Electronics Specialists Conference*, pp. 1043–1047, IEEE, 2007.

[35] T. Mikura, K. Nakahara, K. Ikeda, K. Furukuwa, and K. Onitsuka, "New substrate for micro dc-dc converter," in *56th Electronic Components and Technology Conference 2006*, pp. 5–pp, IEEE, 2006.

[36] J. Qiu and C. R. Sullivan, "Design and fabrication of vhf tapped power inductors using nanogranular magnetic films," *IEEE Transactions on Power Electronics*, vol. 27, no. 12, pp. 4965–4975, 2012.

[37] S. Prabhakaran, C. R. Sullivan, and K. Venkatachalam, "Measured electrical performance of v-groove inductors for microprocessor power de-

livery," *IEEE Transactions on Magnetics*, vol. 39, no. 5, pp. 3190–3192, 2003.

[38] C. R. Sullivan, D. V. Harburg, J. Qiu, C. G. Levey, and D. Yao, "Integrating magnetics for on-chip power: A perspective," *IEEE Transactions on Power Electronics*, vol. 28, no. 9, pp. 4342–4353, 2013.

[39] A. J. Hanson, J. A. Belk, S. Lim, C. R. Sullivan, and D. J. Perreault, "Measurements and performance factor comparisons of magnetic materials at high frequency," *IEEE Transactions on Power Electronics*, vol. 31, no. 11, pp. 7909–7925, 2016.

[40] N. Wang, T. O'Donnell, R. Meere, F. M. Rhen, S. Roy, and S. C. O'Mathuna, "Thin-film-integrated power inductor on si and its performance in an 8-mhz buck converter," *IEEE Transactions on Magnetics*, vol. 44, no. 11, pp. 4096–4099, 2008.

[41] C. Feeney, N. Wang, S. Kulkarni, Z. Pavlović, C. Ó. Mathúna, and M. Duffy, "Optimization of coupled stripline microinductors in power supply on chip applications," *IEEE Transactions on Power Electronics*, vol. 31, no. 8, pp. 5805–5813, 2015.

[42] C. Feeney, N. Wang, S. C. Ó. Mathúna, and M. Duffy, "A 20-mhz 1.8-w dc–dc converter with parallel microinductors and improved light-load efficiency," *IEEE Transactions on Power Electronics*, vol. 30, no. 2, pp. 771–779, 2014.

[43] J.-W. Park, F. Cros, and M. G. Allen, "Planar spiral inductors with multilayer micrometer-scale laminated cores for compact-packaging power converter applications," *IEEE Transactions on Magnetics*, vol. 40, no. 4, pp. 2020–2022, 2004.

[44] N. Wang, J. Barry, J. Hannon, S. Kulkarni, R. Foley, K. McCarthy, K. Rodgers, F. Waldron, M. Barry, D. Casey, *et al.*, "High frequency dc-dc converter with co-packaged planar inductor and power ic," in *2013 IEEE 63rd Electronic Components and Technology Conference*, pp. 1946–1952, IEEE, 2013.

[45] M. Ludwig, M. Duffy, T. O'Donnell, P. McCloskey, and S. C. Ó. Mathùna, "Pcb integrated inductors for low power dc/dc converter," *IEEE Transactions on Power Electronics*, vol. 18, no. 4, pp. 937–945, 2003.

[46] R. Meere, T. O'donnell, N. Wang, N. Achotte, S. Kulkarni, and S. O'mathuna, "Size and performance tradeoffs in micro-inductors for high frequency dc-dc conversion," *IEEE Transactions on Magnetics*, vol. 45, no. 10, pp. 4234–4237, 2009.

[47] M. Brunet, T. o'Donnell, L. Baud, N. Wang, J. O'Brien, P. McCloskey, and S. C. O'Mathuna, "Electrical performance of microtransformers for dc-dc converter applications," *IEEE Transactions on Magnetics*, vol. 38, no. 5, pp. 3174–3176, 2002.

[48] S. Iyengar, T. M. Liakopoulos, and C. H. Ahn, "A dc/dc boost converter toward fully on-chip integration using new micromachined planar inductors," in *30th Annual IEEE Power Electronics Specialists Conference. Record.(Cat. No. 99CH36321)*, vol. 1, pp. 72–76, IEEE, 1999.

[49] P. Galle, X. Wu, L. Milner, S.-H. Kim, P. Johnson, P. Smeys, P. Hopper, K. Hwang, and M. G. Allen, "Ultra-compact power conversion based on a cmos-compatible microfabricated power inductor with minimized core losses," in *2007 Proceedings 57th Electronic Components and Technology Conference*, pp. 1889–1894, IEEE, 2007.

[50] T. O'Donnell, N. Wang, M. Brunet, S. Roy, A. Connell, J. Power, C. O'Mathuna, and P. McCloskey, "Thin film micro-transformers for future power conversion," in *Nineteenth Annual IEEE Applied Power Electronics Conference and Exposition, 2004. APEC'04.*, vol. 2, pp. 939–944, IEEE, 2004.

[51] E.-J. Yun, M. Jung, C. I. Cheon, and H. G. Nam, "Microfabrication and characteristics of low-power high-performance magnetic thin-film transformers," *IEEE transactions on magnetics*, vol. 40, no. 1, pp. 65–70, 2004.

[52] S. Musunuri, P. L. Chapman, J. Zou, and C. Liu, "Design issues for monolithic dc-dc converters," *IEEE Transactions on Power electronics*, vol. 20, no. 3, pp. 639–649, 2005.

[53] T. O'Donnell, N. Wang, R. Meere, F. Rhen, S. Roy, D. O'Sullivan, and C. O'Mathuna, "Microfabricated inductors for 20 mhz dc-dc converters," in *2008 Twenty-Third Annual IEEE Applied Power Electronics Conference and Exposition*, pp. 689–693, IEEE, 2008.

[54] B. Sun, R. Burgos, and D. Boroyevich, "2 w gate drive power supply design with pcb-embedded transformer substrate," in *2017 IEEE Applied Power Electronics Conference and Exposition (APEC)*, pp. 197–204, IEEE, 2017.

[55] T. Fujiwara, "Planar integrated magnetic component with transformer and inductor using multilayer printed wiring board," *IEEE transactions on magnetics*, vol. 34, no. 4, pp. 2051–2053, 1998.

[56] A. M. Pernía, M. J. Prieto, J. M. Lopera, J. Reilly, S. S. Linton, and C. Quiñones, "Thick-film hybrid technology for low-output-voltage dc/dc converter," *IEEE Transactions on Industry Applications*, vol. 40, no. 1, pp. 86–93, 2004.

[57] I. Kowase, T. Sato, K. Yamasawa, and Y. Miura, "A planar inductor using mn-zn ferrite/polyimide composite thick film for low-voltage and large-current dc-dc converter," *IEEE Transactions on Magnetics*, vol. 41, no. 10, pp. 3991–3993, 2005.

[58] A. Ball, M. Lim, D. Gilham, and F. C. Lee, "System design of a 3d integrated non-isolated point of load converter," in *2008 Twenty-Third*

Annual IEEE Applied Power Electronics Conference and Exposition, pp. 181–186, IEEE, 2008.

[59] Y. Su, Q. Li, M. Mu, and F. C. Lee, "High frequency inductor design and comparison for high efficiency high density pols with gan device," in *2011 IEEE Energy Conversion Congress and Exposition*, pp. 2146–2152, IEEE, 2011.

[60] K. W. E. Cheng, K. Ding, S. L. Ho, W. Fu, J. Wang, and S. Wang, "Polymer-bonded nizn ferrite magnetic cores mixed with titanium (iv) isopropoxide (c12h28o4ti)," *Journal of applied physics*, vol. 109, no. 7, p. 07A514, 2011.

[61] D. V. Harburg, A. J. Hanson, Y. Song, J. Qiu, R. Tian, C. G. Levey, C. R. Sullivan, and D. Otten, "Measured performance and microfabrication of racetrack power inductors," in *2013 IEEE Energy Conversion Congress and Exposition*, pp. 614–620, IEEE, 2013.

[62] S. Prabhakaran, Y. Sun, P. Dhagat, W. Li, and C. R. Sullivan, "Microfabricated v-groove power inductors for high-current low-voltage fast-transient dc-dc converters," in *2005 IEEE 36th Power Electronics Specialists Conference*, pp. 1513–1519, IEEE, 2005.

[63] D. Yao, C. G. Levey, R. Tian, and C. R. Sullivan, "Microfabricated v-groove power inductors using multilayer co–zr–o thin films for very-high-

frequency dc–dc converters," *IEEE Transactions on Power Electronics*, vol. 28, no. 9, pp. 4384–4394, 2012.

[64] M. H. Lim, J. D. van Wyk, F. C. Lee, and K. D. Ngo, "A class of ceramic-based chip inductors for hybrid integration in power supplies," *IEEE Transactions on Power Electronics*, vol. 23, no. 3, pp. 1556–1564, 2008.

[65] K. Moon, S. Hong, H. Kim, and J. Kim, "A fabrication of dc-dc converter using ltcc niznu ferrite thick films," in *2005 IEEE International Magnetics Conference (INTERMAG)*, pp. 1109–1110, IEEE, 2005.

[66] J.-W. Lim, H.-J. Kim, Y.-S. Oh, H.-S. Kim, and S.-T. Lim, "Embedded flexible fe–si–al powder composite film inductor for low power dc–dc converters," *IEEE Transactions on Applied Superconductivity*, vol. 28, no. 3, pp. 1–5, 2018.

[67] K. H. Kim, J. Kim, H. J. Kim, S. H. Han, and H. J. Kim, "A megahertz switching dc/dc converter using febn thin film inductor," *IEEE Transactions on Magnetics*, vol. 38, no. 5, pp. 3162–3164, 2002.

[68] C.-S. Kim, S. Bae, H.-J. Kim, S.-E. Nam, and H.-J. Kim, "Fabrication of high frequency dc-dc converter using ti/fetan film inductor," *IEEE transactions on magnetics*, vol. 37, no. 4, pp. 2894–2896, 2001.

[69] J. Kim, M. Kim, J.-K. Kim, F. Herrault, and M. G. Allen, "Anisotropic nanolaminated conife cores integrated into microinductors for high-

frequency dc–dc power conversion," *Journal of Physics D: Applied Physics*, vol. 48, no. 46, p. 462001, 2015.

[70] A. Moazenzadeh, F. S. Sandoval, N. Spengler, V. Badilita, and U. Wallrabe, "3-d microtransformers for dc–dc on-chip power conversion," *IEEE Transactions on Power Electronics*, vol. 30, no. 9, pp. 5088–5102, 2014.

[71] S. Kelly, C. Collins, M. Duffy, F. M. Rhen, and S. Roy, "Core materials for high frequency vrm inductors," in *2007 IEEE Power Electronics Specialists Conference*, pp. 1767–1772, IEEE, 2007.

[72] W. Huang and B. Lehman, "A compact coupled inductor for interleaved multiphase dc–dc converters," *IEEE Transactions on Power Electronics*, vol. 31, no. 10, pp. 6770–6775, 2016.

[73] H. Jia, J. Lu, X. Wang, K. Padmanabhan, and Z. J. Shen, "Integration of a monolithic buck converter power ic and bondwire inductors with ferrite epoxy glob cores," *IEEE transactions on Power Electronics*, vol. 26, no. 6, pp. 1627–1630, 2010.

[74] S. Tang, S. R. Hui, and H.-H. Chung, "A low-profile power converter using printed-circuit board (pcb) power transformer with ferrite polymer composite," *IEEE Transactions on Power Electronics*, vol. 16, no. 4, pp. 493–498, 2001.

[75] C.-H. Chia, R. C.-H. Chang, P.-S. Lei, and H.-M. Chen, "A two-phase fully-integrated dc–dc converter with self-adaptive dcm control and gipd passive components," *IEEE Transactions on Power Electronics*, vol. 30, no. 6, pp. 3252–3261, 2014.

[76] S. Kulkarni, D. Li, D. Jordan, N. Wang, and C. Ó. Mathúna, "Pcb embedded bondwire inductors with discrete thin-film magnetic core for power supply in package," *IEEE Journal of Emerging and Selected Topics in Power Electronics*, vol. 6, no. 2, pp. 614–620, 2018.

[77] D. Jordan, G. Wei, L. Ye, D. Lordan, P. Podder, A. Masood, K. Rodgers, C. . Mathúna, and P. McCloskey, "High q-factor pcb embedded flip-chip inductors with multilayer cztb magnetic sheet for power supply in package (pwrsip)," *IEEE Journal of Emerging and Selected Topics in Power Electronics*, vol. 9, no. 1, pp. 102–110, 2021.

Chapter 2

State of the Art

This chapter reviews the current state of the art technologies, and future technological developments, for integrating the magnetic component of voltage regulators into advanced organic substrates for Power Supply in Package (PwrSiP) applications. In this chapter the various strengths and weakness of the individual integration technologies are discussed along with the major roadblocks relating to the integration of the magnetic passive using a particular integration method. There are 4 integration technologies considered, as follows: 1) Bulk Ferrite Cores embedded in PCB substrate; 2) ferrite particles dispersed in a polymer matrix; 3) ferrite tapes integrated in Low Temperature Co-Fired Ceramic (LTCC); and 4) integrated thin film magnetics in advanced organic substrates, which is the focus of our work. Finally this chapter discusses potential technologies for the realisation of PwrSiP required for future electronic devices.

The chapter is structured as follows. Section 2.1 gives an in depth discussion on the different ways of integrating the magnetic component into the substrates. In this section particular case studies are used to highlight the key benefits achieved by integrating the magnetic passive into the substrate. These case studies highlight the need of the magnetic passive component to operate efficiently at ever increasing frequencies in order to continue the trend of miniaturisation of the power supply. Hence, the various forms of the magnetic component are discussed along with their strengths and limitations. Furthermore, this section also considers the key challenges associated with using a particular magnetic integration technology.

Section 2.2 compares the performance of the microinductors fabricated via the manufacturing techniques outlined in Section 2.1. The devices are quantified using three figures of merit which compare the DC and AC performance of the microinductors. These microinductors are then compared against state of the art Micro-Electromechanical System (MEMS) fabricated microinductors as a benchmark. Thus the reader can have an understanding of when to use a particular integration technology based on their application specific requirements.

Section 2.3 discusses future magnetic materials, alloys compositions, and morphologies required for future PwrSiP applications. These materials, and,

more importantly, their morphologies, are compared against the current magnetic materials being used in PwrSiP applications and the reasons why they are the ideal candidate to be the magnetic component in future PwrSiP applications are discussed. Whence, they key challenges in incorporating these materials into standard PCB manufacturing to form complete PwrSiP are discussed. Finally the conclusions of this chapter are provided in Section 2.4.

2.1 PwrSiP: Integration of the Magnetic Component

In this section we review the different manufacturing techniques used integrated the magnetic component of the voltage regulator forming a PwrSiP application. As stated earlier the four main methods considered are: 1) Embedding Bulk ferrite cores into the PCB substrate; 2) integrating Ferrite Polymer Composite(s) (FPC) into the PCB substrate; 3) integrating ferrite tapes with standard LTCC manufacturing; 4) integrating magnetic thin films into the PCB substrate. This section provides a review of the strengths and weaknesses of those techniques.

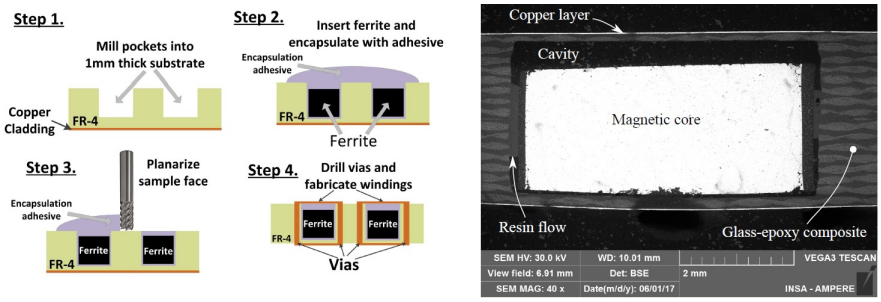

Figure 2.1: (Left [1]) Standard ferrite embedding process. (Right [2]) Cross section of ferrite embedded in glass-epoxy composite.

2.1.1 Embedded Bulk Ferrites

In more recent years there has been a move towards the embedding of the bulk magnetic ferrite into the PCB substrate in order to reduce the footprint required for the magnetic component of the power supply module. The embedding of the magnetic core, fully outlined in [1, 2], involves the hollowing out of a cavity in the prepreg layers which will house the core within the substrate and then the application of pressure and heat in order to form a seal, cf Fig. 2.1. The use of a cavity reduces the risk of delamination and minimises the amount of stress on the core. The embedding of the magnetic core within the prepreg layers allows the remaining active components of the power supply module to be placed above the now embedded magnetic core rather than alongside it, thus utilising the normally dead space on the PCB, further reducing parasitics associated with redundant electrical interconnections, and increasing the inductance and power densities.

Indeed Sun et al. [3, 4] show that by embedding the magnetic component within the substrate higher power densities can be achieved along with high efficiencies. In their work they demonstrate an isolated gate drive using an embedded toroidal transformer with a bulk ferrite core as the magnetic isolation. They achieve a power densities of 73 W/in^3 and an efficiency of 85%. However they found that the higher power densities achieved with the embedded toroidal transformer resulted in a higher parasitic inter-winding capacitance (1.6 pF) when compared to the larger embedded coplanar transformer (0.77 pF) in their work. This increase in capacitance can have detrimental effects on the dynamic voltage response and hence hampers the efficiency of the overall Dynamic Voltage and Frequency Scaling (DVFS) power grid. Therefore there is a potential trade-off between the efficiency of the power transformer and the transient response of its transfer characteristic. The footprint of the embedded coplanar transformer, including all the active components mounted on the PCB, was 23 $\times$ 18 mm^2, whereas the footprint of the embedded toroidal transformer was 13 $\times$ 13 mm^2. Thus by using the embedded toroidal transformer they reduced the amount of PCB required for the gate drive by 59%. Furthermore they compared both transformers as a 2W Gate drive power supply and found that the toroidal transformer had an overall efficiency of 85% versus the coplanar transformer's efficiency of 74%. The better efficiency of the toroidal transformer over the coplanar was due to a more efficient use of the magnetic core which resulted in less magnetic material required by the toroidal transformer. The more efficient

use of the magnetic material was a direct consequence of the higher winding density of the toroidal transformer.

However, with this increased power density achieved by embedding the ferrite core within the substrate, the thermal stability of the core must be considered, as a mismatch between the Coefficient of Thermal Expansion (CTE) of the core and the substrate can result in delamination issues or the cracking of the core. The effects on the thermal stability of embedding the ferrite core was investigated by Salas et al. [5], who found that by embedding the core within the substrate resulted in a 27 degree C increase in the temperature of the core as compared to a non-embedded core. The temperature difference between the embedded ferrite core and the standard ferrite core is illustrated in Fig. 2.2.

They concluded that the increase in the temperature of the magnetic core was the result of decreasing the cross sectional area of the core (a requirement for the embedding process) which, so long as the current of the two devices remained constant, resulted in an increase in the magnetic flux density. Thus, one can conclude from this, particularly where large magnetic flux densities are involved, there exists a fundamental trade-off between the thickness of the embedded core and delamination issues, and the temperature of the core.

The reliability of the substrate to endure thermal induced stresses was tested

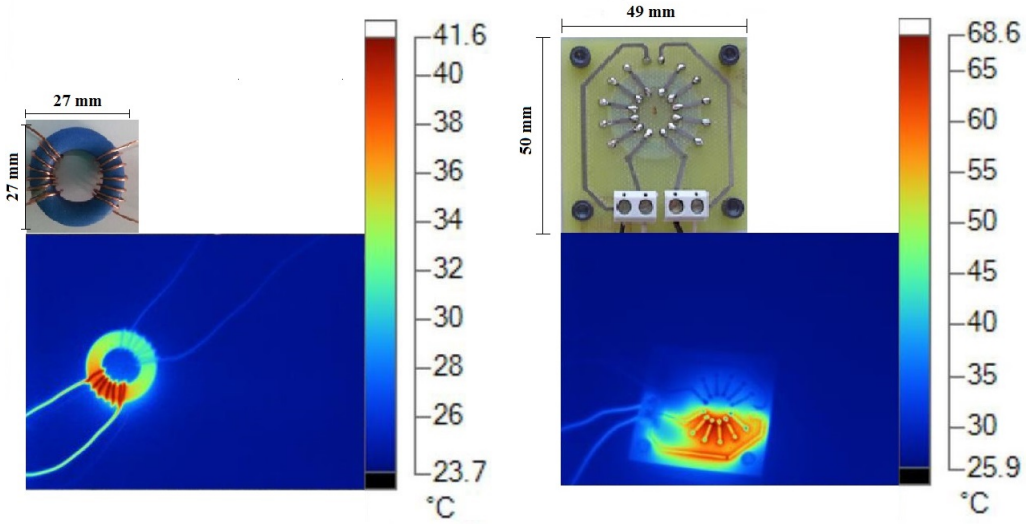

Figure 2.2: [5](Left) Thermal image of standard ferrite toroidal transformer. (Right) Thermal image of embedded ferrite toroidal transformer.

by Perrin et al. [6] who subjected various substrates, with embedded bulk ferrite cores, to thermal cycling in order to see if failure would be induced. The temperature cycling spanned -55 degrees C to 200 degrees C at a cooling/heating rate of 20 degrees C per minute, and at both extremes the temperature was held constant for 20 minutes. This was repeated 1000 times. Figs. 2.3 & 2.4 show the result of this temperature cycling.

As can be seen from Fig. 2.3, delamination of the FR-4 substrate, and cracking of the ferrite core has occurred resulting in the failure of the device. The cracking of the ferrite core would result in the introduction of unwanted air gaps resulting in a decrease in the inductance gain from the material. This drop in inductance would have adverse effects on the power supply module

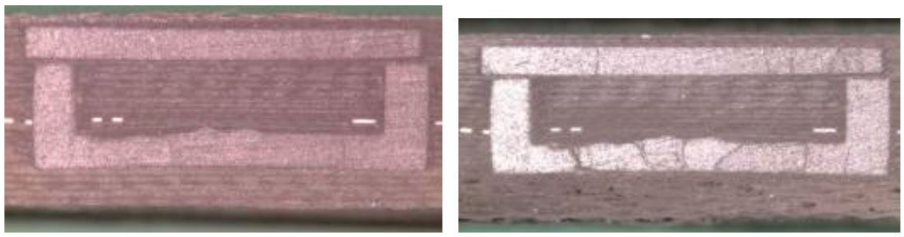

Figure 2.3: [6](Left) FR-4 samples before thermal testing. (Right) FR-4 samples after 150 temperature cycles.

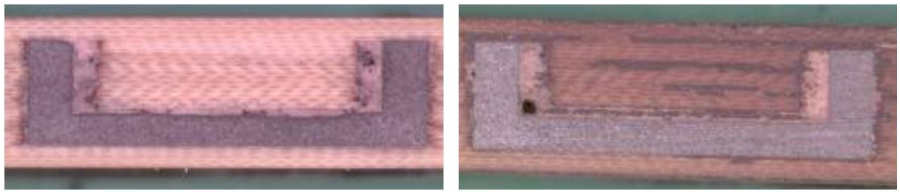

Figure 2.4: [6](Left) Panasonic R1515 sample before thermal testing. (Right) Panasonic R1515 samples after 1000 temperature cycles.

and possibly render the power module no longer fit for purpose. In addition to a reduction in inductance, at the cracks there would be magnetic fringing effects which too would reduce the efficiency of the power module. Furthermore the delamination of the FR-4 is more worrying as this may result in the breaking of copper interconnects, or water ingression into the substrate causing an electrical short.

However, as can be seen from Fig. 2.4, no delamination issues or cracking of the embedded core occurred when using the Panasonic R1515 PCB substrate. Thus the choice of PCB substrate when embedding the core is pivotal in the prevention of delamination, or cracking, resulting from heat dissipation by the core into the surrounding substrate.

In addition to a failure of the core or the substrate, the increase in the temperature of the embedded core can have negative effects on the surface mounted electronic components due to the increase in the ambient temperature. This is illustrated in [6] which shows a decrease in transformer efficiency with increasing ambient temperature. Therefore, particularly in power systems which require large currents, the dissipation of heat within the embedded core must be considered.

2.1.2 Ferrite Particles Dispersed in Polymer Matrices

However, despite the advances made in embedding the bulk ferrite material into the substrate, there still persists current handling and frequency limitations to using a bulk ferrite core. There is ongoing research to produce ferrite materials which exhibit high current high frequency performance through the creation of a nano grain structures within the ferrite, which results in a larger ratio of grain boundary to grain volume. Such nano grain structures help prevent the deterioration of the relative permeability at higher frequencies [7, 8]. However the creation of such ferrites normally results in high fabrication costs. A popular cost effective method for circumventing the poor frequency performance of bulk ferrites is to mill the ferrite material into fine particles and then to mix them into a polymer. This has the effect of introducing distributed air gaps within the core, and in doing so, simultaneously increases the frequency stability of the relative permeability of the material

and constrains the motion of the eddy currents to the individual magnetic particles. The reduced mobility of the eddy currents within the core further increases high frequency performance. A major advantage of integrating the magnetic component in this manner is that such FPC lends itself to the use of standard screen printing technologies [9–11], coma blade coating [12, 13], or even advanced additive manufacturing techniques [14].

Both the high frequency performance, and the large current handling capabilities, of polymer ferrite composites are exemplified by the work of Sugawa et al. [11], who fabricated a Carbonyl-Iron Powder (CIP) epoxy composite magnetic core planar inductor for package level Point of Load (POL) power applications that exhibited a quality factor of 15 at 100 MHz while maintaining a 5.5 A superimposed dc current. They fabricated a 1 mm^2 power inductor on a glass substrate using a 54% volume CIP/epoxy, cf Fig. 2.5. As can be seen from the figure there is a good dispersion of the CIP in the epoxy. However there is a discontinuity in the composite core where the copper has been deposited. This discontinuity arises as the copper is electroplated on a 5 μm thick layer of polyimide, which is required in order to planarize the surface. Thus the core resembles a multi-layer stack, which can reduce the efficiency of the core. Note, the 5 μm gap introduces an additional air gap into the FPC core.

They compared their work against [15] and found that they achieved bet-

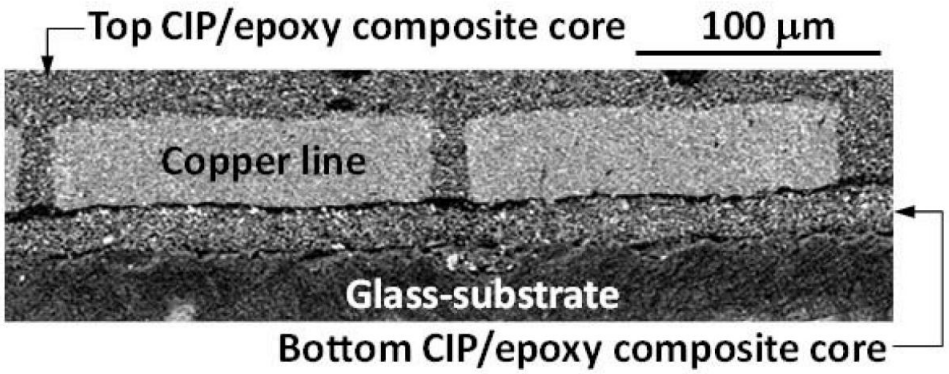

Figure 2.5: [11] Cross sectional SEM image of fabricated planar power inductor with CIP/Epoxy composite core.

ter frequency performance owing to a more homogenous dispersion of the CIP in the polymer as compared to the Fe-based powder, which had the tendency to form clusters within the polymer, and so, by increasing the dispersion of the ferrite within the polymer there is a reduction in magnetic loss at higher frequencies [16]. Thus a highly homogenous distribution of the ferrite powder within the polymer is required for high frequency performance of the embedded inductor utilising FPC.

Furthermore FPC has mostly been used in tandem with bond wire technologies to integrate the magnetic component into the package by several researchers [17–20]. The use of bond wire inductors utilising a FPC offers a cost effective approach for power supply in package applications and can be readily incorporated into the standard PCB manufacturing processes. Traditionally bondwires have been susceptible to breaking caused by mechanical

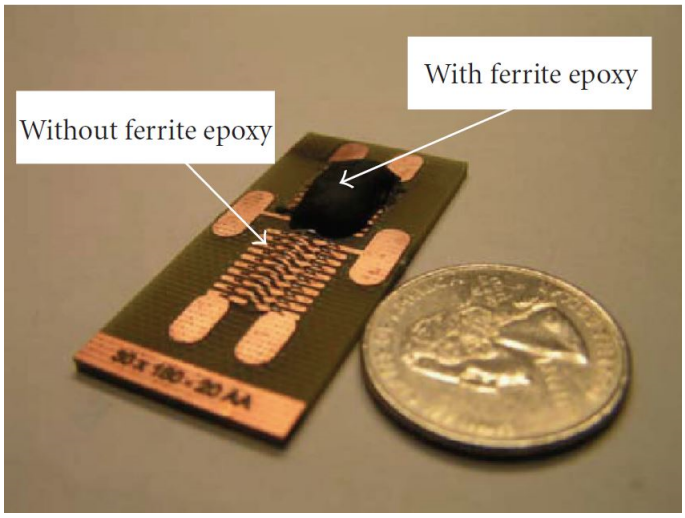

Figure 2.6: [19] Bondwire inductor with ferrite epoxy core fabricated on PCB.

stress resulting in the bondwire coming off from the pad. However, the use of a polymer coating around the bond wire (see Fig. 2.6) will increase the mechanical stability of the inductor and prevent damage being done to the encased bond wire. Thus further increasing their potential use in PwrSiP applications.

The main advantage of bond wire inductors over other MEMS inductors is that the DC resistance of the bond wire is relatively small. Thus the bond wire inductor can achieve better quality factors over MEMS based inductors. Indeed Shen et al. [19, 20] demonstrate a bondwire inductor with ferrite-epoxy coating that achieves a quality factor of 30 to 40 in the 2 to 20 MHz range. Therefore bondwire inductors using a FPC offer a cost effective means of integrating the magnetic component of the power supply module into the

package without a degradation of the quality of power supply module.

The use of FPC is not limited to screen printed inductors or bondwire inductors, it can be readily used by additive manufacturing processes. Indeed the use of additive manufacturing techniques, an example of which is 3D printing, to integrate the magnetic component into the substrate has been investigated by several researchers [21–24] and provides a good route to manufacture highly complex designs with relative ease. Advanced structures can be designed using 3D FEM modelling software, such as Maxwell Ansys, Cadence, or HFSS, and rapidly manufactured by exporting the 3D structure to the 3D printer. This enables researchers to deploy optimisation algorithms to design highly specific inductors for power supply applications and to have the output design of such optimisation algorithms realised with relative ease. Indeed the 3D printing of a ferrite core was performed by L. Liu et al. [14], and could easily incorporated into the process described by W. Liang et al. [25], cf Fig. 2.7. Perhaps the main tractability of 3D printing the magnetic core and the

that the distribution of the magnetic field within the core can be controlled in a manner not available to other fabrication techniques. Such control over the interaction of the magnetic field and the core can be utilised to increase the amount of current which can be handled by the inductor without the magnetic core saturating.

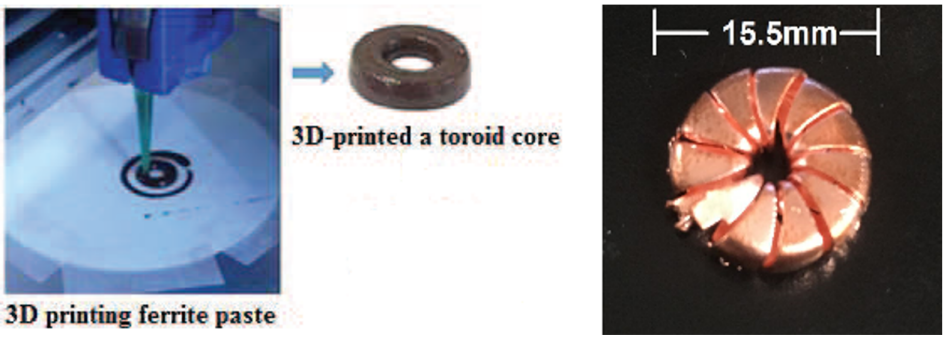

Figure 2.7: (Left [14]) 3D printed toroid core using a FPC. (Right [25]) Electroplated toroidal inductor on 3D printed scaffold.

The use of polymer ferrite composites offers a good solution to high current high frequency power applications. They are easily integrated into the substrate through the use of standard PCB technologies, such as screen printing, ink jet printed, or through the use of additive technology. However they have a lower inductance density than bulk ferrites or thin film magnetics, and therefore offer reduced power densities.

2.1.3 Ferrite Tapes & Low Temperature Co-Fired Ceramic (LTCC)

The use of LTCC for high density electronic interconnections has been used by the microelectronic packaging industry for several decades and there is extensive published research on integrating the magnetic component into this substrate forming a single stack for power supply applications [26–34]. The integration of magnetics into the LTCC stack is rather simple due to the

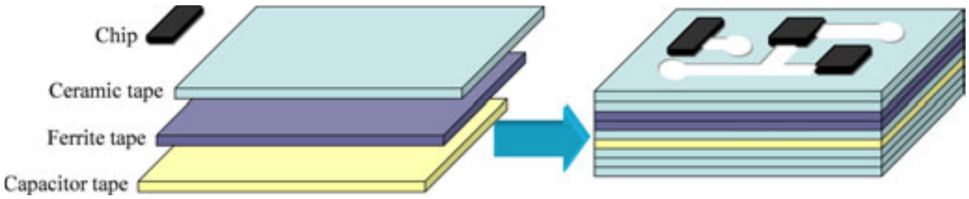

Figure 2.8: [33] Structure of integrated dc-dc converter based on LTCC technology.

technology being based on the binding of glass ceramic films pressed together under low temperature (1000 degrees C). Therefore, in principle one must only add a ferrite tape, with conduction paths printed onto it, into the stack before the binding phase in order for the magnetic component to be integrated into the LTCC substrate, cf Fig. 2.8. In non-planar inductors holes are first punched into the ferrite tape and then later filled with a conducting paste allowing multi-layer connections in the stack.

However, by integrating a magnetic ferrite sheet into the LTCC stack in this manner there is an increase in unwanted parasitic inductance in areas which are not local to the inductor. The effect of unwanted parasitics on the silver traces manifests itself in the forms of voltage overshoot and ringing [35]. Hence, due to parasitic inductances and capacitances, the current carrying silver trace acts as a transmission line. These parasitics form a second order damped harmonic oscillator. In the case of overshoot and ringing, that second order system is *underdamped*, resulting in a longer time interval required for the transient response of the frequency modulated voltage to die

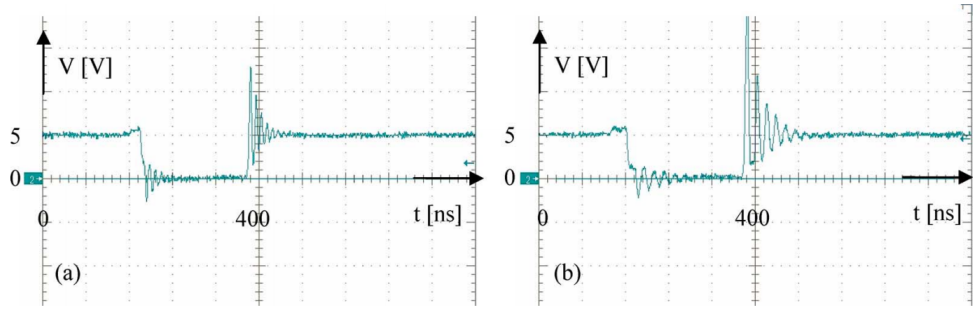

Figure 2.9: [35](Left) Voltage waveform with conductive shield. (Right) Voltage waveform without conductive shield.

out and the system to converge on a steady state, cf Fig 2.9. This can result in serious negative consequences for the DVFS granular power grid when the transient response of the power supply is of a similar order to that of the change in the dynamic load of the processor.

The poor transient performance of the LTCC system is contra to an effective DVFS granular power grid, and so measures are required to curtail the unwanted parasitic inductance inherent to the current LTCC stack. This unwanted parasitic inductance can be mitigated through the use of conductive copper shielding to protect the silver traces [36]. The local magnetic field originating from the current in the silver trace is prevented from entering the ferrite layer of the LTCC substrate by the formation of eddy currents within the conductive shield, which oppose time variations in the magnetic field. Furthermore, as the eddy current formation opposes the rate of change of the magnetic field, higher order harmonics are more heavily damped. This

further reduces the unwanted parasitics caused by the magnetic substrate and smooths out voltage ringing. The effectiveness of the shield on mitigating unwanted parasitic inductance is therefore a function of the frequency spectra of the current, the conductivity of the material, and the thickness of the copper shielding.

Indeed, there have been several reports on low profile coupled inductors using LTCC as a substrate for high current high frequency point of load applications [35, 37, 38]. These LTCC coupled inductors achieve efficiencies of 85% for currents spanning 2 to 20 Amps. For such large currents, care must be taken to insure that the magnetic material in the core does not saturate, as doing so would result in an increase in the energy being dissipated by the core. This is owing to the relationship between the imaginary component of the magnetic susceptibility and the amplitude of the AC driving field. In order to prevent the magnetic core from saturating the DC component of the magnetic field must be cancelled out [38]. This is done by using multiphase coupled inductors which are inversely coupled together in such a manner where the magnetic fields from the two current sources cancel out in the magnetic material. Typically this is achieved by interleaving the copper windings around a shared magnetic core. However this is not strictly required, all that is required is that the linear superposition of the two magnetic fields arising from the current sources add in such a manner as to prevent the core from saturating. Furthermore, it has been shown that

the use of inverse coupling of inductors can improve the efficiency and transient response of voltage regulators [41, 42]. The improved efficiency arises as the load transient response is proportional to the overall inductance in the switching converters. Thus, inverse coupling can be used to reduce the transient component of the inductance while maintaining its steady state value, and so, improve the load transient response of the converter [43]. However, flux cancellation techniques are ill fitted for applications which require higher inductance densities while still maintaining large currents.

Through a judicious choice of core material being used in the LTCC stack, relatively large current and power densities can be achieved without resorting to the use of flux cancellation methods. Such an approach has the benefit of having a larger inductance density and significantly simplified control than its flux cancellation counterpart. The primary requirement of such material is the frequency performance of the relative permeability under large DC bias. That is, the material is required to have a large B_{sat}. The frequency spectra of the relative permeability can be determined by subjecting the material to a large external DC magnetic bias field with a small time-vary AC field superimposed onto it, see 2.1.1. Here the frequency of the AC field is swept over a frequency range of interest. The measurement of the relative permeability frequency spectrum under external DC bias is given in [44].

$$\boldsymbol{B}(t) = \boldsymbol{B}_{dc} + \Delta\boldsymbol{B}e^{-i\omega t} \tag{2.1.1}$$

In addition to having large B_{sat} requirements, the material is also required to have stable μ_r at higher frequencies. This is achieved by selecting a composite alloy wherein the onset of spin, and domain wall, resonance occurs outside the operating frequency of the inductor. The onset of such resonances results in an exponential rise in the loss tangent of the material due to the relative permeability lagging behind the applied field [45, 46]. Furthermore, the material selected must be compatible with the LTCC manufacturing process as inter-diffusion of the core material and the glass ceramic reduces the effective thickness of the copper layer. Such unwanted inter-diffusion ultimately undermines the current handling capabilities of the inductor. In addition, the diffusion of elements from the glass ceramic into the ferrite material can result in a phase change of the ferrite at the potentially ill-defined boundary (high diffusivity of elements will blur the boundary interface). An example of this is the growth of the hematite phase in NiCuZn due to the diffusion of Mg and Al ions from the glass ceramic [47], cf Fig. 2.10. The presence of this phase drastically reduces the relative permeability and the saturation magnetisation of the ferrite, which, undermines the performance of the inductor and any PwrSiP of which it is a part. This is particularly true for thin film ferrites where the boundary behaviour of the material is dominant owing to the large surface area to volume ratio. Thus careful selection of the magnetic core material and glass ceramic substrate is required for good performance of the inductor.

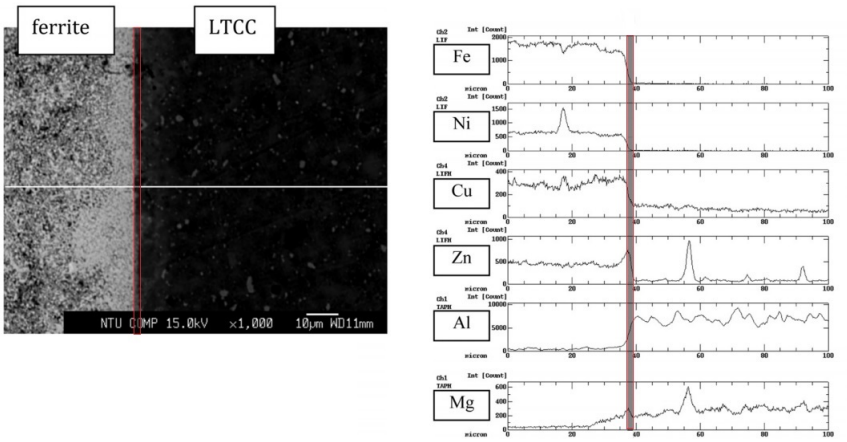

Figure 2.10: Diffusion of Al and Mg into ferrite at interface [47].

One such material combination investigated by Li et al. [48] is NiCuZn ferrite layer and Zn_2SiO_4 ceramic layers. The combination of NiCuZn and Zn_2SiO_4 shows little inter-diffusion between the magnetic layer and the ceramic layer, cf Fig. 2.11. This lack of inter-diffusion further illustrates how the choice of the ceramic is vital for the performance of the inductor as NiCuZn is the same ferrite which exhibited high inter-diffusion in the ceramic layer containing Al and Mg ions in [47].

Furthermore, they demonstrated the viability of this ferrite-ceramic combination by fabricating a $2 \times 1.2 \times 0.9$ mm^3 power inductor using the standard LTCC manufacturing process. They achieved an inductance of 2 μH up to 10 MHz and had a saturation current of 430 mA. The device is very well suited for high current applications as it had a very low DC resistance (0.2 Ohms).

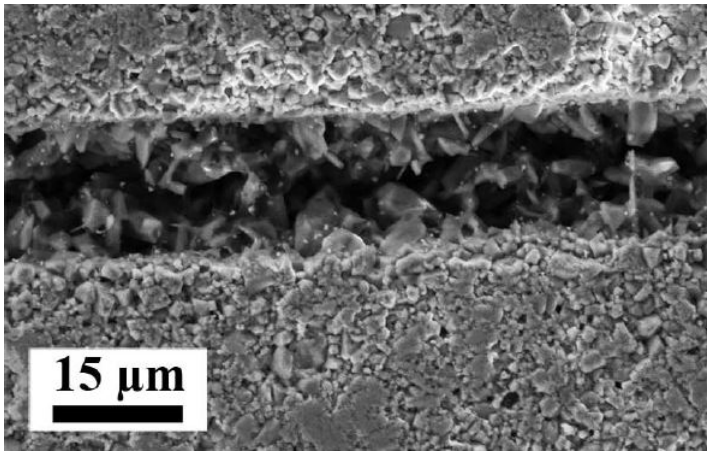

Figure 2.11: [48] SEM image of NiCuZn – Zn_2SiO_4 boundary.

Moreover, they showed that by careful selection of the magnetic material used, and the glass ceramic substrate, high current high inductance density inductors can be mass fabricated using standard LTCC manufacturing.

However, despite the advances being made in integrating the ferrite magnetic component to form a LTCC stack for PwrSiP applications, there still exists issues. The main one being that the use of ferrites as the core magnetic material limits the advantage gained to the lower frequency regimes. This is due to the rise in the imaginary part of the relative permeability at higher frequencies causing the magnetic material to dissipate energy in the form of heat. This issue can be addressed by lowering the relative permeability, via the introduction of distributed air gaps as in the case of FPC. However, in doing so, the gain in using the magnetic material is also reduced. This breakdown of the relative permeability is due to the ferrite material inability

to respond in time to the changing magnetic field i.e. the alignment of the magnetic domains within the ferrite lag behind the applied magnetic field. The fundamental reason for this is that the magnetic reversal process of ferrites is dominated by domain wall dynamics, and not coherent rotation of domains. This magnetisation reversal process is more lossey as domain walls may become pinned by local defects within the material. Thus, for the full benefit of integrating the magnetic component into the LTCC stack, there is a need for a core magnetic material which has high μ_r, high B_{sat}, and wherein the magnetisation reversal dynamics are dominated by the coherent rotation of the individual magnetic domains.

2.1.4 Thin Film Magnetics in Advanced Organic Substrates

This thesis focused on the integration of soft magnetic alloys into the package substrate is of particular interest due to the large relative permeability, high saturation current, and low hysteresis losses of these materials as compared to ferrites. In the past soft permalloy materials were electroplated directly onto the PCB substrate in such a manner as to form a closed magnetic core around the current carrying copper traces [49, 50], cf Fig. 2.12. This approach offers a very scalable solution for industry as large panels of PCBs can be cheaply electroplated, and so is a very tractable solution to question of integrating magnetics into package.

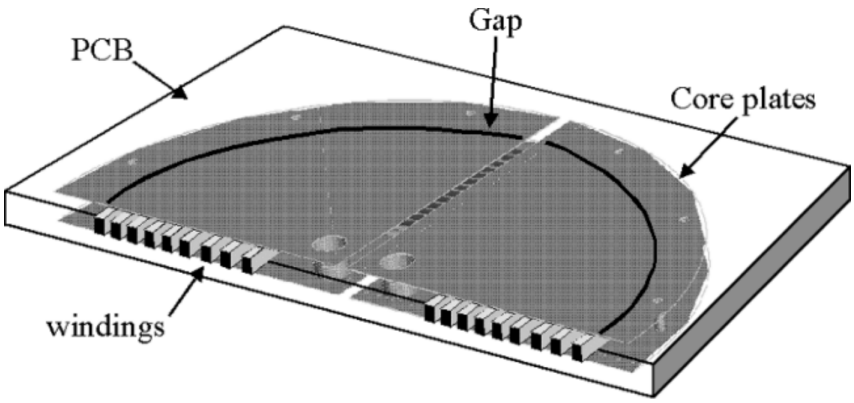

Figure 2.12: [50] Half view of PCB integrated inductor with electroplated $Ni_{80}Fe_{20}$.

The use of a closed magnetic core, using through hole vias plated with magnetic material to connect the top and bottom cores, eliminates the air gap in which the magnetic field lines of an open magnetic core would have to close. The reduction of the relative permeability of a gapped magnetic core is a direct consequence of Gauss' and Ampere's law for magnetism, see Eqs. 2.1.2 – 2.1.3.

$$\nabla \cdot \boldsymbol{B} = 0 \tag{2.1.2}$$

$$\oint_l \boldsymbol{B} \cdot \, d\boldsymbol{l} = \int_{\boldsymbol{A}} \boldsymbol{J} \cdot d\boldsymbol{A} + \frac{\eta}{c^2} \int_{\boldsymbol{A}} \frac{\partial}{\partial t} \boldsymbol{E} \cdot d\boldsymbol{A} \tag{2.1.3}$$

In Eq. 2.1.3 η is the refractive index of the magnetic material. Normally

the ratio of the refractive index to the speed of light is very small and the second term on the RHS of the equation is omitted. Evaluating the closed loop integral in Eq. 2.1.3 over the length of the magnetic core and the length of the air gap yields Eq. 2.1.4 as an expression for the effective permeability.

$$\mu_{eff} = \frac{\mu_{core}}{1 + \mu_{core}\frac{L_{gap}}{L_{core}}} \tag{2.1.4}$$

From Eq 2.1.4 it is evident that the closed core arrangement takes full advantage of the magnetic material as the effective permeability of the material is not diminished by the presence of the air gap. Furthermore, during the electroplating of the soft magnetic material onto the substrate, a strong in plane anisotropy can be readily induced which is pertinent to the low loss performance of the material at higher frequencies. Consequently, the electroplating of the soft magnetic component onto the PCB is a scalable and cheap method for the integration of the magnetic component into the package.

However, with the ever increasing operating frequency required to reduce the energy storage components in the power converter, the thickness of the films must be reduced in order to mitigate eddy current loss. As the magnetic films become thinner the surface boundary effects of the thin film become more important. In this regard, depositing the material onto a rough surface leads to a degradation in material performance as there will exist a stray

magnetic field at the rough boundary. Such a field ultimately increases the coercivity of the material, and so increase hysteresis loss. Therefore, in the case of thin film magnetics, additional steps must be taken to insure that the surface on which the film will be deposited is smooth as deposition onto a rough surface ultimately increases the coercive losses [51].

Advanced thin film magnetics have already been integrated on chip via sputtering and have shown good performance in the high frequency range [52, 53]. However the integrating of the magnetic component on chip involves expensive MEMS fabrication. Therefore there is extensive interest to integrate these advanced magnetic materials into PCB, or other organic substrates, as they offer lower fabrication costs and can have significantly higher current carrying abilities due to the easily deposited thicker copper traces. The sputtering of such advanced thin film magnetic materials onto a polyimide substrate containing copper traces was recently done in [54, 55], and has been demonstrated in the area of flexible electronics [56]. Qui et al. [54, 55] successfully developed a tapped power inductor which achieved a power density of 645 W/Inch^2 and had an efficiency of 93.8%. In order to obtain such high power densities, and inductor efficiency, they fabricated a multi-layer thin film stack of nanogranular Co-Zr-O. The use of the multi-layer stack increases the amount of magnetic material, while, at the same time, limits the motion of the eddy currents to within an individual layer. Such a stack therefore reduces eddy current loss, and improves inductor efficiency.

However careful modelling of the stack must be performed to ensure high frequency performance as capacitive coupling between the layers can give rise to displacement currents [57, 58]. Such currents reduce the volume of useful magnetic material within the core and give rise to energy loss.

Furthermore, when depositing magnetic thin films onto organic substrates, care must be taken to ensure good material morphology. This is due to the critical importance of material morphology in relation to the soft magnetic properties. Indeed, Li et al. [59] demonstrate this importance by DC magnetron sputtering FeCo thin films onto glass, and an organic Polyvinylidene Fluoride (PVDF) substrate. They found that the average grain size of the FeCo deposited on PVDF was much larger than that of its glass deposited counterpart. The increase in the average grain size ultimately undermines the ultra-low coercive loss of the material which is obtained in amorphous materials via the averaging out of the long range magneto-crystalline anisotropies as described by Herzer's model [60, 61]. The formation of the larger grain structures on the PVDF was attributed to the much lower thermal conductivity of the PVDF substrate. Therefore one must consider the effect that the substrate, in combination with the deposition technique, will have on the morphology of the material.

Moreover, the magnetic component need not be directly fabricated on the package substrate. It has been well demonstrated that a magnetic core tape

can be fabricated, via melt-spinning, etc..., and then latter embedded, or integrated by other means, into the package. For example, Sanders et al. [62] used laser patterned silicon steel to create an 80 layer stack which was latter embedded in PCB. More recently Kulkarni et al. [63] used wirebond technology to integrate thin Vitrovac magnetic films to a PCB substrate. Thus showing that advanced magnetic materials can be fabricated outside of the standard PCB manufacturing process and then later incorporated into the package by either embedding the film in prepreg, or using wirebond technologies. This concept forms the basis of the work demonstrated in this thesis.

2.2 Benchmarking & Performance Analysis of Integrated Magnetics

In this section of the thesis the performance of the PwrSiP and Power Supply on Chip (PwrSoC) DC-DC converters with integrated magnetics are benchmarked and compared. The benefit of such a comparison being that it can quantify the performance of thin film magnetics in advanced organic substrates in relation to that of their contemporaneous alternative integrated magnetic technologies i.e., embedded bulk ferrites, ferrite tapes and LTCC, Si integrated magnetics. This enables the identification of the strengths and weaknesses of thin film magnetics in advanced organic substrates used as the magnetic passive component in PwrSiP applications.

However it is challenging to carry out such a comparison since it is hard to accurately benchmark the overall device performance as different power converters may have very different specifications. Hence, it is necessary to quantify what we mean by 'performance' by defining several key Figures of Merit (FOMs) from which one may infer device performance, depending on the application in which the device is being used.

Unfortunately such a more generalised Figure of Merit (FOM) view ultimately results in a loss of accuracy, and, to this point, there exists no standardised set of FOMs used by the research community to benchmark overall device performance. Furthermore, the task of correctly benchmarking device performance against contemporary devices is exacerbated as different researchers use different FOMs and one is often presented with an incomplete set, from which device performance can only be interpolated from the incomplete data. Therefore, in order to make meaningful progress in benchmarking device performance it is necessary to discuss the FOMs typically used by the research community, and to explain the significance of each.

The more typical FOMs used to describe performance are as follows: 1) the dc inductance value, L_{dc}; 2) the dc resistance value, R_{dc}; 3) the current at which the magnetic core saturates, $\mathrm{I_{sat}}$ (note this is intrinsically related to the B_{sat} of the magnetic core); 4) the overall footprint of the inductor

structure; 5) the Q-factor of the inductor, Q; and 6) the operating frequency. To facilitate the ease of comparison, the set of FOMs is separated into those which describe the DC performance of the inductor (1 - 4), and those which describe the AC (5 - 6), i.e., in subsection 2.2.1 the FOMs which are used to describe the DC performance are discussed; in subsection 2.2.2 the FOMs which are used to describe the AC performance are discussed; and finally, in subsection 2.2.3 a hybrid figure of merit which merges the DC and AC performance is discussed.

2.2.1 DC - Analysis

The main FOMs used to describe the DC electrical performance of the inductor are: the inductance; the dc resistance; the current at which the magnetic core saturates; and the overall physical footprint the device occupies on the PCB. Both the inductance, and the saturation current relate to the energy storage capabilities of the inductor, whereas the dc resistance pertains to the energy dissipation of the inductor through the unwanted creation of heat. Thus, for effective PwrSiP applications, the maximum energy storage to energy dissipation, in a minimal footprint, is desired. So long as the applied current is less than the I_{sat} of the magnetic core, this is numerically described as the inductance to resistance ratio per unit footprint, and forms one of the most important FOMs for the suitability of an inductor to a PwrSiP application [64]. Indeed the output efficiency of a typical Buck converter with

integrated magnetics is related to the L_{dc}/R_{dc} ratio via Eq. 2.2.1 [65].

$$\frac{L_{dc}}{R_{dc}} = \frac{P_o \times (1-D)}{f \times I_r \times Powerloss_{dc}} \tag{2.2.1}$$

Hence, researchers can use Eq. 2.2.1 to determine the minimum L_{dc}/R_{dc} ratio permissible for a given efficiency.

To illustrate that there exists a fundamental trade-off between the energy density and the power dissipation of an inductor consider the general expression of inductance for a highly coupled inductor, and its resistance Eqs. 2.2.2 & 2.2.3.

$$L_{dc} = \frac{N^2 \mu_{eff} A_m}{l_m} = N^2 K_1 \tag{2.2.2}$$

$$R_{dc} = N \frac{\rho l}{A_c} = N K_2 \tag{2.2.3}$$

Here N is the number of turns comprising the inductor; μ_{eff} is the effective relative permeability of the core; A_m is the closed surface through which the magnetic field lines pass; l_m is the length of the magnetic field line; ρ is the resistivity of the copper; and finally, A_c represents the cross sectional area of the copper. From inspection of the above expressions it is evident that there is a linear relationship between the inductance and the resistance, see Eq. 2.2.4

$$\frac{L_{dc}}{R_{dc}} = N \frac{K_1}{K_2}. \tag{2.2.4}$$

Thus, as long as $K_1 > K_2$, the energy efficiency of the device monotonically increases with the number of turns. Such an assertion would be true were the device not constrained by footprint. However, for a given footprint, the cross sectional area of the conducting wire must be decreased in order to facilitate the additional turns, and in doing so, the DC resistance of the inductor is compromised. Indeed it is reported by X. Fang et al. [66] that the L_{dc}/R_{dc} ratio of a solenoid inductor is proportional to the square root of the physical footprint.

$$\frac{L_{dc}}{R_{dc}} \propto \sqrt{A_{ind}} \tag{2.2.5}$$

It is clear from Eq. 2.2.5 that the L_{dc}/R_{dc} rapidly diminishes with decreasing inductor footprint (A_{ind}). In figure 2.13 the L_{dc}/R_{dc} vs footprint is plotted for devices found in the literature (note these values are provided in table 2.1 subsection 2.2.2). These devices are grouped based on the magnetic integration methods outlined in section 2.1. By comparing all these groups against the air core devices it is evident that the presence of the magnetic core increases the L_{dc}/R_{dc} ratio. This is a direct consequence of Eq. 2.2.2 which states that this ratio is directly proportional to the effective permeability of the magnetic core. Furthermore, the fundamental trade-off between the L_{dc}/R_{dc} and footprint manifests itself in this graph as no device makes it into the top left hand corner, which, represents the maximum energy stored to energy dissipated per unit footprint.

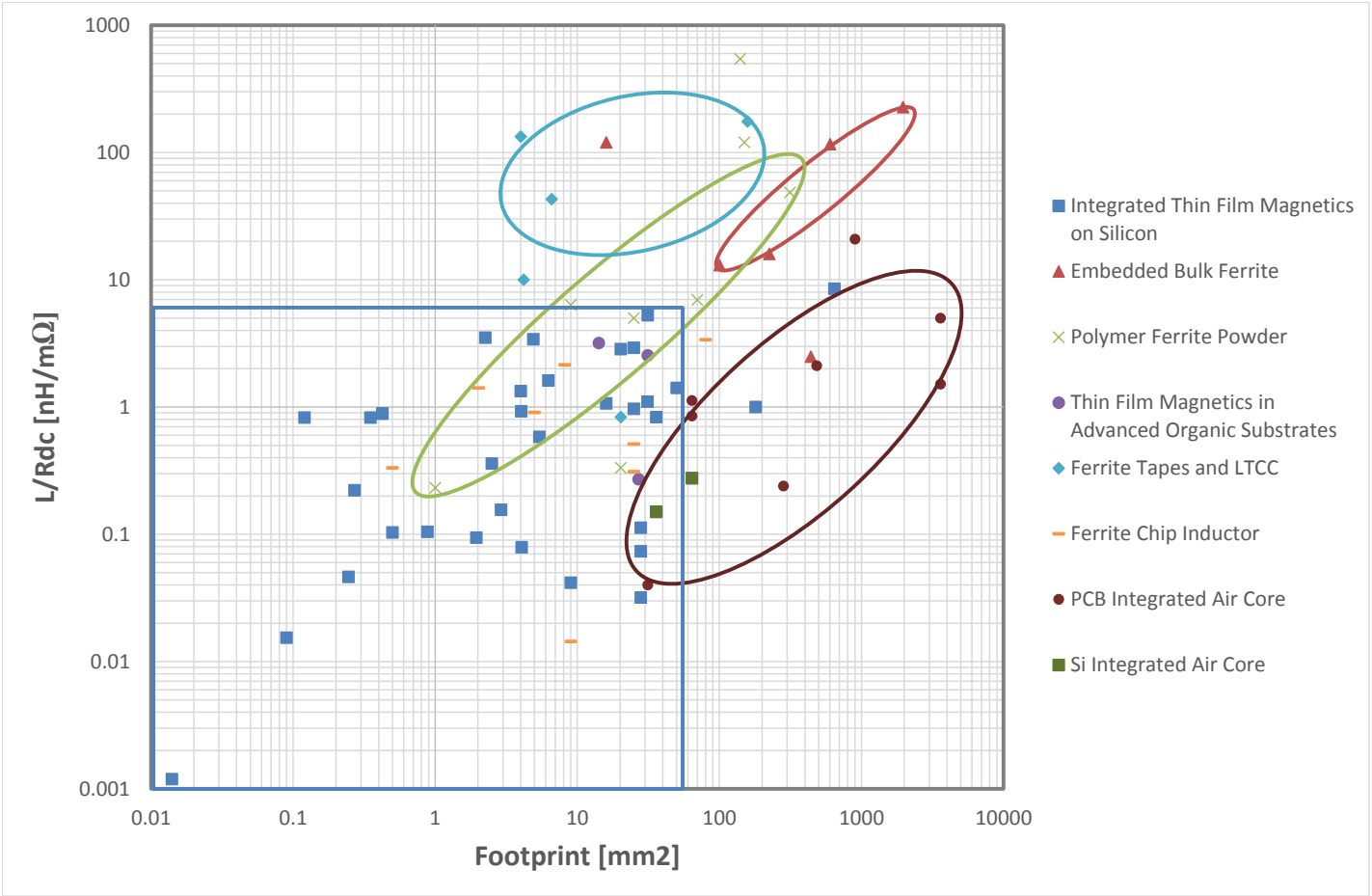

Figure 2.13: Inductance to resistance ratio vs footprint of PwrSiP & PwrSoC applications found in literature. Note top left of graph is desired area for PwrSiP & PwrSoC applications. See table 2.1 for details.

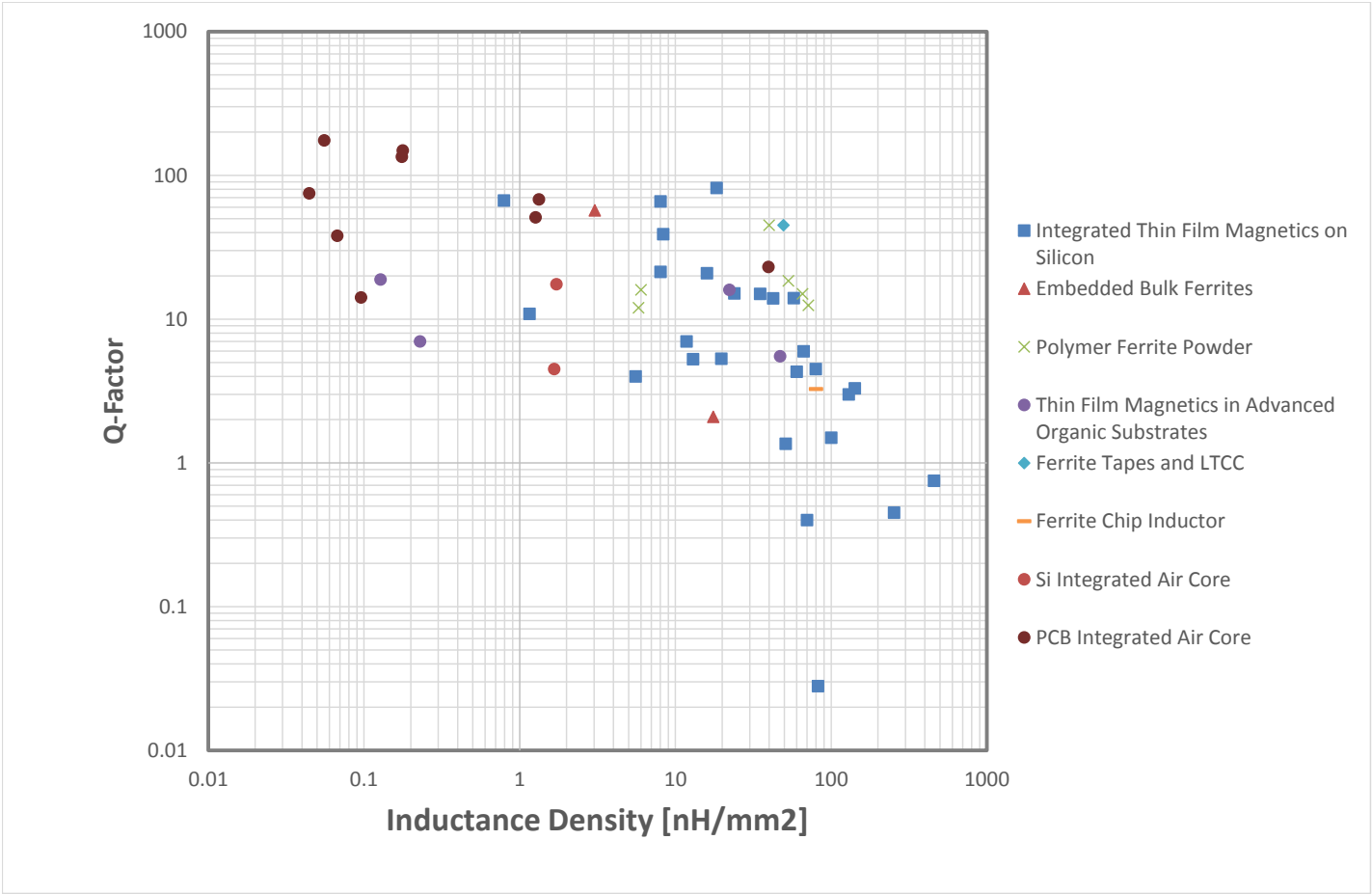

Figure 2.14: Q-Factor vs footprint of PwrSiP & PwrSoC applications found in literature. Note top right of graph is desired area for PwrSiP & PwrSoC applications. See table 2.1 for details.

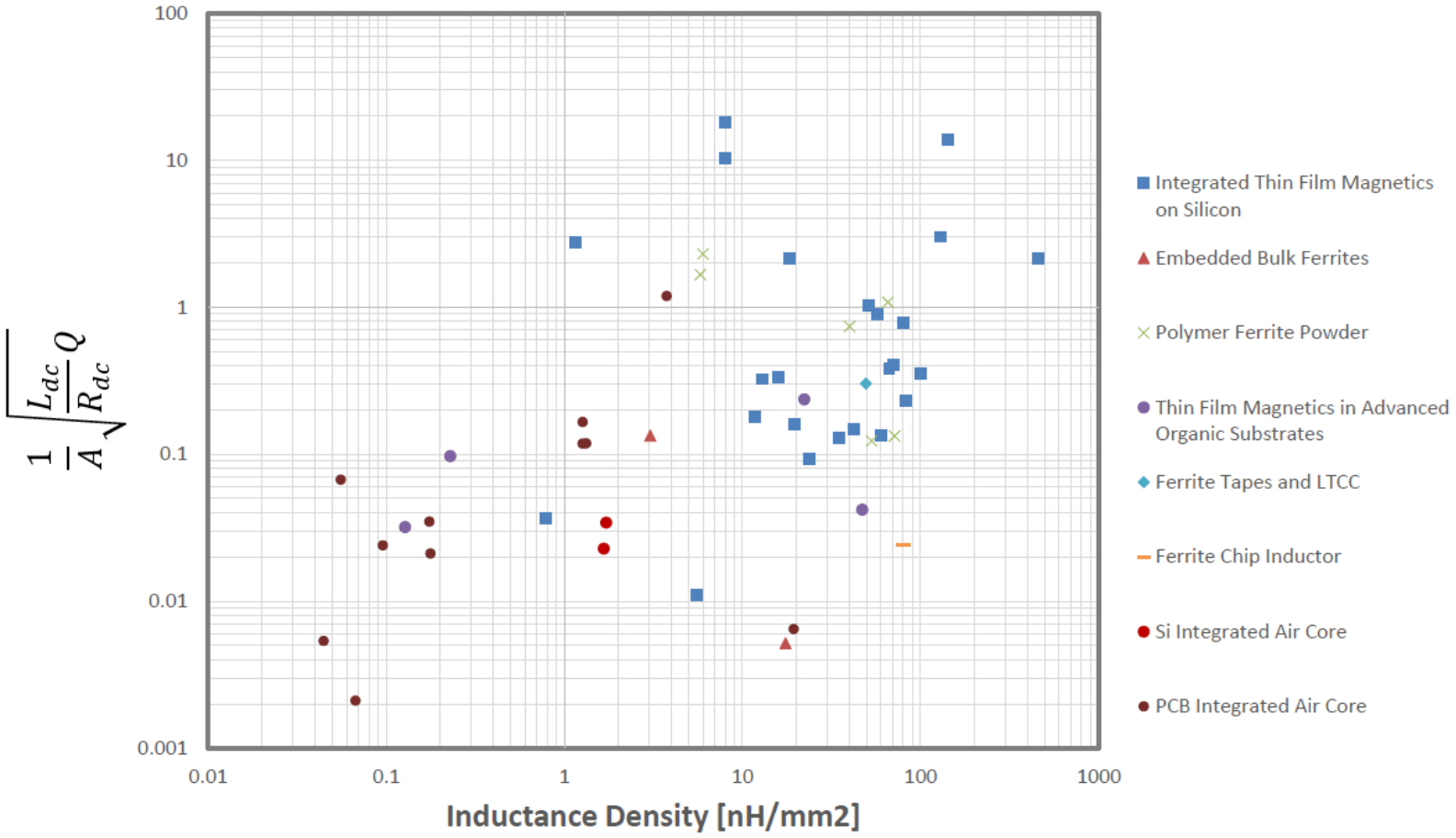

Figure 2.15: AC-DC FOM vs inductance density of PwrSiP & PwrSoC applications found in literature. Note top right of graph is desired area for PwrSiP & PwrSoC applications. See table 2.1 for details.

Power Supply in Package Inductors								
Inductor Type	Footprint [mm^2]	FOM	L/R_{dc} [$nH/m\Omega$]	Q	Material Q	Author	Institution	Year
Spiral	1	2.309	.333	16	FeCNO	Sugawa [11]	Shinshu University	2013
Spiral	1	1.67	0.23	12	ZnFe	Yazaki [71]	Shinshu University	2014
Spiral	1	1.19	0.25	9.5	Air Core	Yazaki [71]	Shinshu University	2014
Spiral	9	1.08	6.34	15	FeBSiC	Endo [72]	Tohoko University	2015
Spiral	20.25	0.74	5	45	NiZn	Bang [9]	Kwangwoon University	2009
Spiral	64	0.17	1.13	100	Air Core	Madsen [73]	Technical University of Denmark	2013
Spiral	70	0.13	6.94	12.5	FeSiAl	Lim [13]	Hanyang University	2018
Spiral	9	0.024	0.014	3.27	$Y_3Fe_5O_{12}$	Bechir [74]	University de Lyon	2015
Spiral	912	0.006	1.05	33	Air Core	Olivio [75]	Ecole Polythechnique Federale de Lausanne	2013
Spiral	600	0.002	0.13	8	NiFe	Park [76]	Georgia Institute of Technology	2004
Solenoid	27	0.24	2.54	16	CoNiFe	Kim [77]	Georgia Institute of Technology	2015
Solenoid	64	0.12	1.13	51	Air Core	Madsen [73]	Technical University of Denmark	2013
Solenoid	14.2	0.01	0.27	7	CoFeHfO	Li [70]	Stanford University	2009
Toroid	225	0.13	15.95	57	Ferrite	Dou [78]	Technical University of Denmark	2018
Toroid	900	0.07	20.83	175	Air Core	Biglarbegian [79]	University of North Carolina at Charlotte	2015
Toroid	484	0.035	2.11	135	Air Core	Liang [80]	Stanford University	2016
Toroid	31.36	0.032	0.05	18.85	CoZrO	Qiu [81]	Dartmouth	2013
Toroid	31.36	0.024	0.04	14.14	Air Core	Qiu [81]	Dartmouth	2013
Toroid	282	0.021	0.24	149	Air Core	Kamby [82]	Technical University of Denmark	2012
Toroid	440	0.005	2.48	2.09	MnZn	Salas [5]	Universidad Carlos III de Madrid	2016
Power Supply on Chip Inductors								
RaceTrack	0.27	3.02	0.22	3	NiFe	Wang [83]	IBM	2012
RaceTrack	4.03	2.16	0.93	81.8	NiFe	Feeney [84]	NUI Galway	2015
RaceTrack	0.01	2.14	0.001	0.74	CZTB	Wu [85]	Arizona State University	2012
RaceTrack	0.25	1.02	0.05	1.36	NiFe	Sturken [86]	AMD	2013
RaceTrack	2.5	0.9	0.36	24	NiFe	Meere [87]	Tyndall National Institute	2009
RaceTrack	1.95	0.38	0.09	5.98	NiFe	Feeney [88]	NUI Galway	2015
RaceTrack	5.4	0.32	0.58	5.26	NiFe	Wang [89]	Tyndall National Institute	2013
RaceTrack	4.06	0.16	0.08	5.3	NiFe	Feeney [88]	NUI Galway	2015
RaceTrack	25	0.15	0.98	13.93	CoZrO	Harburg [90]	Dartmouth	2013
Stripline	0.42	18.24	0.89	66	CoZrO	Yao [91]	Maxim Integrated	2013
Stripline	0.12	13.75	0.83	3.3	NiFe	Morrow [92]	Intel Corporation	2011
Stripline	2.26	2.74	3.58	10.9	CoZrO	Prabhakaran [53]	Dartmouth	2005
Spiral	25	0.18	2.92	7	FeHfN	Kuo [93]	National Tsing Hua University	2012
Spiral	16	0.13	1.07	4.31	CoHfTaPd	Katayama [94]	Fuji Electric Corp. R&D Ltd.	2000
Solenoid	0.88	0.78	0.1	4.5	CoZrTa	Lee [68]	Virginia Tech	2012
Toroid	2.9	0.54	0.16	16	MnZn	Fang [95]	The Hong Kong University of Science and Technology	2013
Toroid	31.36	0.33	5.26	20.9	NiFe	Orlando [96]	STMicroelectronics	2006
Toroid	36	0.16	0.83	39	Fe	Yu [97]	Georgia Institute of Technology	2014

Table 2.1: Comparison of integrated magnetics for PwrSiP versus PwrSoC.

Note, although Figs. 2.14 & 2.15 are discussed in Sections 2.2.2 & 2.2.3 they are presented here for the reader's ease of comparison with Fig. 2.13. Moreover, Fig. 2.13 makes clear the division between PwrSiP, and PwrSoC, applications as the former clearly demonstrate better L_{dc}/R_{dc}, whereas the latter clearly exhibit smaller footprints. This is a natural consequence of the very different fabrication methods of PCB vs Si manufacture. The Si processes can clearly exhibit a much smaller copper width to line spacing ratio, and so results in a smaller footprint, whereas the PCB process, forgoing the better line spacing, can achieve much better L_{dc}/R_{dc} ratios through the ease at which thicker copper can be deposited. Hence, it is very much the manufacturing constraints pertaining to PCB and Si fabrication which serves to partition Fig. 2.13.

Although this FOM provides useful information on the device performance it does not include the current handling capabilities of the magnetic core, nor does it account for the various other loss mechanisms that can exist within the device. Therefore it is not entirely suitable to accurately predict whether an inductor will perform well in a given PwrSiP application, and so another FOM is required in order to account for circumstances in which there exists other loss mechanisms of the inductor, and not only DC conduction loss. Such other loss mechanisms include: magnetic core hysteresis losses; eddy current loss within the core; and so on. In the next subsection we discuss

another key FOM in which this issue is redressed.

2.2.2 AC - Analysis

To account for the aforementioned losses we begin by using Poynting's Vector [67] and the conservation of field energy. This approach is incredibly useful as it can be used to determine a relationship between the energy within the system, and the power dissipation of the system. Formally Poynting's vector can be given by Eq. 2.2.6,

$$\frac{\partial u}{\partial t} = \nabla \cdot \boldsymbol{S} - \boldsymbol{E} \cdot \boldsymbol{J}. \tag{2.2.6}$$

Here u is the energy density within the system; $\boldsymbol{S}$ is Poynting's vector and pertains to the flow of energy out of the system viz electromagnetic radiation; and $\boldsymbol{E} \cdot \boldsymbol{J}$ is the total mechanical work being done within the system. The main tractability of this approach is that we can now very easily determine the ratio of the energy density stored within the system to the average power loss. The average power dissipated by the system per cycle is readily determined by integrating Eq. 2.2.6 over one time period, and so then, by determining the ratio of energy density to power dissipated per cycle we have arrived at another key FOM – the quality factor, Q.

$$= \frac{u}{\frac{1}{T}\int_0^T \frac{\partial u}{\partial t} dt} \qquad = \frac{Energy\ Stored}{Average\ Power\ Dissipated\ per\ Cycle} \tag{2.2.7}$$

$$Q = \frac{\omega L}{R_{ac} + R_{rad}} \tag{2.2.8}$$

Here R_{rad} is the radiation resistance term. Typically the inductors operate in the "quasi-static" frequency range where $\omega << c$ (where c is the speed of light) and so the radiation resistance term is often omitted from the Q-Factor. Therefore, the only loss mechanism considered within the system is the mechanical work being done. A key advantage of this fundamental approach is that it illustrates the link between the mechanical work being done within the magnetic core, be it through the formation of eddy currents, or the motion of magnetic domains, to the resistance of the inductor. Hence, it is quite clear that although the presence of the magnetic material greatly increases the energy density stored by the magnetic field (see Fig. 2.13 for empirical data or Eq. 1.2.3 for the theory), but it also gives rise to new loss mechanisms within the magnetic core that an air core inductor would not have. This is best illustrated by the work of Lee et al. [68] who explicitly state the contribution of the magnetic core to the Q-Factor, see Eq. 2.2.9

$$Q = \omega \frac{L_{air\ core} + \Delta L}{R_{air\ core} + \omega \frac{\mu''}{\mu'} \Delta L} \tag{2.2.9}$$

Thus the efficiency of the inductor with an integrated magnetic core is largely determined by the gain in inductance due to the magnetic core and the magnetic core's loss tangent (μ''/μ'). Normally there is a tipping point operating

frequency whereat the frequency dependent losses within the magnetic core exceed the benefit of the core in terms of energy density. Whence the ratio of μ''/μ' ultimately determines the useful bandwidth of the magnetic material. The challenge for future PwrSiP applications is therefore to extend the magnetic materials useful bandwidth into the higher frequency ranges. This can be achieved through judicious choice of the magnetic material, i.e. materials with inherently higher B_{sat} e.g., CoFeHfo, CoNbZr, and FeGab have been demonstrated to outperform the air-core equivalent in the 100 MHz range [69], and/or through the use of micropatterning techniques [70].

Figure 2.14 shows the Q-Factor vs Inductance density of devices found in the literature. There is a clear trend of decreasing Q-Factor with increasing inductance density. Considering that the inductance density is proportional to the energy density this highlights the difficulty for future PwrSiP applications which ideally would like to maximise energy density in order to facilitate the ongoing miniaturisation trend, and minimise power dissipation.

It is clear from Fig. 2.14 that Si based inductors with integrated magnetic cores exhibit the highest inductance densities. This is to be expected as the minimum line spacing between adjacent copper tracks is of critical importance in determining the overall footprint, and so any density based FOM, of the device. However, several of the PwrSiP inductors that utilise FPC, Ferrite Tapes & LTCC, and Thin Film Magnetics in Advanced Organic substrates match the Si based inductors in terms of equal Inductance density

and Q-Factor performance (see top right of Fig. 2.14).

In order to enumerate the fundamental trade-off between the inductance density and the quality factor of the inductor there is a need for a new FOM. The FOM that we propose combines the L_{dc}/R_{dc} ratio and the Q-Factor, and so it acts to directly map the fundamental trade-off between energy density and power dissipation to a singular scalar value. This is discussed in the next section.

2.2.3 AC-DC - Analysis

The proposed FOM to measure the trade-off between the AC performance and the DC performance of the inductor multiples the L_{dc}/R_{dc} with the Q-factor of the device and normalises per unit footprint (see Eq. 2.2.10). Here the square root is taken in order to reduce the absolute value of the FOM. The main benefit of this FOM is that there exists a multiplicative effect of poor performance i.e., devices which underperform in one area, be it the AC performance or DC performance, are scored poorly. Hence, the measured inductor needs to have both good AC and DC performance.

$$FOM = \frac{1}{A}\sqrt{\frac{L_{dc}}{R_{dc}}Q} \tag{2.2.10}$$

In Fig. 2.15 the hybrid FOM is plotted against the inductance density of devices reported in the literature. The requirement of good AC and DC

performance is best illustrated by the integrated air core inductors which all scored highly in terms of Q-factor per inductance density, but score very poorly with this hybrid FOM. This is to be expected as intuitively the presence of the magnetic core should improve both the energy density within the core and the Q-factor of the core up to the point where the losses within the magnetic core do not exceed the gain in the energy density.

Furthermore, although the PwrSiP inductors have outperformed their Si-based counterparts in terms of DC performance, they have failed to outperform their Si PwrSoC counterparts in terms of the hybrid AC-DC FOM. Considering that the Q-Factor of the device is related to the energy density vs the power dissipation density, it is clear that PwrSiP based inductors do not have favourable energy density to power dissipation as compared to PwrSoC devices.

Therefore, in terms of the thin film magnetics devices there has been a degradation in performance of the material which is entirely related to the substrate on which it is deposited. In our work we have found that the surface condition of the substrate plays a critical role in the overall performance of the magnetic material. This is later discussed in chapters 3 & 5 of the thesis.

2.3 Future Magnetic Morphologies & Alloy Compositions for PwrSiP

With the ever increasing switching speeds required for the miniaturisation of power supplies, there exists a need for novel magnetic materials which exhibit excellent low loss high frequency performance. Thin film magnetics, based on soft magnetic alloys with a crystalline lattice, to a degree meet these requirements due to their magnetic reversal process being dominated by in plane coherent rotation of the individual magnetic domains. Nevertheless they still have internal anisotropy energies which act as a form of memory to the prior magnetic state of the system. In other words, these internal energies within the alloys create a system which inherently has hysteresis. Thus they will ultimately have higher hysteresis losses than a system comprising a morphology with no such anisotropies.

Amorphous magnetic alloys and Bulk Metallic Glasses (BMG) are ideally suited to be the magnetic material used in high frequency integrated PwrSiP in future electronic applications. The primary reason for this being that both morphologies lack a long range atomic order, and, as such, the magnetocrystalline anisotropy randomly fluctuates over a scale that is much smaller than the domain wall width. Thus, the magnetocrystalline anisotropy is averaged over several exchange lengths and has no effect on the long range magnetisation reversal process. This long range cancellation of the magnetocrystalline

anisotropy is a prerequisite for the materials in order to have ultra-low coercive losses, viz. Herzer [61], and therefore is an essential requirement of the morphology of the magnetic material being used in future PwrSiP applications.

In addition to the averaging out of the magnetocrystalline anisotropy, the lack of atomic order in amorphous alloys and bulk metallic glasses results in a much higher resistivity of the alloy. The increase in resistivity arises due to the decreased expected time to collision of electrons, which is a direct consequence of the absence of a crystal lattice due to the high degree of atomic disorder. Thus, eddy current losses inside the amorphous alloys are significantly lower than that of their highly structured crystalline counterparts, and so, for a given frequency, the overall inductance of the power regulator can be increased by using a thicker magnetic layer without the need to adopt a more costly multi-layer stack, or laminated core stack (caveat : see chapter 5 section 5.4).

Moreover, there are no microstructural discontinuities (grain boundaries or precipitates) on which magnetic domains can be pinned, since the material is magnetically homogenous over lengths comparable to the magnetic exchange interaction, and hence the intrinsic coercivity is small. It is for these reasons that amorphous magnetic alloys and BMGs can have 60-70 percent lower core losses as compared to conventional crystalline iron silicon cores [98].

Therefore, owing to the superior performance of amorphous metallic alloys and BMGs, they are an ideal candidate to be the magnetic component in future PwrSiP Applications. The following subsections will now focus on the two main families of amorphous metallic alloys and BMGs.

2.3.1 Iron Based Amorphous Alloys

Amorphous alloys which are primarily based on Iron are typically characterised as having a large magnetisation saturation, relatively low magnetic permeability, and a higher coefficient of magnetostriction as compared to their amorphous cobalt counterparts. Normally high magnetostriction is undesired as it gives rise to greater coercive losses. However, in the case of thin film magnetics the preferred orientation of the magnetisation is in plane as this reduces the internal energy of the system via the minimisation of the internal demagnetisation field. Furthermore a weak anisotropic field may be induced, by means of magnetic annealing or off axis deposition, to control the magnetisation reversal process [99], and so, in conjunction with the high magnetostriction coefficient of amorphous iron, strain applied along the hard axis of the thin film can be used to drastically reduce coercivity of the film by increasing the in plane uniaxial anisotropy field [100]. This reduces the area bound by the hysteresis loop reducing the power loss per cycle of the core.

However the application of strain along the easy axis increases the square-

Alloy Composition	B_{sat} [T]	Tc [C]	μ [kOe]	Hc [Oe]	$\rho[\mu\Omega cm]$	Nominal Thickness [μm]
$Fe_{80}B_{20}$	1.57	320	374	0.04	140	0.1 - 0.5
$Fe_{82}B_{10}Si_8$	1.52	300	415	0.17	130	0.1 - 20
$Fe_{67}Co_{18}B_{14}Si_1$	1.75	200	415	0.08	130	0.1 - 20
$Fe_{81}B_{13.5}Si_{3.5}C_2$	1.57	300	415	0.08	125	0.1 - 20
M4-Grade Si Steel*	2.03	735	12	0.09	46	25 - 650
H2-Grade Si Steel*	2.03	735	30	0.09	46	25 - 650

Table 2.2: Magnetic properties of several Fe-based amorphous alloys compared to crystalline Si steel [103] (*Note final two entries are crystalline.).

ness of the hysteresis loop, and so, the large coefficient of magnetostriction makes amorphous iron based alloys ideally suited for strain gauge sensors. Indeed amorphous based iron magnetic cores have been commercialized as magnetic rotation torque and strain sensors (comprising FeBSiNb and FeCoBSiNb) and magnetic core inductors (comprising FeCr(B,Si,P,C)) with respective trademarks “Liqualloy”, and “SENNTIX” [101, 102].

Note, due to the high magnetostriction of Fe-Based amorphous alloys care must be taken when embedding amorphous iron into package as the effect of unwanted strain (strain along the easy axis) arising from the embedding process can drastically reduce transformer performance. Table 2.2 shows a comparison of some of the magnetic properties of amorphous iron based cores and compares them against crystalline steel. It is evident from this table that the amorphous alloys of iron are significantly more suitable for PwrSiP applications than their crystalline counterparts.

2.3.2 Cobalt Based Amorphous Alloys

Amorphous Co based alloys are characterized by relatively low saturation induction, excellent high-frequency soft magnetic properties, and almost zero coefficient of magnetostriction. The use of thin amorphous cobalt films in, or exceeding, the Very High Frequency (VHF) range (30-300 MHz) has been well demonstrated in the semiconductor technologies by several researchers [85, 104]. Such high frequency performance is essential for future power supply in package applications as the operating frequency of the active components migrate towards the higher frequency bands in order to continue the trend of device miniaturization. Thus, amorphous cobalt thin films are an ideal candidate to be the magnetic component of future PwrSiP applications.

Furthermore, the almost zero coefficient of magnetostriction of amorphous cobalt means that they are better suited to undergo an embedding processes, which typically involve some form of binding phase where temperature and pressure are used to form the stack. Thus, amorphous cobalt films can be readily incorporated into the PCB substrate, in lieu of the standard ferrite core, which, being limited to the lower frequency ranges due to the reasons outlined earlier is unlikely to be used in the next generation of future electronic devices if the trend of increasing switching speeds of active devices continues.

2.4 Conclusion

This chapter reviewed the state of the art technologies for the integration of the magnetic components of voltage regulators into advanced organic substrates for Power Supply in Package applications. The various technologies used to integrate the magnetic component into the package were discussed along with their individual strengths and weaknesses. The embedding of the magnetic component into the package has been driven by the prevailing miniaturisation trend in power electronics. This miniaturisation trend is largely enabled by the ever increasing switching speed of the active MOSFET components in the DC-DC converter which results in a reduction in the value of inductance required for energy storage. Hence, there is a need for magnetic materials which exhibit excellent soft magnetic properties in the low part of the very high frequency band (30-300 MHz).

Due to this increased frequency performance requirement of the magnetic passive, some researchers have distributed fine ferrite powders into polymer matrices in order to stymie the high frequency losses associated with ferrite materials. However this has the effect of reducing the permeability of the material, and as such, ultimately undermines the benefit of using a magnetic core as the volume of magnetic material is reduced. Therefore there is a fundamental trade-off between the increased operating frequency and power density of the polymer ferrite composite, which is non-ideal for power supply

in package applications.

Amorphous thin film magnetics are an ideal candidate to be the magnetic component for future power supply in package applications as they exhibit excellent high frequency soft magnetic properties. This is due to the highly unstructured nature of atomic distribution within the amorphous film. Whence, the magnetocrystalline anisotropy is averaged out over several exchange lengths, resulting in ultra-low coercive losses of the material during magnetisation reversal. Furthermore, the resistivity of amorphous magnetic alloys is much higher than their crystalline counterparts owing to increased electron scattering caused by the lack of a crystal lattice.

Ultimately this chapter acts as the backdrop in which our work is compared. In later chapters when our fabrication techniques are discussed the reader has the understanding of other manufacturing techniques and thus is more able to draw inferences between our approach and results, and those produced by other methods. Furthermore, this chapter investigated the various FOMs used to characterise the efficacy of magnetic components within Pwr-SiP applications, and their individual strength and weakness were discussed. Hence, this chapter better equips the reader with the background knowledge to judge our work in integrated thin film magnetics.

Bibliography

[1] D. Bowen, D. Basu, C. Krafft, and I. Mayergoyz, "Fabrication and evaluation of pcb-embedded broadband signal transformers with custom machined racetrack-shaped ferrite cores for ethernet applications," *IEEE Transactions on Magnetics*, vol. 53, no. 11, pp. 1–5, 2017.

[2] R. Caillaud, C. Buttay, R. Mrad, J. Le Leslé, F. Morel, N. Degrenne, S. Mollov, and C. Martin, "Design, manufacturing and characterization of printed circuit board embedded inductors for power applications," in *2018 IEEE International Conference on Industrial Technology (ICIT)*, pp. 694–699, IEEE, 2018.

[3] B. Sun, R. Burgos, and D. Boroyevich, "2 w gate drive power supply design with pcb-embedded transformer substrate," in *2017 IEEE Applied Power Electronics Conference and Exposition (APEC)*, pp. 197–204, IEEE, 2017.

[4] B. Sun, R. Burgos, D. Boroyevich, R. Perrin, C. Buttay, B. Allard, N. Quentin, and M. Ali, "Two comparison-alternative high tempera-

ture pcb-embedded transformer designs for a 2 w gate driver power supply," in *2016 IEEE Energy Conversion Congress and Exposition (ECCE)*, pp. 1–7, IEEE, 2016.

[5] R. A. Salas, "Computer-aided design, manufacturing and test of a ferrite toroidal planar transformer integrated in a printed circuit board," in *2016 3rd International Conference on Information Science and Control Engineering (ICISCE)*, pp. 276–281, IEEE, 2016.

[6] R. Perrin, B. Allard, C. Buttay, N. Quentin, W. Zhang, R. Burgos, D. Boroyevic, P. Preciat, and D. Martineau, "2 mhz high-density integrated power supply for gate driver in high-temperature applications," in *2016 IEEE Applied Power Electronics Conference and Exposition (APEC)*, pp. 524–528, IEEE, 2016.

[7] H.-I. Hsiang and J.-L. Wu, "Copper-rich phase segregation effects on the magnetic properties and dc-bias-superposition characteristic of nicuzn ferrites," *Journal of Magnetism and Magnetic Materials*, vol. 374, pp. 367–371, 2015.

[8] S. Yan, L. Dong, Z. Chen, X. Wang, and Z. Feng, "The effect of the microstructure on the dc-bias superposition characteristic of nicuzn ferrite," *Journal of Magnetism and Magnetic Materials*, vol. 353, pp. 47–50, 2014.

[9] D. H. Bang and J. Y. Park, "Ni-zn ferrite screen printed power induc-

tors for compact dc-dc power converter applications," *IEEE Transactions on Magnetics*, vol. 45, no. 6, pp. 2762–2765, 2009.

[10] E. J. Brandon, E. E. Wesseling, V. Chang, and W. B. Kuhn, "Printed microinductors on flexible substrates for power applications," *IEEE transactions on Components and Packaging Technologies*, vol. 26, no. 3, pp. 517–523, 2003.

[11] Y. Sugawa, K. Ishidate, M. Sonehara, and T. Sato, "Carbonyl-iron/epoxy composite magnetic core for planar power inductor used in package-level power grid," *IEEE Transactions on Magnetics*, vol. 49, no. 7, pp. 4172–4175, 2013.

[12] G. Cao, H.-J. Kim, S.-T. Lim, G.-S. Han, *et al.*, "An embedded inductor using sendust powder composite films for step-up dc–dc converter," *IEEE Transactions on Magnetics*, vol. 50, no. 11, pp. 1–4, 2014.

[13] J.-W. Lim, H.-J. Kim, Y.-S. Oh, H.-S. Kim, and S.-T. Lim, "Embedded flexible fe–si–al powder composite film inductor for low power dc–dc converters," *IEEE Transactions on Applied Superconductivity*, vol. 28, no. 3, pp. 1–5, 2018.

[14] L. Liu, T. Ge, Y. Yan, K. Ngo, and G. Lu, "Uv-assisted 3d-printing of soft ferrite magnetic components for power electronics integration," in *2017 International Conference on Electronics Packaging (ICEP)*, pp. 447–450, IEEE, 2017.

[15] H. Ito, A. Takeuchi, S. Okazaki, H. Kobayashi, Y. Sugawa, A. Takeshima, M. Sonehara, N. Matsushita, and T. Sato, "Fabrication of planar power inductor for embedded passives in lsi package for hundreds megahertz switching dc–dc buck converter," *IEEE Transactions on Magnetics*, vol. 47, no. 10, pp. 3204–3207, 2011.

[16] Y. Wu, P. Zhu, and R. Sun, "Preparation and magnetic properties of silane modified ni-zn ferrite and its epoxy composites," in *2011 IEEE International Conference on Information and Automation*, pp. 879–881, IEEE, 2011.

[17] H. Jia, J. Lu, X. Wang, K. Padmanabhan, and Z. J. Shen, "Integration of a monolithic buck converter power ic and bondwire inductors with ferrite epoxy glob cores," *IEEE transactions on Power Electronics*, vol. 26, no. 6, pp. 1627–1630, 2010.

[18] J. Lu, H. Jia, A. Arias, X. Gong, and Z. J. Shen, "On-chip bondwire transformers for power soc applications," in *2008 Twenty-Third Annual IEEE Applied Power Electronics Conference and Exposition*, pp. 199–204, IEEE, 2008.

[19] J. Lu, H. Jia, A. Arias, X. Gong, and Z. J. Shen, "On-chip bondwire magnetics with ferrite-epoxy glob coating for power systems on chip," *Advances in Power Electronics*, vol. 2008, 2008.

[20] Z. J. Shen, J. Lu, X. Cheng, H. ngwei Jia, *et al.*, "On-chip bondwire

inductor with ferrite-epoxy coating: A cost-effective approach to realize power systems on chip," in *2007 IEEE Power Electronics Specialists Conference*, pp. 1599–1604, IEEE, 2007.

[21] T. Burress, "Benchmarking ev and hev technologies," *Oak Ridge National Laboratory*, 2014.

[22] B. J. Kang, C. K. Lee, and J. H. Oh, "All-inkjet-printed electrical components and circuit fabrication on a plastic substrate," *Microelectronic Engineering*, vol. 97, pp. 251–254, 2012.

[23] G. McKerricher, J. G. Perez, and A. Shamim, "Fully inkjet printed rf inductors and capacitors using polymer dielectric and silver conductive ink with through vias," *IEEE Transactions on Electron Devices*, vol. 62, no. 3, pp. 1002–1009, 2015.

[24] Y. Yan, C. Ding, K. D. Ngo, Y. Mei, and G.-Q. Lu, "Additive manufacturing of planar inductor for power electronics applications," in *2016 International Symposium on 3D Power Electronics Integration and Manufacturing (3D-PEIM)*, pp. 1–16, IEEE, 2016.

[25] W. Liang, L. Raymond, M. Praglin, D. Biggs, F. Righetti, M. Cappelli, B. Holman, and J. R. Davila, "Low mass rf power inverter for cubesat plasma thruster using 3d printed inductors," in *2016 IEEE 17th Workshop on Control and Modeling for Power Electronics (COMPEL)*, pp. 1–7, IEEE, 2016.

[26] M. Hagymási, A. Roosen, R. Karmazin, O. Dernovsek, and W. Haas, "Constrained sintering of dielectric and ferrite ltcc tape composites," *Journal of the European Ceramic Society*, vol. 25, no. 12, pp. 2061–2064, 2005.

[27] J.-C. Jao, P. Li, and S.-F. Wang, "Characterization of inductor with ni–zn–cu ferrite embedded in b2o3–sio2 glass," *Japanese Journal of Applied Physics*, vol. 46, no. 9R, p. 5792, 2007.

[28] H.-J. Kim, Y.-J. Kim, and J.-R. Kim, "An integrated ltcc inductor embedding nizn ferrite," *IEEE transactions on magnetics*, vol. 42, no. 10, pp. 2840–2842, 2006.

[29] L. Wang, Y. Pei, X. Yang, B. Song, Z. Wang, and G. Zhao, "Evaluation of ltcc capacitors and inductors in dc/dc converters," in *2010 Twenty-Fifth Annual IEEE Applied Power Electronics Conference and Exposition (APEC)*, pp. 2060–2065, IEEE, 2010.

[30] M. H. F. Lim, Z. Liang, and J. D. van Wyk, "Low profile integratable inductor fabricated based on ltcc technology for microprocessor power delivery applications," *IEEE transactions on components and packaging technologies*, vol. 30, no. 1, pp. 170–177, 2007.

[31] R. Matz, D. Götsch, R. Karmazin, R. Männer, and B. Siessegger, "Low temperature cofirable mnzn ferrite for power electronic applications," *Journal of electroceramics*, vol. 22, no. 1-3, pp. 209–215, 2009.

[32] A. Roesler, J. Schare, and C. Hettler, "Integrated power electronics using a ferrite-based low-temperature co-fired ceramic materials system," in *2010 Proceedings 60th Electronic Components and Technology Conference (ECTC)*, pp. 720–726, IEEE, 2010.

[33] L. Wang, Z. Hu, Y.-F. Liu, Y. Pei, X. Yang, and Z. Wang, "A horizontal-winding multipermeability ltcc inductor for a low-profile hybrid dc/dc converter," *IEEE Transactions on Power Electronics*, vol. 28, no. 9, pp. 4365–4375, 2013.

[34] L. Wang, Y. Pei, X. Yang, and Z. Wang, "Design of ultrathin ltcc coupled inductors for compact dc/dc converters," *IEEE Transactions on Power Electronics*, vol. 26, no. 9, pp. 2528–2541, 2011.

[35] M. H. F. Lim, J. D. van Wyk, and F. C. Lee, "Hybrid integration of a low-voltage, high-current power supply buck converter with an ltcc substrate inductor," *IEEE Transactions on Power Electronics*, vol. 25, no. 9, pp. 2287–2298, 2010.

[36] M. H. Lim, Y. Dong, J. D. van Wyk, F. C. Lee, and K. D. Ngo, "Shielded ltcc inductor as substrate for power converter," in *2007 IEEE Power Electronics Specialists Conference*, pp. 1605–1611, IEEE, 2007.

[37] Q. Li, Y. Dong, F. C. Lee, and D. J. Gilham, "High-density low-profile coupled inductor design for integrated point-of-load converters," *IEEE Transactions on Power Electronics*, vol. 28, no. 1, pp. 547–554, 2012.

[38] Q. Li and F. C. Lee, "High inductance density low-profile inductor structure for integrated point-of-load converter," in *2009 Twenty-Fourth Annual IEEE Applied Power Electronics Conference and Exposition*, pp. 1011–1017, IEEE, 2009.

[39] R. Hergt, R. Hiergeist, I. Hilger, W. A. Kaiser, Y. Lapatnikov, S. Margel, and U. Richter, "Maghemite nanoparticles with very high ac-losses for application in rf-magnetic hyperthermia," *Journal of Magnetism and Magnetic Materials*, vol. 270, no. 3, pp. 345–357, 2004.

[40] C. H. Li, P. Hodgins, and G. Peterson, "Experimental study of fundamental mechanisms in inductive heating of ferromagnetic nanoparticles suspension (fe3o4 iron oxide ferrofluid)," *Journal of Applied Physics*, vol. 110, no. 5, p. 054303, 2011.

[41] D. Hou, Y. Su, Q. Li, and F. C. Lee, "Improving the efficiency and dynamics of 3d integrated pol," in *2015 IEEE Applied Power Electronics Conference and Exposition (APEC)*, pp. 140–145, IEEE, 2015.

[42] W. Huang and B. Lehman, "A compact coupled inductor for interleaved multiphase dc–dc converters," *IEEE Transactions on Power Electronics*, vol. 31, no. 10, pp. 6770–6775, 2016.

[43] P.-L. Wong, P. Xu, P. Yang, and F. C. Lee, "Performance improvements of interleaving vrms with coupling inductors," *IEEE Transactions on Power Electronics*, vol. 16, no. 4, pp. 499–507, 2001.

[44] L. Huan, X. Tang, H. Su, H. Zhang, and Y. Jing, "Effects of sio 2 concentration on the dc-bias-superposition characteristics of the nicuzn ferrites," *Journal of Materials Science: Materials in Electronics*, vol. 26, no. 5, pp. 3275–3281, 2015.

[45] H. Su, H. Zhang, X. Tang, and Y. Jing, "Influence of microstructure on permeability dispersion and power loss of nizn ferrite," *Journal of Applied Physics*, vol. 103, no. 9, p. 093903, 2008.

[46] T. Tsutaoka, "Frequency dispersion of complex permeability in mn–zn and ni–zn spinel ferrites and their composite materials," *Journal of Applied Physics*, vol. 93, no. 5, pp. 2789–2796, 2003.

[47] Y.-H. Lee, W.-C. Kuan, and W.-H. Tuan, "Inter-diffusion between nicuzn-ferrite and ltcc and its influence on magnetic performance," *Journal of the European Ceramic Society*, vol. 33, no. 1, pp. 95–103, 2013.

[48] Y. Li, Y. Xie, R. Chen, L. Han, D. Chen, and H. Su, "A multilayer power inductor fabricated by cofirable ceramic/ferrite materials with ltcc technology," *IEEE Transactions on Components, Packaging and Manufacturing Technology*, vol. 7, no. 9, pp. 1402–1409, 2017.

[49] M. Ludwig, M. Duffy, T. O'Donnell, P. McCloskey, and S. C. Ó. Mathùna, "Pcb integrated inductors for low power dc/dc converter,"

IEEE Transactions on Power Electronics, vol. 18, no. 4, pp. 937–945, 2003.

[50] M. Ludwig, M. Duffy, T. O'Donnell, P. McCloskey, and S. C. ÓMathùna, "Design study for ultraflat pcb-integrated inductors for low-power conversion applications," *IEEE transactions on magnetics*, vol. 39, no. 5, pp. 3193–3195, 2003.

[51] M. Vopson, J. Naylor, T. Saengow, E. G. Rogers, S. Lepadatu, and Y. Fetisov, "Development of flexible ni80fe20 magnetic nano-thin films," *Physica B: Condensed Matter*, vol. 525, pp. 12–15, 2017.

[52] S. Lu, Y. Sun, M. Goldbeck, D. R. Zimmanck, and C. R. Sullivan, "30-mhz power inductor using nano-granular magnetic material," in *2007 IEEE Power Electronics Specialists Conference*, pp. 1773–1776, IEEE, 2007.

[53] S. Prabhakaran, Y. Sun, P. Dhagat, W. Li, and C. R. Sullivan, "Micro-fabricated v-groove power inductors for high-current low-voltage fast-transient dc-dc converters," in *2005 IEEE 36th Power Electronics Specialists Conference*, pp. 1513–1519, IEEE, 2005.

[54] J. Qiu and C. R. Sullivan, "Inductor design for vhf tapped-inductor dc-dc power converters," in *2011 Twenty-Sixth Annual IEEE Applied Power Electronics Conference and Exposition (APEC)*, pp. 142–149, IEEE, 2011.

[55] J. Qiu and C. R. Sullivan, "Design and fabrication of vhf tapped power inductors using nanogranular magnetic films," *IEEE Transactions on Power Electronics*, vol. 27, no. 12, pp. 4965–4975, 2012.

[56] H. Wu, M. Khdour, P. Apsangi, and H. Yu, "High-frequency magnetic thin-film inductor integrated on flexible organic substrates," *IEEE Transactions on Magnetics*, vol. 53, no. 11, pp. 1–7, 2017.

[57] D. Yao and C. R. Sullivan, "Calculation of eddy-current loss in multilayer magnetic films considering displacement current," *Journal of Applied Physics*, vol. 105, no. 7, p. 07A335, 2009.

[58] D. Yao and C. R. Sullivan, "Effect of capacitance on eddy-current loss in multi-layer magnetic films for mhz magnetic components," in *2009 IEEE Energy Conversion Congress and Exposition*, pp. 1025–1031, IEEE, 2009.

[59] D. Li, Z. Wang, X. Han, Y. Li, X. Guo, Y. Zuo, and L. Xi, "Improved high-frequency soft magnetic properties of feco films on organic ferroelectric pvdf substrate," *Journal of Magnetism and Magnetic Materials*, vol. 375, pp. 33–37, 2015.

[60] G. Herzer, "Anisotropies in soft magnetic nanocrystalline alloys," *Journal of Magnetism and Magnetic Materials*, vol. 294, no. 2, pp. 99–106, 2005.

[61] G. Herzer, "Modern soft magnets: Amorphous and nanocrystalline materials," *Acta Materialia*, vol. 61, no. 3, pp. 718–734, 2013.

[62] Y. E. Zhang and S. R. Sanders, "In-board magnetics processes," in *30th Annual IEEE Power Electronics Specialists Conference. Record.(Cat. No. 99CH36321)*, vol. 1, pp. 561–567, IEEE, 1999.

[63] S. Kulkarni, D. Li, D. Jordan, N. Wang, and C. Ó. Mathúna, "Pcb embedded bondwire inductors with discrete thin-film magnetic core for power supply in package," *IEEE Journal of Emerging and Selected Topics in Power Electronics*, vol. 6, no. 2, pp. 614–620, 2018.

[64] P. Herget, N. Wang, E. J. O'Sullivan, B. C. Webb, L. T. Romankiw, R. Fontana, G. Decad, and W. J. Gallagher, "Limits to on-chip power conversion with thin film inductors," *IEEE transactions on magnetics*, vol. 49, no. 7, pp. 4137–4143, 2013.

[65] C. Ó. Mathúna, N. Wang, S. Kulkarni, and S. Roy, "Review of integrated magnetics for power supply on chip (pwrsoc)," *IEEE Transactions on Power Electronics*, vol. 27, no. 11, pp. 4799–4816, 2012.

[66] X. Fang, R. Wu, L. Peng, and J. K. Sin, "A novel integrated power inductor with vertical laminated core for improved l/r ratios," *IEEE Electron Device Letters*, vol. 35, no. 12, pp. 1287–1289, 2014.

[67] R. P. Feynman, "Feynman lectures on physics. volume 2: Mainly electromagnetism and matter," *Reading, Ma.: Addison-Wesley, 1964,*

edited by Feynman, Richard P.; Leighton, Robert B.; Sands, Matthew, 1964.

[68] D. W. Lee, K.-P. Hwang, and S. X. Wang, "Fabrication and analysis of high-performance integrated solenoid inductor with magnetic core," *IEEE Transactions on Magnetics*, vol. 44, no. 11, pp. 4089–4095, 2008.

[69] M. Yamaguchi, K. Suezawa, Y. Takahashi, K. Arai, S. Kikuchi, Y. Shimada, S. Tanabe, and K. Ito, "Magnetic thin-film inductors for rf-integrated circuits," *Journal of magnetism and magnetic materials*, vol. 215, pp. 807–810, 2000.

[70] L. Li, D. W. Lee, K.-P. Hwang, Y. Min, T. Hizume, M. Tanaka, M. Mao, T. Schneider, R. Bubber, and S. X. Wang, "Small-resistance and high-quality-factor magnetic integrated inductors on pcb," *IEEE Transactions on Advanced Packaging*, vol. 32, no. 4, pp. 780–787, 2009.

[71] Y. Yazaki, K. Ishidate, K. Hagita, Y. Kondo, S. Hattori, M. Sonehara, T. Sato, T. Watanabe, Y. Seino, and N. Matsushita, "Embedded planar power inductor in an organic interposer for package-level dc power grid," *IEEE Transactions on Magnetics*, vol. 50, no. 11, pp. 1–4, 2014.

[72] Y. Endo, H. Sato, T. Miyazaki, M. Yamaguchi, H. Kamada, M. Takahashi, M. Sakamoto, S. Maita, N. Kato, Y. Yorozu, *et al.*, "Study on the electric performances of planar inductor with fe-system magnetic flake

composite integrated for sip dc-to-dc converter applications," *IEEE Transactions on Magnetics*, vol. 51, no. 11, pp. 1–4, 2015.

[73] M. Madsen, A. Knott, M. A. Andersen, and A. P. Mynster, "Printed circuit board embedded inductors for very high frequency switch-mode power supplies," in *2013 IEEE ECCE Asia Downunder*, pp. 1071–1078, IEEE, 2013.

[74] M. Bechir, D. Yaya, F. Kahlouche, M. Soultan, K. Youssouf, S. Capraro, J. Chatelon, and J. Rousseau, "Magnetic inductor model which take into account permeability and loss tangent of the magnetic material," in *2015 Symposium on Design, Test, Integration and Packaging of MEMS/MOEMS (DTIP)*, pp. 1–4, IEEE, 2015.

[75] J. Olivo, S. Carrara, and G. De Micheli, "A study of multi-layer spiral inductors for remote powering of implantable sensors," *IEEE transactions on biomedical circuits and systems*, vol. 7, no. 4, pp. 536–547, 2013.

[76] J.-W. Park, F. Cros, and M. G. Allen, "Planar spiral inductors with multilayer micrometer-scale laminated cores for compact-packaging power converter applications," *IEEE Transactions on Magnetics*, vol. 40, no. 4, pp. 2020–2022, 2004.

[77] J. Kim, M. Kim, J.-K. Kim, F. Herrault, and M. G. Allen, "Anisotropic nanolaminated conife cores integrated into microinductors for high-

frequency dc–dc power conversion," *Journal of Physics D: Applied Physics*, vol. 48, no. 46, p. 462001, 2015.

[78] Y. Dou, Z. Ouyang, P. Thummala, and M. A. Andersen, "Pcb embedded inductor for high-frequency zvs sepic converter," in *2018 IEEE Applied Power Electronics Conference and Exposition (APEC)*, pp. 98–104, IEEE, 2018.

[79] M. Biglarbegian, N. Shah, I. Mazhari, and B. Parkhideh, "Design considerations for high power density/efficient pcb embedded inductor," in *2015 IEEE 3rd Workshop on Wide Bandgap Power Devices and Applications (WiPDA)*, pp. 247–252, IEEE, 2015.

[80] W. Liang, L. Raymond, and J. Rivas, "3-d-printed air-core inductors for high-frequency power converters," *IEEE Transactions on Power Electronics*, vol. 31, no. 1, pp. 52–64, 2015.

[81] J. Qiu, D. V. Harburg, and C. R. Sullivan, "A toroidal power inductor using radial-anisotropy thin-film magnetic material based on a hybrid fabrication process," in *2013 Twenty-Eighth Annual IEEE Applied Power Electronics Conference and Exposition (APEC)*, pp. 1660–1667, IEEE, 2013.

[82] P. Kamby, A. Knott, and M. A. Andersen, "Printed circuit board integrated toroidal radio frequency inductors," in *IECON 2012-38th An-*

nual Conference on IEEE Industrial Electronics Society, pp. 680–684, IEEE, 2012.

[83] N. Wang, E. J. O'Sullivan, P. Herget, B. Rajendran, L. E. Krupp, L. T. Romankiw, B. C. Webb, R. Fontana, E. A. Duch, E. A. Joseph, *et al.*, "Integrated on-chip inductors with electroplated magnetic yokes," *Journal of Applied Physics*, vol. 111, no. 7, p. 07E732, 2012.

[84] C. Feeney, N. Wang, S. C. O'Mathuna, and M. Duffy, "Design procedure for racetrack microinductors on silicon in multi-mhz dc–dc converters," *IEEE Transactions on Power Electronics*, vol. 30, no. 12, pp. 6897–6905, 2015.

[85] H. Wu, D. S. Gardner, W. Xu, and H. Yu, "Integrated rf on-chip inductors with patterned co-zr-ta-b films," *IEEE Transactions on Magnetics*, vol. 48, no. 11, pp. 4123–4126, 2012.

[86] N. Sturcken, E. J. O'Sullivan, N. Wang, P. Herget, B. C. Webb, L. T. Romankiw, M. Petracca, R. Davies, R. E. Fontana, G. M. Decad, *et al.*, "A 2.5 d integrated voltage regulator using coupled-magnetic-core inductors on silicon interposer," *IEEE Journal of solid-state circuits*, vol. 48, no. 1, pp. 244–254, 2012.

[87] R. Meere, T. O'donnell, N. Wang, N. Achotte, S. Kulkarni, and S. O'mathuna, "Size and performance tradeoffs in micro-inductors for

high frequency dc-dc conversion," *IEEE Transactions on Magnetics*, vol. 45, no. 10, pp. 4234–4237, 2009.

[88] C. Feeney, N. Wang, S. C. Ó. Mathúna, and M. Duffy, "A 20-mhz 1.8-w dc–dc converter with parallel microinductors and improved light-load efficiency," *IEEE Transactions on Power Electronics*, vol. 30, no. 2, pp. 771–779, 2014.

[89] N. Wang, J. Barry, J. Hannon, S. Kulkarni, R. Foley, K. McCarthy, K. Rodgers, F. Waldron, M. Barry, D. Casey, *et al.*, "High frequency dc-dc converter with co-packaged planar inductor and power ic," in *2013 IEEE 63rd Electronic Components and Technology Conference*, pp. 1946–1952, IEEE, 2013.

[90] D. V. Harburg, A. J. Hanson, Y. Song, J. Qiu, R. Tian, C. G. Levey, C. R. Sullivan, and D. Otten, "Measured performance and microfabrication of racetrack power inductors," in *2013 IEEE Energy Conversion Congress and Exposition*, pp. 614–620, IEEE, 2013.

[91] D. Yao, C. G. Levey, R. Tian, and C. R. Sullivan, "Microfabricated v-groove power inductors using multilayer co–zr–o thin films for very-high-frequency dc–dc converters," *IEEE Transactions on Power Electronics*, vol. 28, no. 9, pp. 4384–4394, 2012.

[92] P. R. Morrow, C.-M. Park, H. W. Koertzen, and J. T. DiBene, "Design and fabrication of on-chip coupled inductors integrated with mag-

netic material for voltage regulators," *IEEE Transactions on Magnetics*, vol. 47, no. 6, pp. 1678–1686, 2011.

[93] Y.-M. Kuo and J.-G. Duh, "Application of nanocrystalline fehfn soft magnetic films to power inductors," *Journal of Magnetism and Magnetic Materials*, vol. 324, no. 6, pp. 1084–1087, 2012.

[94] Y. Katayama, S. Sugahara, H. Nakazawa, and M. Edo, "High-power-density mhz-switching monolithic dc-dc converter with thin-film inductor," in *2000 IEEE 31st Annual Power Electronics Specialists Conference. Conference Proceedings (Cat. No. 00CH37018)*, vol. 3, pp. 1485–1490, IEEE, 2000.

[95] X. Fang, R. Wu, L. Peng, and J. K. Sin, "A novel silicon-embedded toroidal power inductor with magnetic core," *IEEE Electron Device Letters*, vol. 34, no. 2, pp. 292–294, 2013.

[96] B. Orlando, R. Hida, R. Cuchet, M. Audoin, B. Viala, D. Pellissier-Tanon, X. Gagnard, and P. Ancey, "Low-resistance integrated toroidal inductor for power management," *IEEE transactions on magnetics*, vol. 42, no. 10, pp. 3374–3376, 2006.

[97] X. Yu, J. Kim, F. Herrault, and M. G. Allen, "Silicon-embedded toroidal inductors with magnetic cores: Design methodology and experimental validation," in *2014 IEEE Applied Power Electronics Conference and Exposition-APEC 2014*, pp. 763–767, IEEE, 2014.

[98] R. C. O'handley, *Modern magnetic materials: principles and applications*. Wiley, 2000.

[99] J. M. Coey, *Magnetism and magnetic materials*. Cambridge university press, 2010.

[100] G. Lebedev, B. Viala, J. Delamare, and O. Cugat, "Voltage-controlled uniaxial magnetic anisotropy in soft magnetostrictive ferromagnetic thin films," *IEEE Transactions on Magnetics*, vol. 47, no. 10, pp. 4037–4040, 2011.

[101] A. Inoue and A. Takeuchi, "Recent development and application products of bulk glassy alloys," *Acta Materialia*, vol. 59, no. 6, pp. 2243–2267, 2011.

[102] A. Inoue, F. Kong, Y. Han, S. Zhu, A. Churyumov, E. Shalaan, and F. Al-Marzouki, "Development and application of fe-based soft magnetic bulk metallic glassy inductors," *Journal of Alloys and Compounds*, vol. 731, pp. 1303–1309, 2018.

[103] C. Suryanarayana and A. Inoue, "Iron-based bulk metallic glasses," *International Materials Reviews*, vol. 58, no. 3, pp. 131–166, 2013.

[104] H. Wu, M. Lekas, R. Davies, K. L. Shepard, and N. Sturcken, "Integrated transformers with magnetic thin films," *IEEE Transactions on Magnetics*, vol. 52, no. 7, pp. 1–4, 2016.

Chapter 3

Planarisation & Fabrication of Releasable Magnetic Thin Films

3.1 Introduction

The primary focus of this thesis is the design, mathematical modelling, and characterisation of magnetic thin films used in Power Supply in Package (PwrSiP) applications. Those topics are respectively treated in chapters 5 & 4. However, it is important for the reader to understand the fabrication processes used for the integration of magnetic thin films. Hence, this chapter forms a supplemental body to those chapters, and the publications which underpin them. The electrodepositions and sputtering herein were performed

by R. Anthony, Z. Ghaferi, L. Ye, D. Lordan, and G, Wei. They are rightly accredited on the publications using these magnetic films which have arisen from this thesis.

The integration of magnetic thin films in PCB and silicon substrate was originally investigated by Tyndall researchers more than 20 years ago and was the subject of a number of publications [2–6] as well as a granted patent in 2005. The aim of that continuing body of work was, and still is, the furtherance of magnetic thin films used as the magnetic passive component in Power Supply on Chip (PwrSoC) and PwrSiP applications. To that end, this work has benefited from numerous individual contributors who have furthered the field of integrated magnetics within Tyndall. It has taken over 10 years for the work to generate enough industry interest for it to get EU funding under the H2020 GaNonCMOS project [EU-H2020-NMBP-2016-721107]. This work builds upon the integration techniques developed throughout those 20 years.

The original foray of Tyndall researchers into the field of integrated magnetics for PwrSiP saw the successful electrodeposition of permalloy onto PCB substrate [2]. However, even in that seminal work, there was no mention of internal anisotropy structures within the permalloy film, nor was there mention of the role of the underlying PCB substrate and its inherent surface roughness on the magnetisation dynamics of the permalloy film. One reason

for this was the lack of available instrumentation at the time. Hence, that original work had to be supplemented by the fabrication of magnetic films on PCB substrate, along with the characterisation of those films in terms of 1) surface roughness; 2) hysteresis loop; and 3) permeability.

Furthermore, although the original work considered the impact on eddy current losses within the magnetic thin films, the proposed solution at the time was the mitigation of eddy current loss through limitation of the film thickness. And indeed, this was a very successful approach. However, a consequence of this approach was the reduced volume of magnetic material permissible as the switching frequency of the converter increased. This is *not* a tractable solution for high frequency PwrSiP. This issue was remedied by the creation of the multilayer structure wherein multiple magnetic films are stacked on top of each other whilst being electrical separated by dielectric insulating layers.

This chapter outlines the fabrication methods used to create the single layer and multilayer $Ni_{45}Fe_{55}$ and CZTB magnetic cores that were ultimately integrated into the PCB substrate. There were 5 types of magnetic cores fabricated as part of this research, as follows: 1) single layer $Ni_{45}Fe_{55}$ electroplated onto bare PCB substrate; 2) single layer $Ni_{45}Fe_{55}$ electroplated onto a planarised PCB substrate; 3) released single layer $Ni_{45}Fe_{55}$; 4) released multilayer $Ni_{45}Fe_{55}$; and finally 5) released multilayer CZTB.

The structure of the chapter is as follows: In section 3.2 the experimental process for the electrodeposition of $Ni_{45}Fe_{55}$ onto PCB substrate is given. This Section also presents the base material characterisation and performance analysis; Section 3.3 pertains to the planarisation of the PCB substrate. The planarisation process is required in order to address the poor magnetic performance observed due to the inherent roughness of the underlying PCB substrate. Note, the resultant improved magnetic performance of the thin films caused by the planarisation process is treated by Ghaferi et al. in [1]; As an alternative to the surface treatment of the PCB to optimise the performance of the eletrodeposited magnetic films, a novel concept was investigated in this thesis. This involved the liberation of magnetic thin films deposited on an releasable polymer layer spun on an silicon substrate. This novel release process is presented in section 3.4; and finally conclusions are provided in Section 3.5.

3.2 Electrodeposition of $Ni_{45}Fe_{55}$ Magnetic Thin Film on PCB Substrate

A 125 nm seed layer of $Ni_{80}Fe_{20}$ was deposited onto the PCB substrate via the reduction of Pd^{2+} to Pd^{0} in a Borane based Ni-Fe electroless bath. Inspection of the seed layer under a Scanning Electron Microscope (SEM) showed a complete coverage of the PCB substrate with the seed layer and no cracks

or delamination were observed (see Fig. 3.1). However, there was non-uniformity in the thickness of the seed layer which resulted from the surface conditions of the underlying PCB substrate, spurring localised growths [7].

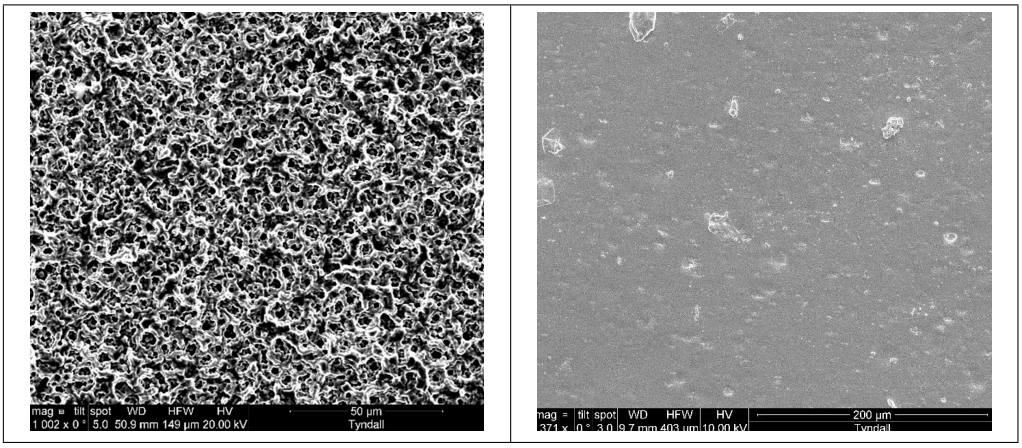

Figure 3.1: Electroless deposited $Ni_{80}Fe_{20}$ seed layer on rough side of PCB; (right) Electroless deposited $Ni_{80}Fe_{20}$ seed layer on smooth side of PCB.

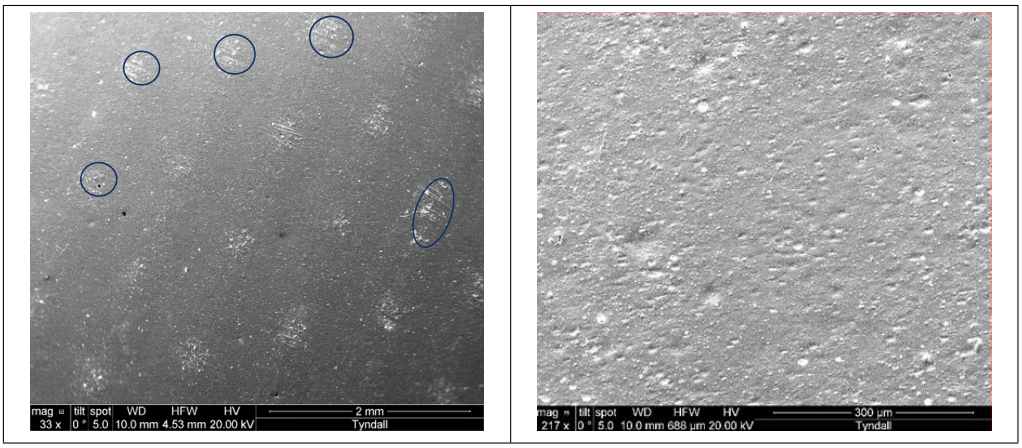

Figure 3.2: (Left) Image of $Ni_{45}Fe_{55}$ surface; (right) Zoomed in image on rough patches.

A 6.7 μm thick $Ni_{45}Fe_{55}$ magnetic core was electroplated onto the seed layer. $Ni_{45}Fe_{55}$ is chosen as the core material over $Ni_{80}Fe_{20}$ due to its greater sheet resistivity allowing for thicker magnetic cores for a given high frequency requirement. Hence, $Ni_{45}Fe_{55}$ has a higher drop off frequency than that of $Ni_{80}Fe_{20}$. Note the drop off frequency is the frequency at which there is a reduction of 20% in the permeability of the film. The plating was performed in the presence of an external magnetic field in order to induce an anisotropic internal energy structure within the film. SEM imaging of the core revealed further localised areas of high surface roughness, shown in Fig. 3.2. The roughness of the plated core originates from the inherent roughness of the PCB substrate on which it was deposited.

In Fig. 3.3 the magnetic properties of the $Ni_{45}Fe_{55}$ film are plotted. It is evident from Fig. 3.3 (left) that although the deposition took place in the presence of an external, aligning, magnetic field, the presence of which is to enforce a magnetic ordering on the system and hence produce an anisotropic film, the system is largely isotropic on a macroscopic scale. It is indeed possible that there exists a random distribution of local anisotropies within the film, however, they must average out as there was no net isotropy observed within the film. Note, Kerr imaging would have needed to be performed in order to determine this. The largely isotropic nature of the film deposited on PCB is more evident when compared against the hysteresis loops of a

Axis	B_{sat}[nWb]	B_r[nWb]	H_c[Oe]	H_k[Oe]
Easy	126.7	76.7	1.11	1.79
Hard	135	43.58	1.16	4.85
Si-Hard	665	22	0.3	11

Table 3.1: Hysteresis loop properties of 6.7 μm thick $Ni_{45}Fe_{55}$ electroplated onto PCB substrate and nominal Silicon comparator of 2.5 μm thickness(see Fig. 3.4).

thin film deposited on Silicon, cf Fig. 3.4. Furthermore, the low frequency permeability value (200, see Fig. 3.3 (right)) of the thin film is lower than that expected for the 6.7 μm thick core ($\sim$ 380, see Fig. 3.4 (right)), and the drop off frequency for both axes is nearly the same. Both of which indicate a failure to induce uniaxial anisotropy and that the sample is close to isotropic (see Table 3.1 for exact comparison).

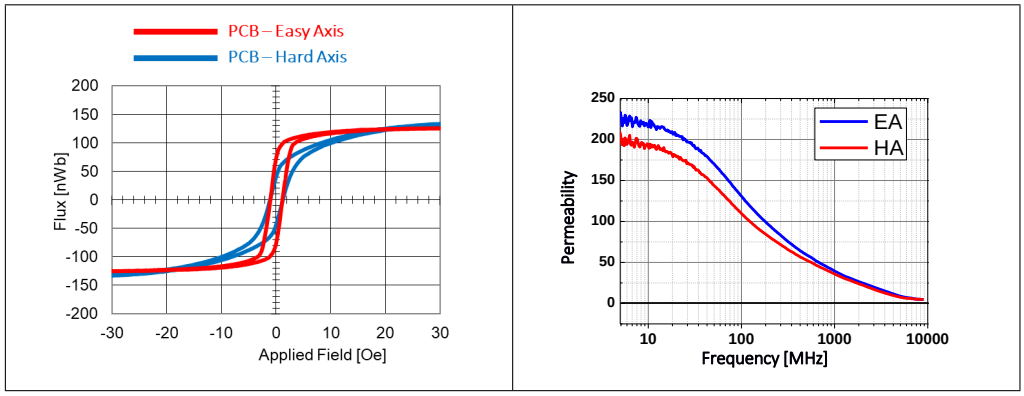

Figure 3.3: (left) Hysteresis loop of electro-deposited $Ni_{45}Fe_{55}$ magnetic core on PCB substrate; (right) Permeability plot of $Ni_{45}Fe_{55}$ magnetic core electro-deposited on PCB substrate.

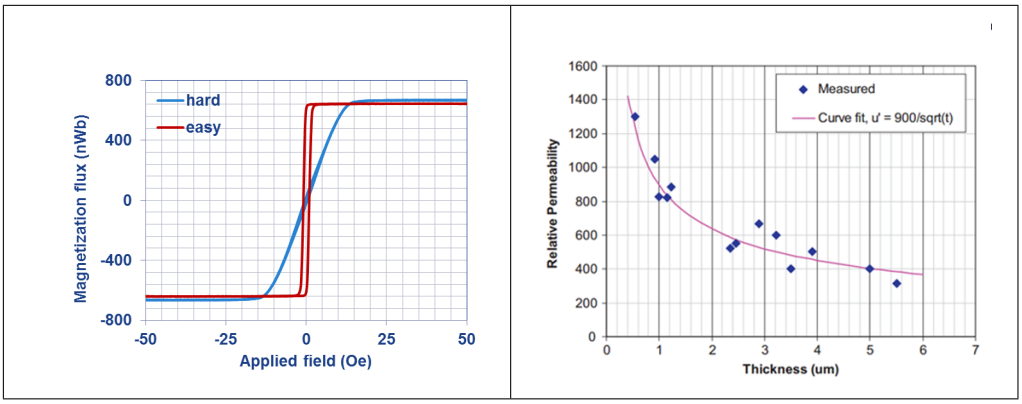

Figure 3.4: (left)Hysteresis loop of electroplated $Ni_{45}Fe_{55}$ on Silicon substrate. Note the anisotropic nature of the film.;(right) Experimental results for $Ni_{45}Fe_{55}$ on Silicon substrate [11].

The BH loop properties of the "easy" and "hard" axes are given in Table 3.1 along with a comparator $Ni_{45}Fe_{55}$ film deposited on a Silicon substrate. Note, in the original work the on the deposition of permalloy films on PCB substrate the internal anisotropy of the film was not investigated. Hence, there was no way to determine if magnetic properties of that permalloy film were effected by the underlying substrate. Indeed, there would be no reason to assume that a film deposited on silicon would behave differently to one deposited on PCB. In our work it is clear that there is a marked degradation in the magnetic properties of the $Ni_{45}Fe_{55}$ deposited onto the PCB substrate as compared to that deposited onto the Silicon substrate. The degradation of the soft magnetic properties is linked to the surface roughness of the substrate [8–10] and dealt with in chapter 5 of this thesis.

Fig. 3.5 shows the effect of film thickness on the permeability of $Ni_{45}Fe_{55}$ electroplated onto the PCB substrate in the presence of an external magnetic field. Note the typical deposition rate for $Ni_{45}Fe_{55}$ bath is between 2.2 μm and 3.8 μm per hour depending on the age of the bath. This can be compared to the results of O'Donnell et al. [11] in Fig. 3.4. It is reported in literature [11, 12] that there is an inverse proportionality between the thickness of the film and its permeability i.e., the thinner the $Ni_{45}Fe_{55}$ film the larger the permeability. However, it is clear on comparing the permeability results for the $Ni_{45}Fe_{55}$ films electroplated onto the PCB substrate that this inverse proportionality did not hold. Indeed the thinner films had far lower permeabilities than the thicker films – contra to [11]. Note [11] attributes the inverse relationship between film thickness and permeability to *Villiari effect* [13] where stress built up in the thicker films reduces the permeability through magnetoelastic effects. Hence the thicker the film, the smaller the permeability. However, in our case this relation no longer holds. Indeed, this break from the expected relationship between film thickness and permeability is attributed to the surface roughness of the film. This is a key issue for the integration of magnetic thin films in PwrSiP and forms a cornerstone of this thesis. The effect of surface roughness on the characteristics of magnetic thin films is treated in section 5.3.

Cross sections of the thin films deposited on PCB and Silicon substrates were taken to compare the films, cf. Fig. 3.6. It is evident from these

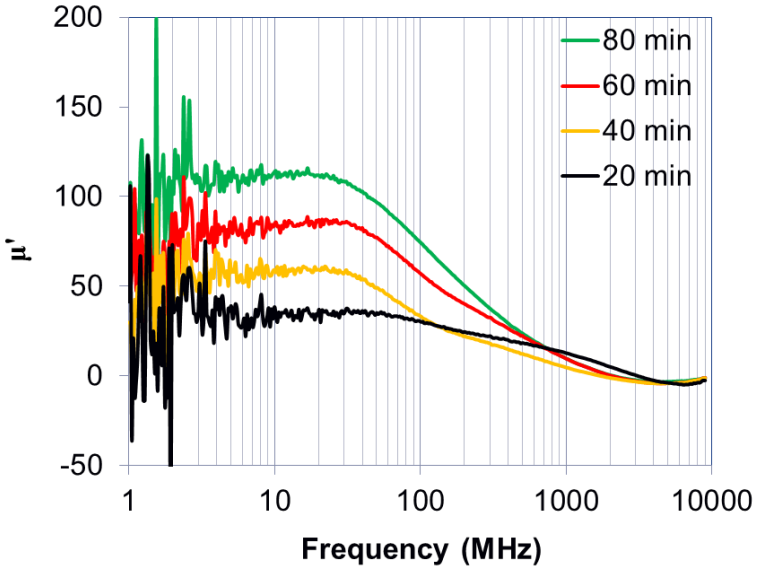

Figure 3.5: Permeability of electrodeposited of $Ni_{45}Fe_{55}$ cores on PCB substrate. Here the film thickness is related to the deposition time shown in the legend positioned at the top left of the graph. Note, there is a clear trend of decreasing permeability with decreasing film thickness.

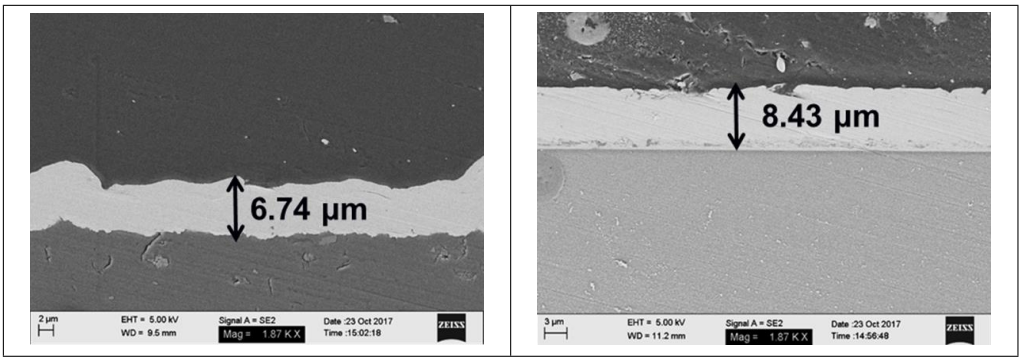

Figure 3.6: (left) Cross Section of Electroplated $Ni_{45}Fe_{55}$ core on PCB substrate; (right) Cross section of Electroplated $Ni_{45}Fe_{55}$ core on Silicon substrate. Note the electrodeposition time for both films was 80 minutes.

Substrate	Average Thickness [μm]	Standard Deviation [nm]
PCB	6.74	1047
Si	8.43	< 1

Table 3.2: Surface topography of PCB vs Silicon substrate shown in Fig. 3.6. There variance shown is the deviation of the films surface from the average thickness measurement and so represents the roughness. Measurements performed with Tencore Profilometer.

cross sections that the film deposited on the PCB substrate had far greater deviations in surface normality as compared to the Silicon deposited film. Tencor Profilometer measurements were performed in order to determine the differences of topography between the two substrates (see Table 3.2). Note in Table 3.2 the roughness of the films was determined by scanning the substrate and calculating the deviation from the average height along the length of the scan.

Therefore in order to improve the magnetic properties of the thin film it

was decided to investigate the planarisation of the PCB substrate prior to the deposition of the magnetic seed layer and the core.

3.3 Planarisation of PCB Substrate

This section of the chapter relates to the planarisation of the PCB substrate and comprises two subsections, as follows: 1) In 3.3.1 various polymers were first spun onto a Silicon substrate. The topographies were then measured prior to, and after the deposition of the magnetic core and finally the magnetic properties were measured. These then formed a reference with which the magnetic properties obtained via the PCB planarisation were compared. Moreover, the Silicon reference is important as it was used to determine the effect of the underlying polymer layer on the magnetic performance of the thin film. 2) In 3.3.2 various polymers were spun onto a PCB substrate. Again, the topographies were measured prior to, and after, the deposition of the core to determine the efficacy of the planarisation process – and the magnetic properties were measured.

3.3.1 Polymer Coating Spun onto a Silicon Substrate

The topography of the Silicon substrate was measured using a Tencor Profilometer prior to the "planarisation" (note the quotation around planarisation is only to highlight the fact that the Silicon substrate is already planar) of the substrate. The polymers Polyimide (PI) and BCB were spun onto the

Polymer	Average Roughness [nm]	Standard Deviation [nm]
PI	2.7	1.9
BCB	0.59	0.14

Table 3.3: Topology of Silicon substrate with spun on polymer coating.

Polymer	B_{sat} [nWb]	B_r [nWb]	H_c [Oe]	H_k [Oe]
PI	306.2	19.7	0.63	10.32
BCB	378	24	0.5	9.6

Table 3.4: Magnetic properties of 30 minute electro-deposited $Ni_{45}Fe_{55}$ on planarised Silicon substrate.

Silicon substrate at 2000 rpm for 30 seconds and then cured. The topographies of the substrates were again measured and the values are provided in Table 3.3.

$Ni_{45}Fe_{55}$ was electroplated onto the polymer coatings and the magnetic characterisations were performed with a BH loop tracer (SHB, MESA 200 HF, at 10 Hz) and a Ryowa Permeameter, cf Fig. 3.7. The magnetic thin films deposited on the planarised Silicon substrate all had a well-defined easy and hard magnetic axes and relative permeability which comported with O'Donnell et al. [11], i.e., there was no observed degradation in the magnetic thin films caused by the presence of the underlying polymer layer.

However, there are significant adhesion issues after electroplating the magnetic core on the polymer coatings as the samples all failed initial scotch tape testing. This is illustrated in Fig. 3.8. Note the mode of failure was the

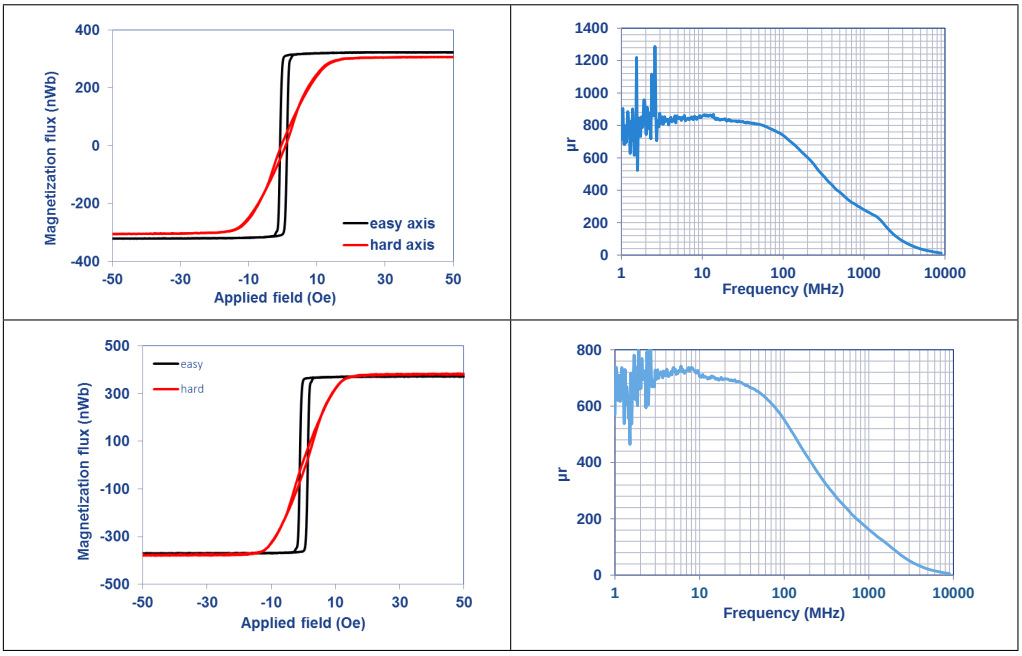

Figure 3.7: Magnetic properties of 30 minute electrodeposited Ni45Fe55 core on planarised Silicon substrate. PI top; BCB bottom.

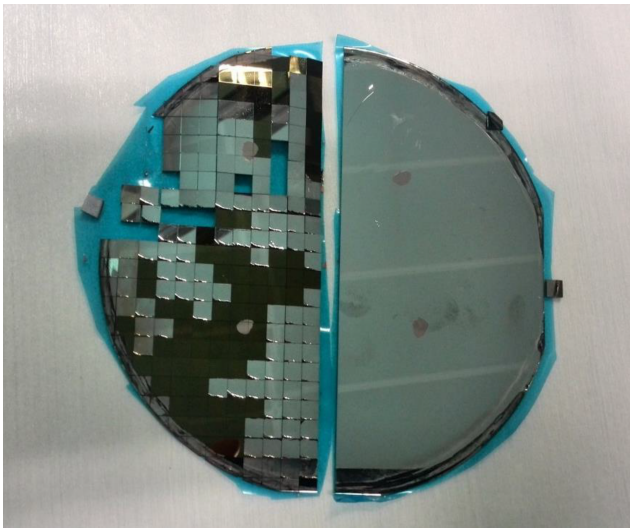

Figure 3.8: Planarised Silicon wafer with spun on BCB polymer coating.

polymer lifting off of the Silicon substrate.

The low adhesion between the polymer coatings and the Silicon substrate was attributed to the ultra-smooth Silicon substrate. O_2 and N_2 plasma treatment of the polymers [14] also failed to increase adhesion. However, it was realised that the low adhesion between the Silicon substrate and the spun on polymer layer could be utilised as a release mechanism for liberating magnetic materials deposited on Silicon in a manner not dissimilar to [15–17] who use sacrificial layers to partially or fully liberate the magnetic material from the Silicon substrate, and so, the release of the magnetic core through the use of a low adhesion layer provided a novel means to integrate the magnetic core into substrate/package applications. This is discussed fully in Section 3.4.

3.3.2 Polymer Coating Spun onto a PCB Substrate

In the previous section the effect of a planarising agent spun onto a Silicon substrate was investigated. The was done to determine whether the planarising agent itself had an adverse effect on the magnetisation dynamics of the thin film. In this regard, the ultra smooth Silicon substrate was used as means to characterise the effect of the planarising agent on the magnetisation dynamics as the issue of surface roughness was marginalised. In this section the planarisation of the PCB substrate is investigated.

The planarisation and characterisation process of the PCB substrate is as follows. BCB was spun onto the PCB substrate at 2000 rpm for 30 seconds, and then cured. The substrate surface post planarisation was characterised using the Tencor Profileometer and the results are shown in Table 3.5.

Planarising Polymer Agent	Average Roughness After Planarisation [nm]	Standard Deviation After Planarisation [nm]
Bare PCB	152	18.8
BCB on PCB	42.1	20.4
BCB on Silicon	0.59	0.14

Table 3.5: Topographical data of PCB substrate post planarisation process. Note Bare is before planarising the PCB substrate.

Fig. 3.9 shows the magnetic properties of the $Ni_{45}Fe_{55}$ electroplated thin film on the planarising agent BCB and the exact magnetic properties are given

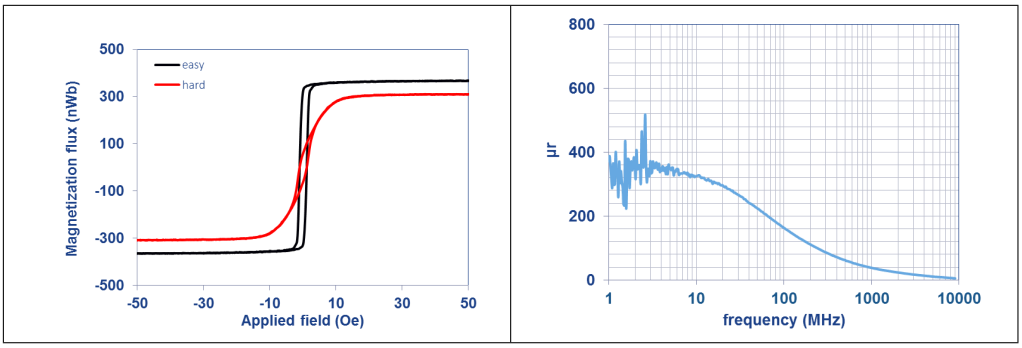

Figure 3.9: Magnetic properties of 30 minute electro-deposited $Ni_{45}Fe_{55}$ core on planarised PCB substrate with BCB planarising polymer.

Polymer	B_{sat} [nWb]	B_r [nWb]	H_c [Oe]	H_k [Oe]
Bare	273	112	2.7	6
BCB	309	64	1.05	5.75

Table 3.6: Magnetic properties of 30 minute electro-deposited $Ni_{45}Fe_{55}$ on planarised PCB substrate.

in Table 3.6. There is a marked improvement in the induction of anisotropy in the thin films as there is clear distinction between the easy and hard magnetic axis. Furthermore, there is a circa 5 fold increase in the permeability of the thin film deposited on the PCB planarised with BCB as compared to the permeability of the thin film deposited on the unplarised PCB substrate (cf Fig. 3.5). Hence, the use of the BCB planarising polymer improved the soft magnetic properties of the thin films on the PCB substrate. Indeed, there was a relationship between the improved magnetic performance and the overall reduction in the substrate roughness.

However, despite the improved magnetic performance, the thin films de-

Polymer	B_{sat} [nWb]	B_r [nWb]	H_c [Oe]	H_k [Oe]
Bare PCB	273	112	2.7	6
Bare Silicon	665	22	0.3	11
BCB on PCB	309	64	1.05	5.75
BCB on Silicon	378	24	0.5	9.6

Table 3.7: Magnetic properties of 30 minute electro-deposited $Ni_{45}Fe_{55}$ on planarised PCB substrate versus Silicon substrate.

posited on the Silicon substrate outperformed those deposited on the planarised PCB substrate. This is evident when comparing the coercive field of the thin films given in Table 3.7.

However, the magnetic properties of the thin films deposited on Silicon post planarisation was better than the thin films deposited on the planarised PCB substrate. Therefore, although a vast improvement of the magnetic characteristics of the thin films post planarisation was achieved, Silicon grade performance of the magnetic thin film was not obtained. Further cementing the pernicious effect of even a little surface roughness in the efficacy of magnetic thin films for PwrSiP applications.

3.4 Releasable Magnetic Thin Films from Silicon Substrate

In the previous sections the methods for planarising the PCB substrate were discussed in detail. It was of interest that the polymers spun onto the Silicon

substrate had poor adhesion due to the smoothness of the silicon. Given that the polymer layer suffered from poor adhesion to the Silicon substrate this provided on opportunity to deposit the magnetic thin film on Silicon and to release, and later incorporate them into the PCB package. The release process for the $Ni_{45}Fe_{55}$ and amorphous CZTB multilayer stack (used in chapter 4 of the thesis) is outlined in this section. The release uses the low adhesion between the Silicon substrate and the PI used in the planarisation process, outlined above, to liberate the deposited magnetic material from the Si substrate. The planarising polymer layer's function is to now act as a release layer between the Silicon and the deposited magnetic core. Note, despite both BCB and PI having low adhesion to the Silicon substrate, PI is ultimately selected to be the release layer as it was more compatible to the embedding process due to similar Coefficient of Thermal Expansion (CTE) coefficients of PI and the prepreg layers in the PCB build up. This is discussed in section 4.4. The magnetic core is released from the Silicon substrate through the application of mechanical stress to the PI release layer, cf Fig. 3.10.

The fabrication process for the released NiFe magnetic cores is as follows:

1. Silicon substrate was cleaned using an RF plasma at 1 kW for 25 minutes at an Argon pressure of 5.5 mTorr.

2. A PI release layer was spun onto the Silicon-wafer at 2000 rpm for 30

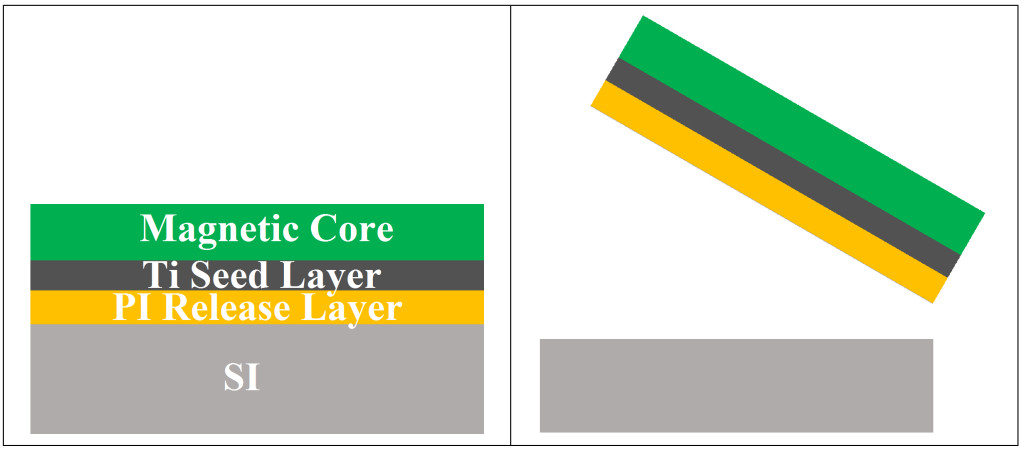

Figure 3.10: (left) Schematic diagram of releasable magnetic core from Silicon substrate prior to release. (right) Diagram of releasable magnetic core from Silicon substrate post release.

seconds, achieving a thickness of 9 μm.

3. The PI layer was cured at 260°C for 2 hrs.

4. A 20 nm Ti seed layer was sputter deposited onto the polymer layer using a "Nordiko 2550 magnetron sputterer" at 300 W using an argon pressure of 1.5 mTorr.

5. A 2 μm $Ni_{45}Fe_{55}$ magnetic core was electroplated onto the Ti layer.

6. A 2 μm thick PI insulating layer was spun onto the electroplated $Ni_{45}Fe_{55}$, and cured.

7. Steps 3 - 5 were repeated for the multilayer core.

8. A final protective layer of PI was spun on and baked.

The release process developed for the NiFe core was extended to CZTB, as follows:

1. Silicon substrate was cleaned using an RF plasma at 1 kW for 25 minutes at an Argon pressure of 5.5 mTorr.

2. A PI release layer was spun onto the Silicon-wafer at 2000 rpm for 30 seconds, achieving a thickness of 9 μm.

3. The PI layer was cured at 260°C for 2 hrs.

4. A 20 nm Ti seed layer was sputter deposited onto the polymer layer using a "Nordiko 2550 magnetron sputterer" at 300 W using an argon pressure of 1.5 mTorr.

5. A 250 nm CZTB layer was sputter deposited onto the Ti seed layer using a "Nordiko 2550 magnetron sputterer" at 1 kW using an argon pressure of 1.5 mTorr.

6. A 15 nm AlN dielectric separation layer was deposited onto the CZTB layer by reactive sputtering of an aluminium target (1 kW) and nitrogen gas.

7. Steps 5 & 6 was repeated until a total of 16 magnetic layers had been deposited.

The images flowchart relating to the fabrication process of the releasable multilayer CZTB magnetic core are shown in Fig. 3.11.

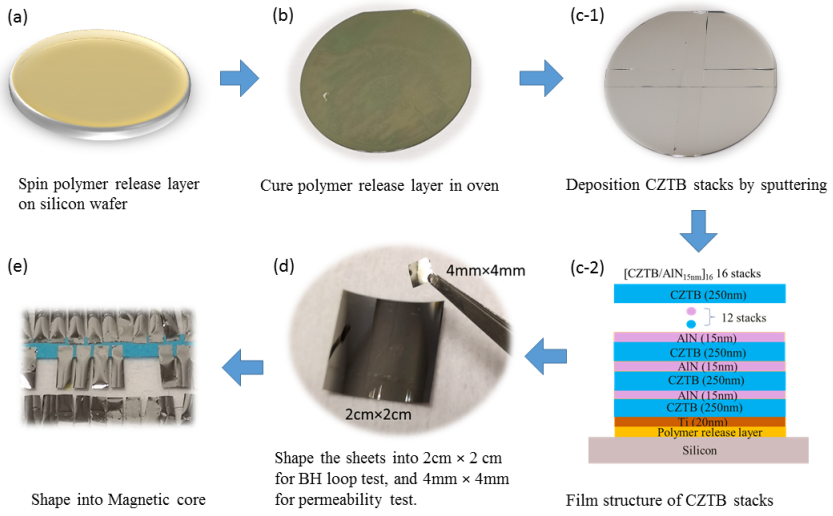

Figure 3.11: a) Silicon-Substrate with spun on polymer release layer; b) polymer release layer post cure; c-1) post sputter of CZTB stacks on polymer release layer; c-2) Structural diagram of multi-layer CZTB magnetic sheet; d) 2cm × 2cm sample for BH loop measurement and 4mm × 4mm sample for permeability measurement (see Section 4.3.2); e) Magnetic core samples post cut for inductor fabrication (see Section 4.3.3).

The PI layer successfully protected the magnetic core during the release process as no cracking was observed after the release. Indeed, the use of PI as a protective coating was selected as it was shown to improve the ability of the released magnetic core to be fully embedded between the prepreg layers of the PCB stack (see Section 4.4). Furthermore, the polymer facilitated the cutting of the magnetic core, for an experimental inductor structure (see Section 4.3), using a scalpel and ruler.

Fig. 3.12 shows the hysteresis and permeability plots for a post release dual layer NiFe magnetic core. This core structure maintains a near constant permeability up until 100 MHz. Thus, high inductance drop-off frequency of the magnetic core, along with well-defined easy and hard magnetic axes, make this a suitable candidate to be the magnetic component in PwrSiP applications. However, the distinction between the magnetic axes, although clearly distinguishable, is not ideal. Indeed, the magnetic hard axis of the core exhibits *transcritical* behaviour [18] which can give rise to stripe domain formations - increasing the materials loss tangent at higher frequencies, and ergo undermine device performance. This is undesirable for high performance PwrSiP. This is reflected in the drop-off freqeuncy of the CZTB stack being 100MHz, as opposed to the 1.9GHz expected drop-off frequency, along with a diminished primary resonance peak. These effects are discussed in detail in section 5.4 and appendix A.

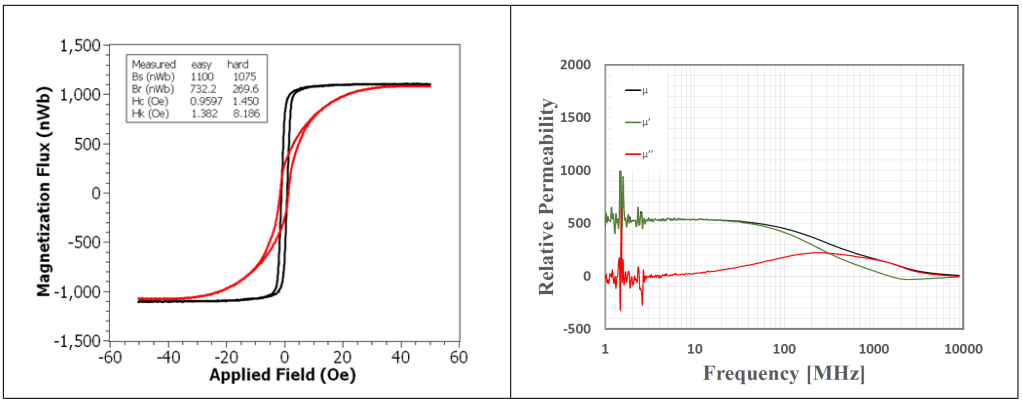

Figure 3.12: Magnetic characterisation of released multilayer (2 × 2 μm) NiFe magnetic core. (left) Hysteresis loops; (right) Permeability plots.

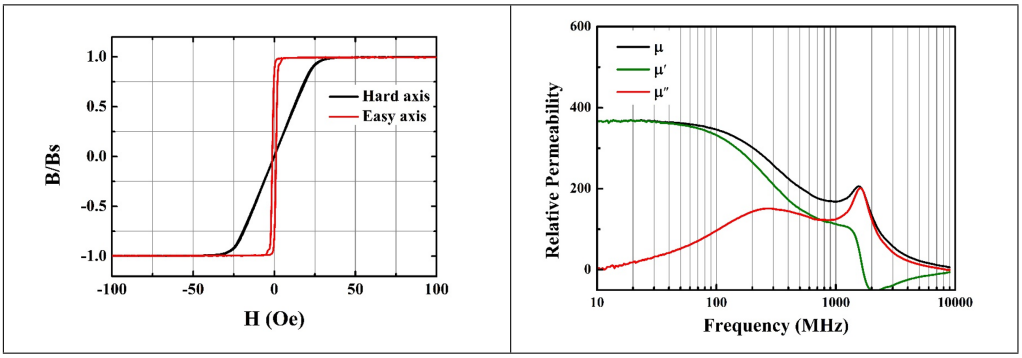

Figure 3.13: Magnetic characterisation of released multilayer (16 × 250 nm) CZTB magnetic core. (left) Hysteresis loops; (right) Permeability plots.

Fig. 3.13 shows the magnetic characteristics of the released CZTB multilayer magnetic core. The released CZTB maintains an excellent, incredible well defined, easy and hard magnetic axes with no *transcritical* behaviour. Furthermore, the CZTB multilayer core exhibits a flat permeability response up until 100 MHz, along with a near ideal hysteresis loop. The NiFe core however, also has a near flat permeability response up until 100 MHz, does

not exhibit as ideal a hysteresis loop. Therefore, the multilayer CZTB magnetic core shows more promise as an ideal magnetic candidate than multilayer NiFe. Indeed, such a core structure was used as the magnetic passive in a Flip-Chip inductor which achieved an excellent quality factor (this is presented in more detail in chapter 4 Section 4.3).

Both multilayer NiFe and CZTB magnetic cores were sent to PCB company, AT&S, who was collaborating with the Tyndall Integrated Magnetics team, in the H2020 GaNonCMOS consortium, to investigate the embedding of magnetic materials in PCB. The results of the embedding process are discussed in section 4.4.

3.5 Conclusion

The surface roughness of the PCB substrate is a major limiting factor to the successful integration of the magnetic component forming a complete Pwr-SiP application. The PCB substrate surface roughness severely degraded the "soft" magnetic properties of the electroplated $Ni_{45}Fe_{55}$ thin films as compared to their Silicon-counterparts i.e. there was a marked increase in the coercivity of the thin films as well as a decrease in the overall permeability of the films. The adverse effect of the surface roughness on the soft magnetic properties was more notable in the thinner films. This is contra to O'Donnel et al. who show that the permeability of soft thin film magnetics is inversely

proportional to the film thickness. The initial permeability of the $2\mu m$ film electro-deposited on the non-planarised PCB substrate was 200 as compared to the expected 600. Furthermore, the surface roughness of the substrate resulted in an inability to induce uniaxial anisotropy within the magnetic film. Indeed, the magnetic properties of the "easy" and "hard" axes were almost identical and the magnetic film was almost isotropic.

The issue of surface roughness of the PCB substrate was addressed through a planarisation process. The PCB substrate was planarised with various spun on polymers. The reduction in the surface roughness of the PCB substrate resulted in improved soft magnetic properties i.e., the permeability of the thin film on PCB substrate was identical to its Si counterpart and there was an improvement in both the coercive, and anisotropy, fields within the thin film. However, the films still had larger coercivity than those deposited on Silicon and there was low adhesion between the substrates (both PCB and Silicon) and the planarising polymer agent.

The low adhesion between the Silicon substrate and the planarising polymer agent was used as a release mechanism through which magnetic thin films deposited on the Silicon substrate could be released and later incorporated into the PCB package i.e., the planarising polymer agent was used as a polymer release layer. There was no degradation of the soft magnetic properties of the thin films deposited on the polymer release layer. Hence, the

use of a polymer release layer provide a means for the use of integrated thin film magnetics which had already been demonstrated in high performance PwrSoC applications to be used in PwrSiP applications.

3.6 Postamble

In this chapter the effect of surface roughness on the magnetisation dynamics of thin films were characterised, and methods to address this issue were presented. However, no modelling, or deep understanding, of this issue has so far been presented. Considering the critical importance that surface roughness played in the efficacy of thin film magnetics used in PwrSiP applications, it would be remiss not to do so. Two approaches were developed to better understand *how* surface roughness effects the magnetisation dynamics of magnetic thin films. These approaches are discussed in chapter 5.

Bibliography

[1] Z. Ghaferi and P. McCloskey, "Characterization and enhancement of magnetic performance of electrodeposited ni45fe55 on pcb for high frequency application," *Journal of Magnetism and Magnetic Materials*, p. 166708, 2020.

[2] S. O'Reilly, M. Duffy, T. O Donnell, P. McCloskey, S. C. O. Mathuna, M. Scott, and N. Young, "New integrated planar magnetic cores for inductors and transformers fabricated in mcm-l technology," *International Journal of Microcircuits and Electronic Packaging*, vol. 23, no. 1, pp. 62–69, 2000.

[3] M. Ludwig, M. Duffy, T. O'Donnell, P. McCloskey, and S. C. O. Mathuna, "Pcb integrated inductors for low power dc/dc converter," *IEEE Transactions on Power Electronics*, vol. 18, no. 4, pp. 937–945, 2003.

[4] M. Brunet, T. O'Donnell, J. O'Brien, P. McCloskey, and C. O'Mathuna, "Design study and fabrication techniques for high power density microtransformers," in *APEC 2001. Sixteenth Annual IEEE Applied Power*

Electronics Conference and Exposition (Cat. No.01CH37181), vol. 2, pp. 1189–1195 vol.2, 2001.

[5] N. Wang, J. Barry, J. Hannon, S. Kulkarni, R. Foley, K. McCarthy, K. Rodgers, F. Waldron, M. Barry, D. Casey, J. Rohan, J. O'Brian, M. Hegarty, A. Kelleher, S. Roy, and C. . Mathúna, "High frequency dc-dc converter with co-packaged planar inductor and power ic," in *2013 IEEE 63rd Electronic Components and Technology Conference*, pp. 1946–1952, 2013.

[6] R. Meere, T. O'Donnell, N. Wang, N. Achotte, S. Kulkarni, and S. C. O'Mathuna, "Size and performance tradeoffs in micro-inductors for high frequency dc-dc conversion," *IEEE Transactions on Magnetics*, vol. 45, no. 10, pp. 4234–4237, 2009.

[7] Y. Ee, Z. Chen, S. Xu, L. Chan, K. See, and S. Law, "Electroless copper deposition as a seed layer on tisin barrier," *Journal of Vacuum Science & Technology A: Vacuum, Surfaces, and Films*, vol. 22, no. 4, pp. 1852–1856, 2004.

[8] F. M. Rhen and S. Roy, "Dependence of magnetic properties on micro- to nanostructure of conife films," *Journal of Applied Physics*, vol. 103, no. 10, p. 103901, 2008.

[9] C. Craus, G. Palasantzas, A. Chezan, J. T. M. De Hosson, D. Boerma, and L. Niesen, "The influence of the surface topography on the magneti-

zation dynamics in soft magnetic thin films," *Journal of applied physics*, vol. 97, no. 1, p. 013904, 2005.

[10] Y.-P. Zhao, R. Gamache, G.-C. Wang, T.-M. Lu, G. Palasantzas, and J. T. M. De Hosson, "Effect of surface roughness on magnetic domain wall thickness, domain size, and coercivity," *Journal of Applied Physics*, vol. 89, no. 2, pp. 1325–1330, 2001.

[11] T. O'Donnell, N. Wang, S. Kulkarni, R. Meere, F. M. Rhen, S. Roy, and S. O'Mathuna, "Electrodeposited anisotropic nife 45/55 thin films for high-frequency micro-inductor applications," *Journal of Magnetism and Magnetic Materials*, vol. 322, no. 9-12, pp. 1690–1693, 2010.

[12] M. Feldmann and S. Buttgenbach, "Novel microrobots and micromotors using lorentz force driven linear microactuators based on polymer magnets," *IEEE Transactions on Magnetics*, vol. 43, no. 10, pp. 3891–3895, 2007.

[13] A. Bieńkowski, "Magnetoelastic villari effect in mn–zn ferrites," *Journal of magnetism and magnetic materials*, vol. 215, pp. 231–233, 2000.

[14] G. Rozovskis, J. Vinkevičius, and J. Jačiauskiene, "Plasma surface modification of polyimide for improving adhesion to electroless copper coatings," *Journal of adhesion science and technology*, vol. 10, no. 5, pp. 399–406, 1996.

[15] V. Mattoli, V. Pensabene, T. Fujie, S. Taccola, A. Menciassi, S. Takeoka, and P. Dario, "Fabrication and characterization of ultra-thin magnetic films for biomedical applications," *Procedia Chemistry*, vol. 1, no. 1, pp. 28–31, 2009.

[16] J.-W. Park, F. Cros, and M. G. Allen, "A sacrificial layer approach to highly laminated magnetic cores," in *Technical Digest. MEMS 2002 IEEE International Conference. Fifteenth IEEE International Conference on Micro Electro Mechanical Systems (Cat. No. 02CH37266)*, pp. 380–383, IEEE, 2002.

[17] B. Löchel and A. Maciossek, "Electrodeposited magnetic alloys for surface micromachining," *Journal of the Electrochemical Society*, vol. 143, no. 10, pp. 3343–3348, 1996.

[18] A. V. Svalov, I. R. Aseguinolaza, A. Garcia-Arribas, I. Orue, J. M. Barandiaran, J. Alonso, M. L. FernÁndez-Gubieda, and G. V. Kurlyandskaya, "Structure and magnetic properties of thin permalloy films near the "transcritical" state," *IEEE Transactions on Magnetics*, vol. 46, no. 2, pp. 333–336, 2010.

Chapter 4

Embedding of Released Magnetic Thin Films in Advanced Organic Substrates

4.1 Introduction

This chapter relates to the manufacture of inductors with embedded released magnetic cores. There were three main manufacturing methods considered for the integration of the released magnetic thin films in an inductor structure, each forming a generation of inductors more suitable for Power Supply in Package (PwrSiP) than the last. The three generations of inductor structures are shown for clarity in Fig 4.1.

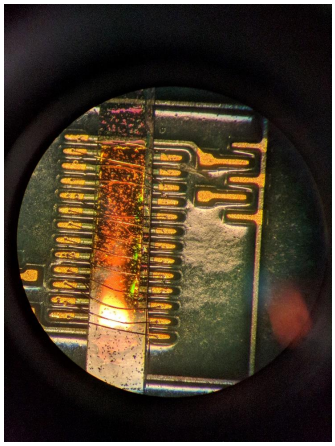

(a)

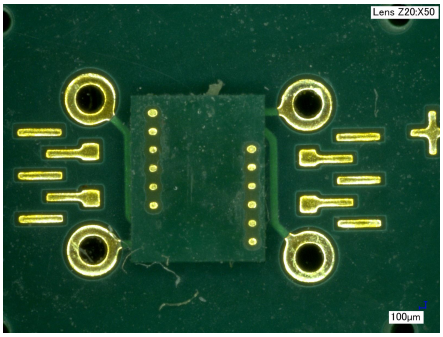

(b)

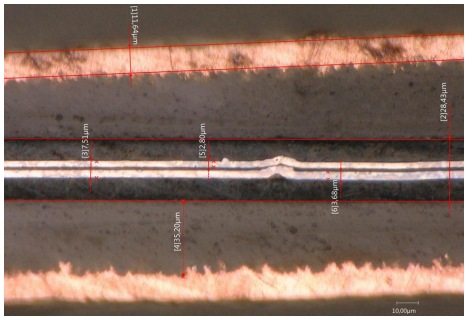

(c)

Figure 4.1: (a) Prototype of first generation wirebond inductor under microscope. (b) Second generation Flip-Chip inductor under microscope. (c) Cross section of dual layer NiFe magnetic core embedded in prepeg layers of PCB substrate for third generation inductor structure. Note a finalised third generation inductor could not be fabricated as AT&S had to cease manufacturing efforts in response to the public health emergency caused by COVID-19.

The first generation inductor structure with integrated thin film magnetics was referred to as the *wirebond inductor*. The wirebond inductor was intended to allow rapid prototyping of an inductor structure with an integrated released thin film magnetic core. The primary purpose of this was that it allowed testing of the efficacy of the released thin film magnetic core in an inductor structure without the core undergoing a fabrication process involving temperatures and pressures which could effect the magnetic properties of the core. In this regard, the fabrication process was considered non-invasive to the released thin film magnetic core, and that it would not effect the cores magnetic properties. Hence, the advantage of this approach was that it facilitated rapid prototyping that allowed us to check the efficacy of the released magnetic core in an inductor structure for PwrSiP applications, and so it provided a Bill of Health for the release process used to liberate the magnetic thin films from the Silicon substrate (as discussed in section 3.4).

However, the first generation wirebond inductor was not considered a truly *fully embedded* solution as the released thin film magnetic core was still relatively exposed to the outside environment as it was not fully housed within a singular PCB structure. Furthermore, the fabrication technique for the wirebond inductor is very different of the fabrication technique used to create a fully embedded solution wherein the released thin film magnetic core is within the PCB substrate. Most notable, in a fully embedded solution electroplated copper traces would be used as the current carrying conductor

rather than wirebonds. Hence, the electrical results for the wirebond inductor structure are not indicative of the electrical performance of released thin film magnetics integrated into PwrSiP.

The second generation inductor structure addressed the concern that electrical results of the first generation structure were not indicative of a fully embedded inductor with an integrated released thin film magnetic core by adopting a *Flip-Chip* fabrication method wherein the released thin film magnetic core would be encapsulated between two adjacent PCBs. From an idealogical standpoint this approach more truly represents a fully embedded inductor with an integrated thin film magnetic core as the thin film core is sandwiched between layers of PCB substrates. This is similar to a fully embedded thin film magnetic core sandwiched between layers of prepreg in the PCB stack.

Furthermore, this approach also used electroplated copper traces as the current carrying conductor. And so, the electrical results of the Flip-Chip inductor are representative of an inductor structure fully embedded in the prepreg layers of the PCB stack. The only difference being that a fully embedded solution would use solid copper vias as interconnects and the Flip-Chip approach used solder balls. Hence, the electrical characteristics of a fully embedded inductor with a thin film magnetic core can be inferred from the results of the Flip-Chip inductor. These are the reasons why the Flip-Chip inductor

was chosen as the intermediary step between the wirebond inductor, and the fully embedded inductor.

The third generation inductor structure integrated the released magnetic thin film into the prepeg layers of the PCB stack, which could then be incorporated into a standard over-moulded package. Thus, the third generation inductor is truly a fully embedded magnetic passive for PwrSiP applications as it is manufactured within the standard PCB and packaging manufacturing processes. That is, it is the successful insertion of a released magnetic thin film core within the flow process of PCB manufacturing. Due to this complex challenge, and the specialised machinery required for PCB manufacturing, this work was carried out in partnership with AT&S who specialise in PCB manufacturing. Because of AT&S's involvement and efforts the third generation inductor was referred to as *AT&S Embedded Inductor*. This collaborative effort was possible thanks to Tyndall National Institute's involvement in the EU GaNonCMOS consortium.

The AT&S embedded inductor had several advantages over the Flip-Chip inductor, namely a reduced footprint as a result of the AT&S's advanced manufacturing which had a smaller minimum copper line spacing constraint, reduced resistance as the solder balls would be replaced with solid copper vias, and better mechanical stability and protection from the environment as the released magnetic thin film would be housed inside an over-moulded

package. Unfortunately a finalised working inductor could not be manufactured as AT&S had to cease manufacturing efforts in response to the public health emergency caused by COVID-19.

However, significant progress was made in regards to the physical embedding of the released magnetic thin film inside the prepreg layers of the PCB stack. Indeed, after many failed attempts, a dual layer NiFe core was successfully embedded in the prepreg layers. Further, a multilayer CZTB magnetic core was also successfully embedded. Thus, we had demonstrated that thin film magnetics released from a Silicon substrate could be embedded in the prepreg layers of the PCB stack and form a magnetic passive for PwrSiP applications.

The structure of this Chapter is as follows: section 4.2 introduces the wirebond inductor; in section 4.3 the manufacturing process and electrical results of the Flip-Chip inductor are discussed; in 4.4 the embedding results of the released thin film magnetic cores embedded by AT&S are discussed.

4.2 Generation 1: Wirebond Inductor Structures With Released Magnetic Core for Power Supply in Package

This section builds upon our existing work for the manufacturing of wirebond inductors using chemically thinned Vitrovac cores for PwrSiP applications [1]. As noted in our earlier work the majority of the prior art of PCB inductor structures with integrated magnetics has focused largely on developing racetrack, spiral, and toroidal structures [2–5] with a plated, or embedded, magnetic core. An alternative approach to create PCB inductors with integrated magnetics was to use standard bond wire technology to form the closed current loops required for an inductor with a surface mounted magnetic thin film. Furthermore, although this approach had been well demonstrated to work for PCB magnetics that utilised Ferrite Polymer Composite(s) (FPC) cores [6–8], it had not been demonstrated for thin film magnetics.

As noted in section 2.1.2, there are several drawbacks associated with using FPC cores. The main drawback being the reduced permeability of the core, a consequence resulting from the distributed air gap in the FPC required to stave off high frequency hysteretic losses. For this reason, and other reasons outlined in section 2.1.2, the FPC core is not considered as an ideal magnetic material for future PwrSiP applications. Hence, in our

work in [1] chemically thinned Vitrovac magnetic cores were used because of its higher relative permeability and higher magnetic saturation than typical ferrite or FPC cores.

This current work furthers our prior art by replacing the Vitrovac core with a released electroplated $Ni_{45}Fe_{55}$ magnetic thin film. $Ni_{45}Fe_{55}$ was chosen over CZTB due to its relative ease of deposition, and that due to time constraints, we were looking to create a rapid prototype which could be used to determine the efficacy of the release process. Once again, the overall electrical performance of the inductor structure was not considered paramount.

The structure of this section is as follows: Sub-section 4.2.1 outlines the exact manufacturing process of the wirebond inductor structure; Results and discussion are provided in sub-section 4.5; and finally conclusions are provided in sub-section 4.2.3.

4.2.1 Manufacturing Process of Wirebond Inductor With Released Magnetic Core

This section outlines the exact manufacturing process used for the wirebond inductor. Observations of the manufactured inductor are then provided. The following are manufacturing steps for the wirebond inductor.

1. The multilayer $Ni_{45}Fe_{55}$ (3×2.5 μm) magnetic core was cut to the

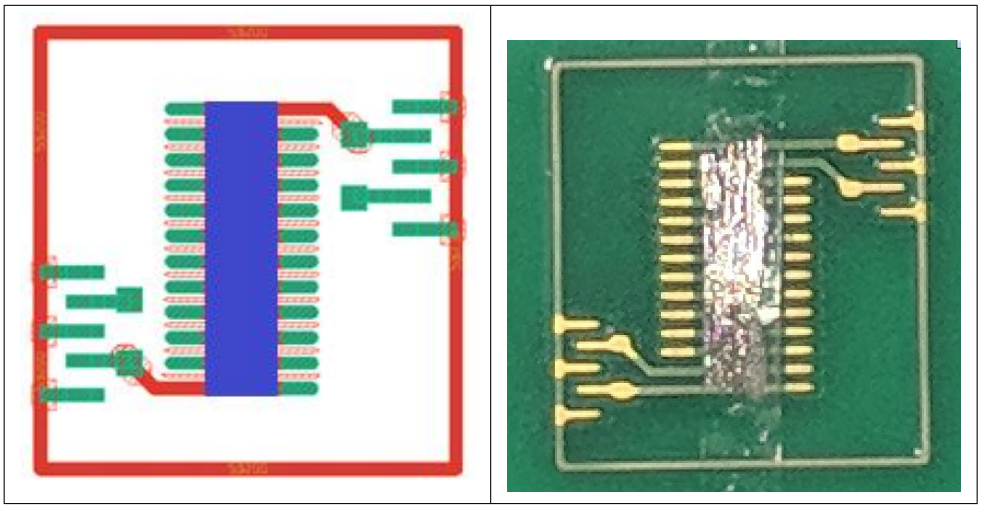

Figure 4.2: (left) Schematic diagram of PCB wirebond inductor prior to wire bonding step. Red are Copper Traces. Green are exposed Pads. Blue is the mounted released magnetic core. (Right) Image of PCB wirebond inductor prior to wire bonding step.

dimensions of the inductor structure using a scalpel and ruler.

2. The shaped magnetic core was placed onto Sellotape. This step facilitated handling of the thin film magnetic core.

3. The mounted magnetic core is then manually placed between the pads of the PCB (see figure 4.2).

4. The PCB with the mounted magnetic core is then inspected under a microscope to ensure that there is no electrical connection between the magnetic core and the exposed pads, or that the Sellotape has not covered the pads.

5. 25 μm gold wirebonds are then wirebonded to the exposed NiAu to

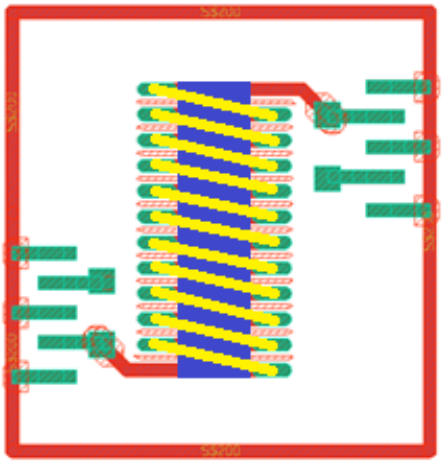

Figure 4.3: Schematic diagram of finalised PCB wirebond inductor. Red are Copper Traces. Green are exposed Pads. Yellow are the 25 μm Au wirebonds. Blue is the mounted released magnetic core.

create the electrical connections required for the solenoid inductor (see figure 4.3)

6. The manufactured device is then inspected under a microscope to ensure that there are no observable physical defects in the device (see figure 4.4).

From Fig. 4.4 it is clear that we have succesfully integrated the released NiFe thin film onto the PCB substrate using the wirebond technology in the same manner as before in [1]. There was no observable short between the released thin film magnetic core and the NiAu pads used for the wirebonds. Furthermore, there were no electrical shorts between the wirebonds and the magnetic core. Thus, demonstrating that the manufacturing process could be used as an outline for the integration of released magnetic thin films for

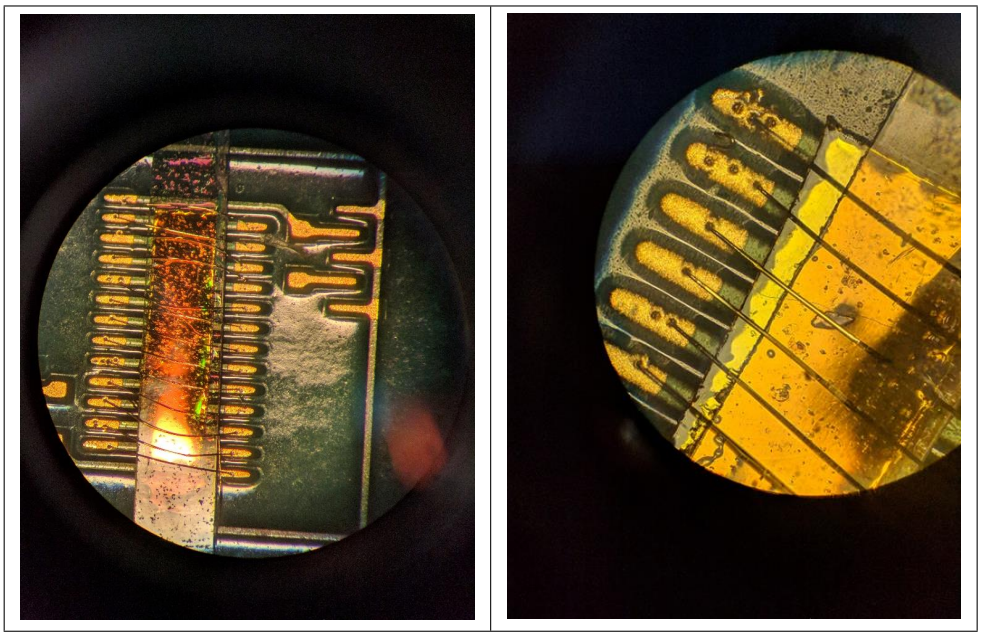

Figure 4.4: Visual microscopic inspection of manufactured PCB wirebond inductor for efficacy of process.

PwrSiP applications in an industrial setting. However, the elements of the process involving manual cutting and placing of the core would needed to be replaced with more accurate machine ones. Such as, machine dicing of the core, along with an automated pick and place.

However, although this process demonstrates the validity of this manufacturing approach for a prototype PwrSiP application, it is clear that the wirebond structure is not physically durable. This is evident from the bending of the wirebonds in response to environmental forces. Furthermore, there are a number of indentations on the gold pad where the wirebonds had come undone from the pad and needed to be redone. This highlights the mechanical frailty of the wirebond inductor. It should be noted here that a wirebond inductor that used FPC as the magnetic material would not have this issue as the wirebonds would effectively have an over-moulded plastic covering providing shielding from the environment. However, once more, the wirebond inductor was meant to be a rapid prototype for testing the efficacy of the release process used to free the magnetic thin films from the Silicon substrate, and so design durability was not a priority consideration.

The next section provides electrical characterisations of the wirebond inductor.

4.2.2 Results & Discussion

The inductance and resistance of the first generation wirebond inductor were measured using a Vector Network Analyser (VNA). Two port 400 μm pitch Z10-GS-400 probes from FormFactor Inc. were used for the measurement. The VNA and probes were calibrated for the 300 KHz to 100 MHz frequency range. The results of this measurement are presented in Fig. 4.5 and accompanying data is provided in Table 4.1.

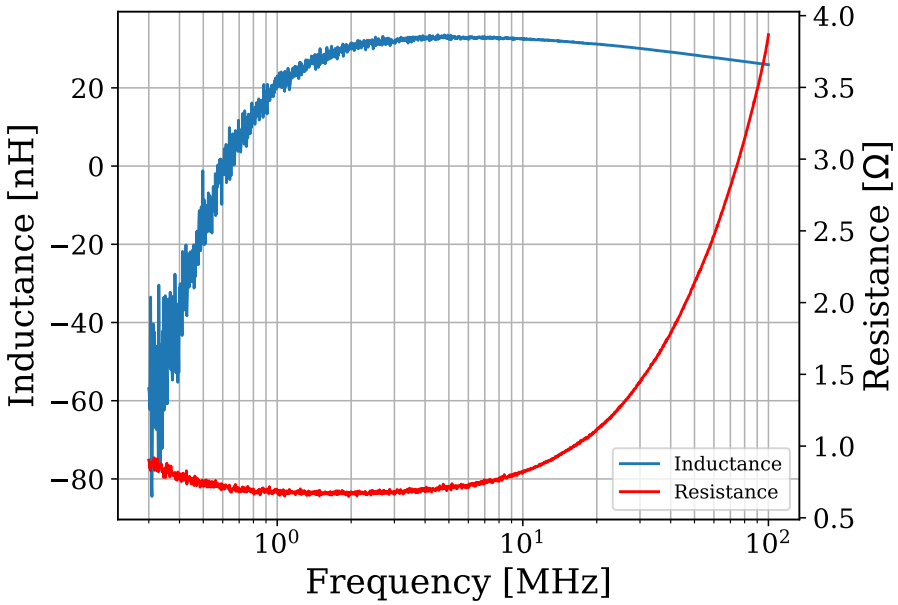

Figure 4.5: Inductance & Resistance plot of first generation wirebond inductor with released multilayer NiFe core.

The first thing to note from Fig. 4.5 is that the manufacturing process outlined in section 4.2.1 is verified by the obtention of inductance and resis-

Footprint [mm^2]	L_{dc} [nH]	R_{dc} [mΩ]	L_{den} [$\frac{nH}{mm^2}$]	$\frac{L_{dc}}{R_{dc}}$ [$\frac{nH}{m\Omega}$]	Q_{40}	$\frac{1}{A}\sqrt{\frac{L_{dc}}{R_{dc}}Q_{40}}$
3.465	32.4	488. 56	9.35	0.065	4.09	4.72

Table 4.1: Electrical characteristics of first generation wirebond inductor with released multilayer NiFe core. Note, the Q-Factor of the device is reported at 40 MHz. This is for ease of comparison with a device that is presented in section 4.3.

tance values. Note, there is electrical noise on the measurements less than 2 MHz, and so the DC measurements are determined using backwards extrapolation from the data. The wirebond inductor retains a near flat inductance response across the measured frequency range, with a 6 nH drop observed at 100 MHz. The flatness of the frequency response is vital for low power dissipation in DC-DC power converters. One may think that a flat response is only required around the switching frequency of the primary power MOSFET. However, it is important to realise that the primary power MOSFET is effectively *sampling* the input voltage, and in doing so, creating higher order spectral harmonics [9]. These harmonics are seen by the inductive element in the converter and can produce additional loss depending on the inductance drop-off. This is why, although it may seem unnecessary, it is beneficial for the inductor to have a flat frequency response far beyond the switching frequency of the converter.

Furthermore, the drop off in inductance directly contributes to the AC resistance of the inductor. The is illustrated in Fig. 4.6 where two mathematical

models for AC resistance are regressed onto the measured resistance of the wirebond inductor. The first model regressed shows the skin effects where growing magnetic field lines growing from within the centre of the conductor push the electrons outwards towards the surface, and in doing so, reduce the useful volume of the conducting material. This causes an exponential rise in resistance and is represented by Eq. 4.2.1. In Eq. 4.2.1 R_{dc} is the DC resistance of the inductor, λ is a growth factor related to the skin depth, and f is the frequency.

The second model regressed incorporates skin effects along with the resistance arising from the drop-off in inductance. This is represented by Eq. 4.2.2. In Eq. 4.2.2 L_{Drop} is the drop off in inductance. It is important to note that the drop-off term acts in an identical way as an equivalent series inductance. The regressed values for R_{dc}, λ, and L_{Drop} are presented in Table 4.2.

$$R_{ac} = R_{dc}e^{\lambda 2\pi f} \tag{4.2.1}$$

$$R_{ac} = \sqrt{(R_{dc}e^{\lambda 2\pi f})^2 + (2\pi f L_{Drop})^2} \tag{4.2.2}$$

Equation	Rdc [mΩ]	λ	L_{Drop} [nH]
4.2.1	755.93	2.82×10^{-9}	-
4.2.2	488. 56	1.01×10^{-9}	5.85

Table 4.2: Parameters of Non-Linear model fit determined by regressing equations 4.2.1 & 4.2.2 onto the measured AC resistance of the wirebond inductor. See Fig. 4.6

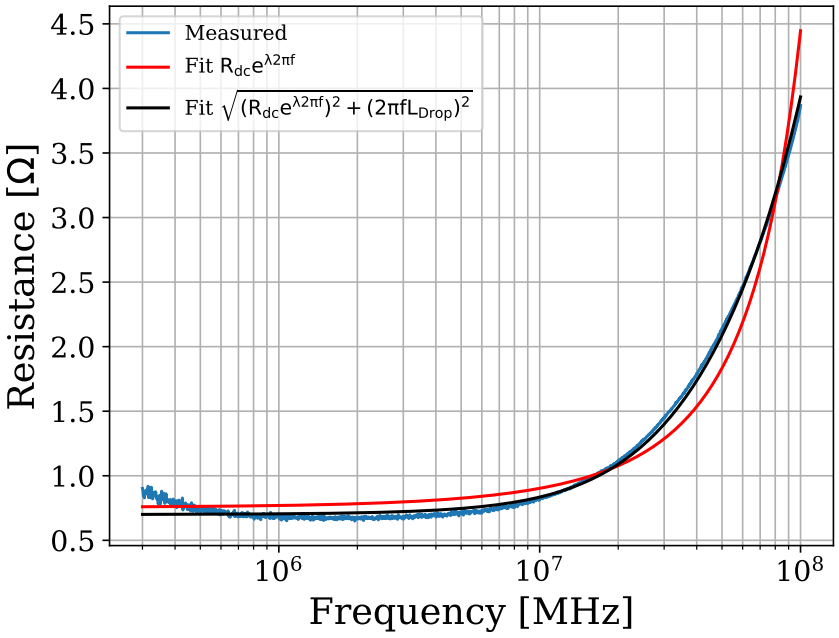

Figure 4.6: Non-linear model for AC resistance caused by skin depth effects (Eq. 4.2.1) and drop off in inductance (Eq. 4.2.2) regressed onto measured resistance of wirebond inductor.

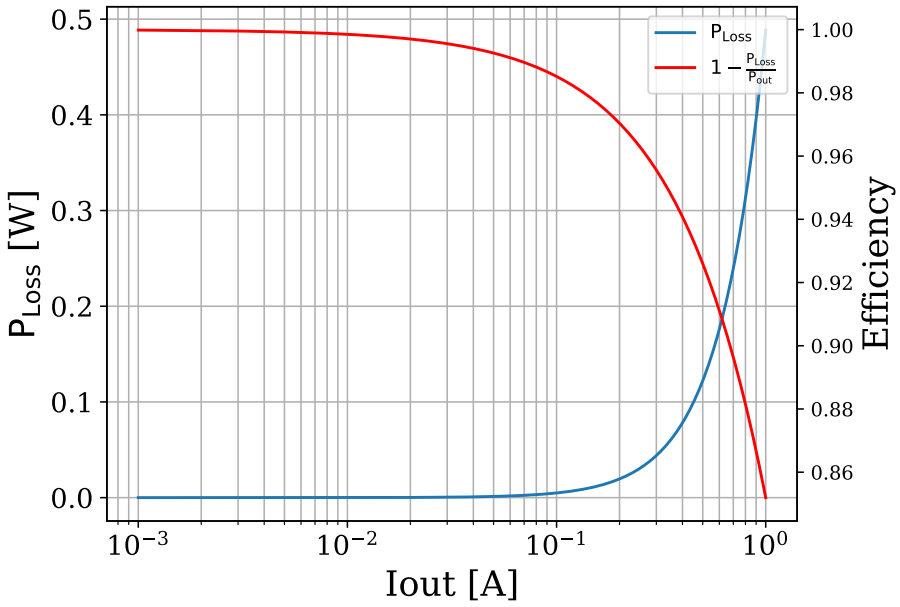

Figure 4.7: Theoretical equivalent series resistance power dissipation by wirebond inductor used as the magnetic passive in DC-DC buck converter.

The high R_{dc} of the wirebond inductor makes it unsuitable for low power PwrSiP applications where the amperage drawn is more than a few tens of milliamps. For example, consider a nominal DC-DC buck converter with an output voltage of 3.3 volts. Considering only the power dissipated by the R_{dc} of the wirebond inductor, the efficiency of this hypothetical converter rapidly decreases as the load current increases, cf Fig. 4.7. This highlights the need for the magnetic passive to have a low equivalent series resistance in order minimise conduction losses in the DC-DC converter.

The Quality Factor of the wirebond inductor is shown in Fig. 4.8. As discussed earlier in section 2.2.2 the quality factor of the inductor is a key Figure

of Merit (FOM) used to determine the ratio of the energy stored per cycle to the average energy dissipated per cycle. Therefore, while the Q-Factor is increasing, the device is storing more energy per cycle than it is dissipating. As mention in section 2.2.2 the frequency whereat the Q-factor begins to decrease can be seen as the useful bandwidth of the inductor. For the wirebond inductor the Q-factor is increasing up until circa 100 MHz. The high bandwidth of the inductor is attributed to the frequency stability of the inductance.

$$Q = \frac{\omega L}{R} \tag{4.2.3}$$

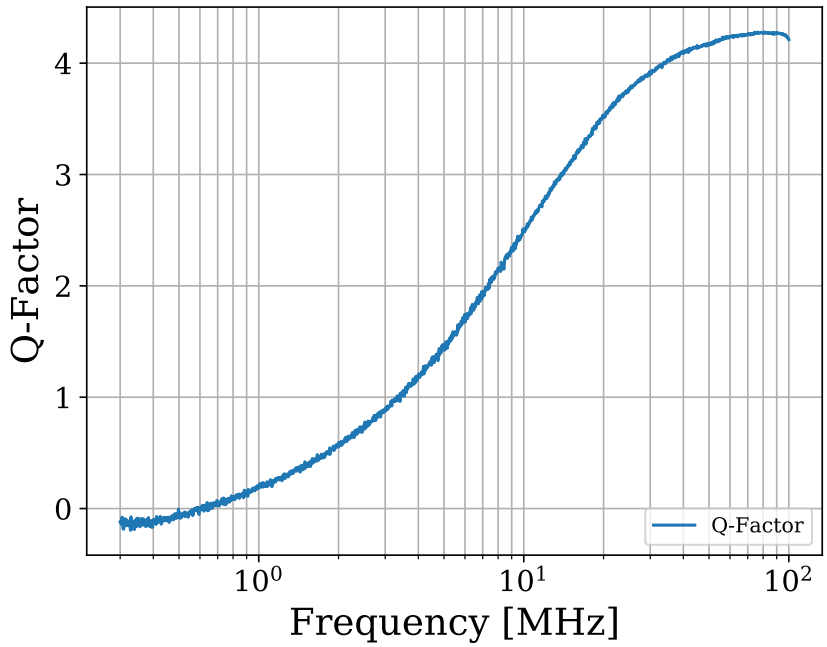

Figure 4.8: Quality Factor plot of first generation wirebond inductor with released multilayer NiFe core.

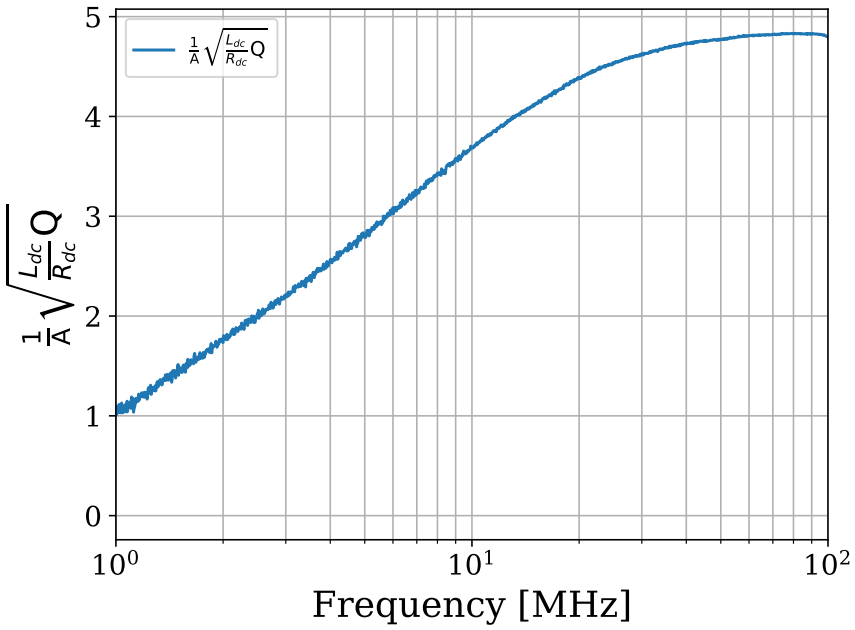

Figure 4.9: AC-DC FOM developed in section 2.2.3 for first generation wirebond inductor.

However, as illustrated in Fig. 4.7 the 100 MHz bandwidth does not necessitate that a DC-DC converter using the wirebond inductor will have a high efficiency. The low suitability of the wirebond inductor to low power PwrSiP applications is further indicated by the fact that the Q-Factor is less than 1 in the typical MOSFET switching frequency range of 200 KHz to 1 MHz.

The hybrid FOM developed in section 2.2.3 is plotted in Fig. 4.9. This FOM combines both the DC and AC aspects of the wirebond inductor. This further shows that the wirebond inductor is ill suited to be the magnetic passive for low power PwrSiP applications due to its high DC resistance.

4.2.3 Conclusion

This section of the thesis presented the wirebond manufacturing technique used to create rapid prototype inductors to verify the magnetic thin film release process. Electrical characteristics for the wirebond inductor were obtained. The wirebond inductors had an almost flat inductance frequency response up until 100 MHz. However, the wirebond inductors had a high R_{dc} which reduced the overall quality factor of the device. Due to the high R_{dc} and low Q-factor at typical MOSFET switching frequencies the devices is unsuited to be the magnetic passive in low power PwrSiP applications.

4.2.4 Postamble

The weakness of the Gen-1 inductor was its inherently high R_{dc} and resultant low Q-Factor. In order to address both of these issues the next generation of devices is required to have a lower R_{dc}. Thus, the wirebond integration technique must be replaced with one that allows the use of thicker copper.

4.3 Generation 2: High Q-Factor PCB Embedded Flip-Chip Inductors with Released Multi-Layer Amorphous CZTB Magnetic Thin Films for PwrSiP

This section was published in the *Journal of Emerging and Selected Topics in Power Electronics* [10].

This Section demonstrates a novel solenoid inductor fabrication technique to embed a multi-layer,thin-film, CZTB magnetic material within a PCB. The PCB embedded inductor uses standard 2oz (70 μm) copper PCB manufacturing processes. The embedded solenoid inductor structure is formed by enclosing the multi-layer, thin-film, CZTB magnetic core between two PCBs. The multi-layer CZTB is mounted onto one of the PCBs and a Flip-Chip, solder reflow process is performed to form the electrical connections between the two PCBs.

The main advantage of embedding the magnetic core in this manner is the low R_{dc} value which can be achieved due to the copper thicknesses that can be achieved with PCB in comparison to those available for direct integration on Silicon (see Table 4.7) as the result of interconnecting multiple copper layers. This method increases the effective copper thickness of the trace without re-

sulting in an increased line-spacing that would normally be required in order to facilitate the use of thicker copper. Hence, this method of device manufacture results in a smaller device footprint for a nominal copper thickness.

The structure of this Section is as follows; Subsection 4.3.1 details the inductor design and Finite Element Modelling; Subsection 4.3.2 discusses the magnetic characterisation of the multi-layer CZTB magnetic core is discussed; Subsection 4.3.3 outlines the manufacturing process used to create the Flip-Chip inductor; in subsection 4.3.4 the results of the electrical characterisation of the Flip-Chip inductor are presented and the findings are discussed; and finally, subsection 4.3.5 concludes the main findings of the Section.

4.3.1 Inductor Design & Finite Element Modelling

Finite Element Model(ling) (FEM) was used to obtain a 3D model of the inductor structure that exhibited the desired electrical characteristics. The FEM was performed with Maxwell Ansys v. 16 using the Eddy Current solver package to perform a frequency sweep on a range of iterated designs. In this design space, 70×2 μm copper thickness was selected in order to minimise the R_{dc}. Here the 70×2 μm represents the two 70 μm copper traces connected with microvias to form a loop of the solenoid inductor. However, the use of 70×2 μm copper thickness placed design constraints on the minimum copper trace width, and the minimum line-spacing between adjacent traces. These constraints reflect the manufacturing capabilities of the PCB

Copper Thickness [μm]	Min Copper Trace Width [μm]	Min Copper Linespacing [μm]
70	154.2	228.6

Table 4.3: Design constraints of Gen II Flip-Chip Inductor from PCB manufacturer.

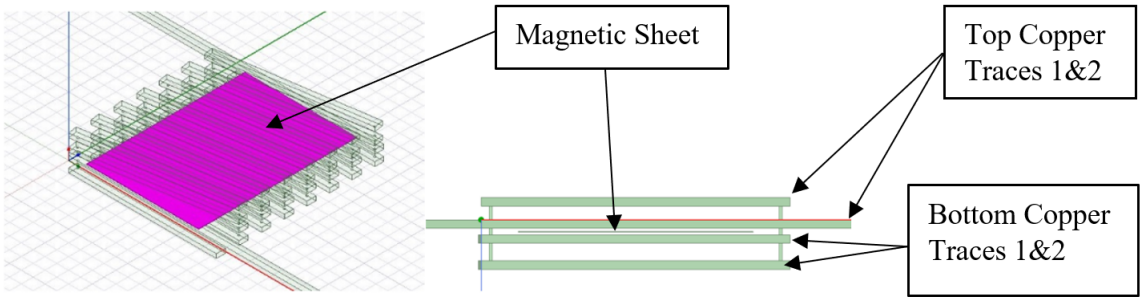

Figure 4.10: (Left) FEM of inductor structure. Pink is the magnetic core. (Right) FEM of inductor showing copper trace interconnections.

manufacturer. They are listed in Table. 4.3.

Fig. 4.10 shows the simulated inductor structure and the dimensions of the inductor are presented in Table 4.4.

Note that the simulation of a 16 $\times$ 250 nm thin-film magnetic core is not

Device Length [mm]	Device Width [mm]	Magnetic Core Thickness [μm]	Magnetic Core Permeability
2.9	2.5	4	360

Table 4.4: Dimensions of Gen II Flip-Chip inductor FEM

feasible due to the extreme aspect ratio of the core (the smallest dimension is 250 nm whereas the largest dimension is in the order of millimetres). This results in intractably long simulation run times for the thin-film multilayer core structure resulting from the dense mesh structure that Ansys needs to perform the Finite Element simulation. Hence it is necessary to approximate the magnetic core as a single 4μm thick core. The magnetic core properties (i.e. real and imaginary relative permeability) used in the simulation were taken from small-signal measurements of the manufactured multi-layer CZTB magnetic core. The imaginary component of the measured relative permeability spectrum represents the small-signal losses due to eddy currents and hysteresis 4.11. Thus, the FEM extrapolates all losses that arise within the core from the loss tangent of the material. However, in order to prevent a "double counting" of the eddy current losses within the 4 μm core it is necessary to set simulated conductivity of the core to a very small value ($\sim$ 1 S/m) in order to suppress additional eddy current losses.

Furthermore, the effect of the multi-layer thin-film magnetic core being approximated as a solid 4μm core is accounted for by the decreased permeability of the material shown in Fig. 4.11. Indeed, a single CZTB layer of thickness 250nm has a relative permeability in the order of 800 [11] and the multilayer structure has a permeability of 360. The R_{ac} of the model is simulated using the multi-layer thin-film CZTB magnetic core's loss tangent obtained from the permeability, cf 4.11. The inductor structure was also simulated without

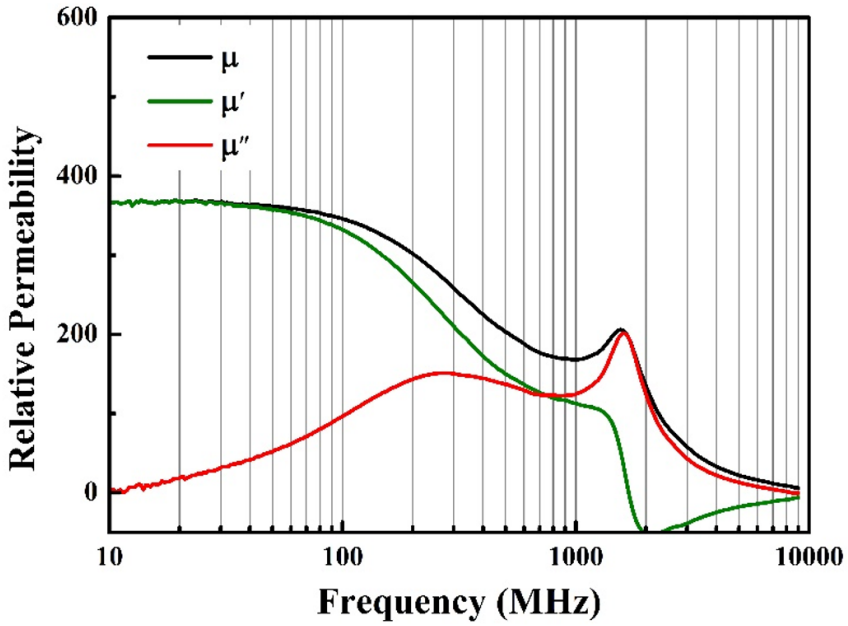

Figure 4.11: Permeability plot of the multi-layer thin-film CZTB magnetic core.

a magnetic core. This air core inductor was to serve as a reference for the inductance enhancement resulting from the addition of the magnetic core. The results of the FEM are presented in Subsection 4.3.4.

In order to understand the deviation between the simulated electrical results and the measured electrical results presented in Section V it is useful to use the analytical models (Eq. 4.3.1 - Eq. 4.3.6) for the inductance and resistance outlined in [12].

$$L_{aircore} = \frac{10\pi\mu_0 N^2 a^2}{9a + 10l_m} \tag{4.3.1}$$

Here N are the number of turns in the solenoid; lm is the length of the solenoid (which equals the length of the magnetic core); μ_0 is the vacuum permeability; and a is the modified cross sectional area of the solenoid outlined in Eq. 4.3.2

$$a = \sqrt{\frac{(w_a + 2D_s)(t_a + 2t_c)}{\pi}}. \tag{4.3.2}$$

Here w_a is the width of the air core; D_s is the diameter of the solder ball; t_a is the thickness of the air core; and t_c is the copper thickness. In Eq. 4.3.3 ΔL is the increase in the inductance of the device caused by the presence of the magnetic core.

$$\Delta L = \frac{\mu_0 \mu_r N^2 A_m}{l_m(1 + N_d(\mu_r - 1))} \tag{4.3.3}$$

Here μ_r is the relative permeability of the magnetic core (see Figure 4.11), in Subsection 4.3.2); A_m is the cross sectional area of the magnetic core; and N_d is the demagnetisation tensor of the thin film. Normally in the case of thin film magnetics the demagnetisation tensor is $(0\hat{x}, 0\hat{y}, 1\hat{z})$ as there is no stray magnetic field due to the boundary conditions of the thin film [13], and so for thin film magnetics N_d is near zero in plane.

As the cross section of the magnetic core comprises multiple magnetic layers it is necessary to sum over all the layers in order to determine the net magnetic cross section. This is given in Eq. 4.3.4.

$$A_m = \sum_i tm_i \cdot wm_i \tag{4.3.4}$$

Here tm_i and wm_i are the thickness and width of the ith magnetic layer, respectively. The resistance of the solenoid inductor is given by Eq. 4.3.5, as outlined in [12], with the addition of a resistance term for the solderballs interconnecting the two PCBs.

$$R_{aircore} = 2N\rho_c \left(\frac{l_c}{w_c t_c} + \frac{s_V + 2g_V}{w_V t_c} + \frac{t_c + t_a}{S_V^2} \right) + 8N\rho_s \frac{l_s}{\pi D_s^2} \tag{4.3.5}$$

Here ρ_c is the resistivity of the copper; l_c is the cooper length; $w_c t_c$ is the cross sectional area of the copper; s_V is width of the copper via; l_s is the length of the solder ball; and ρ_s is the resistivity of the solder ball. The overall resistance of the device with the magnetic core is given by Eq. 4.3.6

$$R_{MC} = R_{aircore} + \omega \frac{\mu''}{\mu'} \Delta L \tag{4.3.6}$$

Here μ''/μ' is the loss tangent of the material measured in Subsection 4.3.2. It is clear when comparing the analytical expressions for the inductance gain caused by the magnetic core and the resistance of the device that small variations within the shape of the magnetic core result in a small variation in the inductance of the device and a larger variation within the resistance of the device. The larger variation in the resistance of the device stems from the fact that the device's resistance is proportional to the product of the gain in the inductance caused by the magnetic core and the loss tangent of the magnetic core. The larger variation in the device resistance as compared to the inductance is shown later in Figure 4.20 of Subsection 4.3.4.

4.3.2 Magnetic Characterisation of Thin-Film CZTB Multi-Layer Core for High Frequency Application

The amorphous multi-layer CZTB magnetic cores (16×250 nm) were fabricated using dc-magnetron sputtering (Nordiko Advanced Energy NDX 2500-W Magnetron PVD system) from a single alloy target material $Co_{84}Zr_4Ta_4B_8$ (atomic %). The structural properties of the films were investigated by X-Ray Diffraction (XRD), Phillips Xpert diffractometer, Cu Kα-1.54 Å). The XRD 2θ-scan spectrum revealed a broad maximum in the range of $2\theta = 40$-50° without any Bragg peaks and hence confirmed the amorphous structure of the films. The results of the XRD 2θ-scan are plotted in Figure 4.12. The magnetic anisotropy of the 2cm $\times$ 2cm released multi-layer CZTB magnetic core were investigated by using BH-loop tracer (SHB, MESA 200 HF, at 10 Hz) at room temperature. By recording the BH loops along different directions, the anisotropy distribution across the samples can be recorded. A square-shaped BH-loop of the multi-layer CZTB magnetic core was observed along the easy axis, while a low hysteresis BH-loop was recorded along hard axis (90 degree away from easy axis), which suggested the multi-layer CZTB magnetic core has a good in-plane uniaxial magnetic anisotropy. The multi-layer core had a measured coercivity of 0.15 Oe along the hard-magnetic axis. The results of these are shown in Figure 4.13.

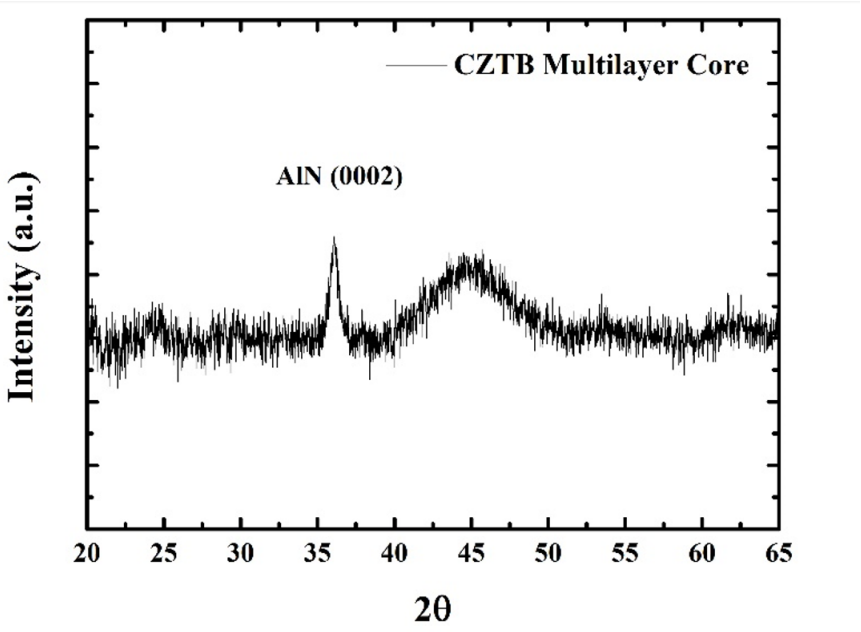

Figure 4.12: XRD scan of multi-layer amorphous CZTB stack.

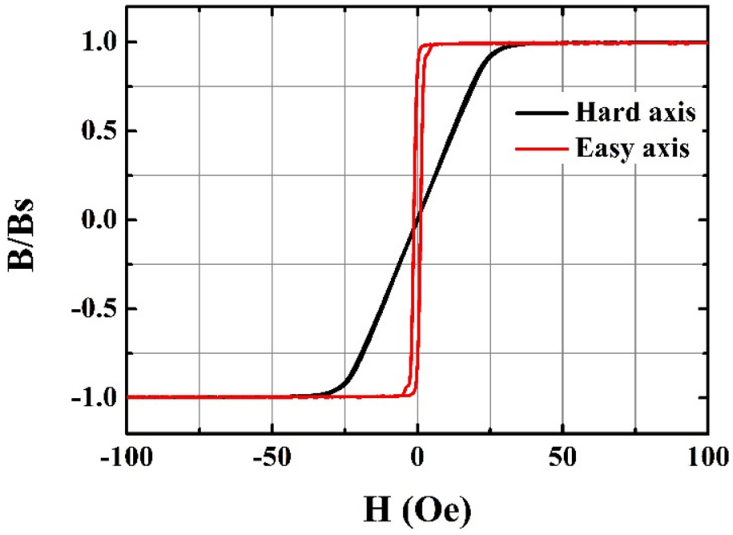

Figure 4.13: Normalised Hysteresis loops of the multi-layer amorphous CZTB stack.

The high-frequency (10 MHz – 9 GHz) permeability of films was measured along the hard axis of the 4mm × 4mm multi-layer sample using the Ryowa Permeameter, cf Figure 4.14. The relative permeability of the sample at 40 MHz was measured to be 367. Figure 4.14 shows that the real part of the relative permeability remains constant at frequencies below 100 MHz. From this it can be expected that the manufactured inductor will have a constant inductance at frequencies below 100 MHz. However, there is an increase in the imaginary component of the permeability in this range. This increased imaginary component will cause additional hysteresis losses within the multi-layer core and will negatively affect the measured AC resistance of the manufactured device. Hence the rise in the imaginary component of the magnetic core will reduce the Quality Factor of the manufactured device.

4.3.3 Manufacturing Process of Flip-Chip Inductor

This subsection pertains to the integration of the multi-layer CZTB magnetic core into PCB using a Flip-Chip approach. This method involved the placement of the magnetic sheet between two distinct PCBs with copper traces. The two PCBs were designated "upper" and "lower". Schematics of both are shown in Figure 4.15.

The "upper" and "lower" PCBs contain the necessary copper traces to form a solenoid inductor once the reflow process is complete. 150 μm diameter holes were placed in the soldermask of the two PCBs in order to expose the

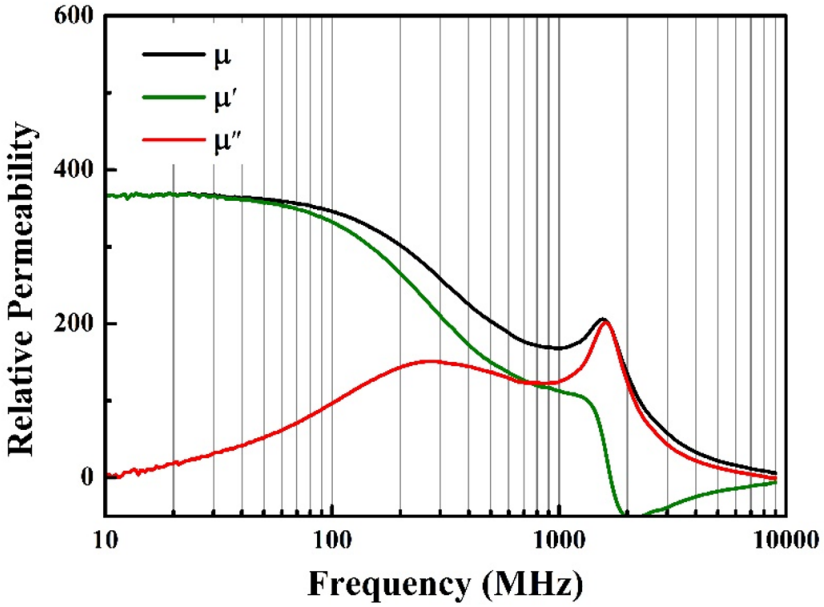

Figure 4.14: Ryowa Permeameter plot of the multi-layer amorphous CZTB magnetic stack.

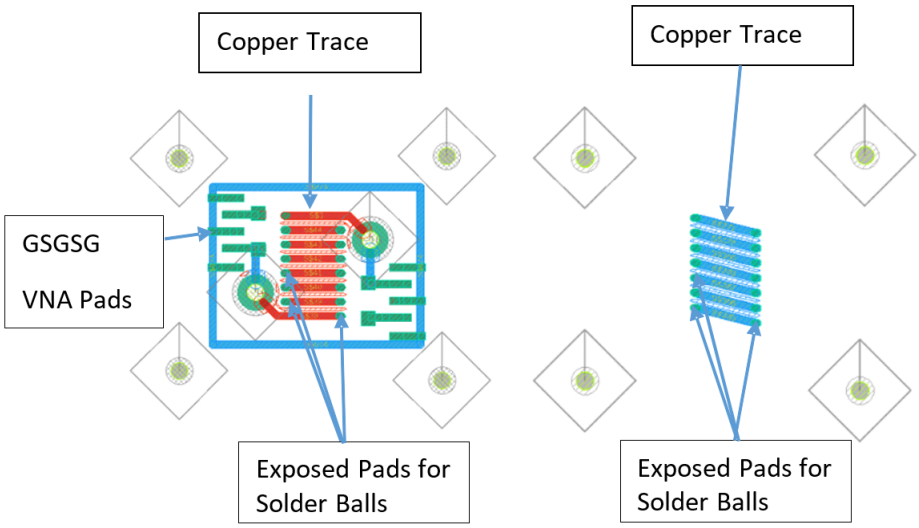

Figure 4.15: PCB schematic diagram of Gen II Flip-Chip Inductor. (Left) lower PCB; (Right) upper PCB.

underlying copper pads. Electroless deposition of NiAu is performed on the exposed copper pads in order to prevent oxidation of the copper. Solder balls are then mounted onto the NiAu pads and a reflow process is performed. The manufacturing process of the Flip-Chip inductor is as follows:

1. 200 μm diameter solder balls were mounted by hand onto the exposed pads of the "lower" PCB, cf. Figure 4.16 (left).

2. A preliminary solder reflow was performed at 180°C for 90 seconds. This reflow permanently fixed the solder balls to the pads and was done to facilitate further handling of the device.

3. The released CZTB multi-layer sheet was further cut to 2 mm $\times$ 2.8 mm using a scalpel and ruler.

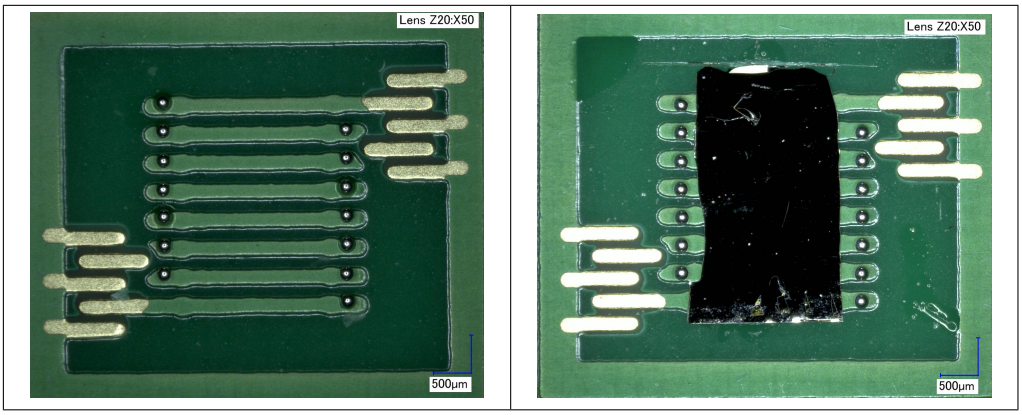

Figure 4.16: (Left) lower PCB with mounted solder balls; (Right) lower PCB with affixed multi-layer CZTB magnetic core.

4. The released multi-layer CZTB magnetic core was manually placed onto the "lower" PCB using a tweezers and was fixed to the board using glue, cf. Figure 4.16 (right).

5. The holes in the soldermask of the "upper" and "lower" PCB were aligned using a "Finetech Fineplacer Lambda".

6. The "upper" PCB was Flip-Chipped onto the "lower" PCB using the "Finetech Fineplacer Lambda".

7. The final solder reflow was performed at 180°C for 90 seconds.

An X-Ray image of the device was taken in order to verify the manufacturing process, cf. Figure 4.17. As can be seen from Figure 4.17 the solder successfully reflowed between the two PCBs.

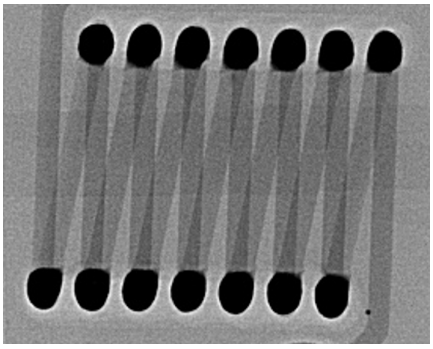

Figure 4.17: X-Ray image of Gen II Flip-Chip inductor.

4.3.4 Electrical Characterisation of Flip-Chip Inductor

The electrical measurements of the manufactured device were performed using a VNA. As can be seen in Fig. 4.15, the devices have a standardised GSGSG pin layout to facilitate electrical characterisation. The VNA was calibrated for the 300 kHz to 100 MHz frequency range and the 2-port S-parameters were measured using 400 μm pitch Z10-GS-400 probes from FormFactor Inc., cf. Figure 4.18.

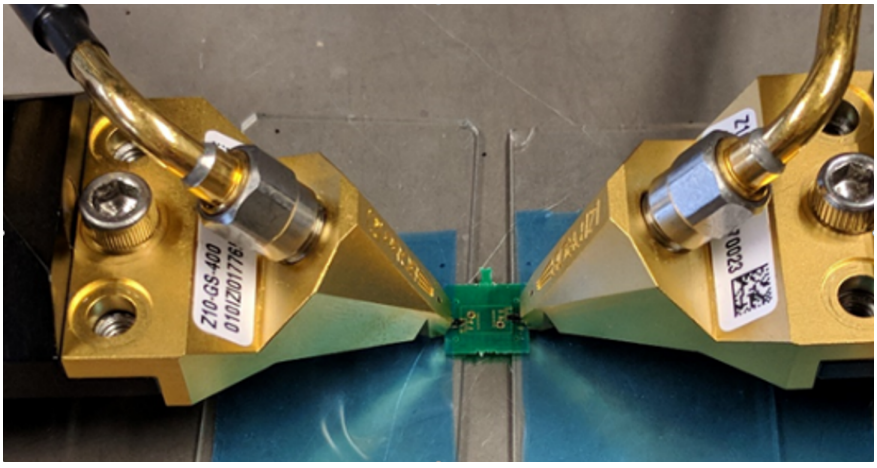

Figure 4.18: VNA electrical characterisation of Gen II Flip-Chip inductor.

Footprint [mm^2]	L_{dc} [nH]	R_{dc} [mΩ]	L_{den} [$\frac{nH}{mm^2}$]	$\frac{L_{dc}}{R_{dc}}$ [$\frac{nH}{m\Omega}$]	Q_{max}	$\frac{1}{A}\sqrt{\frac{L_{dc}}{R_{dc}}Q_{max}}$
7.25	52	102	7.17	0.51	23.29	15.06

Table 4.5: Electrical characteristics of Gen-2 Flip-Chip inductor with released multilayer thin-film CZTB core. Number of layers = 16.

The measured and FEM model electrical characteristics are plotted in Figure 4.19, and presented in Table 4.5. From Fig. 4.19 it is clear that the manufactured inductor maintains a stable inductance across the 0.3 – 100 MHz frequency range. This is very desirable for PwrSiP applications as it shows that Flip-Chip inductor can be used as the magnetic energy storage component in a variety of DC-DC converter topologies operating at different frequencies without a reduction in magnetic performance. Not only that, the frequency stability of the Flip-Chip inductor means that it is very suitable to be the magnetic energy storage component in DC-DC converters that utilise input signals whose Fourier decomposition comprises multiple higher order harmonics, such as a pulse train.

Note that the spread in the measured inductance and resistance values below 4 MHz in Figure 4.19 arises from instrumentation noise. The electrical characteristics of the measured device are compared against the simulated device in Table 4.6. Note the FEM model assumes Cu interconnects rather

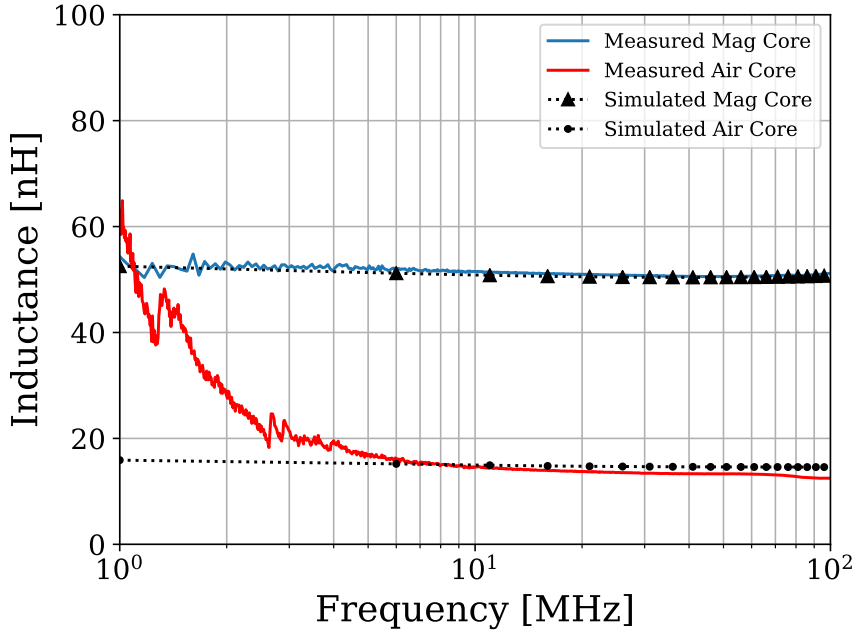

(a)

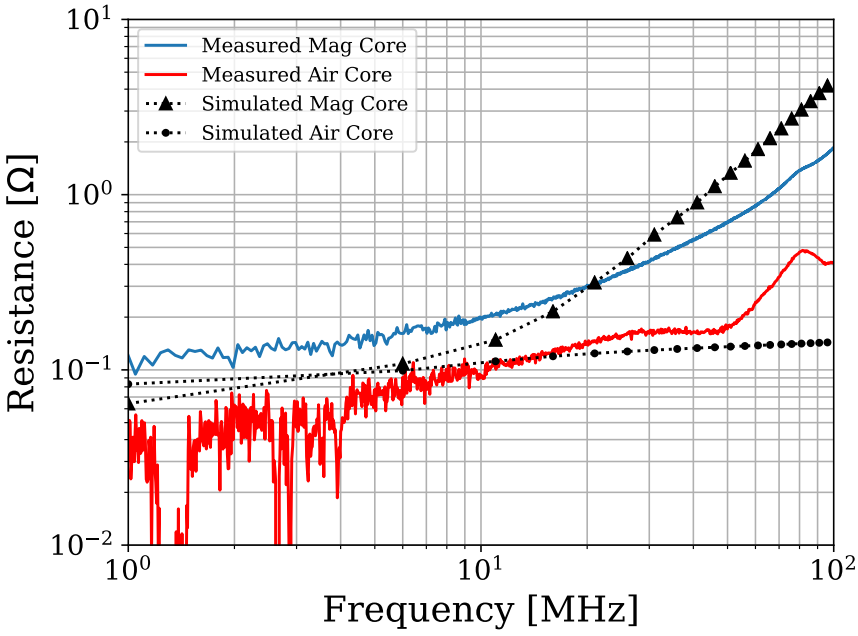

(b)

Figure 4.19: Measured VNA results of manufactured device (Colour). (a)Inductance. (b)Resistance; ♦ FEM results with magnetic core; – Air Core FEM results.

	L_{dc} [nH]	R_{dc} [mΩ]	L_{40} [nH]	R_{40} [mΩ]	Q_{40}
Manufactured	52	102	50.5	551	23
Simulated	52.5	64.2	50.4	885	14.3
Analytic	73.6	108.7	-	-	-

Table 4.6: Electrical Characteristics of manufactured Gen II Flip-Chip inductor versus simulated FEM. The discrepancy between the simulated and manufactured Q-Factor is explained in the histogram shown in Fig. 4.24 (Note the convention L_{40} is used to denote the inductance at 40 MHz.)

than solder balls. Hence there is a mismatch between the measured R_{dc} and the simulated R_{dc}.

Furthermore, there is very good agreement between the measured inductance (52 nH) of the manufactured device and the simulated inductance (52.5 nH) of the FEM. The simulated inductance of the air core device was 16 nH at low frequencies. On comparison of the air core inductor with the magnetic sheet inductor it is shown that the use of the magnetic sheet increased the inductance by a factor of 3.27. Note, that the increase in the inductance is orders of magnitude lower than the relative permeability of the multi-layer core, presented in Subsection 4.3.1. This is a consequence of Gauss's divergence theorem and the closure of the magnetic field lines through the air, which, reduces the effective permeability of the multi-layer magnetic core.

The discrepancy between the simulated R_{ac} and the measured R_{ac} are explained by variations between the multi-layer CZTB magnetic sheet samples used for the permeability measurement and for device fabrication. This is

due to the manual nature of the assembly process. To verify this, the electrical statistics of all the manufactured devices are shown in Figure 4.20. It is clear from these histograms that there are deviations in the electrical performance which arise during the manufacturing assembly process. This variance in the electrical performance can be reduced by replacing the manual handling components in the manufacturing process with more reliable automated ones.

In Figure 4.21 the average electrical characteristics of the fabricated batch are shown against the simulated FEM. There is a much greater agreement between the simulated electrical results and the average electrical results on the manufactured devices. Note there is large measurement noise sub 4 MHz and as such it is better in this region to backwards extrapolate the data from the noise free region of the graphs.

Considering that the multi-layer CZTB magnetic core had a constant permeability in the 0.3 – 100 MHz frequency range, the frequency stability of the manufactured inductors indicate that the insulating dielectric laminations between magnetic layers were sufficient to supress the formation of eddy currents within the multi-layer magnetic core. Such eddy currents within the magnetic core would have reduced the useful volume of magnetic material and a fall off in inductance with increasing frequency would have been observed. Moreover, eddy currents within the magnetic core would result in

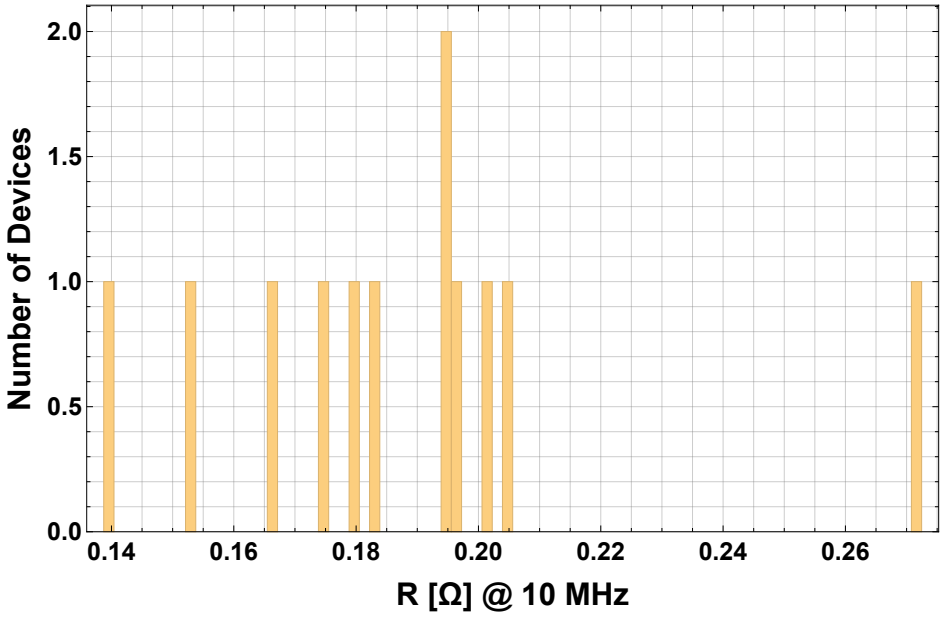

(a)

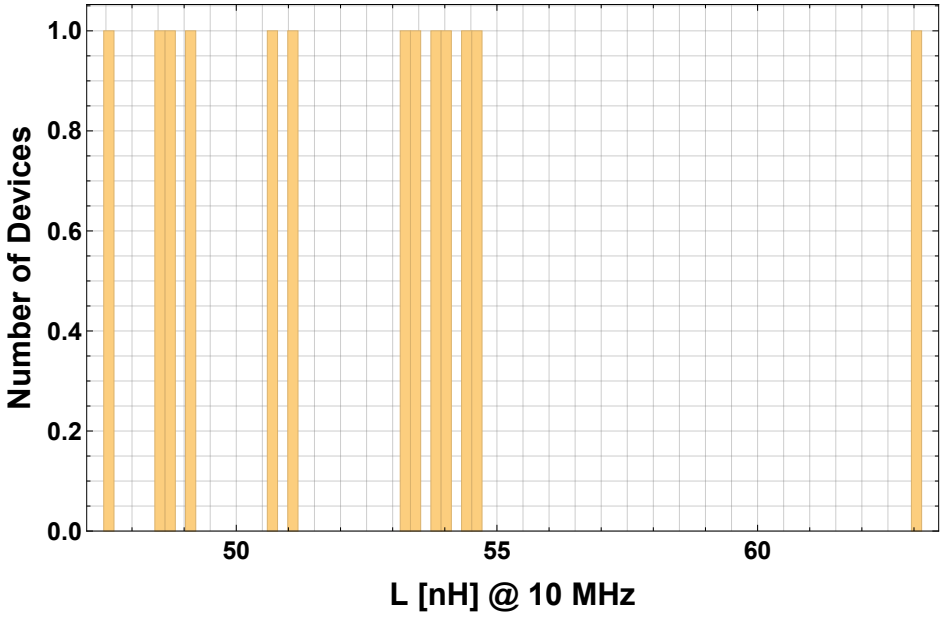

(b)

Figure 4.20: (Left) Histogram plot of manufactured Gen II Flip-Chip batch resistance. (Right) Histogram plot of manufactured Gen II Flip-Chip batch inductance. (Note 1 device resistance is omitted from the histogram as considerable exceeded the 0.14 – 0.3 Ohm range, i.e., it was an outlier in terms of resistance.)

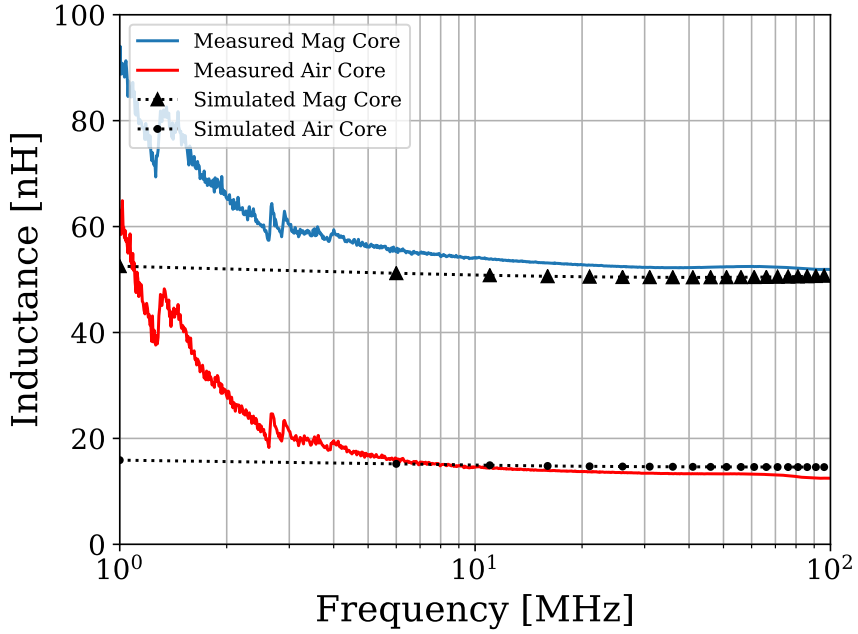

(a)

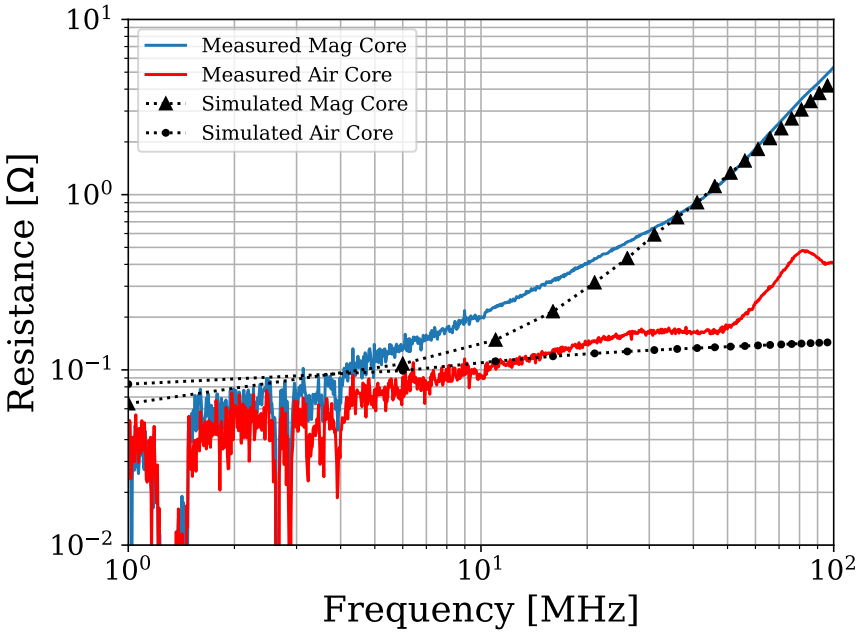

(b)

Figure 4.21: Average inductance & resistance measurements of second generation Flip-Chip inductor. Measurements performed using VNA. (a) Inductance. (b) Resistance.

energy loss that would negatively impact the overall efficiency of any DC-DC converter that the inductor is used in. Hence, the use of the multi-layer magnetic core structure improves the efficiency of the inductor by increasing the energy density stored in the magnetic field and by reducing the energy being dissipated by eddy currents.

Indeed, consider again the example of a nominal DC-DC buck converter with an output voltage of 3.3 volts (shown in section 4.2.2). Considering only the power dissipated by the R_{dc} of the wirebond inductor, the efficiency of this hypothetical converter rapidly decreases as the load current increases, cf Fig. 4.22. The Gen-1 wirebond inductor had a predicted efficiency of 86% at one Amp, whereas the Gen-2 Flip-Chip inductor has a predicted efficiency of 97%. Thus highlighting the importance of low DC resistance.

The ratio between the energy stored per cycle and the energy dissipated per cycle is referred to as the Quality Factor. The quality factor (plotted in Figure 4.23a) of the device was determined using the formula $\omega L/R$. Here the values of L and R are the frequency dependent inductance and resistance plotted in Fig. 4.19 and ω is the angular frequency. The manufactured device obtains a peak quality factor of 23 at 40 MHz. The very good Q-Factor of the Flip-Chip inductor is a result of the inductor's ability to maintain a flat inductance value across the 0.3 – 100 MHz frequency range. This is largely due to the intrinsic frequency stability of the multi-layer CZTB's permeabil-

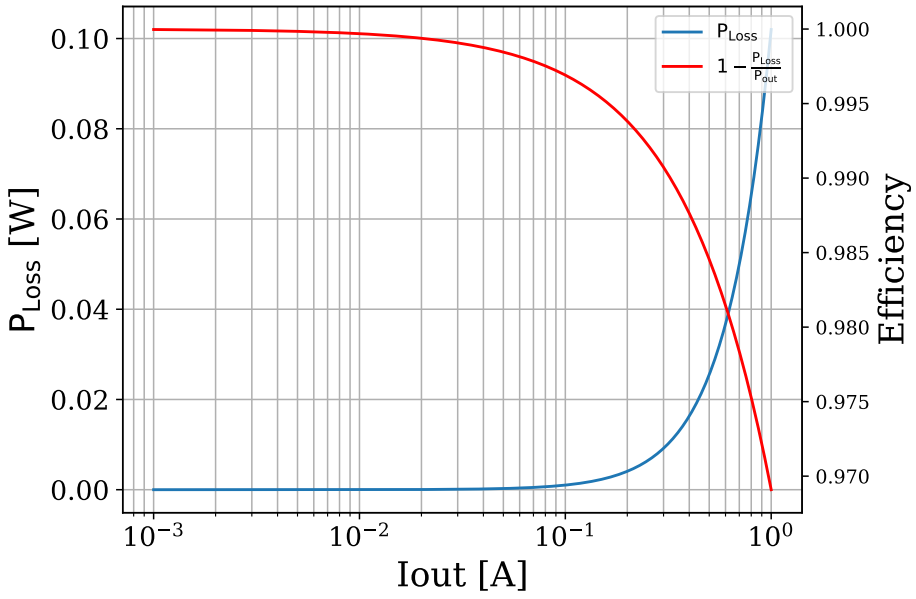

Figure 4.22: Theoretical equivalent series resistance power dissipation by wirebond inductor used as the magnetic passive in DC-DC buck converter.

ity, as presented in Subsection 4.3.2, and, the suppression of eddy current formation through the use of the laminated multi-layer structure. Although the use of a multi-layer magnetic core increases the energy stored by the magnetic field, and so increases the energy density of the inductor, there are additional loss mechanisms that occur as a result of the magnetisation reversal process. Hence, there is a tipping point wherein the gain in the inductor's energy density is equalled by the losses which arise in the magnetic core and the copper windings. For the manufactured device this tipping point occurs around 40 MHz, after which the losses within the magnetic core begin to exceed the gain caused by the increase in energy density. This results in a reduction in the quality factor of the device after 40 MHz.

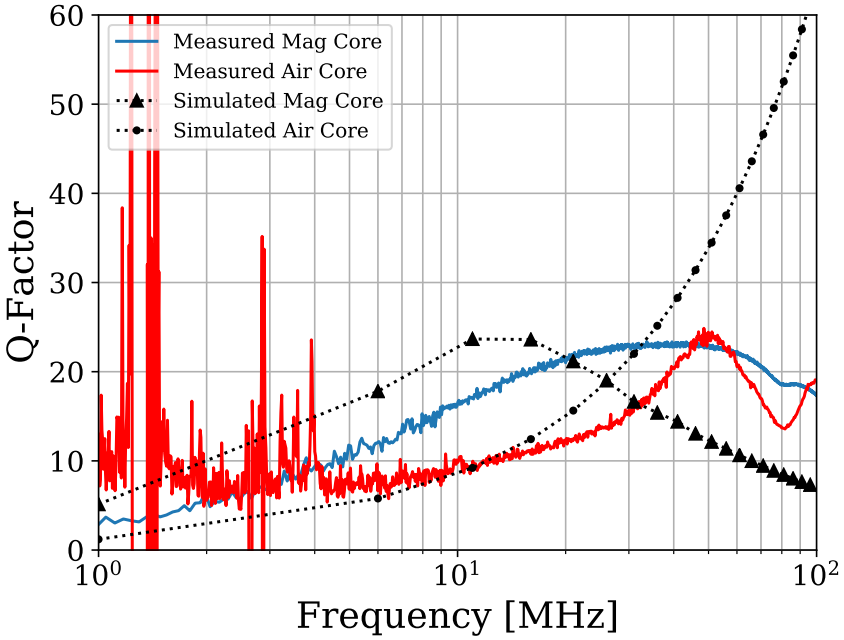

(a)

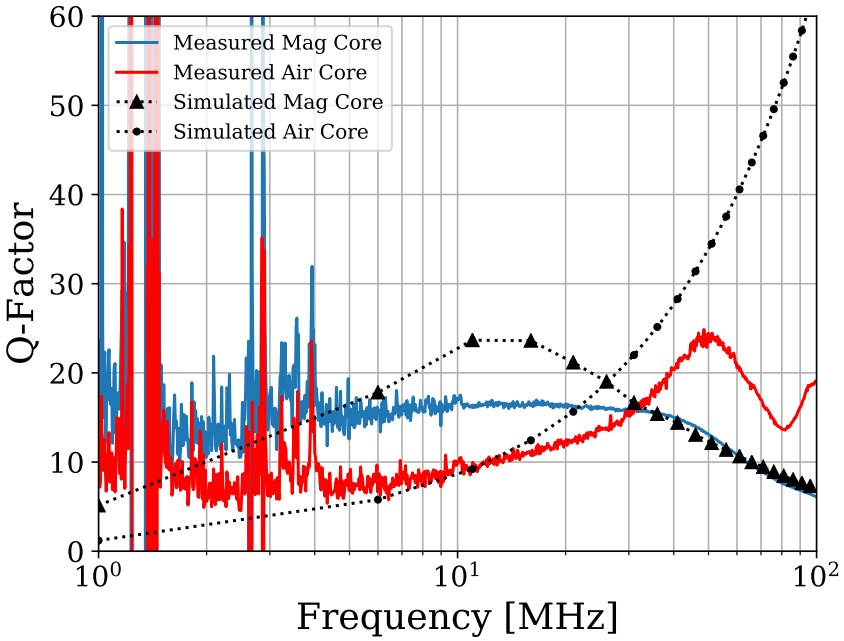

(b)

Figure 4.23: Quality factor of second generation Flip-Chip inductors measured using a VNA. (a) Highest recorded Q-Factor. (b) Average Q-Factor of batch.

In Figure 4.24 the histogram of the maximum quality factor of the manufactured devices is plotted. This is to further illustrate that the shape variations in the magnetic core affect the manufactured inductors performance. Hence, more accurate methods are required to cut the magnetic core during the fabrication process.

In Fig 4.25 the hybrid FOM derived in section 2.2.3 is plotted. The high FOM is a strong indicator that the Flip-Chip inductor with released multilayer thin-film CZTB magnetic core is well suited for PwrSiP applications as it has good DC and AC performance in terms of L/R_{dc} and Q-Factor. Indeed, this is demonstrated in section 4.5 where the Gen-1, Gen-2, and Gen-3 inductors are compared against the wider state of the art technologies for both PwrSiP & Power Supply on Chip (PwrSoC) technologies.

In Table 4.7 the Flip-Chip inductor is compared against devices that were reported in literature. The Flip-Chip inductor achieves a very small footprint as compared to the other PCB inductors presented in Table. 4.7. Normalising per unit area shows that the Flip Chip inductor outperforms most of the inductors in terms of Quality Factor. The inductor fabricated by [12] outperforms the Flip-Chip inductor in terms of a normalised Quality Factor due to its very small size. However, it should be noted that the inductor fabricated by [12] has a much larger DC resistance than the Flip-Chip inductor

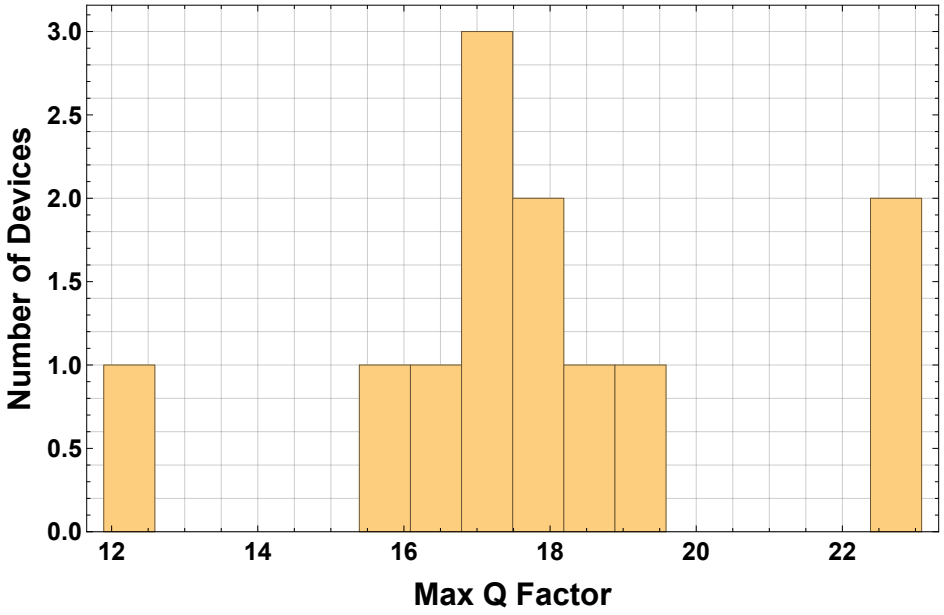

Figure 4.24: Histogram of maximum Gen II Flip-Chip inductor's Q-Factors.

and hence would not be as suitable to high current DC-DC converters. It is clear from this table that embedding the multi-layer CZTB magnetic core in PCB using the Flip-Chip method results in a better Quality Factor per unit area than several of the devices found in the literature and is a good trade-off between footprint and electrical performance. It is very noteworthy that the quality factor of the PCB devices exceeds those of the Si devices. The higher Quality Factor of the PCB devices is explained by their much lower R_{dc}. This reduction in the R_{dc} of the PCB devices is due to much thicker copper used in the inductor structures. In this work 140 μm copper thickness is used compared to the 5 – 40 μm thickness used in the Si devices. Hence, the thicker copper traces readily available to the standard PCB manufacturing

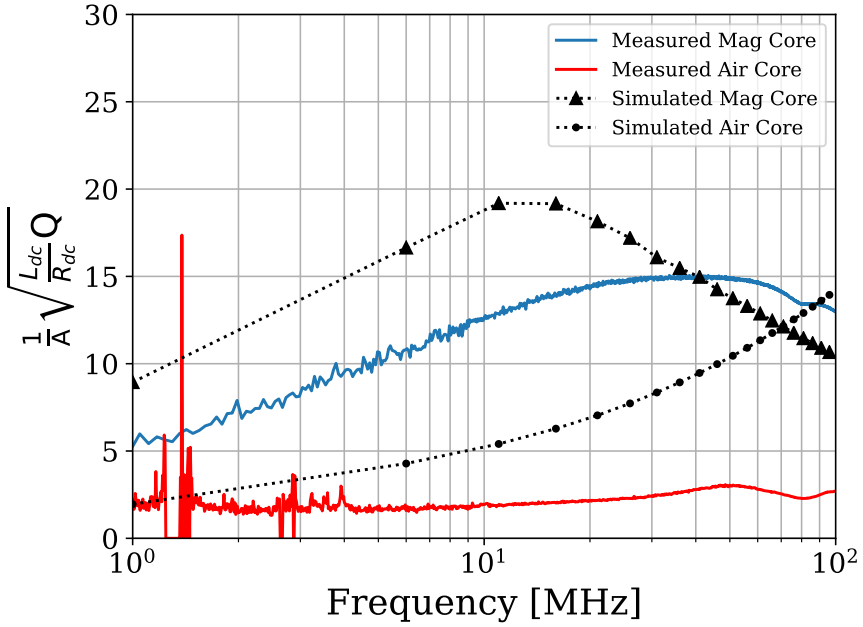

(a)

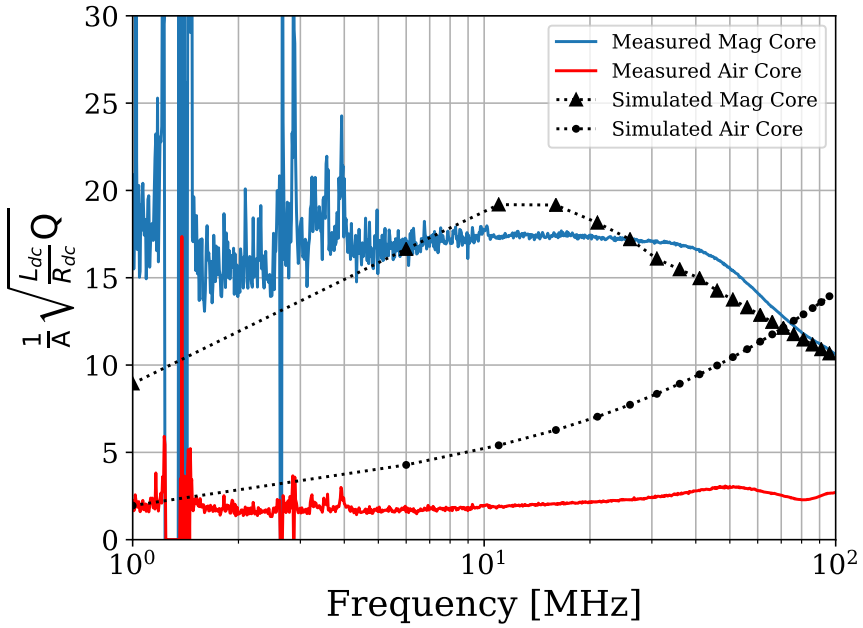

(b)

Figure 4.25: Hybrid AC-DC FOM derived in section 2.2.3 for Flip-Chip inductors. (a) FOM for Flip-Chip inductor with highest Q-Factor. (b) FOM for Flip-Chip inductor with average Q-Factor of batch.

Device Substrate	Footprint [mm^2]	Height [mm]	Peak Quality Factor @ Frequency	Normalised Peak Q	R_{dc} [Ω]	L_{dc} [nH]	L_{den} [$\frac{nH}{mm^2}$]	Material	Reference
PCB	7.25	1.46	23.29 @ 40 MHz	3.212	0.102	52	7.17	CZTB	This Work
Si	25	0.685	15.1 @ 8.3 MHz	0.604	0.844	34	1.36	CoZrO	[14]
Si	0.88	0.015*	6.5 @ 25 MHz	7.386	0.67	70	79.54	CoZrTa	[12]
PCB	31.36	0.35	35 @ 105 MHz	1.116	0.05	5	0.16	CoZrO	[15]
PCB	27	1	20 @ 4 MHz	1.35	–	630	23.33	CoNiFe	[16]

Table 4.7: Electrical characteristics of devices found in literature. (* The authors do not include the thickness of the Si-Substrate.)

processes makes the integration of the magnetic component in package a very tractable solution for low loss DC-DC power converters.

4.3.5 Conclusion

This Section presents a novel manufacturing process for the Gen-2, embedded multi-layer thin film magnetic inductors for PwrSiP applications. The multi-layer CZTB magnetic core is placed between two distinct PCBs and a solder reflow process is used to form the electrical connections between the two boards, embedding the magnetic core. The manufactured inductor demonstrated a peak quality factor of 23 at 40 MHz. The Flip-Chip inductor was compared against several devices found in the literature. It had a higher quality factor than its Si counterparts due to the much lower R_{dc} obtained by using 140 μm thick copper traces. The low R_{dc} and high quality factor obtained show that the Flip-Chip inductor with an embedded multi-layer CZTB magnetic core is an excellent candidate for PwrSiP applications.

4.3.6 Postamble

The Gen-2 approach, just like the Gen-1 approach, is a simple and cost effective fabrication method for the embedding of the magnetic core. The use of a secondary PCB layer decreases the R_{dc} and increases the mechanical stability of the manufactured component as compared to one that is fabricated using wirebonds.

However, although the Gen-2 inductor improved upon the L/R_{dc} ratio, the use of solder-balls in lieu of solid copper vias ultimately undermines the performance of the device in terms of resistance. Further, this fabrication method does not truly embed the released magnetic thin film in package. In this regard, the Gen-2 inductor was a necessary stepping stone towards the fully embedded solution presented in section sec: ATS

4.4 Generation 3: AT&S Embedded Inductor Structures With Released Multilayer Magnetic Cores

4.4.1 Introduction

The prior two sections outline the need for integrated magnetics in DC-DC power converters and the means of actually fabricating them. The first approach to the integration process was the use of wirebonds. This was found to have too high a winding resistance to make it fit for purpose. The second approach used flip-chip technologies and addressed the issue of high winding resistance by using only copper traces in the PCB copper layer in the inductor structure ie.e, no wirebonds were used. The third approach was to use a full embedding process and have the released magnetic thin film integrated between the prepreg layers in the PCB stack and to use the copper layers of the stack for the creation of the inductor. This fully embedding approach has the advantage of being smaller due to enhanced AT&S manufacturing capabilities. Note, the weakness in terms of the resistance of the Flip-Chip approach were the solder ball interconnects. In the fully embedding approach these solder ball interconnects would be replaced by solid copper through vias. Hence they would have lower resistance.

Unfortunately due to COVID-19 no physical inductor structures were ac-

tually manufactured as AT&S had severely restricted operations. However, despite the lack of an inductor structure being manufactured, significant progress had been made towards the embedding of the released magnetic thin film in the prepreg layers. As such, that progress will be presented in this section of the thesis. This structure of this section is as follows: Sub-section 4.4.2 details the process used to embed the released magnetic thin films in the prepreg layers of the PCB stack; Sub-section 4.4.3 provides the results and discussion of those embedding efforts; Finally, conclusions are presented in sus-section 4.4.5.

4.4.2 Embedding Process for Released Magnetic Thin Films

This section of the thesis pertains to the embedding of released magnetic materials within the prepreg layers of the PCB stack and was done in collaboration with the PCB manufacturing company AT&S. The embedding and test flow process for the magnetic component in the PCB stack is as follows:

1. Creating a 50 μm cavity in one of the prepreg layers to house the magnetic core.

2. Lamination of the prepreg layers at 220C and 2.5 bar pressure for 3 hrs.

3. Resultant embedded magnetic component is then thermally cycled using a solder reflow process, as follows:

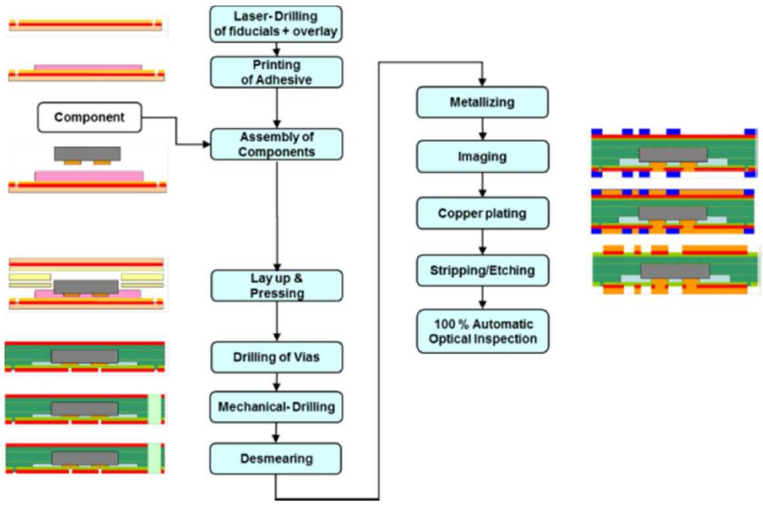

Figure 4.26: AT&S build up process for embedding of components within the PCB stack.

(a) Device Under Test (DUT) exposed to 250 C for duration of 1 hr.

(b) DUT cooled to 95 C.

(c) Thermal cycling of DUT repeated 10 times.

AT&S's component embedding process is shown in Figure 4.26.

The results of the embedding process on various released magnetic thin films are discussed in sub-section 4.4.3.

Figure 4.27: Cross section of released single layer $Ni_{45}Fe_{55}$ with protective Kapton tape after 6th thermal cycle. Note delamination and void in prepreg layers.

4.4.3 Embedded Released Magnetic Thin Film Results & Discussion

Initial embedding tests were performed on released $Ni_{45}Fe_{55}$ magnetic core with a protective layer of Kapton tape applied to the surface of the magnetic core. The reliability of the magnetic embedded process with Kapton tape was tested using the thermal cycling outlined above. Device failure was observed after 6th thermal cycle due to severe outgassing from the Kapton tape resulting in delamination between the prepreg and Kapton tape. Note, outgassing from the release Polyimide (PI) layer was not observed. This is most likely due to the exposure of the PI release layer to 260 C for 2 hrs during the curing phase of the release magnetic core fabrication process (see section 3.4). A cross section of the failed device is shown in Figure 4.27.

A second embedding run was performed on a released $Ni_{45}Fe_{55}$ multilayer core with SU8 used as the insulating dielectric layer. SU8 was selected in

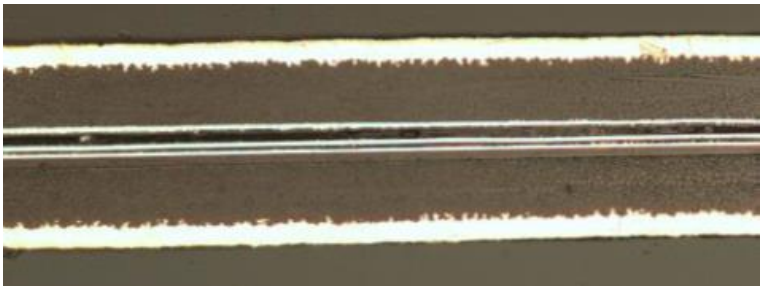

Figure 4.28: Cross section of embedded multilayer magnetic core with SU8 dielectric. Note delamination of magnetic core observed.

this run as it is a preferable dielectric layer than PI due to the lower bake temperature required. Whence, the magnetic layer is exposed to lower temperatures during the core fabrication process. Note, there was no protective layer of Kapton tape during this embedding run due to the outgassing issues mentioned above. Figure 4.28 shows a cross section of the DUT after 10 thermal cycles. It is clear that there has been delamination of the magnetic core that had direct contact to the prepreg layer of the PCB stack. Note, no such declamation occurred on the magnetic layer that had an underlying PI layer (recall PI is used as the release polymer). Hence, due to the antisymmetric nature of the mode of failure, a difference between the Coefficient of Thermal Expansion (CTE) of the interface materials was attributed as the likely cause of failure. Note, no outgassing was observed in the sample.

To confirm that stresses arising from a CTE mismatch between the interface layers is the underlying cause of the delamination a third embedding run was performed on a single released NiFe layer without a protective poly-

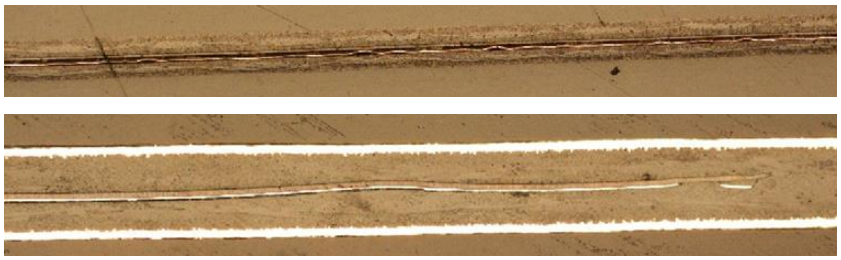

Figure 4.29: (Upper) Cross section of released $Ni_{45}Fe_{55}$ DUT without copper inlays after 10 thermal cycles. (Lower) Cross section of released $Ni_{45}Fe_{55}$ DUT with copper inlays after 10 thermal cycles.

mer coating on the upper layer. There were two DUT for this test, as follows: 1) A DUT without copper inlays, cf Fig. 4.29 Upper; 2) a DUT with copper inlays, cf Fig. 4.29 Lower. A cross section of the DUT after thermal cycling is given in Figure 4.29. The DUT without copper inlays had more severe delamination and warping than its counterpart with copper inlays. Furthermore, slight delamination is observed in DUT with copper inlays on the side of the material without the underlying PI layer. This further indicates that a CTE mismatch is the cause of failure and not outgassing from a polymer coating as the effect of outgassing would be exacerbated in the DUT with the copper inlays - the Cu inlays trapping the gas and increasing the pressure gradient within the copper.

Given that fewer delaminations were observed between the PI – prepreg interface for all samples, a fourth embedding run was performed with a released multilayer magnetic core with a spun on protective PI layer. Hence, this core had a protective upper and lower PI layer. Once more there were two DUTs

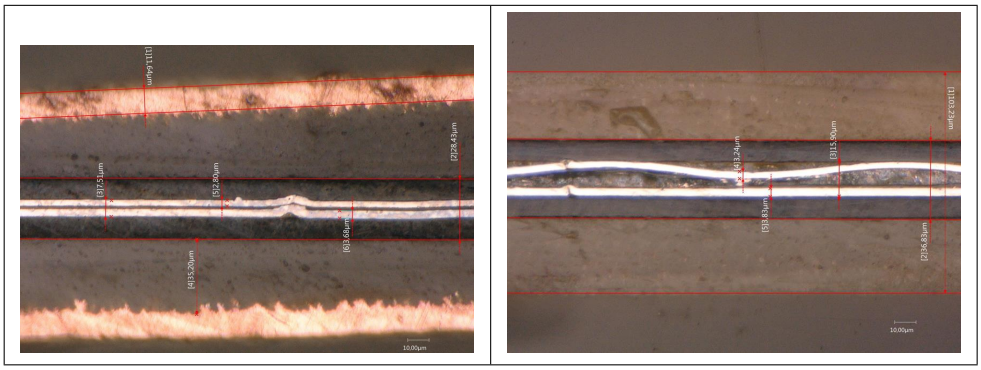

Figure 4.30: (Left) Cross section of released $Ni_{45}Fe_{55}$ with spun protective PI layers DUT with copper inlays. (Right) Cross section of released $Ni_{45}Fe_{55}$ with spun protective PI layers DUT without copper inlays.

for thermal cycling, as follows: 1) DUT with copper inlay, cf Figure 4.30 Left; 2) DUT without copper inlay, cf Figure 4.30 Right. Note the presence of the PI layers were not sufficient to prevent delamination due to thermally induced stress at the interface arising from CTE mismatch. This is evident as the DUT without copper inlays failed the thermal cycling. However, the DUT with copper inlays was successfully embedded i.e., no delaminations were observed.

After the successful demonstration of the emebedding process both CZT (x32) and NiFe (x2) multilayer magnetic cores were sent to AT&S for embedding. Preliminary magnetic characterisations of the two cores were using a Ryowa permeameter. The permeability results for the CZT core are presented in Fig. 4.31. There is no notable effect of the embedding process on the dynamic permeability of the CZT multilayer structure. As such the next

steps for this would be the fabrication of an actual inductor structure with the CZT multilayer structure as the core material. Fig. 4.32 shows the dynamic permeability of a dual layer $Nie_{45}Fe_{55}$ core. Comparing this to the non embedded core presented earlier (see fig. 3.12) it is clear that there is an almost 5 fold decrease in the low frequency permeability. As $Ni_{45}Fe_{55}$ has a high magnetostrictive coefficient it is believed that compression stress acting on the film during the embedding process has resulted in the observed decrease in permeability. Notably, CZT does not have a high magnetostrictive coefficient. Indeed the issue of magnetosatiction on the magnetic performance of Iron vs Cobalt alloys was discussed in sections 2.3.1 & 2.3.2. Thus compressive stress in the CZT film would not necessitate a decrease in performance.

4.4.4 Inductor Design & Finite Element Modelling

FEM was used to create an inductor structure that had an embedded 32 layer CZT core as part of the EU GaNonCMOS project. The FEM was performed with Maxwell Ansys v. 16 using the Eddy Current solver package. The designs comported to AT&S's manufacturing constraints in terms of copper thickness, and minimum linespacing. The simulated inductors physical dimensions are presented in Table 4.8. The 55μm copper thickness constraint was challenging in terms of producing an inductor structure with a high L/R_{dc} ratio. Furthermore, unlike the Flip-Chip inductor, multiple copper layers could not be used to improve the L/R_{dc} as AT&S's manufacturing

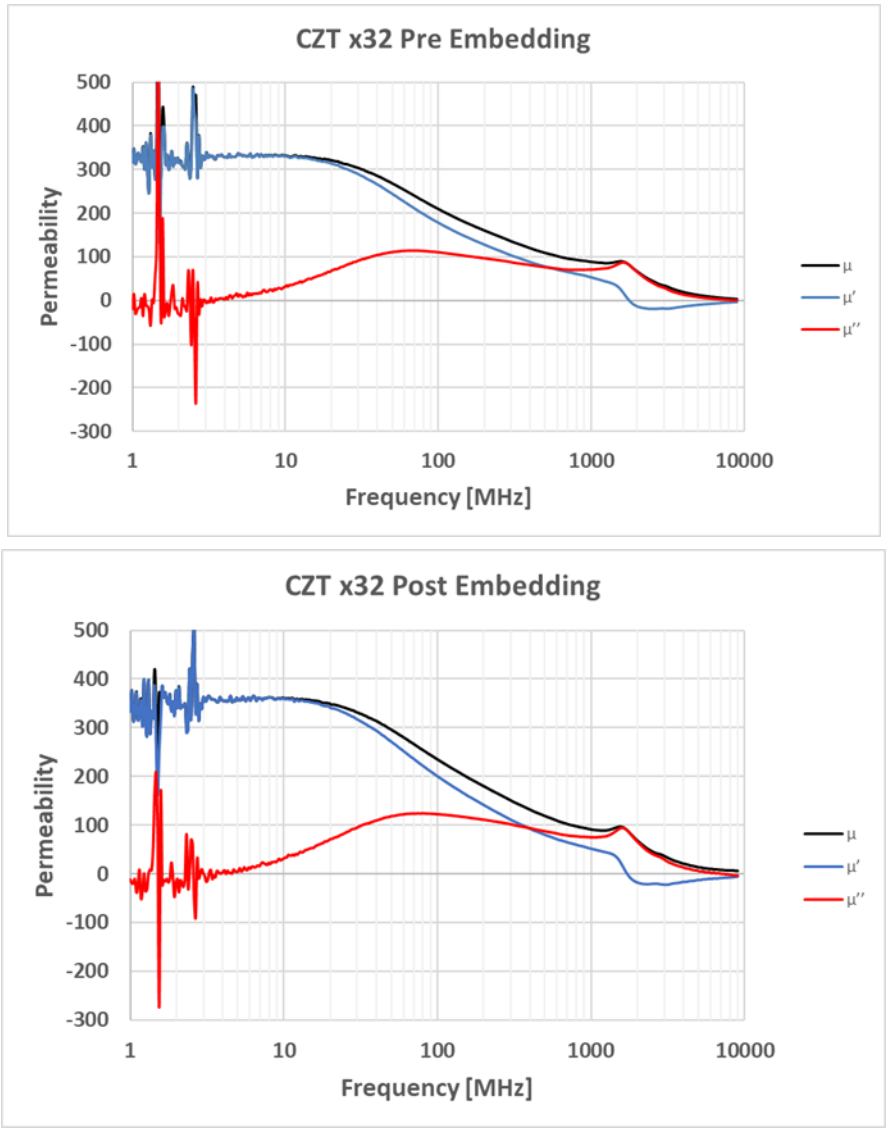

Figure 4.31: Magnetic characterisation of 32 layer CZT magnetic core pre (top) and post (bottom) AT&S embedding.

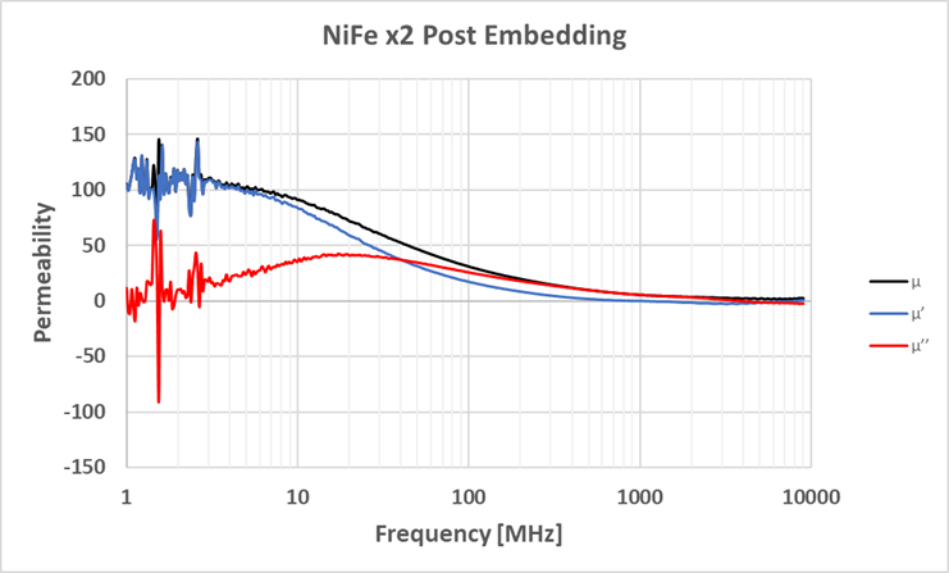

Figure 4.32: Magnetic characterisation of 2 layer $Ni_{45}Fe_{55}$ magnetic core post AT&S embedding.

Device Length [mm]	Device Width [mm]	Magnetic Core Thickness	Magnetic Core Permeability	Copper Thickness [μm]	Copper Trace Width [μm]	Copper Lines-pacing [μm]
2.4	6	8	500	55	300	50

Table 4.8: Dimensions of Gen III AT&S embedded inductor FEM.

process was limited to 4 copper layers in the prepreg stack and this inductor was to be part of a nested coupled inductor. The FEM model for the Gen-3 inductor structure is shown in Fig. 4.33.

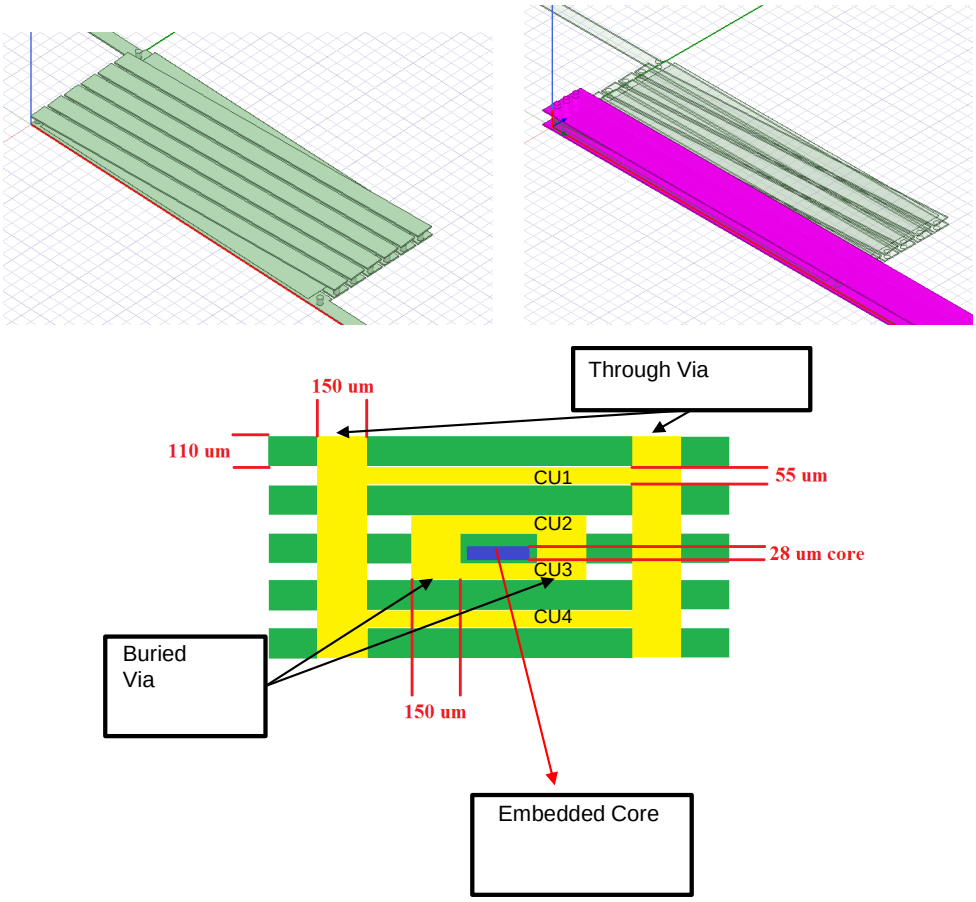

Figure 4.33: (Top Left)FEM of primary inductor structure with embedded released 32 layer CZT core for EU GaNonCMOS coupled inductor. (Top-Right) Primary and secondary windings for coupled inductor structure. (Bottom) Illustration of nested coupled inductor with embedded released thin film magnetic core in prepreg layers of PCB stack.

The inductors were simulated over the 1 - 100 MHz frequency range. This design was to be used as the magnetic passive in a 20 - 30 MHz DC-DC converter for the GaNonCMOS project. The inductance requirement for the

Footprint [mm^2]	L_{dc} [nH]	R_{dc} [mΩ]	L_{den} [$\frac{nH}{mm^2}$]	$\frac{L_{dc}}{R_{dc}}$ [$\frac{nH}{m\Omega}$]	Q_{max}	$\frac{1}{A}\sqrt{\frac{L_{dc}}{R_{dc}}Q_{max}}$
14.4	153.23	316	10.64	0.48	38.7	9.51

Table 4.9: Simulated electrical characteristics of third generation AT&S embedded inductor with released multilayer x32 CZT core.

design was between 100 nH and 200 nH depending on the final switching frequency of the converter. The 32 layer CZT core was chosen to improve the inductance density and thereby reduce the overall footprint of the inductor on the PCB. The simulated electrical results for this design are presented in Table 4.9.

Figure 4.34 shows the inductance and resistance performance of the primary inductor structure. The simulated Gen-3 inductor achieved a 150 nH at 1 MHz and had a 10 nH inductance drop across the simulated frequency range. This is unlike the Flip-Chip inductor which did not have an appreciable inductance drop over the same frequency range. Indeed, the permeability response of the 32 layer CZT core has a much more notable drop-off at frequency. Whereas the 16 layer CZTB core does not begin to drop-off until 100 MHz, the drop-off in the 32 layer core begins in the 20 - 30 MHz range. There is ongoing discussions as to the underlying causes resulting in the diminished performance of the 32 layer core vs the 16 layer core. At time of writing, there are two prevailing ideas as to the cause. The first is that capacitive coupling between the magnetic layers is the cause as there is an increase in

the amount of displacement current. The second is that magnetic coupling between the layers is the cause as there exists an inter-layer magnetic torque, resulting in an increase in out-of-plane magnetic switching. However, future work is needed to identify, and solve, the diminishing performance of the multilayer stack with increasing layer numbers.

The Q-Factor for the simulated inductor is presented in Fig. 4.35a. Recall from section 2.2.2 that the Q-Factor is an indicator of how well the inductor stores energy on a cycle by cycle basis. Thus, with a Q-Factor of 38.7, the simulated AT&S Gen-3 inductor is well suited for high frequency low power PwrSiP applications. Furthermore, the hybrid AC-DC FOM shown in 4.35b also indicates that the Gen-3 inductor is well suited to low power PwrSiP applications. An in depth comparison of the Gen-3 inductor vs the state of the art is provided in the next section (section 4.5).

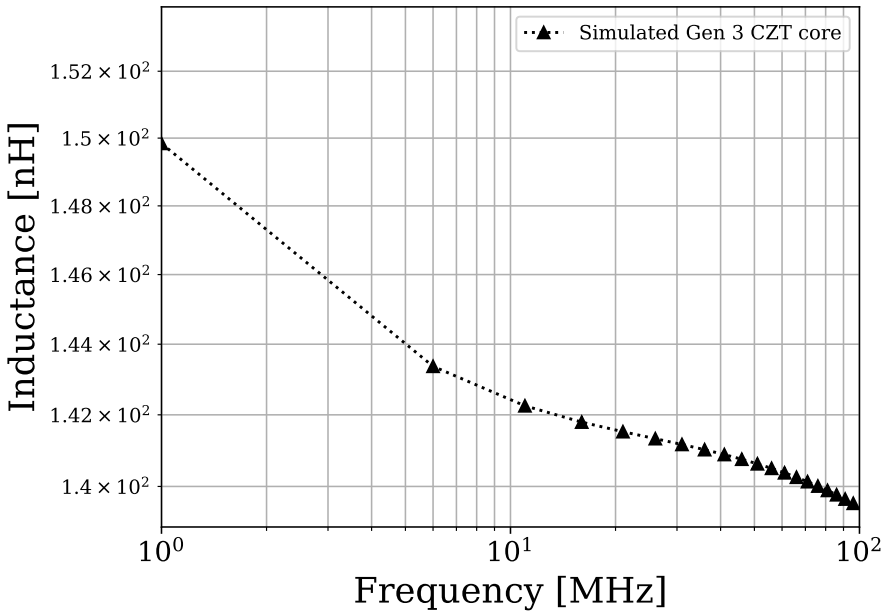

(a)

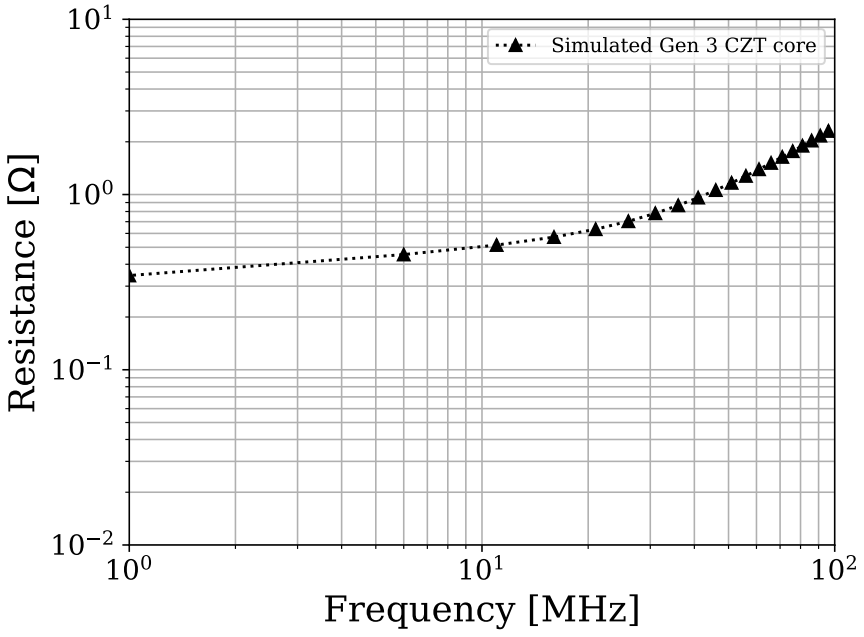

(b)

Figure 4.34: FEM Inductance (a) and Resistance (b) simulated results for AT&S embedded inductor with released 32 layer CZTB magnetic core.

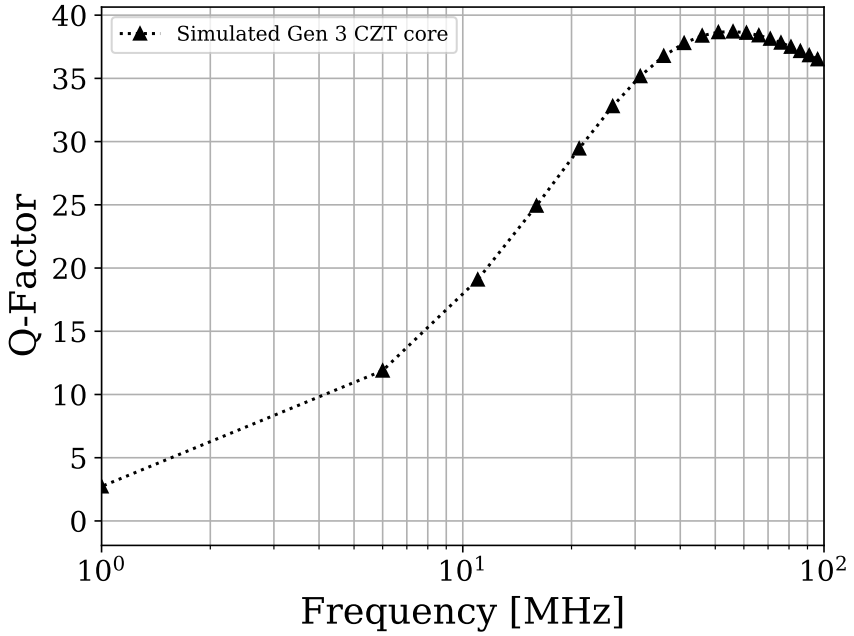

(a)

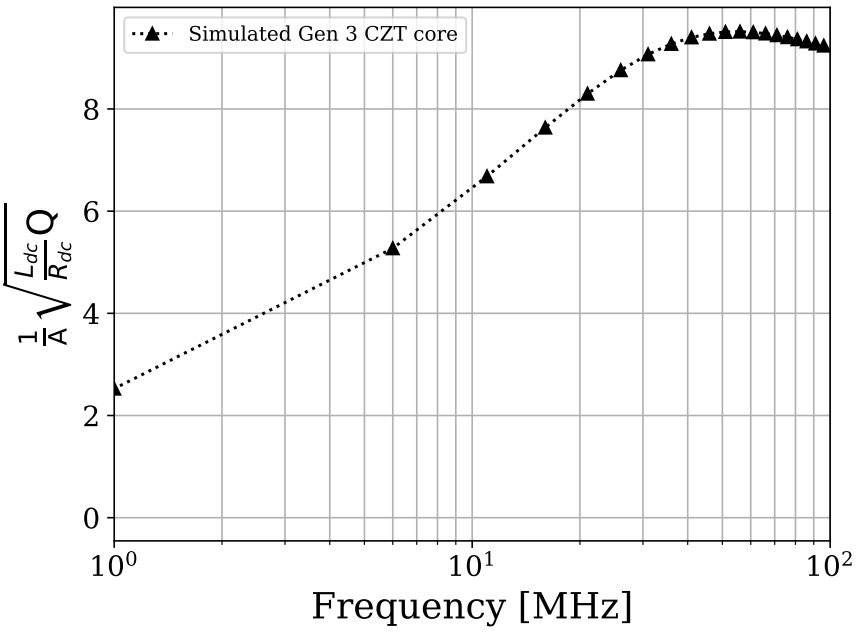

(b)

Figure 4.35: FEM Quality Factor (a) and AC-DC FOM (b) simulated results for AT&S embedded inductor with released 32 layer CZTB magnetic core.

4.4.5 Conclusion

In this section a successful embedding process for released magnetic materials in the prepreg layers of the PCB stack was demonstrated. Two main failure modes were observed from this process. The first being delamination and voids forming in the prepreg layers of the PCB stack due to outgassing from the polymer materials originally used in the magnetic core fabrication. The second being the delamination of the prepreg layers due to mechanical stress arising from a CTE mismatch at the interface of the prepreg layers and the embedded cores. Both these issues were resolved by judicious choice of the polymers used in the multilayer stack, both as the dielectric insulation layer separating the individual magnetic layers within the magnetic core, and the protective polymer layer applied to the outside of the core. Preliminary magnetic characterisation of the CZT multilayer core showed no effect of the embedding process on the magnetic characteristics of the core. However, the same was not true for the embedded NiFe core which showed severely degraded magnetic performance post embedding.

The successful embedding of the CZT magnetic core is a key accomplishment for the realisation of integrated magnetics in PwrSiP applications. This crucial step now accomplished enables the manufacture of embedded inductors with integrated magnetic cores for use in Power Supply in Package applications. Next steps and future work would see the creation of a physical inductor structure with the released magnetic core.

4.5 Integrated Thin Film Magnetics for Pwr-SiP Applications & the State of the Art

In this section the three generations of inductor structures are compared against the state of the technologies for PwrSiP applications and the generational differences between the structures is highlighted. In particular, this section shows the weaknesses of the earlier generations and how the later generations addressed them. For ease of cross comparison between the inductors their nomenclature, physical dimensions, and core materials are summarised in Table 4.10.

It is important to note that two types of the Flip-Chip inductors were fabricated. The first type is different to the one presented in section 4.3 as it used a released NiFe core rather than a released CZTB core. This facilitated a fairer cross comparison between these two generations of inductors as they both used the same core material and also the underlying PCB used in the fabrication of the wirebond inductor is the same as the one used in the NiFe Flip-Chip inductor. The second type of Flip-Chip inductor was the one presented in section 4.3. This is a larger device in order to facilitate a higher inductance requirement. Furthermore, the device used thicker copper and a CZTB core in order to improve upon the $\frac{L_{dc}}{R_{dc}}$ ratio and Q-factor.

	Device Length [mm^2]	Device Width [mm^2]	Copper Trace Width [μm]	Copper Thickness [μm]	Magnetic Core
Gen-1	2.1	1.65	154.2	-	x3 NiFe
Gen-2.a	2.1	1.65	154.2	70	x3 NiFe
Gen-2.b	2.9	2.5	154.2	140	x16 CZTB
Gen-3	2.4	6	300	50	x32 CZT

Table 4.10: Physical dimensions of manufactured inductor structures for PwrSiP applications. Note Gen-3 was only simulated.

4.5.1 Cross Comparison of Gen-1, Gen-2, & Gen-3 Inductors for PwrSiP Applications

The main advantage of the wirebond approach is the cost effectiveness and ease of device manufacture. Indeed for a particular inductance value required both the wirebond inductor and the Flip-Chip inductor can produce near identical inductance. To prove this a Flip-Chip inductor was designed to match the inductance of the first generation wirebond inductor. This is illustrated in Fig. 4.36a from which it is clear that the inductance profile of the NiFe wirebond and Flip-Chip inductors are indistinguishable from one another. Furthermore, the drop-off in inductance of the NiFe core is identical for both the wirebond and Flip-Chip inductor. Thus, the drop-off in inductance at frequency is due to the core material used. This can therefore be addressed by using a magnetic core with a better permeability response at frequency.

The second generation Flip-Chip inductor that utilised CZTB as the mag-

netic core has a flat inductance response across the measured frequency range. The CZTB core was demonstrated to have a flat magnetic permeability frequency response up until 100 MHz (see Fig. 4.14). The third generation inductor has a larger inductance than both the Flip-Chip and wirebond inductor as it was designed to provide the primary magnetising inductance for a transformer as part of the EU GaNonCMOS project. As the Gen-3 inductor used AT&S's advanced manufacturing techniques it has the highest inductance density of the three generations of inductor.

From Fig. 4.36a it is clear that the three generations of inductors can be used as the magnetic passive in DC-DC converters which require a flat inductance response in the 1 - 100 MHz frequency range. Therefore, if inductance is the singular criterion required by a DC-DC converter the wirebond inductor is the better choice due to its inherent simplicity.

However, with this ease of manufacture comes a trade off in performance. Namely, the main disadvantage of the wiredbond inductor is the much higher R_{dc} value of the device. This is due to the inherently poorer electrical conductivity of the 25 μm wirebonds used in the first generation inductor as compared to standard 70 μm PCB copper traces used in the second generation inductor. The higher DC resistance of the wirebond inductor is clearly illustrated in Fig. 4.36b. Furthermore, the CZTB Flip-Chip inductor has the lowest resistance due to the use of 140 μm thick copper traces. This makes

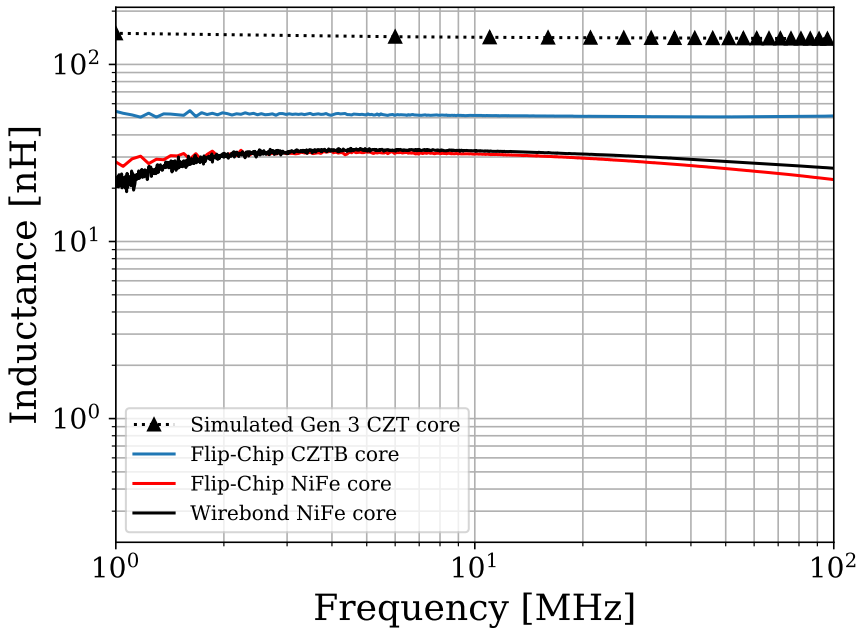

(a)

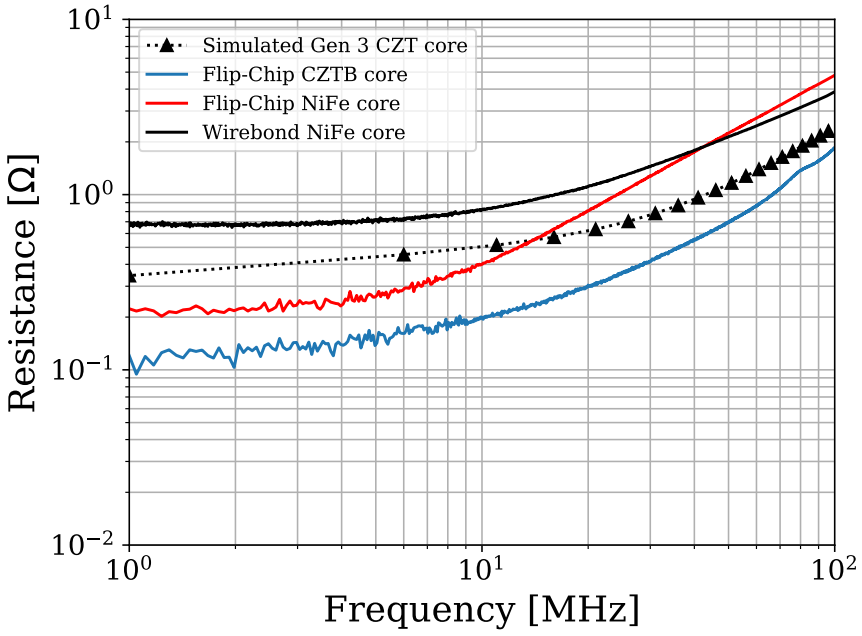

(b)

Figure 4.36: (a) Inductance comparison of the three generations of inductor structures. (b) Resistance comparison of the three generations of inductor structures.

	Footprint [mm^2]	L_{dc} [nH]	R_{dc} [mΩ]	L_{den} [$\frac{nH}{mm^2}$]	$\frac{L_{dc}}{R_{dc}}$ [$\frac{nH}{m\Omega}$]	Q_{max}	$\frac{1}{A}\sqrt{\frac{L_{dc}}{R_{dc}}Q}$
Gen-1	3.465	32.4	488	9.35	0.065	4.28	4.83
Gen-2.a	3.465	31.2	173	9.24	0.18	5.03	8.81
Gen-2.b	7.25	52	102	7.17	0.51	23.29	15.06
Gen-3	14.4	153.23	316	10.64	0.48	38.7	9.51

Table 4.11: Electrical characteristics of the three generations of inductor structures. Here the Gen-2.a device used the NiFe core and the Gen-2.b device used the CZTB core. Note Gen-3 are the simulated results for an embedded CZTB core.

the CZTB Flip-Chip inductor more suited to low power PwrSiP applications as the much larger resistance of the wirebond inductor will have higher conduction losses in a DC-DC converter.

The Q-Factor of the inductors is shown in Fig. 4.37a. This figure clearly illustrates the superiority of the CZTB designs as compared to those using NiFe. This is for twofold reasons. Firstly, the improved Q-Factor of the CZTB inductors is due to the flatness of CZTB's permeability frequency response which results in lower loss tangent when compared to NiFe. Secondly, the CZTB inductors have a larger $\frac{L_{dc}}{R_{dc}}$ ratio (see Table 4.11), and therefore inherently dissipates less energy than that of its NiFe counterpart. This is due to the linear proportionality between energy density and inductance density, and the linear relationship between energy dissipation and device resistance.

Figures 4.36 & 4.37a clearly demonstrate that the Gen-3 and Gen-2.b inductors are more suited to PwrSiP applications than the Gen-1 and Gen-2.b

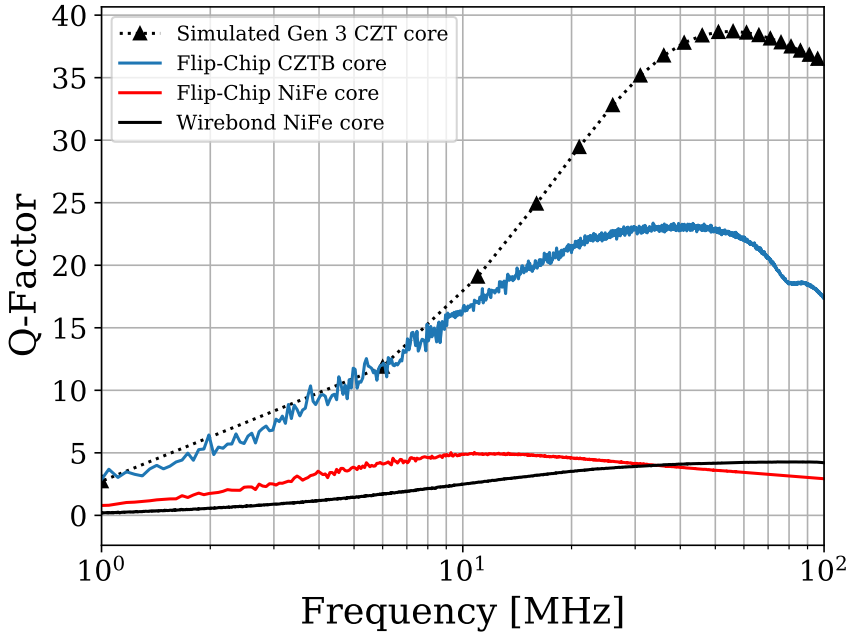

(a)

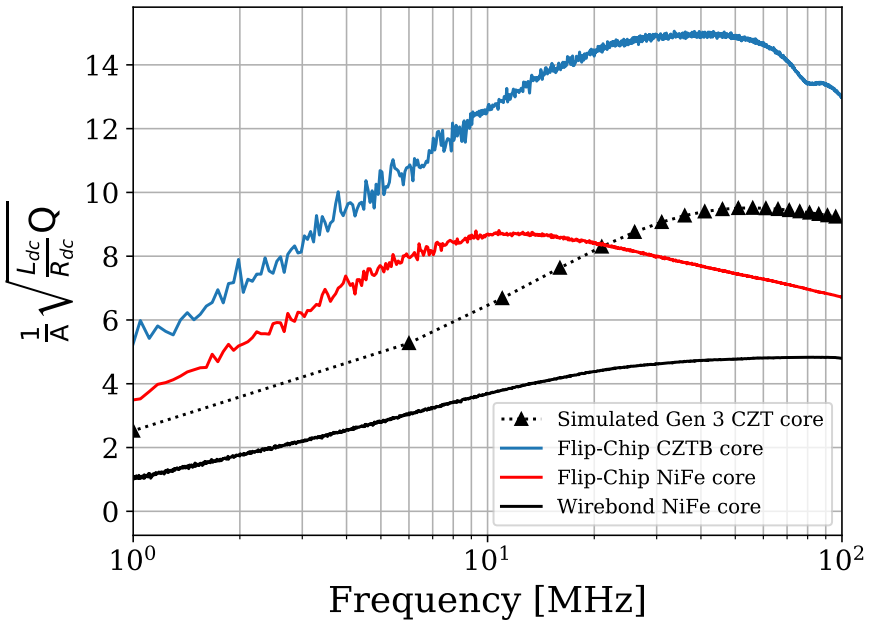

(b)

Figure 4.37: (a) Quality factor comparison of the three generations of inductor structures. (b) Hybrid AC-DC FOM comparison of the three generations of inductor structures.

devices. However, Fig. 4.37b tells a slightly more nuanced story as the Gen-3 inductor does not outperform either of the Gen-2 devices in terms of the hybridised FOM. This is due to the Gen-3 inductor being 2-4 times the area of the Gen-2 devices without have a 2-4 times improvement in inductance density. This shows the difficulty in achieving PwrSiP devices which have large inductances, and are small. Indeed, this is a key disadvantage that PwrSiP devices face compared to PwrSoC devices.

However, released thin film magnetic cores integrated into an organic package can be successful at producing inductors which can be competitive in terms of inductance density per unit resistance against their PwrSoC contemporaries. This is illustrated in Fig. 4.38 were $\frac{\mathrm{L}}{\mathrm{R_{dc}}}$ vs footprint of the three generations of inductors considered in this thesis are compared against the state of the art devices in both the scientific literature, and industry available devices. The Gen-2 and Gen-3 devices perform averagely against their silicon counterparts. This is impressive considering that the minimum linespace of the Gen-2 device was 228.6 μm, which is a 10x order of magnitude greater than that of silicon. And so, this disparity between Gen-2 device and Silicon devices results in far greater footprints for PCB based devices for a given inductance requirement.

Furthermore, the Gen-2.b and the Gen-3 inductor are better in terms of energy density to energy loss than the majority of devices found in the lit-

erature. Consider the CZTB Flip-Chip inductor's inductance density and Q-Factor. It has already been established in section 2.2.2 that there exists a fundamental trade-off between these two quantities, and yet, this device outperforms the majority of the existing prior art. Indeed, there only 6 devices in the literature which outperform the CZTB Flip-Chip inductor in terms of Quality Factor and inductance density, cf Fig. 4.39. For the Gen-3 device that number diminishes to 3, and only one of them is a PwrSoC solution.

For the combined AC-DC FOM, only one device outperforms the CZTB Flip-Chip inductor. Once again this is a PwrSoC device, and as was established in the discussion of Gen-2.b vs Gen-3 this FOM heavily favours smaller devices as the footprint of the device is the only term not inside the square root. Had the Gen-3 device been able to use 4 copper layers in its design, as was the case for Gen-2.b, it would have had twice the $\frac{L_{dc}}{R_{dc}}$ ratio. This would have resulted in a $\sqrt{2}$ increase in the hybrid AC-DC FOM, putting it on par with the highest PwrSoC device found in the literature by Morrow et al. [17].

Furthermore, the hybrid AC-DC FOM and the inductance density both favour small devices. Plotting the same FOM against inductance, not inductance density, tells a very different story. Using this criterion, no device has simultaneously a higher inductance and a higher FOM than the Gen-2.b and Gen-3 inductors. From Fig. 4.41 it is clear that the Gen-2.b and Gen-3 devices are part of a hard line of resistance which no device has yet to push

past. In this regard, the Gen-2.b and Gen-3 inductors are at the forefront of the state of the art. And so, integrated thin film magnetics is at the forefront for PwrSiP and PwrSoC applications.

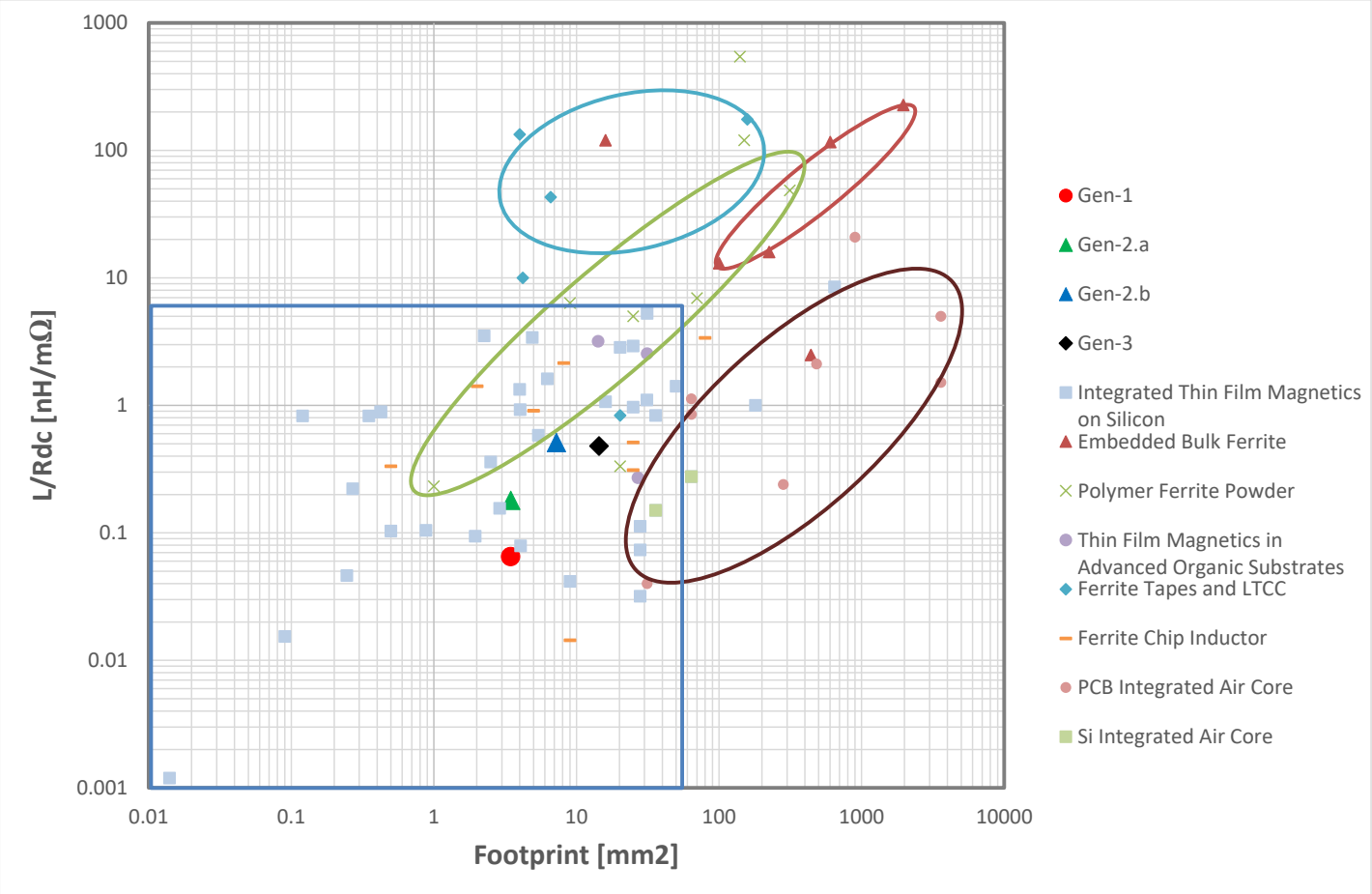

Figure 4.38: Comparison of Inductance to resistance ratio vs footprint of Gen-1, Gen-2, & Gen-3 devices compared to PwrSiP & PwrSoC applications found in literature. Note top left of graph is desired area for PwrSiP & PwrSoC applications. See table 2.1 for details.

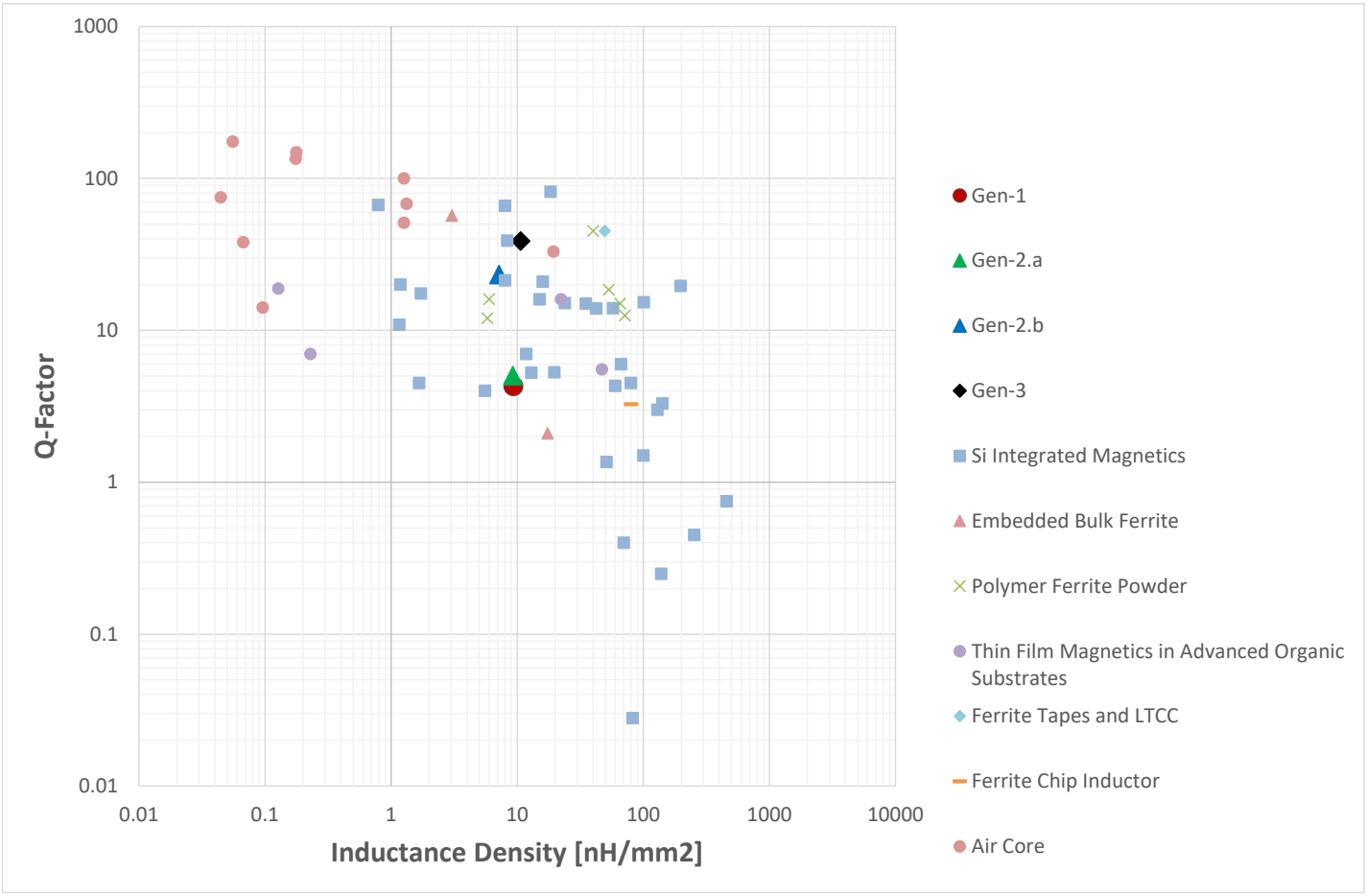

Figure 4.39: Q-Factor vs Inductance density of Gen-1, Gen-2, & Gen-3 devices compared to PwrSiP & PwrSoC applications found in literature. Note top right of graph is desired area for PwrSiP & PwrSoC applications. See table 2.1 for details.

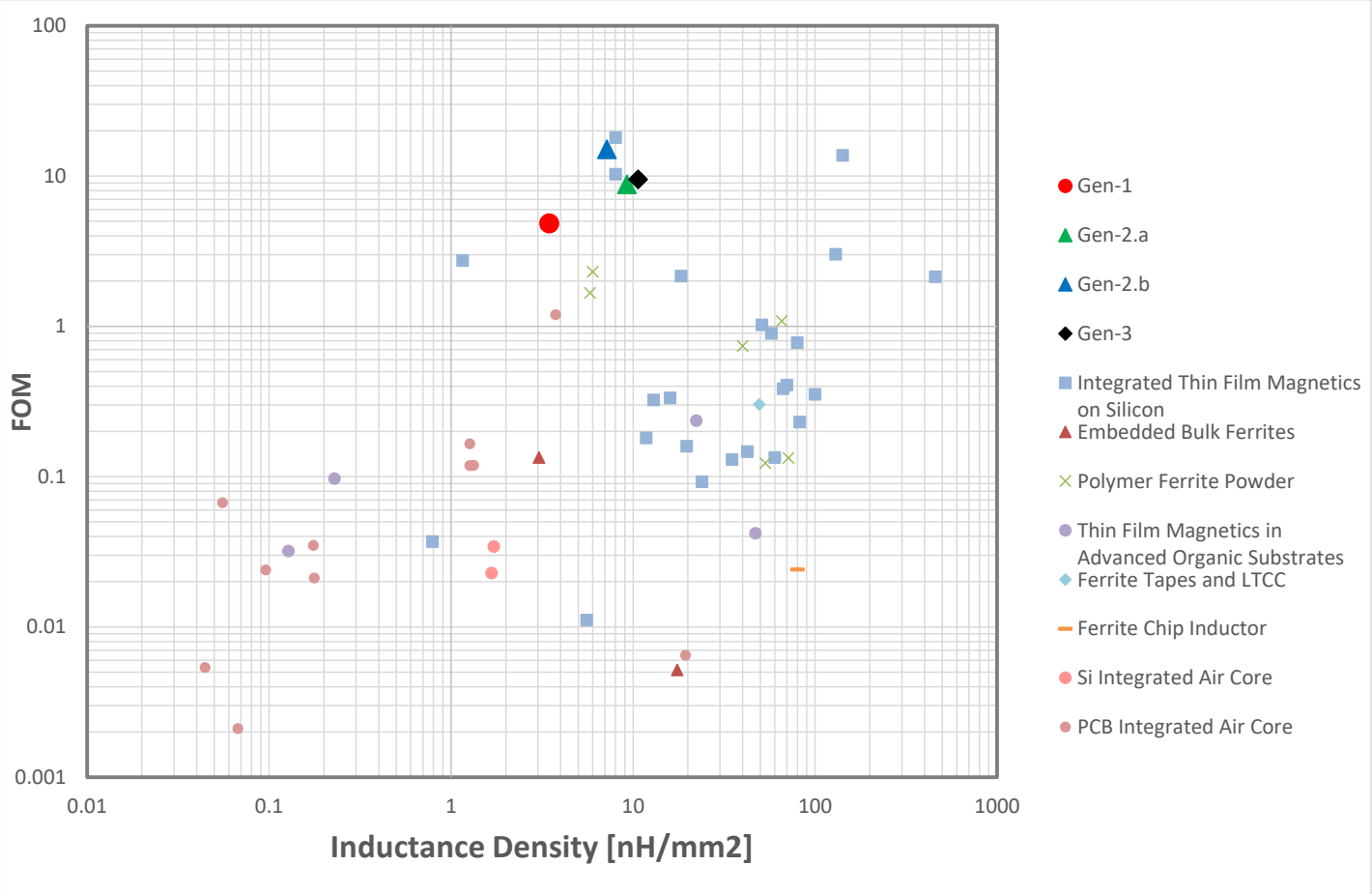

Figure 4.40: FOM vs Inductance density of Gen-1, Gen-2, & Gen-3 devices compared to PwrSiP & PwrSoC applications found in literature. Note top right of graph is desired area for PwrSiP & PwrSoC applications. See table 2.1 for details.

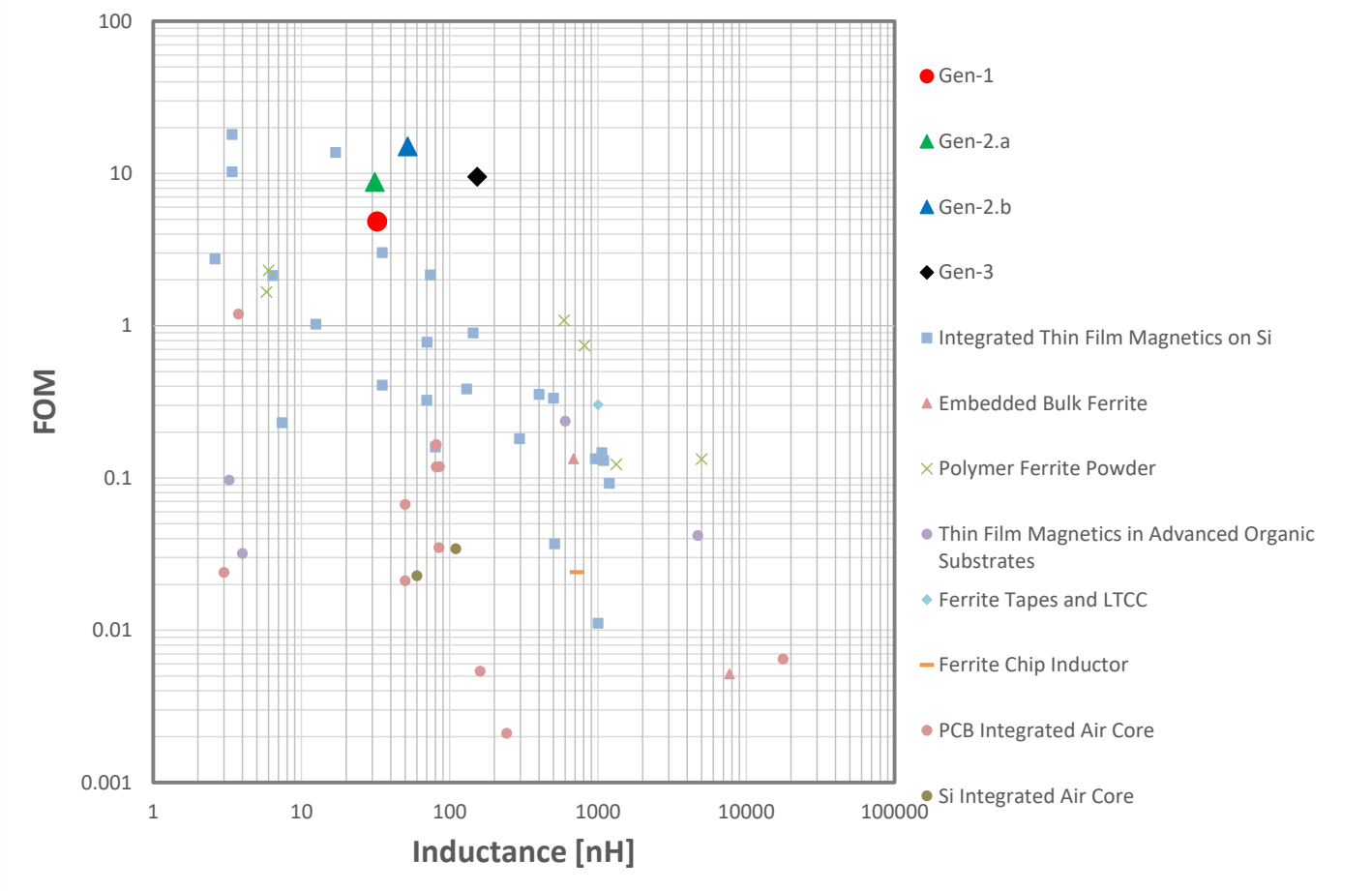

Figure 4.41: FOM vs Inductance of Gen-1, Gen-2, & Gen-3 devices compared to PwrSiP & PwrSoC applications found in literature. Note top right of graph is desired area for PwrSiP & PwrSoC applications. See table 2.1 for details.

4.6 Conclusion

This Chapter presented manufacture techniques for the embedding of released magnetic cores in advanced organic substrates, done so in order to realise Power Supply in Package applications which utilise integrated magnetic solutions. The use of integrated magnetics in PwrSiP applications has been shown to improve the electrical characteristics of the magnetic passive component used in the power supply module. The manufacturing techniques used to integrate the magnetic component into the PCB substrate were as follows: 1) A wirebond approach wherein the released magnetic core was affixed to an underlying PCB substrate with parallel copper traces and exposed pads. Wirebonds were then used to form electrical connections between the adjacent copper traces, hence forming a solenoidal inductor with integrated magnetic core; 2) A Flip-Chip method which sandwiched the released magnetic core between two adjacent PCBs and then used a solder reflow process to form the electrical connections between the two PCBs, and binding the magnetic within; 3) In collaboration with AT&S released magnetic cores were fully embedded within the PCB stack. The key findings of our work are presented below.

In section 4.2 the Gen-1 wirebond inductor was presented. The successful fabrication of the functioning Gen-1 inductor proved the concept of releasable thin film magnetics for PwrSiP applications. Thus, the issue of direct de-

position of the magnetic core on the PCB substrate (discussed in detail in Chapters 3 & 5) are addressed by utilising Si Fabrication of the magnetic core with an integrated polymer release layer allowing the core to be liberated from the Si substrate and then incorporated into package. However, the Gen-1 inductor suffered from poor L/R_{dc} ratios, Q-Factors, and the hybrid FOM. And so, it was ill suited to be the magnetic passive in a DC-DC power converter in package.

In Section 4.3 the novel Gen-2 Flip-Chip inductor with integrated magnetic core was presented. The Gen-2 inductor was able to achieve a much lower R_{dc} value than Gen-1 counterpart. The much reduced R_{dc} of the Gen-2 device was a result of the net 140 μm thick copper used in the device. This resulted in a 9 fold improvement in the L/R_{dc} ratio, a 5 fold increase in Q-Factor, and a 3 fold increase in the hybrid FOM. Thus, the Gen-2 inductor could be used as the magnetic passive in a PwrSiP application.

However, the use of solder balls as the interconnection between adjacent PCBs increases the R_{dc} and parasitic capacitances of the manufactured device. Such parasitics and higher R_{dc} ultimately limit the frequency and current handling abilities of the inductor. Therefore, it is desirable to manufacture an integrated magnetic inductor wherein the magnetic core is fully embedded in the prepreg stack. In Section 4.4 the Gen-3 inductor was presented. This inductor saw the successful embedding of a released multilayer

magnetic cores in the prepreg stack. Initial challenges of severe outgassing resulting in delaminations of the PCB stack were redressed through judicious choice of the polymers used in the fabrication of the released magnetic cores. Further issues of delaminations due to Coefficient of Thermal Expansion mismatches were fixed by spin coating on a protective PI layer on the released magnetic core. Note the core already had a PI layer underneath it as a result of the release process.

Finally, in section 4.5 the three generations of inductor structures were compared against the existing state of the art. The Gen-2 and Gen-3 inductors were found to be at the leading edge of magnetic passive technologies. Thus proving that released thin film magnetics can be integrated into package and used as the magnetic passive for PwrSiP applications.

Bibliography

[1] S. Kulkarni, D. Li, D. Jordan, N. Wang, and C. Ó. Mathúna, "Pcb embedded bondwire inductors with discrete thin-film magnetic core for power supply in package," *IEEE Journal of Emerging and Selected Topics in Power Electronics*, vol. 6, no. 2, pp. 614–620, 2018.

[2] C. Ó. Mathúna, N. Wang, S. Kulkarni, and S. Roy, "Review of integrated magnetics for power supply on chip (pwrsoc)," *IEEE Transactions on Power Electronics*, vol. 27, no. 11, pp. 4799–4816, 2012.

[3] M. Ludwig, M. Duffy, T. O'Donnell, P. McCloskey, and S. C. Ó. Mathùna, "Pcb integrated inductors for low power dc/dc converter," *IEEE Transactions on Power Electronics*, vol. 18, no. 4, pp. 937–945, 2003.

[4] M. Wang, J. Li, K. Ngo, and H. Xie, "Silicon molding techniques for integrated power mems inductors," *Sensors and Actuators A: Physical*, vol. 166, no. 1, pp. 157–163, 2011.

[5] C. Marxgut, J. Muhlethaler, F. Krismer, and J. W. Kolar, "Multiobjec-

tive optimization of ultraflat magnetic components with pcb-integrated core," *IEEE Transactions on Power Electronics*, vol. 28, no. 7, pp. 3591–3602, 2012.

[6] H. Jia, J. Lu, X. Wang, K. Padmanabhan, and Z. J. Shen, "Integration of a monolithic buck converter power ic and bondwire inductors with ferrite epoxy glob cores," *IEEE transactions on Power Electronics*, vol. 26, no. 6, pp. 1627–1630, 2010.

[7] Z. J. Shen, J. Lu, X. Cheng, H. ngwei Jia, *et al.*, "On-chip bondwire inductor with ferrite-epoxy coating: A cost-effective approach to realize power systems on chip," in *2007 IEEE Power Electronics Specialists Conference*, pp. 1599–1604, IEEE, 2007.

[8] J. Lu, H. Jia, A. Arias, X. Gong, and Z. J. Shen, "On-chip bondwire magnetics with ferrite-epoxy glob coating for power systems on chip.," *International Journal of Power Management Electronics*, 2008.

[9] R. G. Lyons, *Understanding digital signal processing, 3/E*. Pearson Education India, 2004.

[10] D. Jordan, G. Wei, L. Ye, D. Lordan, P. Podder, A. Masood, K. Rodgers, C. O'Mathuna, and P. McCloskey, "High q-factor pcb embedded flip-chip inductors with multi-layer cztb magnetic sheet for power supply in package (pwrsip)," *IEEE Journal of Emerging and Selected Topics in Power Electronics*, pp. 1–1, 2020.

[11] A. Masood, P. McCloskey, C. Ó. Mathúna, and S. Kulkarni, "Co-based amorphous thin films on silicon with soft magnetic properties," *AIP Advances*, vol. 8, no. 5, p. 056109, 2018.

[12] D. W. Lee, K.-P. Hwang, and S. X. Wang, "Fabrication and analysis of high-performance integrated solenoid inductor with magnetic core," *IEEE Transactions on Magnetics*, vol. 44, no. 11, pp. 4089–4095, 2008.

[13] J. M. Coey, *Magnetism and magnetic materials*. Cambridge university press, 2010.

[14] D. Hou, F. C. Lee, and Q. Li, "Very high frequency ivr for small portable electronics with high-current multiphase 3-d integrated magnetics," *IEEE Transactions on Power Electronics*, vol. 32, no. 11, pp. 8705–8717, 2016.

[15] J. Qiu, D. V. Harburg, and C. R. Sullivan, "A toroidal power inductor using radial-anisotropy thin-film magnetic material based on a hybrid fabrication process," in *2013 Twenty-Eighth Annual IEEE Applied Power Electronics Conference and Exposition (APEC)*, pp. 1660–1667, IEEE, 2013.

[16] J. Kim, M. Kim, J.-K. Kim, F. Herrault, and M. G. Allen, "Anisotropic nanolaminated conife cores integrated into microinductors for high-frequency dc–dc power conversion," *Journal of Physics D: Applied Physics*, vol. 48, no. 46, p. 462001, 2015.

[17] P. R. Morrow, C.-M. Park, H. W. Koertzen, and J. T. DiBene, "Design and fabrication of on-chip coupled inductors integrated with magnetic material for voltage regulators," *IEEE Transactions on Magnetics*, vol. 47, no. 6, pp. 1678–1686, 2011.

Chapter 5

Numeric & Analytic Analysis of Magnetic Thin Films

5.1 Introduction

This chapter of the thesis pertains to the numeric and analytic models that were developed in order to characterise, and better understand, the experimental observations reported in Chapter 3. Such understanding is pertinent to improve the magnetic thin films performance in terms of being a suitable material for Power Supply in Package (PwrSiP) applications. Hence, the purpose of this section is to identify the challenges facing the integration of magnetic thin films and how those challenges manifest themselves in degraded material performance.

The structure of this chapter is as follows: In Section 5.2 the magnetisation dynamics of magnetic thin films were investigated using MicroMagnetic modelling tools. Initially the Object Orientated MicroMagnetic Framework (OOMMF)[1] was used to investigate the magnetisation dynamics of various anisotropy distributions within the magnetic thin film.

However, it was found that due to the numeric difficulty of the problem such Central Processing Unit (CPU) based MicroMagnetic simulators are unable to solve large magnetic systems of real world dimensions e.g., $4mm \times 4mm \times 1\mu m$, within a reasonable timeframe. Hence, there was a need to develop a MicroMagnetic modelling tool that utilised the superior numerical abilities of modern Graphics Processing Unit (GPU)s for performing the magnetic calculations. A GPU simulator was written in C++ and used the Object Oriented Programming (OOP) paradigm. This approach allowed the creation of magnetic objects which store the base magnetic properties. Thus, the complex magnetic system comprising N magnetic objects could be modelled by numeric methods. It was hoped that this approach could later be used to model the effect of surface roughness on the magnetisation dynamics of the thin films.

In Section 5.3 the effect of the surface roughness of the underlying PCB substrate, on which the magnetic thin film is being deposited, is treated using Brown's [2] continuous diffusion of magnetic spins model [3]. Brown's

continuous diffusion model was originally developed in order to describe the influence of a thermal heat bath on the magnetisation dynamics of an ensemble of single domain magnetic particles. In this work Brown's model for thermal noise is used to treat the issue of surface roughness on the magnetisation dynamics of the magnetic thin film. Such an approach is valid as both the thermal, and surface roughness, noise share the exact same statistical properties i.e., both are sources of Additive White Gaussian Noise (AWGN). Hence, the complex problem of modelling a completely deterministic system, whose dynamics are governed by the Landau Lifshitz Gilbert (LLG) equation for multiple interacting magnetic spins, is reduced into a stochastic one. This simplification is achieved by transforming the LLG equation into a magnetic Langevin Equation [4].

In Section 5.4 the thickness dependence of the dynamic magnetic susceptibility of the magnetic thin films is investigated using Brown's model. The dependence of the dynamic magnetic susceptibility is of critical importance to magnetic thin films used in DC-DC power converters. It is well reported in the literature that the thickness of the film is limited by the skin depth. However, it was found that after a certain critical thickness, which is much less than that limited by the eddy currents, there is a breakdown in the uniaxial anisotropy within the film. This breakdown of axial symmetry results in dynamic coupling between the longitudinal and transverse magnetic susceptibility, and so, results in a thickness dependent loss in the magnetic thin

film. Hence for highly efficient PwrSiP applications, the limiting factor of the thin film's thickness is not that which is determined by the eddy currents, rather it should be that thickness at which point it is no longer possible to induce uniaxial anisotropy within the film.

Finally, conclusions of the Chapter are provided in Section 5.5.

5.2 A GPU Accelerated MicroMagnetic Simulator for Modelling Thin Film Magnetic Alloy Systems

This section has been published in the *Journal of Magnetism and Magnetic Materials* ref [5].

This section demonstrates an object orientated GPU accelerated MicroMagnetic simulator designed to model the material characteristics of complex magnetic alloy systems. The GPU simulator was written in C++ and used object orientated programming to create a class that stores the magnetic information required to solve the LLG equation for a distribution of magnetic objects. Each magnetic object can be assigned individual properties based on the alloy distribution of interest. The simulator was verified against standard problem 4 of the Micromagnetic Modelling Activity Group (μmag) [6].

Standard problem 4 is chosen as it provides a benchmark for the modelling tools ability to accurately predict the magnetisation dynamics of a 500nm $\times$ 125nm $\times$ 3nm Permalloy thin film.

This MicroMagnetic simulator is implemented and deployed on the GPU using NVIDIA's highly optimised Compute Unified Device Architecture (CUDA) libraries [7]. The use of the CUDA libraries both reduces the complexity of the C++ code, and improves performance by fully utilising the NVIDIA GPU architecture. Furthermore, as the physical architecture of the NVIDIA GPUs improve (see subsection 5.2.3), these libraries are updated and further optimised. The main drawback of using the CUDA libraries is that the MicroMagnetic simulator can only be implemented on an NVIDIA GPU. Cross-platform GPU MicroMagnetic simulators can written using C++ AMP libraries [8], or OpenCL, allowing the simulator to be implemented on all GPU architectures. However, they are not as optimised to any particular GPU, and code that cannot be executed on the GPU is executed on the CPU instead – increasing the simulation run-time.

The structure of this Section is as follows: Subsection 5.2.1 provides an overview of the C++ software architecture used to create the MicroMagnetic simulator; Subsection 5.2.2 provides the theoretical background on MicroMagnetics; Subsection 5.2.3 pertains to modern GPU architecture and provides a comparison between readily available GPUs; In Section 5.2.4 the

simulator is validated against μmag standard problem 4; and finally conclusions of this Section are given in Subsection 5.2.5.

5.2.1 Software Architecture

The C++ MicroMagnetic simulator is built using the programming paradigm of OOP. The use of OOP allows the creation of abstract data structures which reflect the characteristics of a particular object [9]. Furthermore, complex problems can be decomposed into discrete, simpler, components which are easier to solve. Based on this, we may therefore consider the complex problem of magnetic alloy systems with various material compositions and phases as being comprised of a discrete, simpler, magnetic object. The salient feature of OOP is that objects can have functions, or "methods", which can be called outside of the object to modify their internal data fields. The importance of this being that without such methods the data stored within the object cannot be externally accessed.

In this work a magnetic object is created to represent a singular magnetic moment with the following data fields: 1) a position vector of where the magnetic moment is in the vector space; 2) the orientation of the magnetic moment; 3) the applied field acting on the magnetic moment; 4) the orientation of the anisotropy; 5) the anisotropy energy associated with the magnetic moment; 6) the exchange stiffness constant; and 7) the magnetisation saturation. Note properties 5 – 7 are intrinsic to the magnetic material being

simulated, and as such, are contained within a class object called "Magnetic Material". The data structure of the magnetic object is shown in Figure 5.1.

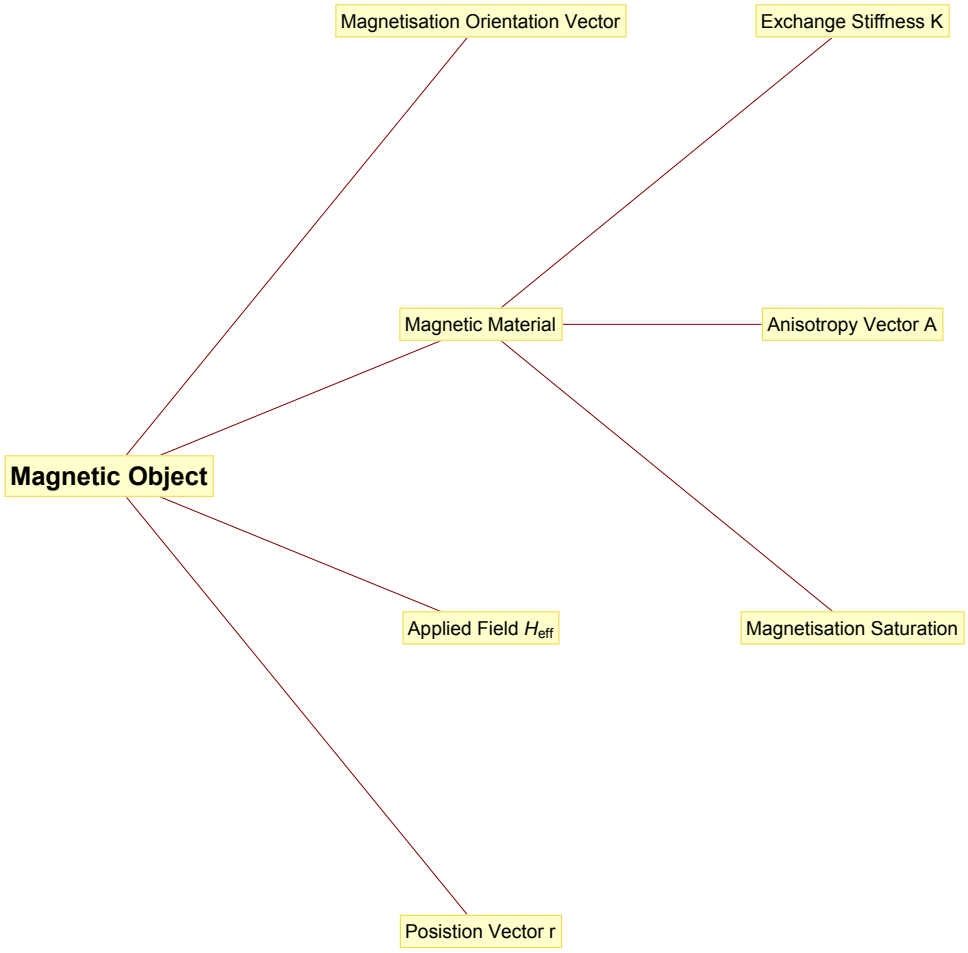

Figure 5.1: Class structure of Magnetic Object. Note "Magnetic Material" is a child class used to store the intrinsic magnetic properties of a material.

The C++ simulator uses a dynamic pointer array to store the N magnetic objects required to describe the magnetic alloy system. The magnetic objects are initially instantiated using the default (NULL) constructor declared in the magnetic object class. The desired geometry of the magnetic system being simulated is achieved by assigning the position vectors of the individual magnetic elements appropriate values. For example, a 2D thin film can be simulated by mapping $[x_i, y_i, 0]$ onto the position vectors of each of the magnetic objects contained in the dynamic pointer array. Here x_i and y_i are the i^{th} elements of the linespace that spans $\mathrm{x_{min}}$ to $\mathrm{x_{max}}$ and $\mathrm{y_{min}}$ to $\mathrm{y_{max}}$, respectively. Furthermore, the morphology and phase of the material can be represented by mapping a non-uniform displacement distribution to the position vectors of the magnetic objects. This is illustrated in Figure 5.2

Various anisotropy, phase, and alloy compistions in X, Y, Z can then be simulated by appropriately assigning the magnetic properties of the ith, jth, kth elements of the dynamic pointer array (note, the array is a 1D structure so an indexing function is required which transforms the i, j, k coordinates to an index position). For example, the Cobalt based alloy system $Co_{80}\gamma_{20}$ could be investigated by assigning 80% of the magnetic objects with the material characteristics of cobalt, and 20% with the properties of γ. More complex material structures that contain physical grains can also be simulated by creating a function that appropriately groups the magnetic objects

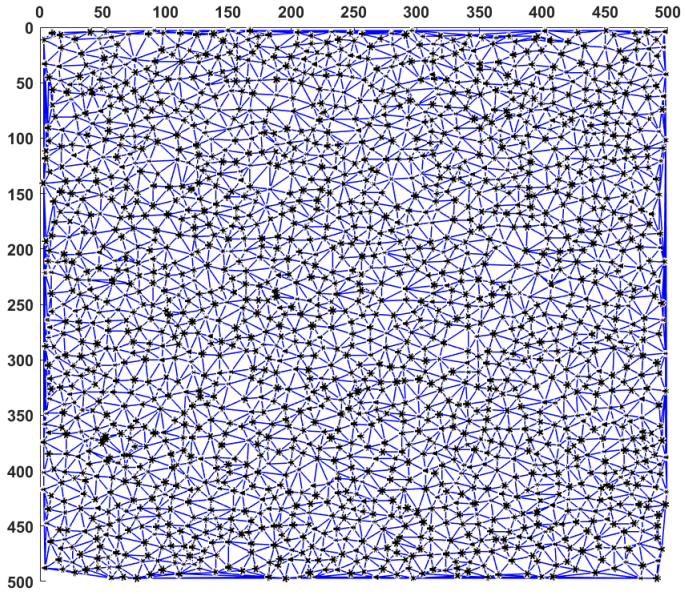

Figure 5.2: Illustration of Complex Magnetic Alloy System. Each black dots represent a Magnetic Object with parameters shown in Figure 5.1. Blue lines represent the distance between neighbouring magnetic objects.

in the dynamic pointer array and then maps the magnetic properties of the grain onto that group.

After all the magnetic objects in the dynamic pointer array have been assigned appropriate values, their data fields are then copied onto to the GPU. Hence, the initial setup of the MicroMagnetic simulation is performed on the CPU and the GPU is used to perform the numeric computations.

5.2.2 MicroMagnetic Computation

The magnetization dynamics of an ensemble of magnetic moments are governed by the Landau-Lifshitz-Gilbert (LLG) equation [2], or gyromagnetic equation, which simply describes the precessional nature of a magnetic moment around an effective field. The LLG equation is given by Eq. 5.2.1

$$\frac{d}{dt}\boldsymbol{M} = -\gamma \boldsymbol{M} \times \boldsymbol{H}_{eff} + \frac{\alpha\gamma}{M_s}\boldsymbol{M} \times (\boldsymbol{M} \times \boldsymbol{H}_{eff}) \tag{5.2.1}$$

Here α is Gilbert's damping coefficient; γ is the gyromagnetic ratio; M_s is the magnetisation saturation; and $\boldsymbol{H}_{eff}$ is the internal effective field acting on the system of magnetic moments. Note, the first term on the right hand side (RHS) of the LLG equation causes the magnetic moment to precess indefinitely around the effective field whilst the second term is a damping term causing the magnetic moment to align with the effective field. The effects of the damping and the effective field on the magnetisation dynamics are

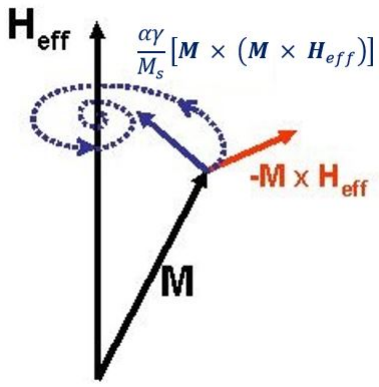

Figure 5.3: Illustration of LLG equation. Image modified from ("https://en.wikipedia.org/wiki/Landau%E2%80%93Lifshitz%E2%80%93Gilbert_equation")

illustrated in Figure 5.3.

The effective field is comprised of several components: 1) the external magnetic field acting on the system $\boldsymbol{H}_{ext}$; 2) the demagnetization field $\boldsymbol{H}_{d}$; 3) the exchange field between neighboring magnetic elements $\boldsymbol{H}_{exc}$; and 4) an anisotropy field $\boldsymbol{H}_{an}$. The expression for $\boldsymbol{H}_{eff}$ is given by Eq. 2 [10].

$$\boldsymbol{H}_{eff} = \boldsymbol{H}_{ext} + \boldsymbol{H}_{d} + \boldsymbol{H}_{exc} + \boldsymbol{H}_{an} = -\nabla_{\boldsymbol{M}} V \tag{5.2.2}$$

It is evident from Eq. 5.2.2 and its realisation in Fig. 5.3 that the magnetic moments precess within metastable energy minima that are shaped by the various applied fields. This is the canonical relationship that links force, to fields, to gradients of potential structures. By way of example consider the Lorentz force in electrostatics, that the force acting on a charge is the product

of that charge and an electric field to which it is subject.

$$\boldsymbol{F}_q = q\boldsymbol{E} \tag{5.2.3}$$

$$m\frac{\boldsymbol{v}_q}{dt} = q\boldsymbol{E} \tag{5.2.4}$$

Here m is the mass of the charge, $\boldsymbol{v}_q$ is the velocity of the charge, and q is simply the charge in Coulombs. Note, the nature of $\boldsymbol{E}$ can be somewhat complex. In a two particle system it is simply Eq. 5.2.5, and the force becomes Eq. 5.2.6.

$$\boldsymbol{E}_a = \frac{q_a}{4\pi\epsilon_0\epsilon_r r^2} \tag{5.2.5}$$

$$\boldsymbol{F}_{a,b} = \frac{q_a q_b}{4\pi\epsilon_0\epsilon_r r_{a,b}^2} \qquad = q_a\boldsymbol{E}_b \tag{5.2.6}$$

In a more complex system it is necessary to describe the $\boldsymbol{E}$ field in terms of Gauss's divergence law. Further, on expressing the vector field in terms of

the gradient of the scalar field, the motion of the particle becomes

$$\frac{\boldsymbol{v}_q}{dt} = \frac{q}{m}\boldsymbol{E} \tag{5.2.7}$$

$$= -\frac{q}{m}\nabla\phi \tag{5.2.8}$$

$$\nabla \cdot \boldsymbol{E} = \frac{\rho}{\epsilon} \tag{5.2.9}$$

$$\nabla \cdot (-\nabla\phi) = \frac{\rho}{\epsilon} \tag{5.2.10}$$

$$\nabla^2\phi = \frac{\rho}{\epsilon} \tag{5.2.11}$$

$$\nabla\phi = \int_V \frac{\rho}{\epsilon} dV \tag{5.2.12}$$

$$\frac{\boldsymbol{v}_q}{dt} = \frac{q}{m}\int_V \frac{\rho}{\epsilon} dV \tag{5.2.13}$$

, and so the motion of the charge is entirely governed by the charge distribution at time t. Note Eq. 5.2.13 is entirely analogues to the LLG Eq. 5.2.1. However, where Eq. 5.2.13 relates to the dynamic motion of a particle, the LLG equation relates to the dynamic motion of magnetic spins.

The next subsections pertain to the calculations of the components of the effective field and to the time evolver used to solve the LLG equation.

Demagnetisation Field

The demagnetisation field arises from the long range dipole-dipole interaction of the magnetic moments attempting to minimise the internal energy of the system [10]. Calculation of the demagnetisation field is by far the most

computationally intense part of the magnetic simulation having a numeric complexity of order $O[N^2]$, where N is the number of magnetic moments. Formally the demagnetisation field can be calculated from Eq. 5.2.14.

$$\boldsymbol{H}_d = -\frac{1}{4\pi}\int_V \nabla\nabla\frac{1}{|\boldsymbol{r}-\boldsymbol{r}'|}\cdot\boldsymbol{M}(\boldsymbol{r}')d\boldsymbol{r}' \tag{5.2.14}$$

It is clear from Eq. 5.2.14 that the demagnetisation field comprises elements from all the magnetic moments. Hence evaluation of the demagnetisation field can result in intractably long run times for larger magnetic systems. In order to reduce the computational hardness of this problem we express the demagnetisation field as the product of the time independent demagnetisation tensor and the time dependent magnetisation, see Eq. 5.2.15.

$$\boldsymbol{H}_{d,i} = -\nu_{i,j}\boldsymbol{M}_j \tag{5.2.15}$$

$$i,j = x,y,z$$

Here ν is the demagnetisation tensor. As ν is time independent it only need be evaluated once using the analytic formulae given in [11]. The benefit of this approach is that the Fast Fourier Transform (FFT) can be performed on ν and $\boldsymbol{M}$, yielding $\tilde{\nu}$ and $\tilde{\boldsymbol{M}}$, and the demagnetisation field determined by taking the inverse FFT of the product of $\tilde{\nu}$ and $\tilde{\boldsymbol{M}}$ [12] (see Eq. 5.2.16). This reduces the numeric hardness of the problem from $O[N^2]$ to $O[N\log N]$ [13]. However, the main drawback of the FFT approach is that zero padding

[14] must be used on the input data in order to avoid issues of circular convolution arising from non-periodic boundary conditions [15]. This places a considerable memory overhead on the GPU evaluating the FFT and reduces the size of the problem that can be simulated.

$$\boldsymbol{H}_{d,i} = FFT^{-1}[\tilde{\nu}_i \cdot \tilde{M}_i] \tag{5.2.16}$$

$$i = x, y, z$$

Exchange Field

The exchange field in this simulator is determined by solving Eq. 5.2.17 using a 6 nearest neighbours scheme outlined in [16] with Neumann boundary conditions. The use of Neumann boundary conditions effectively replace the non-existent magnetic neighbours at the boundary with the centre value.

$$H_{exc,i} = \frac{2A_i}{\mu_0 M_{s,i}} \nabla^2 M_i \tag{5.2.17}$$

Here A is the exchange stiffness of the magnetic object. Note in Eq. 5.2.17 the values of the exchange stiffness and the magnetisation saturation depend on the particular magnetic object. The effect of different exchange stiffness between neighbouring magnetic objects is addressed using Eq. 5.2.18.

$$A_{i,j} = \frac{2A_i A_j}{A_i + A_j} \tag{5.2.18}$$

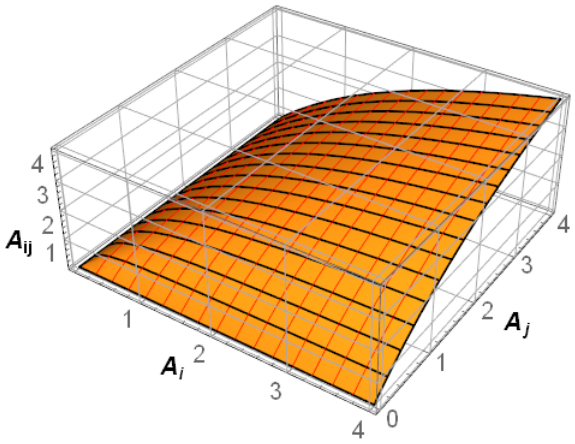

Figure 5.4: Illustration of Effective Exchange Stiffness between neighbouring magnetic objects.

This expression for the effective stiffness between neighbouring magnetic objects is used as it satisfies the following properties [16]:

$$A_{i,j} = A_i = A_j \qquad iff \qquad A_i = A_j \tag{5.2.19}$$

$$\lim_{A_{i\to 0} \| A_{j\to 0}} A_{i,j} = 0 \tag{5.2.20}$$

The exact interpolation of the exchange stiffness between neighbouring magnetic objects is illustrated in Figure 5.4. The interpolation of the effective exchange stiffness enables the simulation of magnetic structures with more than one magnetic element. Hence it is crucial for simulating magnetic alloys.

The calculation of the exchange field reduces to a four nearest neighbours

scheme when a 2D structure is being simulated.

Anisotropy Field

In magnetisation dynamics the anisotropy field describes how the magnetic moment will respond to an external field. In the case of an isotropic material the magnetic response is independent to the direction of the applied field. However, in crystalline magnetic materials, or materials with an induced anisotropy, there is a preferred orientation of magnetisation. If the anisotropy arises from a lattice structure it is referred to as *magnetocrystalline anisotropy*. The effect of magnetic anisotropy on the internal energyscape is given by Eq. 5.2.21.

$$\boldsymbol{H}_{an,i} = \frac{2\boldsymbol{K}_i}{\mu_0 M_{s,i}^2}\boldsymbol{M}_i \tag{5.2.21}$$

Here $\boldsymbol{K}_i$ is the anisotropy vector constant of the i^{th} magnetic object. Note uniaxial, bia-axial, and cubic anisotropies can be achieved by appropriately setting the K vector in the problem setup.

Time Evolver

Euler's forward method is used to solve for a finite time increment the magnetisation dynamics governed by the LLG equation (Eq. 5.2.1). Euler's method approximates the magnetisation state at a time $t + \Delta t$ from the magnetisation state at time t (see Eq. 5.2.22)

$$\boldsymbol{M}(t + \Delta t) = \boldsymbol{M}(t) + \Delta t \frac{d}{dt}\boldsymbol{M}(t) \tag{5.2.22}$$

Note, Euler's method is a very powerful method of numerically solving Ordinary Differential Equations. The accuracy of this method is completely determined by the finite time step and rate of change of the magnetisation. In order to accurately approximate the future magnetisation state, the time step must be much smaller than the rate of change of the magnetisation. Thus there is a trade-off using Euler's forward method between accuracy and simulation runtime. More complex time solvers use adaptive time steps to solve the LLG equation (Eq. 5.2.1).

5.2.3 GPU Architecture

This subsection gives an outline of the recent advances made in the computational capabilities of GPUs in the last five years. The increase in the computational capabilities of GPUs has enabled the creation of MicroMagnetic simulators which can perform numeric calculations up to 200 times faster than their CPU counterparts [17]. Hence, MicroMagnetic simulations that were once infeasible can now be investigated.

Traditionally the biggest bottleneck for GPU based MicroMagnetic simulations is the amount of on board memory available to the simulator. Older GPU graphics cards were limited to $1 - 3$ GB of on board memory. To overcome this memory limitation, data could be stored in the CPU memory and then transferred to the GPU for the computation. Once the computation was completed by the GPU, the resultant data was offloaded back to the CPU

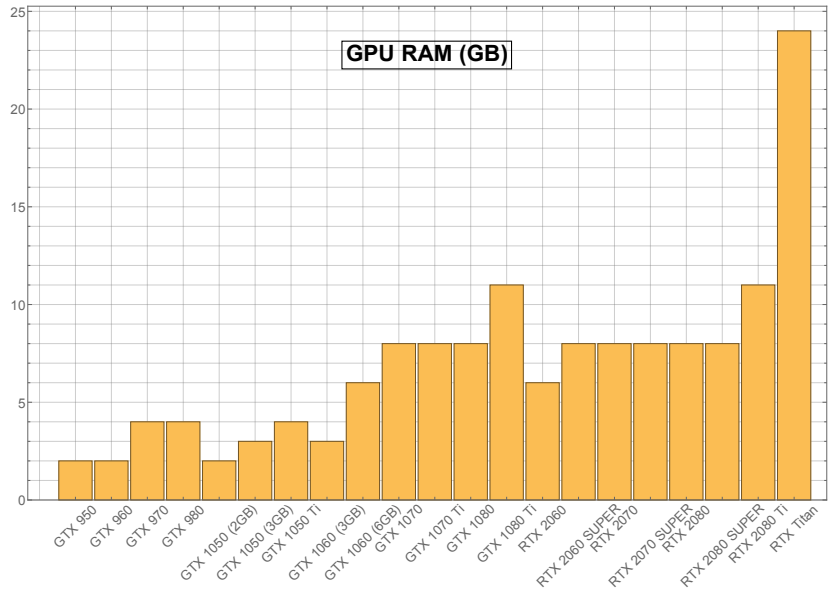

Figure 5.5: On board RAM of NVIDIA graphics cards.

memory. The swapping of data back and forth between the CPU and GPU required careful optimisation of memory access and transfer in order to scale GPU based MicroMagnetic simulators being performed on a GPU with limited memory resources [18–20]. However this is not an ideal solution to the problem as there is a high latency from transferring data between the CPU and GPU. The data bandwidth between the CPU and the GPU is limited by the bandwidth of the PCI/PCI-E port on the motherboard. There are algorithms that can be used to improve the data transfer rate [21]. However, the best practice still remains to minimise the number of transfers between the CPU to GPU and vice-versa [22]. The problem of limited GPU memory has been largely addressed by the growing amount of on board RAM available to modern GPUs, see Figure 5.5.

The majority of NVIDIA GPU models now have at least 8GB of on board RAM, with the RTX Titan having 24GB of on board RAM. Hence, modern GPUs are capable of solving very large magnetic systems due to their improved on board memory storage.

The massive improvement of the computational capabilities of GPUs has resulted from the increased number of CUDA cores on the GPU and the faster data transfer rate between them. Note, each CUDA core is analogous to a single core of a CPU. Where a single CPU can have between 2 – 16 cores, GPUs can have over 1000 CUDA cores (see Figure 5.6(Upper)). The CUDA cores can be used in parallel to simultaneously solve part of computation. Hence, the workload is shared by the number of CUDA cores on the GPU.

Furthermore, the data transfer rate between the CUDA cores (see Figure 5.6(Lower)) is significantly faster than that of the PCI/PCI-E port. Hence, there is less of a latency issue arising from the transferal of data between the CUDA cores. The larger number of CUDA cores and the improved data bandwidth has resulted in GPUs being able to perform between $10^{12} - 10^{13}$ single precision Floating Point Operations per Second (FLOPS). This is shown in Figure 5.7.

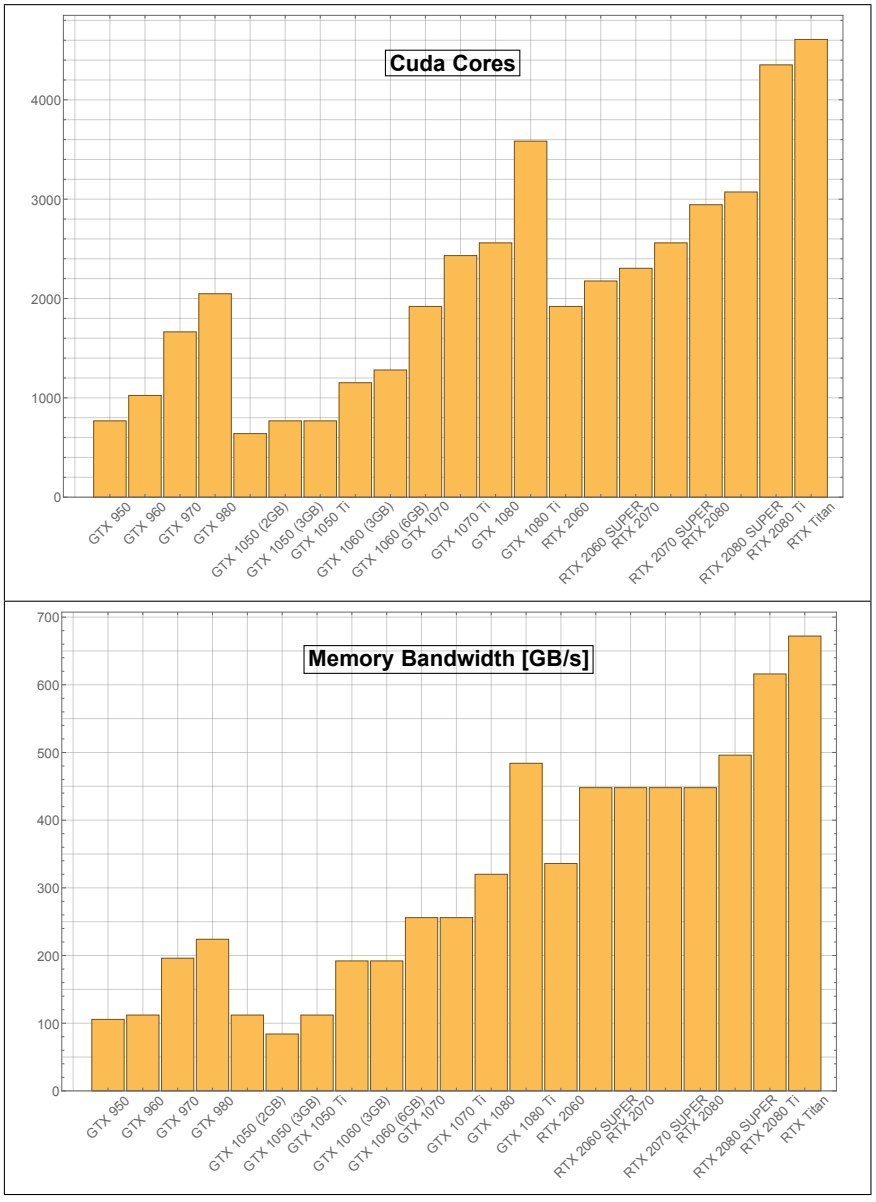

Figure 5.6: (Upper) Number of CUDA core of NVIDIA graphics cards. (Lower) Memory bandwidth of NVIDIA graphics cards.

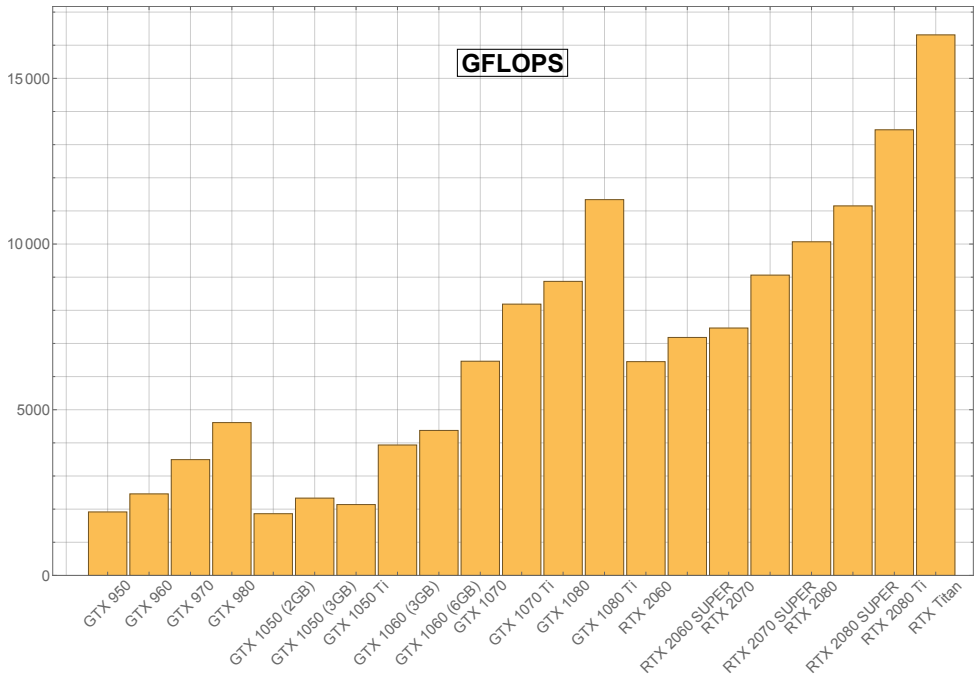

Figure 5.7: Single precision Giga FLOPS of NVIDIA GPUs (higher better)

The improved memory capabilities and numerical power of modern GPUs can be used to solve complex alloy systems that CPU based simulators would not be able solve within a reasonable timeframe. As GPU architectural development is linked to the entertainment industry, the trend of increased on board memory and improved Giga FLOPS (GFLOPS) is likely to continue.

5.2.4 Simulation Results

The GPU MicroMagnetic simulator was then verified against μmag Standard problem #4 [23], which focuses on dynamic aspects of MicroMagnetic computations. The 500nm $\times$ 125nm $\times$ 3nm Permalloy thin film inμmag standard problem 4 was realised by creating 166 $\times$ 42 $\times$ 1 magnetic objects which are separated by 3nm. Each magnetic object is assigned the magnetic properties of Permalloy, shown below.

$$A_{exc} = 1.3 \times 10^{-11} \left[\frac{J}{m}\right] \tag{5.2.23}$$

$$M_{sat} = 8 \times 10^{5} \left[\frac{A}{m}\right] \tag{5.2.24}$$

$$K = 0 \tag{5.2.25}$$

In standard problem 4 the thin film is first brought to an equilibrium state through the application of an external field along the $[1, 1, 1]$ axis until the material has saturated, and then gradually diminishing that field to zero.

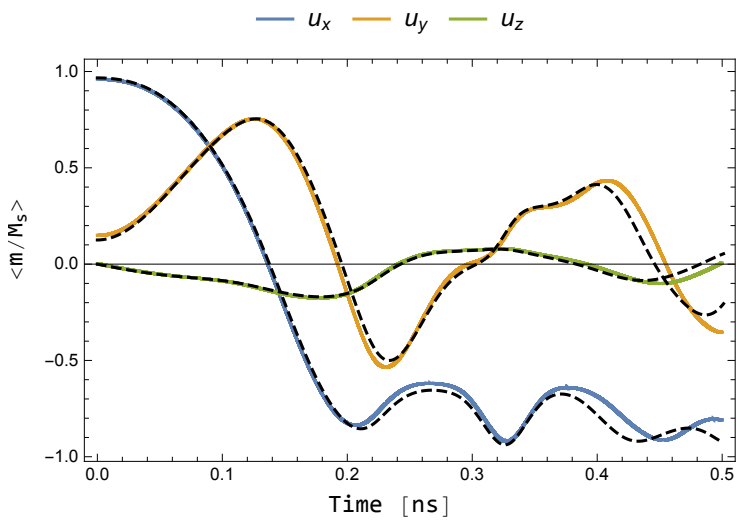

Figure 5.8: Average Magnetisation vs time of standard problem 4. GPU simulator results as solid lines. OOMMF results as dashed lines.

After the equilibrium state has been achieved a small reversal field of magnitude 25 mT is applied 170° counter clockwise from the saturation direction $[1, 0, 0]$. This field is sufficient to cause reversal of the magnetisation in the thin film and the system is allowed to evolve until the new equilibrium position has been attained. The results of the GPU MicroMagnetic simulator are plotted in Figure 5.8 along with the predicted behaviour from OOMMF.

The GPU MicroMagnetic simulator results strongly match those predicted by OOMMF. Therefore the GPU MicroMagnetic simulator is verified and can be used to solve other magnetic systems. Note, the magnetisation reversal dynamics involves many bodies and is highly nonlinear. Therefore the

discrepancy between the two simulators arises from the marginal difference in the initial conditions of the problem. It is clear from Figure 5.8 that the initial My values of the GPU simulator and OOMMF are not equal.

5.2.5 Conclusions

In this section we demonstrated an Object Oriented GPU MicroMagnetic simulator written in C++. The simulator is capable of modelling complex alloy systems comprising various material compositions by appropriately mapping the magnetic properties onto the magnetic objects. The dynamic prediction capabilities of the simulator are verified by solving μmag's standard problem 4 and comparing the GPU simulators results against OOMMF. There is an excellent match between the two simulators results for standard problem 4. The main tractability of the this GPU MicroMagnetic simulator is that it can solve the magnetisation dynamics for complicated alloy systems that traditional CPU based MicroMagnetic simulators would not be able to solve within a reasonable timeframe.

5.2.6 Postamble

Although the GPU simulator was able to reproduce the magnetisation dynamics of a magnetic thin film comporting with mumag standard problem 4, it remains a significant challenge to adapt this software to model the issue of surface roughness in thin film magnetics for PwrSiP applications. Recall

from chapter 3 that the effect of surface roughness on thin films was a major limiting factor to the efficacy of thin films used in PwrSiP applications. The main challenge being the adaptation of the demagnetisation tensor to handle an undetermined, non smooth, boundary in such a way as to allow us to still use the FFT in order to utilise the full computational power of the GPU. At its core the FFT is an extremely efficient algorithm for computing the Discrete Fourier Transform (DFT) (see Eq. 5.2.26).

$$X[m] = \sum_{n=0}^{N-1} x[n] e^{\frac{-j2\pi nm}{N}} \tag{5.2.26}$$

Whereas calculation of the DFT of the sequence $x[n]$ would require N^2 computations, calculation of the FFT of the sequence would require only $\frac{N}{2} log_2 N$. The FFT is able to achieve this remarkable decrease in computations by splitting the input sequence into even and odd components, and performing the DFT on each. Note, the FFT works best when N is an integer power of 2. It is for this reason that micromagnetic simulators work best when the dimensions of the problem are integer multiples of 2.

$$X[m] = \sum_{n=0}^{N/2-1} x[2n] e^{\frac{-j2\pi(2n)m}{N}} + \sum_{n=0}^{N/2-1} x[2n+1] e^{\frac{-j2\pi(2n+1)m}{M}} \tag{5.2.27}$$

A comparison of the number of calculations required by the DFT vs the FFT are shown in fig. 5.9. Calculation of the Demag Tensor could have been achieved by computing the dipole-dipole interaction for all of the magnetic

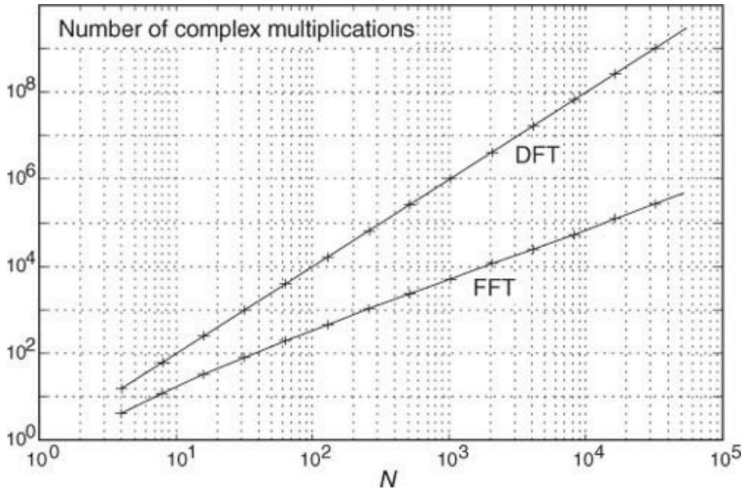

Figure 5.9: Number of computations required by DFT vs FFT [24].

elements in the system and deploying energy minimisation techniques. However, attempts at this resulted in extremely long simulation runtimes as N FFTs were required. Hence the number of numeric computations required went from $ON \log N \rightarrow ON^2 \log N$.

This issue is circumvented by accepting that the deterministic approach of having a system of equations with known initial and boundary conditions is insufficient to address the complex issue of surface roughness in the magnetisation dynamics of thin films. The key word here being *deterministic*. By accepting that the surface roughness causes stochastic effects in the magnetisation dynamics we can take the approach of using statistical mechanics to describe the complex ensemble behaviour in terms of averages. That is, we accept that there is a *stochastic* element to the magnetisation dynamics, and

we adjust our approach accordingly. The results of this new approach are presented in section 5.3.

5.3 Stochastic Magnetic Resonance of Absorption Effects of Surface Morphology in Thin Film Magnetics

This section was published in the *Journal of Magnetism and Magnetic Materials* [3].

The effect of surface roughness in thin film magnetics on magnetic susceptibility and Dynamic Magnetic Hysteresis (DMH) loops are investigated using Brown's continuous diffusion of magnetic spins model [2]. The magnetic relaxation time of the magnetic thin films are determined by regressing the two mode approximation for the magnetic susceptibility onto experimental data obtained for $Ni_{45}Fe_{55}$. This subsection shows a moderate linear correlation between the magnetic relaxation time and the Surface Roughness to Thickness Ratio (SRT). The area of the DMH loops and the non-linear dynamic magnetic susceptibility strongly depend on the magnetic relaxation time and the SRT of the films. The thin films exhibit a strong linear relationship between the coercivity and the SRT, along with a strong logarithmic dependence of the dynamic magnetic susceptibility on the SRT. In this Section we consider the effect of surface roughness on magnetic thin films using Brown's continuous diffusion of magnetic spins model.

The structure of this Section is as follows: Subsection 5.3.1 gives an overview of Brown's model for magnetic spins subject to AWGN; Subsection 5.3.2 provides details of the characterisation of the $Ni_{45}Fe_{55}$ thin films; Subsection 5.3.3 introduces the two mode approximation for magnetic susceptibility and links the magnetic relaxation time to the SRT; Subsection 5.3.4 pertains to the effect of the relaxation time on the DMH loops; and finally conclusions are provided in Section 5.3.5.

5.3.1 Stochastic Fluctuations in Magnetisation Dynamics

The magnetisation dynamics of an ensemble of magnetic spins coupled to a heat bath was considered by Brown [2] in 1963. Brown treated the effect of the bath on the magnetic spins by superimposing a rapidly fluctuating stochastic field onto the deterministic field acting on the magnetic system governed by Gilbert's equation. This is shown in Eq. 5.3.1.

$$\dot{\boldsymbol{M}}(t) = \gamma\{\boldsymbol{M}(t) \times [\boldsymbol{H}(t) + \boldsymbol{h}(t) - \eta\dot{\boldsymbol{M}}(t)]\} \tag{5.3.1}$$

Here $\boldsymbol{H}$ is the deterministic field given as the negative gradient of the internal energy landscape of the ensemble of magnetic particles ($-\frac{dV}{d\boldsymbol{M}}$), $\boldsymbol{h}$ is Brown's stochastic field, η is a damping coefficient driving the system to a dead state, and γ is the gyromagnetic ratio. The stochastic noise field has the following

statistical properties;

$$\overline{\boldsymbol{h}(t)} = 0 \tag{5.3.2}$$

$$\overline{\boldsymbol{h}(t)\boldsymbol{h}(t')} = D(\alpha)\delta(t - t') \tag{5.3.3}$$

with D being a diffusion coefficient related to the damping of the system. Property 5.3.2 states that the average contribution of the noise term to the ensemble is negligible. Property 5.3.3 states that the rapid fluctuation in the noise is independent of frequency, i.e. white noise. The main importance of property 5.3.3 is that the noise term is an ergodic process, and so, the time average of the system is equal to the ensemble average [25]. Combining properties 5.3.2 and 5.3.3 results in a noise term that is additive white Gaussian with zero mean. Now, by property 5.3.3, the damping of the system is related to the noise term viz Eqs. 5.3.4 and 5.3.5.

$$\int_0^\infty \overline{\boldsymbol{h}(t)\boldsymbol{h}(t')}dt' = \frac{1}{2}\int_{-\infty}^\infty \overline{\boldsymbol{h}(t)\boldsymbol{h}(t')}dt' \quad = \frac{D(\alpha)}{2}\int_{-\infty}^\infty \delta(t')dt' \tag{5.3.4}$$

$$D(\alpha) = 2\int_0^\infty \overline{\boldsymbol{h}(t)\boldsymbol{h}(t')}dt \tag{5.3.5}$$

Whence, the dissipative force of the system is being counteracted by the noise term (fluctuation dissipation theorem) [26]. The exact method of solving the diffusion term as a function of damping is given in [4]. Brown then derived a Fokker Planck Equation (FPE) for the evolution of the probability density function of the orientations of the magnetisation on a unit sphere [27], from

which he was able to calculate the magnetic relaxation time for an ensemble of magnetic spins with an induced uniaxial anisotropy.

In this work, the SRT of thin films is treated as a source of additive white Gaussian noise which creates a stochastic magnetic field through the demagnetisation tensor. As additive white Gaussian noise is ergodic, both the thermally induced noise, and the spatially induced noise, are mathematically identical. Thus we may use Brown's diffusion of magnetic spins subject to thermal fluctuations model, to model the effects of surface roughness in thin films.

5.3.2 Experimental Methods

1 μm - 2.6 μm $Ni_{45}Fe_{55}$ magnetic thin films were electrodeposited onto PCB substrates with various surface roughnesses. The height of the films and the surface roughness were measured using a Tencor Profilometer. The surface roughness of the PCB substrate and thin films were measured prior to, and after deposition of the magnetic thin film by performing a line scan on the surfaces and then calculating the deviation from the average height along the length of the scan. The small signal magnetic susceptibility of the films were measured using a wide band complex permeameter (Ryowa Electronics, Japan, Model PMM 9G) on 4mm $\times$ 4mm samples. The DC hysteresis loops of the films were measured using a BH loop tracer (SHB, MESA 200 HF at 10 Hz) on 2cm $\times$ 2cm samples.

5.3.3 Magnetic Susceptibility Effects

This subsection follows the exact mathematics outlined by Coffey et al. in [4] for thermal fluctuations in an ensemble of magnetic particles and applies it to the issue of surface roughness in thin films. The complex magnetic susceptibility of an ensemble of magnetic spins can be determined using linear response theory [28, 29]. The dissipative part of the frequency dependent magnetic susceptibility is related to the spectral density of the equilibrium ensemble average of the magnetic moments by fluctuation dissipation theorem [30]. Hence, the Wiener-Khinchin theorem [31] can be used to express the magnetic susceptibility in terms of an Autocorrelation Function (ACF) by taking the Fourier cosine transformation of the spectral density of the ensemble of magnetic moments.

$$\frac{\chi(\omega)}{\chi} = 1 - i\omega \int C(t) e^{-i\omega t} dt \tag{5.3.6}$$

Here C is the autocorrelation function. The ACF can then be expressed as the sum of an infinite set of decaying exponentials characterised by distinct eigenvalues λ_k of the magnetic system and their corresponding amplitudes a_k, formally given by:

$$C(t) = \sum_k a_k e^{-\lambda_k t}. \tag{5.3.7}$$

It is clear from Eq. 5.3.7 that the ACF comprises all of the decay modes of the magnetisation. In order to determine the magnetic response it is necessary

to consider what the initial decay of the ACF is, and what the longest lived decay mode of the ACF is. These two different timescales then characterise the low- and high-frequency behaviour of the imaginary part of the magnetic susceptibility. As the eigenvalues of the system are exponentially separated from each other, the two relaxation times are often dominated by a single decay mode characterised by the smallest non-vanishing eigenvalue of the system, λ_1.

$$\tau_{int} = \int C(t)dt \tag{5.3.8}$$

$$\approx \frac{a_1}{\lambda_1} \tag{5.3.9}$$

$$\tau_{eff} = -\frac{1}{\dot{C}(0)} \tag{5.3.10}$$

$$\approx (a_1\lambda_1)^{-1} \tag{5.3.11}$$

Hence the ACF, which typically would require all knowledge of the eigenvalues and their corresponding amplitudes of the ensemble of magnetic spins, can be approximated by two exponentials [4]. This is known as the two mode approximation, and is given in Eq. 5.3.12.

$$C(t) \approx \Gamma_1 e^{-t/\tau} + (1-\Gamma_1)e^{-t/\tau_w}. \tag{5.3.12}$$

Therefore, the dynamic magnetic susceptibility can be expressed as the sum of two Lorentzians, namely

$$\frac{\chi(\omega)}{\chi} \approx \frac{\Gamma_1}{1 + i\omega\tau} + \frac{1 - \Gamma_1}{1 + i\omega\tau_w}. \tag{5.3.13}$$

In Eq. 5.3.13 τ is the magnetic relaxation time, and the parameters Γ_1 and τ_w are determined in order to ensure the correct asymptotic behaviour of the magnetic susceptibility at low and high frequencies. They are given by Eqs. 5.3.14 - 5.3.15.

$$\Gamma_1 = \frac{\tau_{int}/\tau_{eff} - 1}{\tau_{int}/\tau - 2 + \tau_{eff}/\tau} \tag{5.3.14}$$

$$\tau_w = \frac{\tau_{int} - \tau}{1 - \tau_{eff}/\tau} \tag{5.3.15}$$

Both the integral relaxation time and the effective relaxation time can now calculated directly from the measured magnetic susceptibility data of the magnetic thin films using Eqs. 5.3.16 - 5.3.17.

$$\tau_{int} = \lim_{\omega \to 0} \frac{\chi_0 - \chi(\omega)}{i\omega\chi(\omega)} \tag{5.3.16}$$

$$\tau_{eff} = \lim_{\omega \to \infty} \frac{\chi_0}{i\omega\chi(\omega)} \tag{5.3.17}$$

The magnetic relaxation times of the thin films with various surface roughness to thickness ratios are then determined using Mathematica's [32] non-linear model fit function to regress Eq. 5.3.13 onto the measured magnetic

susceptibility data of the thin films. The results of the fitted two mode approximation are given in Figure 5.10. As can be seen from Figure 5.10, the two mode approximation accurately describes the thin films magnetic susceptibility response across the measured frequency spectrum. However, the low frequency noise on the measured susceptibility reduces our ability to accurately fit the two mode approximation to the frequency response of the thin films. In this work, moving average filters were used in order to reduce the influence of the low frequency noise on the fit.

Having regressed the two mode approximation onto the magnetic susceptibilities we correlate the magnetic relaxation times with the SRT of their corresponding thin films. There is a moderate linear correlation ($R^2 = 0.63$) between the SRT and the magnetic relaxation time of the thin film, cf Figure 5.11.

From Figure 5.11 it is clear that increasing the SRT results in a thin film with higher relaxation times and hence 'harder' magnetic properties. The deposition of a 'soft' thin film with nominal thickness is therefore limited by the surface condition of the substrate on which the film is being deposited. The degradation of the soft magnetic properties, as a result of the increased magnetic relaxation time, of the thin films with increased roughness are further illustrated in Figure 5.12. Here the coercivity and susceptibility of the thin films are plotted against the SRT with R^2 values of 0.9. There is a rapid

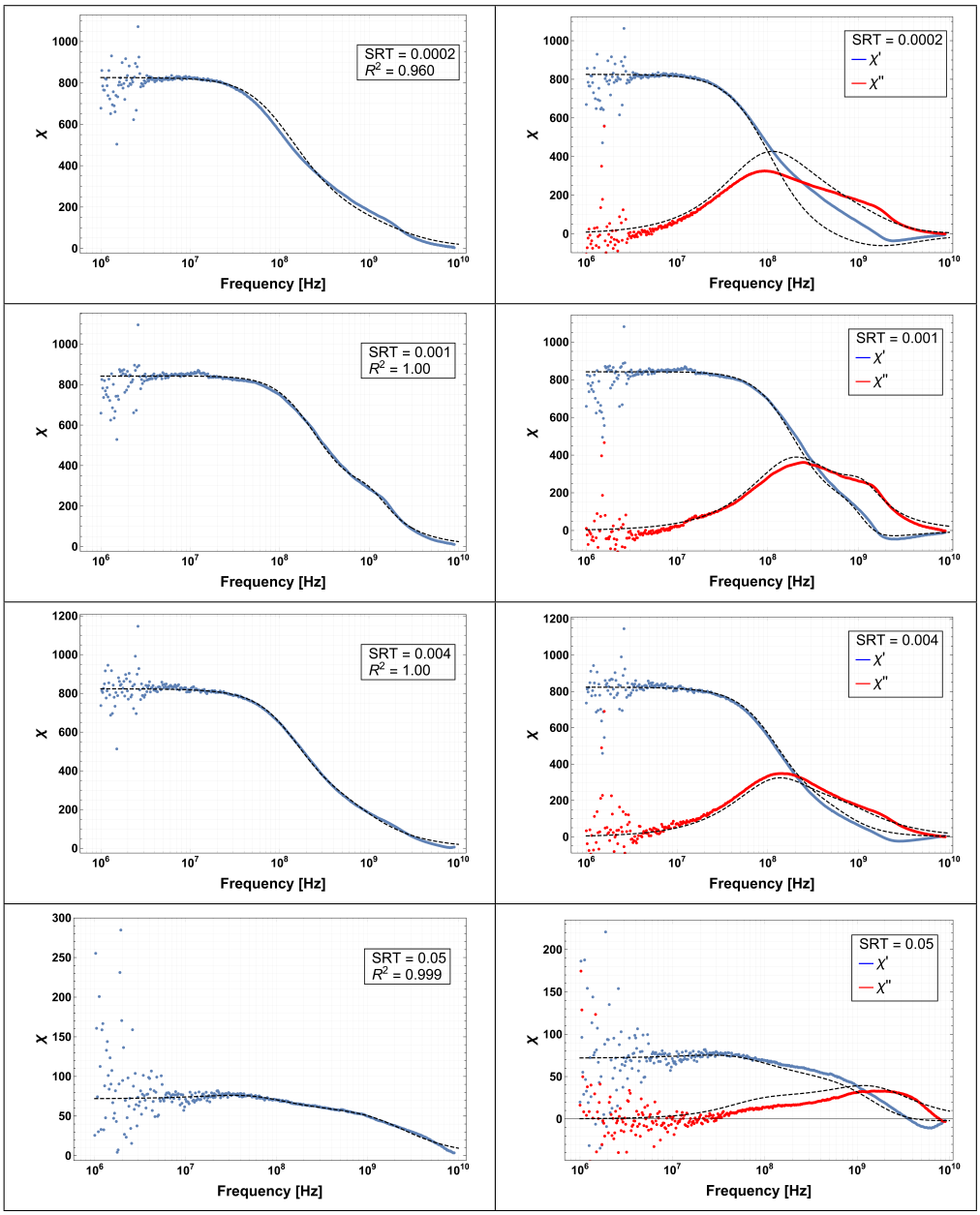

Figure 5.10: Dynamic magnetic susceptibility of $Ni_{45}Fe_{55}$ thin films. Here Ra is the measured surface roughness of the thin films. (Left side) Absolute value of the susceptibility. (Right side) Real and imaginary part of susceptibility. The dashed lines are the fitted two mode approximation.

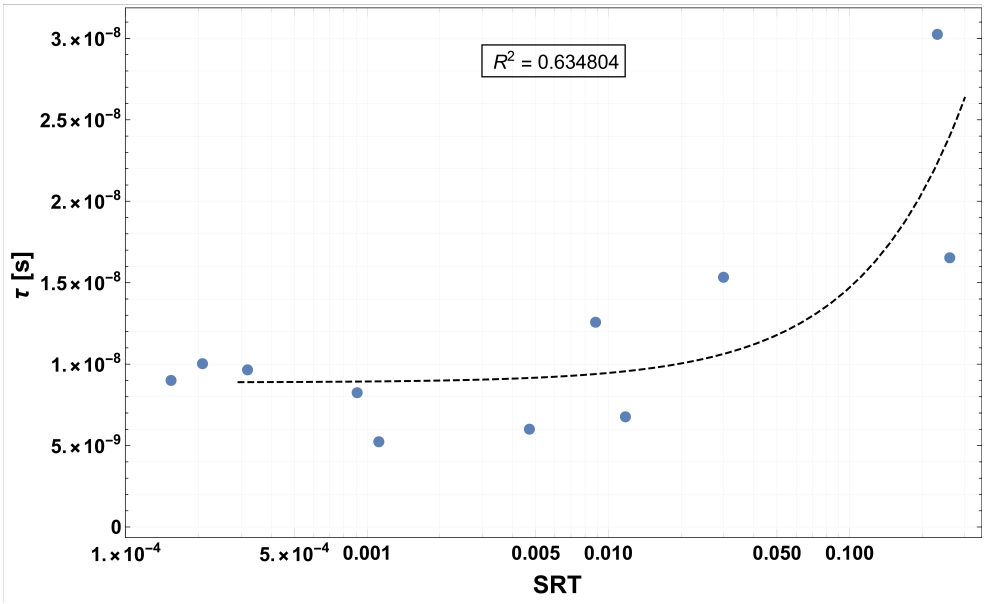

Figure 5.11: Log-Log plot of Magnetic relaxation time (τ[s]) vs SRT.

degradation of the magnetic susceptibility of the films at an SRT of 0.02 - 0.03. The underlying mechanism for this is not currently fully understood and future work is needed to determine the exact physical mechanism causing this. The modelled data are projections of the values of SRT using the least squares fit shown in Figure 5.11. It is clear that increasing the SRT results in poorer magnetic performance of the thin film i.e., it results in a marked increase in the coercivity and decrease in susceptibility of the rougher films.

Hence we have shown how the SRT effects the soft magnetic properties of a thin film by increasing its inherent magnetic relaxation time. This is of critical importance to DC-DC power converters in which we want to use inte-

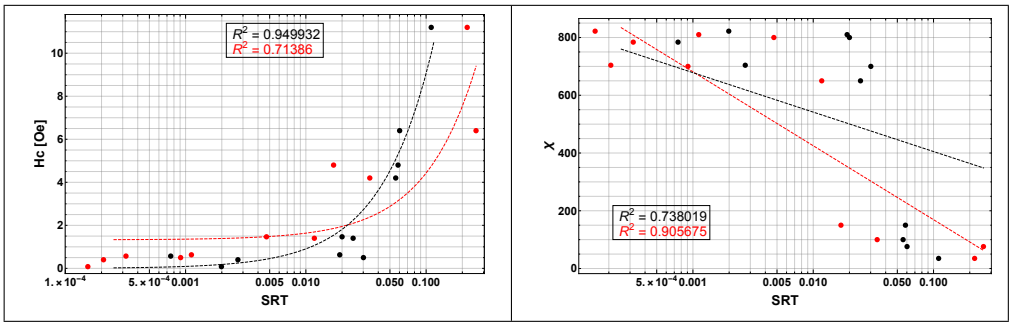

Figure 5.12: (left) Coercivity vs the SRT. (right) Magnetic susceptibility vs SRT. Measured data red; modelled data black.

grated thin film magnetics as the passive storage component in the converter. In the next section we show the influence of magnetic relaxation time and SRT on the shape of the Dynamic Magnetic Hysteresis loops.

5.3.4 Dynamic Magnetic Hysteresis (DMH)

DMH plays an important role in the energy storage of the magnetic passive in DC-DC converters as it pertains to energy loss per cycle of an ensemble of magnetic moments. The theory of DMH was first developed by Gekht [33] in 1974 for isotropic magnetic particles subject to thermal fluctuations and was later extended by Klik [34] to include magnetic particles with an induced uniaxial anisotropy. Conceptually the theory of DMH is quite simple, that the magnetisation response of an ensemble of magnetic spins subject to an external driving field and, therefore by extension, the area enclosed by the hysteresis loop, is a function of the frequency of the driving field. This is

simply given by Eq. 5.3.18

$$A(\omega) = \oint_C \boldsymbol{M}(\omega) \cdot \boldsymbol{H}(\omega)\, dC \tag{5.3.18}$$

Here $A(\omega)$ is the dynamic area enclosed by the hysteresis loops as a function of the angular frequency (ω). The DMH response of an ensemble of magnetic spins subject to an external magnetic field can be determined analytically by using either Brown's continuous diffusion of magnetic spins model [35], or using a non-perturbative ansatz expressing the magnetic Langevin equation with an AC and DC driving field as an infinite set of stochastic differential recurrence relations and averaging the resulting Clebsch-Gordan coefficients over their realisations in phase space yielding a deterministic set of magnetic moments [36]. For the following discussion the reader is highly advised to refer to the work of Coffey and Kalmykov [37] as what follows is drawn directly from their work. Consider first Brown's magnetic Langevin approach by transposing the Gilbert equation (see Eq. 5.3.19) subjected to a magnetic field comprising a deterministic and stochastic field by the damping parameter, η.

$$\frac{d}{dt}\boldsymbol{M}(t) = \gamma[\boldsymbol{M}(t) \times [\boldsymbol{H}(t) + \boldsymbol{h}(t) - \eta\frac{d}{dt}\boldsymbol{M}(t)]] \tag{5.3.19}$$

$$\frac{d}{dt}\boldsymbol{M}(t) + \gamma\eta[\boldsymbol{M}(t) \times \frac{d}{dt}\boldsymbol{M}(t)] = \gamma[\boldsymbol{M}(t) \times (\boldsymbol{H}(t) + \boldsymbol{h}(t))] \tag{5.3.20}$$

As the DMH is related to both $\boldsymbol{M}(t)$ and $\boldsymbol{H}(t) + \boldsymbol{h}(t)$ it is necessary to solve Eq. 5.3.20 in terms of $\boldsymbol{M}(t)$. To do so Eq. 5.3.20 is cross multiplied by $\boldsymbol{M}(t)$. Note for convenience the notation used is changed from $\boldsymbol{M}(t)$ to simply $\boldsymbol{M}$. This yields

$$\frac{d}{dt}\boldsymbol{M} = bM_s\alpha^{-1}[\boldsymbol{M} \times (\boldsymbol{H} + \boldsymbol{h})] - b[\boldsymbol{M} \times [\boldsymbol{M} \times (\boldsymbol{H} + \boldsymbol{h})]] \tag{5.3.21}$$

Here $b = v/(2kT\tau_N)$ and $\alpha = \gamma\eta M_s$. Evaluating Eq. 5.3.21 using the spherical coordinate system, given by relations in Eqs. 5.3.22 - 5.3.24, Eq. 5.3.21 is expressed in terms of two stochastic state variables, namely ϑ and φ.

$$\boldsymbol{M} = M_s \begin{bmatrix} 1 \\ 0 \\ 0 \end{bmatrix} \tag{5.3.22}$$

$$\dot{\boldsymbol{M}} = M_s \begin{bmatrix} 0 \\ \dot{\vartheta} \\ \dot{\varphi}\sin\vartheta \end{bmatrix} \tag{5.3.23}$$

$$\boldsymbol{H} = -\frac{1}{M_s}\frac{\partial V}{\partial \boldsymbol{u}} = -\frac{1}{M_s}\begin{bmatrix} 0 \\ \partial_\vartheta V \\ \frac{1}{\sin\vartheta}\partial_\varphi V \end{bmatrix} \tag{5.3.24}$$

This results in an expression for the magnetisation response in spherical polar coordinates as

$$\dot{\vartheta} = bM_s[h_\vartheta - \alpha^{-1}h_\varphi] - b[\partial_\vartheta V - (\alpha \sin\vartheta)^{-1}\partial_\varphi V] \tag{5.3.25}$$

$$\dot{\varphi} = \frac{bM_s}{\sin\vartheta}[\alpha^{-1}h_\vartheta + h_\varphi] - \frac{b}{\sin\vartheta}[(\sin\vartheta)^{-1}\partial_\varphi V + \alpha^{-1}\partial_\vartheta V] \tag{5.3.26}$$

. The importance of Eqs 5.3.25 & 5.3.26 is made clear when considering the general form of the evolution of an arbitrary function using the rules of vector calculus [38], expressed as Eq. 5.3.27, or using a more succinct notation, Eq. 5.3.28

$$\frac{d}{dt}f[\vartheta(t),\varphi(t)] = \frac{d}{dt}\varphi(t)\frac{\partial}{\partial\varphi}f + \frac{d}{dt}\vartheta\frac{\partial}{\partial\vartheta}f \tag{5.3.27}$$

$$\dot{f} = \dot{\varphi}\partial_\varphi f + \dot{\vartheta}\partial_\vartheta f \tag{5.3.28}$$

Substituting Eqs. 5.3.25 & 5.3.26 into Eq. 5.3.28 results in a stochastic differential equation of motion for the magnetisation, expressed in terms of an arbitrary function, f. Note, for ease of direct comparison Eq. 5.3.21 is stated again.

$$\dot{f} = -bM_s\boldsymbol{h}\cdot[[\boldsymbol{u}\times\nabla f] + \alpha^{-1}\nabla f] - b[\nabla V + \alpha^{-1}[\boldsymbol{u}\times\nabla V]]\cdot\nabla f \tag{5.3.29}$$

$$\frac{d}{dt}\boldsymbol{M} = bM_s\alpha^{-1}[\boldsymbol{M}\times(\boldsymbol{H}+\boldsymbol{h})] - b[\boldsymbol{M}\times[\boldsymbol{M}\times(\boldsymbol{H}+\boldsymbol{h})]]$$

The main accomplishment here being that the stochastic term in the evolution equation of the magnetisation dynamics has been separated out i.e., the right hand side of Eq. 5.3.29 has two terms: the first being the contribution of the random noise field on the magnetisation dynamics; the second being the deterministic driving field. In order to mathematically treat the contribution of the stochastic influence on the magnetisation dynamics it is necessary to average of Eq. 5.3.29 over an infinitesimally small time. Note that this is a clever mathematical trick as $\dot{f}$ in Eq. 5.3.29 remains as $\dot{f}$ and not $\bar{\dot{f}}$.

$$\dot{f} = \lim_{\Delta t \to 0} \frac{b}{\Delta t} \Bigg(- \overline{\int_t^{t+\Delta t} [\nabla V + \alpha^{-1}[\boldsymbol{u}(t' \times \nabla V)]] \cdot \nabla f dt'} \\ - \overline{M_s \int_t^{t+\Delta t} \boldsymbol{h} \cdot [[\boldsymbol{u} \times \nabla f] + \alpha^{-1} \nabla f] dt'} \Bigg) \quad (5.3.30)$$

Evaluating the contribution of the deterministic field to the motion of the magnetisation dynamics yields Eq. ref

$$\lim_{\Delta t \to 0} \frac{b}{\Delta t} \overline{\Bigg(- \int_t^{t+\Delta t} [\nabla V + \alpha^{-1}[\boldsymbol{u}(t' \times \nabla V)]] \cdot \nabla f dt' \Bigg)} \\ = -b \Big(\nabla V + \alpha^{-1} [\boldsymbol{u} \times \nabla V] \Big) \cdot \nabla f \\ = \frac{b}{2} \Big(V \Delta f + f \Delta V - \Delta (V f) \Big) - \frac{b}{a} \Big(\boldsymbol{u} \times \nabla V \Big) \cdot \nabla f \quad (5.3.31)$$

Here Δ is the angular component of the Laplacian operator,

$$\Delta = \frac{1}{\sin\vartheta}\frac{\partial}{\partial\vartheta}\left(\sin\vartheta\frac{\partial}{\partial\vartheta}\right) + \frac{1}{\sin^2\vartheta}\frac{\partial^2}{\partial\varphi^2} \tag{5.3.32}$$

. Next the contribution of the noise field is evaluated by perturbing the arbitrary function for the evolution of the magnetisation dynamics. This is shown in Eq 5.3.33.

$$\begin{aligned} \frac{d}{dt}f[\vartheta(t),\varphi(t)] &= \frac{d}{dt}\varphi(t)\frac{\partial}{\partial\varphi}f + \frac{d}{dt}\vartheta\frac{\partial}{\partial\vartheta}f \\ \frac{d}{dt}f[\vartheta(t^{'}),\varphi(t^{'})] &\approx (1+\delta\boldsymbol{\varphi}(t^{'})\cdot\nabla)f(\vartheta,\varphi) \end{aligned} \tag{5.3.33}$$

Note that $\delta\boldsymbol{\varphi}(t^{'})$ is the infinitesimally rotation vector and is related to the angular velocity of the magnetic moment by $\boldsymbol{\omega} = \dot{\boldsymbol{\varphi}}$. And so, by using the kinematic equation of motion for the magnetic moment ($\dot{\boldsymbol{M}}(t) = \boldsymbol{\omega}(t) \times \boldsymbol{M}(t)$) in conjunction with Eq. 5.3.21 $\delta\boldsymbol{\varphi}(t^{'})$ can be expressed as

$$\delta\boldsymbol{\varphi}(t^{'}) = h^{'}M_s\int_t^{t^{'}}\left([\boldsymbol{u}(t^{''})\times(\boldsymbol{H}(t^{''})+\boldsymbol{h}(t^{''}))] - \alpha^{-1}(\boldsymbol{H}(t^{''})+\boldsymbol{h}(t^{''})\right)dt^{''} \tag{5.3.34}$$

Finally, the noise induced motion of the magnetisation dynamics can be determined with this perturbative approach by substituting Eqs. 5.3.33 & 5.3.34 into 5.3.30, and, after averaging, yields

$$-\lim_{\Delta t\to 0}\overline{\frac{bM_s}{\Delta t}\int_t^{t+\Delta t}\boldsymbol{h}(t')\cdot\left([\boldsymbol{u}(t')\times\nabla)] + \alpha^{-1}\nabla\right)f[\vartheta(t'),\varphi(t')]dt'} = \frac{1}{2\tau_N}\Delta f \tag{5.3.35}$$

Therefore, combining these two terms, the evolution equation for the magnetisation dynamics is simply

$$2\tau_N \dot{f} = \Delta f + \frac{v}{2kT}[V\Delta f + f\Delta V - \Delta(Vf)] - \frac{v}{\alpha kT}[\boldsymbol{u} \times \nabla V] \cdot \nabla f \quad (5.3.36)$$

. Hence, to work out the DMH using Brown's diffusion model and the perturbative approach one need only pick out f and ∇V from Eq. 5.3.36., and then substitute them into Eq. 5.3.18 with $f(t)$ corresponding to $M(\omega)$ and $\nabla V(t)$ corresponding to $H(\omega)$. Note the time domain frequency domain conversion can be done by taking the *Fourier Transform* of Eq. 5.3.36, or by realising that $f(t)$ can be expressed in phasor form as $f(t) = f_0 e^{-j\omega t+\varphi}$, and so the time derivative in Eq. 5.3.36 is simply replaced with the complex frequency operator i.e., $\dot{f}(t) \to -j\omega f(t)$.

Whereas the non perturbative approach seeks to express the magnetisation dynamics in terms of spherical harmonics ($Y_{l,m}(\vartheta, \varphi)$), namely

$$\tau_N \dot{Y}_{l,m} = \sum_{l',s} e_{l,m,l',m+s} Y_{l',m+s}. \quad (5.3.37)$$

Here $e_{l,m,l',m\pm s}$ are related to the Clebsch Gordan coefficients[a] and the indexes determine the shape of the anisotropy plane. It is important to realise that both the Brownian, and the averaging over recurrence relations approach,

[a]The exact relationship between $e_{l,m,l',m\pm s}$ and the Clebsch Gordan coefficients can be found here [39].

transform the static, time-dependent, magnetic response under an AC field. Hence, for a given magnetic relaxation time, the frequency dependent magnetic response can be determined from the static response.

Although earlier it was mentioned that DMH is a function of frequency (see Eq. 5.3.18), it is more accurate to say that it is a function of frequency *and* the inherent magnetic relaxation time of the material. Indeed it is the product of the two that ultimately determines the shape, and the area, of the hysteresis loop. Furthermore, as there was a moderate correlation found between the relaxation time of the measured thin films and the SRT, we can conclude that the SRT of the films will induce a DMH effect by changing the inherent relaxation time. Thus, the effect of SRT on the magnetisation dynamics of thin films can be modelled using DMH. This is illustrated in Figure 5.13. Note, in Figure 5.13 there is a marked tilting and widening of the DMH loop with increasing SRT. This effect is the result of the magnetisation response transitioning from the "adiabatic regime" ($\omega\tau \approx 10^{-4}$), into the "quasi-adiabatic regime" ($\omega\tau \approx 10^{-3} - 10^{-1}$), and ultimately into the "kinetic freezing regime" ($\omega\tau \geq 1$). In the adiabatic limit the ensemble of magnetic moments are able to transition between the metastable anisotropy minima within the period of the applied AC field. However, at a certain frequency, the damping of the magnetic moments cause the magnetic response to indefinitely lag behind the field, and so, the orientation of the magnetic moments remain bound to the initial anisotropy minima that they are in –

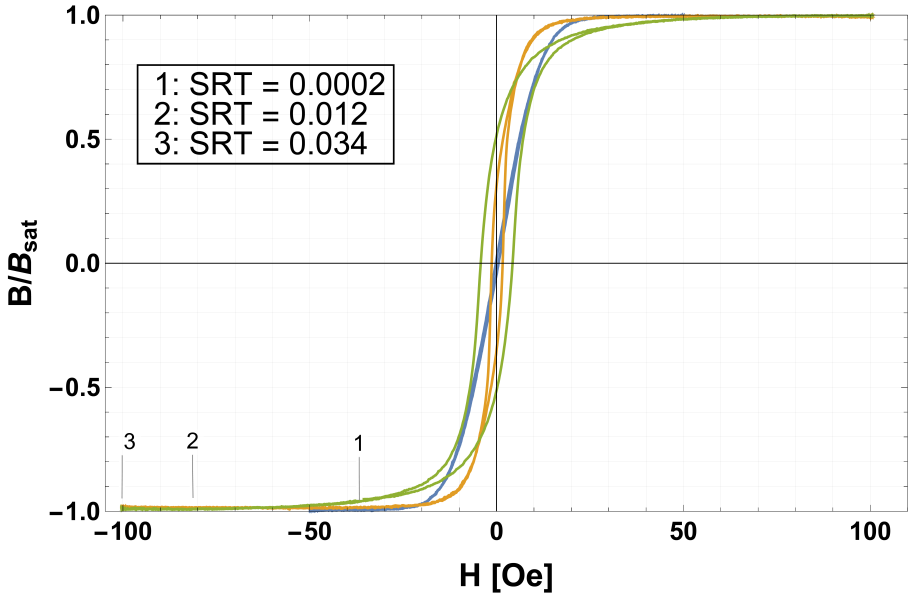

Figure 5.13: Experimentally measured BH loops of the $Ni_{45}Fe_{55}$ thin films exhibiting DMH with varying SRT.

even though it is no longer energy favourable to do so. This is referred to as "kinetic freezing" [40]. This tilting and widening of the DMH loop explains the general trend of increased coercivity and decreased susceptibility shown prior in Figure 5.12.

Furthermore, consider the surface roughness induced noise *field* in relation to the anisotropy field with distinct *easy* and *hard* magnetic axes. When the noise field is superimposed onto the anisotropy field the resultant effect causes anisotropy dispersion. This dispersion of the anisotropy axes results in a misalignment between the applied magnetic field and the hard axis, and so, the magnetisation reversal process enters the "adiabatic", "quasi-adiabatic",

and "kinetic freezing" regimes at different frequencies [41].

Thus far we have shown how the noise induced term caused by the SRT of the thin films, and the effect it has on the magnetisation dynamics and the DMH loops can be *mathematically* calculated. However, this formal approach does not necessitate an understanding of the main phenomenological consequence of noise in magnetic thin films, namely it does not provide the reader with a tangible understanding of Stochastic Resonance. To understand Stochastic Resonance first consider any particle, or magnetic spin, trapped in bistable potential well structure. In the absence of any external field the particle will transition between the two energy minima of the bistable potential in accordance with Transition State Theory (TST). TST dictates that the time to escape the potential well is related to first, the barrier height separating the energy wells, and second, the noise in the system. This is given in Eq. 5.3.38.

$$\Gamma \propto e^{-\frac{\Delta V}{kT}} \tag{5.3.38}$$

Hence there is a natural, cyclical, frequency of transitions of the particle between the two wells which is entirely caused by noise. When a weak AC field is applied to the bistable system it acts as a periodic raising and lowering operator of the local energy minima. This is shown in Fig. 5.14.

Stochastic Magnetic Resonance (SMR) occurs when the frequency of the

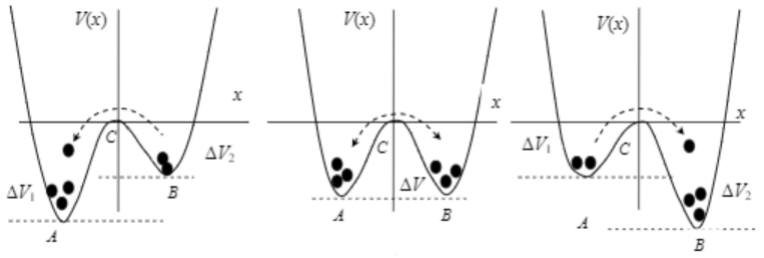

Figure 5.14: Illustration of Stochastic Resonance in bistable potential. Illustration from [42].

applied field synchronises with, or is *harmonious* to, the inter well transitions of the magnetic spin caused by the noise field i.e., the noise field *aides* inter well transitions of the magnetic spin subject to an external AC field. Should this process be *inharmonious*, it *hinders* inter well transitions, and is referred to as Stochastic Magnetic Resonance of Absorption (SMRA). This effect manifests itself in the area of the DMH loops.

The normalised area of the DMH loops are plotted in Figure 5.15. The measured DMH loops are first normalised by the thickness of the magnetic thin films, and are then linearly scaled so that the maximum DMH loop value is one. It is clear that the normalised area of the DMH loops are characterised by SMR [40] with the x-axis relating to the noise parameter. The difference between SMR and SMRA being that SMR pertains to the ability of a magnetic system to transfer energy whilst subject to additive white Gaussian noise, whereas SMRA pertains to the absorption of the input energy by the magnetic system. Both phenomena are related to the dissipative part of

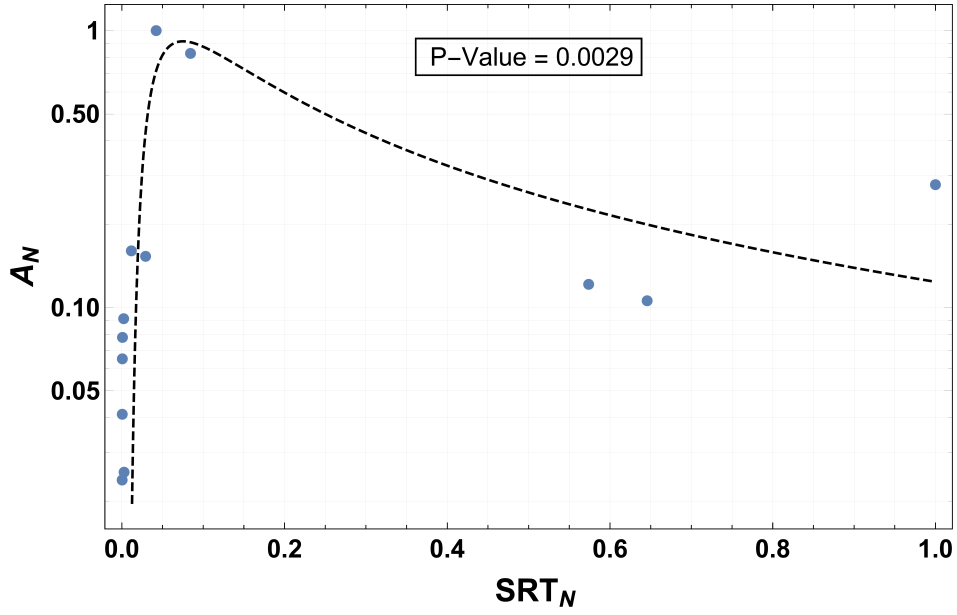

Figure 5.15: Normalised area of the dynamic magnetic hysteresis loops (A_N) vs Normalised Surface Roughness to Thickness Ratio (SRT_N).

the complex susceptibility with the SMR being proportional to $|\chi^2/\chi''|$ and SMRA proportional to χ''. However, with respect to the noise parameter, χ' and χ'' are qualitatively similar [43]. Hence, SMR and SMRA are both characterised by a rapid rise, plateau, and gradual decay.

The normal inverse gamma function is fitted to the normalised area of the DMH loop data (A_N) as it is a generalised form of the various equations used to describe SMR in [44]. A Pearson's value of 0.0029 was obtained for the fit indicating that the SMRA model fitted the measured data with statistical significance. Note the Pearson value, or more commonly known as p-value, is a statistical tool used to determine if the data matches a hypothesis by

chance, or by the soundness of the underlying hypothesis. A p-value of 0.005 or more indicates that the fit is by chance, and the hypothesis must be rejected.

Therefore, the power loss of a magnetic thin film used as the magnetic passive component in a Power Supply on Chip (PwrSoC) or PwrSiP application can then be described as

$$P_L(\omega) = \frac{\omega A(SRT)}{2\pi} \tag{5.3.39}$$

where $A(SRT)$ is the non-normalised area of the DMH loop. Thus, to minimise the power loss in a thin film the SRT ratio must be less than a critical value in order to avoid the maximum of the SMRA curve shown in Figure 5.15. One such way to do this is to employ a small DC bias field to tune SMRA curve, as shown in [45]. However, for a magnetic thin film deposited on a particular substrate (roughness), the easiest way to avoid the maximum of the SMRA curve is to judiciously choose the thickness of the film.

5.3.5 Conclusion

We have treated the problem of surface roughness in thin film magnetics using Brown's continuous diffusion model of magnetic spins subject to thermal fluctuations. The magnetic susceptibility of the thin films was calculated using the two mode approximation, from which the magnetic relaxation time

was determined using Mathematica's Nonlinear Model Fit. We have shown that there is a moderate linear correlation between the SRT and the magnetic relaxation time ($R^2 = 0.63$); a strong linear correlation with the coercivity ($R^2 = 0.71$); and a strong logarithmic correlation between the SRT and the magnetic susceptibility ($R^2 = 0.91$).

Furthermore, we have shown that the influence of thin film surface roughness on the magnetic relaxation time is to cause a Stochastic Magnetic Resonance of Absorption effect in the Dynamic Magnetic Hysteresis (DMH) loops. On lowering the magnetic relaxation time the area enclosed by the DMH loop first increases, and then decreases, with the DMH loop reducing to an almost straight line at $\tau \approx 10^{-10}$ seconds (SRT $\sim 10^{-3}$). Hence, the area of the DMH loop is directly related to the product of the inherent magnetic relaxation time of the thin film and the frequency of the applied external magnetic field exciting the magnetic thin film. The dependence of the magnetic material properties on the surface roughness to thickness ratio is therefore a limiting factor for thin film magnetics used in future PwrSoC and PwrSiP applications.

5.3.6 Postamble

The complex issue of the effect of surface roughness on the magnetisation dynamics of magnetic thin films was successfully treated using Brown's diffusion model (justifying our earlier abandonment of the deterministic ap-

proach, stated in 5.2.5). This is a key accomplishment for the integration of the magnetic thin film into package for PwrSiP applications. The key realisation is the role the surface roughness and *thickness* play on the magnetisation dynamics. Indeed, based on this understanding it would appear that one could mitigate the effect of surface roughness by increasing the film thickness. This raises the question; what is the maximal thickness permissible of a thin film in PwrSiP applications, and consequentially, is there degraded magnetic performance observed when using thicker films. Section 5.4 addresses the thickness dependent effects on the magnetisation dynamics of magnetic thin films.

5.4 Multimodal Behaviour of the Dynamic Susceptibility Spectrum in Amorphous CoZrTaB Magnetic Thin Films

This section was published in the *Journal of Applied Physics* [46].

This section deals with an investigation of the origins of sub Ferromagnetic Resonance (FMR) multimodal behaviour in the magnetic susceptibility spectrum of amorphous CoZrTaB magnetic thin films using Brown's diffusion model describing continuous diffusion of magnetic spins. Brown's diffusion model is regressed onto experimental data for the amorphous CoZrTaB magnetic thin films with thicknesses spanning 80nm – 530nm. The mathematical model presented successfully reproduces the thickness dependent dynamic magnetic susceptibility of the amorphous CoZrTaB magnetic thin films with strong statistical significance. The model proposes the formation of additional energy wells in the uniaxial anisotropy energy plane of the material after a critical film thickness. The sub FMR resonance peaks arise when the frequency of the external excitation field approaches the natural frequency of the well. Furthermore, the additional energy wells in the anisotropy energy plane causes a breakdown in the axial symmetry of the anisotropy energy plane. This breakdown of axial symmetry results in dynamic coupling between the transverse ($\chi_{\perp}$) and longitudinal ($\chi_{\parallel}$) magnetic susceptibility. This

dynamic coupling results in the initial low frequency step down in the magnetic susceptibility observed in the thicker CoZrTaB magnetic thin films. It is found that the application of an external bias magnetic field along the easy axis of the amorphous CoZrTaB magnetic thin films supresses the sub FMR resonance peaks by restoring the axial symmetry of the anisotropy energy plane.

Thus, the ability of soft magnetic CoZrTaB thin films to retain in-plane uniaxial anisotropy is important in order to ensure a low loss tangent ($\chi_{\perp}^{''}/\chi_{\perp}^{'}$) at frequencies spanning 1MHz – 300MHz. The frequency dependent loss tangent is fundamentally determined by the internal anisotropy energy plane [10] as it governs the magnetisation dynamics of the material [47]. Ultra-low loss performance in the 1MHz – 300MHz frequency range is achieved by having a material whose dynamic magnetic susceptibility is governed by transverse magnetic susceptibility ($\chi_{\perp}$), with a single ferromagnetic resonance peak in the GHz frequency range. This is typically achieved by materials with a strong in-plane uniaxial anisotropy energy plane. For such materials the internal anisotropy energy plane is determined by one state variable, namely the colatitude (θ) state variable [48]. Materials with a strong in-plane uniaxial anisotropy have a low loss tangent as the imaginary component of the transverse magnetic susceptibility ($\chi_{\perp}^{''}$) is exceedingly small up until the onset of ferromagnetic resonance.

However, above a critical film thickness shape effects can break the axial symmetry of the internal anisotropy energy plane of the material. This results in the internal anisotropy energy plane being governed by two state variables, namely the colatitude (θ) and azimuthal (ϕ) state variables [48]. As a consequence of the thickness dependent axial symmetry of the anisotropy energy plane, there is a deterioration in the soft magnetic properties [49] and a growing proportion of magnetic spins whose preferred orientation is out of plane [50–52] with increasing film thickness. Moreover, the dependence of the internal anisotropy energy plane on two state variables results in dynamic coupling between the transverse magnetic susceptibility ($\chi_\perp$ and the longitudinal magnetic susceptibility ($\chi_\parallel$)[4]. This dynamic coupling is further detrimental to the high frequency performance of the magnetic material as there is a rise in the low frequency imaginary component of the magnetic susceptibility caused by the presence of $\chi_\parallel^{''}$. The loss contribution of the perpendicular and parallel imaginary components of the magnetic susceptibility are summarized in Eq. 5.4.1

$$\lim_{\omega\to 0}\chi_\perp^{''}(\omega) \lll \lim_{\omega\to 0}\chi_\parallel^{''}(\omega) \tag{5.4.1}$$

$$(1-\kappa)\chi_\perp + \kappa\chi_\parallel = consant \tag{5.4.2}$$

Ideally, as $\chi_\parallel^{''}$ is much larger than $\chi_\perp^{''}$ at low frequencies, the coupling coefficient, κ, should be near zero. And so, the coupling of the transverse and longitudinal magnetic susceptibilities limits the effective useful thickness of

the CoZrTaB film. Note in Eq. 5.4.2 $0 \leq \kappa \leq 1$.

Furthermore, multiple minima in the anisotropy energy plane could be used to explain the existence of the multiple sub FMR resonance peaks observed in the magnetic susceptibility spectrum reported in amorphous CoZrTaB (this work), CoNbZr [53], and CoFeSiB [54], magnetic thin films. The resonance frequencies are determined by the gradient of the anisotropy energy well and the amplitude of the resonance peaks determined by the depth of the anisotropy energy well. Hence, for shallower energy wells the spins have smaller resonance peaks which occur at lower frequencies. The application of an external magnetic field applied to the thin film can alter the gradient of the internal anisotropy energy by raising and/or lowering the barrier heights separating the energy wells [55]. Thus, the multiple sub FMR resonance peaks can be suppressed through the application of an external biasing field. In this work Brown's continuous diffusion model [2] is used to characterise the multimodal behaviour in the magnetic susceptibility spectrum of the amorphous CoZrTaB magnetic thin films.

The structure of this Section is as follows: subsection 5.4.1 outlines the fabrication methods and experimental characterisations of the amorphous CoZrTaB magnetic thin films; subsection 5.4.2 describes Brown's continuous diffusion model [2] used to characterise the magnetic susceptibility spectrum of the amorphous CoZrTaB magnetic thin films; Results and discussions are

provided in subsection 5.4.3; and finally conclusions of the Section are presented in subsection 5.4.4.

5.4.1 Experimental Methods & Measurements

Amorphous $Co_{84}Zr_4Ta_4B_8$ magnetic thin films spanning thicknesses 80nm - 530nm were magnetron sputter deposited at 500 W DC in the presence of an aligning magnetic field [56]. The sputtering chamber was evacuated until a pressure of 10^{-6} Pa was measure, after which Argon gas was pumped into the chamber until a sputter pressure of 0.13 Pa was achieved. The film thicknesses were measured using a DekTak surface profileometer. The atomic composition and amorphous structure of the films were confirmed using X-Ray diffraction (Phillips Xpert diffractometer) and transmission electron microscopy. The dynamic magnetic susceptibilities of the films were measured from 1MHz – 9GHz using a small signal wide band complex permeameter (Ryowa Electronics, Japan, Model PMM 9G) on the 3mm $\times$ 3mm samples. Note, the dimensions of the samples were constant for all thickness, i.e. all samples were 3mm $\times$ 3mm. The results of the atomic composition and material morphology are discussed in [56].

5.4.2 N Minima Anisotropy Model

The dynamic magnetic susceptibility of amorphous magnetic materials subject to a weak AC driving field can be determined using linear response theory

[29].

$$\boldsymbol{M} = \chi \boldsymbol{H} \tag{5.4.3}$$

Here **M** is the magnetisation vector of the thin film; **H** is the magnetic field acting on the thin film; and χ is the dynamic magnetic susceptibility of the thin film. The dynamic magnetic susceptibility of the thin film subject to an external driving field can be expressed as a weighted sum of longitudinal and transverse magnetic susceptibilities. This weighted combination is expressed in Eq. 5.4.4

$$\chi(\omega) = \chi_{\parallel}(0)\chi_{\parallel}(\omega) + \chi_{\perp}(0)\chi_{\perp}(\omega) \tag{5.4.4}$$

Here $\chi_{\parallel}(0)$ and $\chi_{\perp}(0)$ are the static longitudinal and transverse magnetic response. The$\chi_{\parallel}(0)$ and $\chi_{\perp}(0)$ coefficients are determined by the internal anisotropy energy plane of the thin film. The longitudinal component of the magnetic susceptibility can be modelled using the two mode approximation [57] (see Eq. 5.4.5)

$$\chi_{\parallel}(\omega) = \chi_{\parallel}(0)\left(\frac{\Delta_1}{1 + i\omega\tau} + \frac{1 - \Delta_1}{1 + i\omega\tau_w}\right). \tag{5.4.5}$$

Here Δ_1 and τ_w are parameters determined to ensure correct behaviour of $\chi_{\parallel}(\omega)$ at the very low frequency and very high frequency extremes. The transverse magnetic susceptibility response for strong in-plane uniaxial anisotropy

can be determined from the Landau-Lifshitz equation [58] (see Eq. 5.4.6)

$$\chi_{\perp}(\omega) = \chi_{\perp}(0)\frac{(1+\alpha^2)\omega_{pr}^2 + i\alpha\omega\omega_{pr}}{(1+\alpha^2)\omega_{pr}^2 - \omega^2 + i2\alpha\omega\omega_{pr}}. \tag{5.4.6}$$

Here ω_{pr} is the natural precession frequency of the magnetic moments of the thin and α is a viscous damping parameter acting on the magnetic moments. This frequency is determined by the internal gradient of the anisotropy energy plane. Note any vector field can be expressed as the gradient of a scalar potential. Hence the precession frequency is governed by the anisotropy field ($\boldsymbol{H}_{an}$), and gradient of the anisotropy energy plane of the thin film ($\nabla_{\boldsymbol{M}} V$). This relationship between the precession frequency, the anisotropy field, and the anisotropy energy plane is explicitly stated in Eqs. 5.4.7 & 5.4.8. Thus, the shape of the anisotropy energy plane is of critical importance to the precession frequency. Typically, materials with strong in-plane uniaxial anisotropy are characterised by two distinct energy wells separated by a barrier. Thus, each well has its own precession frequency determined by the shape of the well.

$$\omega_{pr} \approx \gamma \boldsymbol{H}_{an} = -\gamma \nabla_{\boldsymbol{M}} V \tag{5.4.7}$$

$$\boldsymbol{H}_{an} = \sqrt{\boldsymbol{H}_{KP}(\boldsymbol{H}_{KP} + 4\pi \boldsymbol{M}_s)} \tag{5.4.8}$$

Note, Eq. 5.4.8 relates the *in-plane uniaxial anisotropy* field ($\boldsymbol{H}_{KP}$) to the *anisotropy* field. Ferromagnetic resonance occurs when the frequency of the

driving field approaches the precession frequency of the well. For a symmetric two well structure the precession frequencies of both wells are identical and so only a single FMR peak is observed at $\omega \to \omega_{pr}$. The amplitude and quality factor of the FMR peak is determined by the shape and depth of the well, along with the viscous damping acting on precession of the magnetic moments. Here the quality factor of the FMR peak refers to the ratio of peak's amplitude to width. Reduction in the barrier height separating the two energy wells causes a dispersion of the precession frequency and results in reduced quality of the FMR peak. That is, the FMR peak becomes smaller and wider.

Eq. 5.4.6 accurately predicts a single FMR peak for materials with in-plane uniaxial anisotropy as both energy wells are identical and there is only a single precession frequency. Therefore, Eq. 5.4.6 must be modified to account for the multiple sub FMR peaks observed in the thicker magnetic films. The Ansatz or assumption of this work is that each sub FMR peak observed in the magnetic films has a corresponding energy well with a distinct precession frequency. Therefore, each distinct energy well will exhibit resonance behaviour as the excitation frequency of the applied external magnetic field approaches the precession frequency of the energy well. This is shown in Eq. 5.4.9

$$\chi_{\perp}(\omega) = \chi_{\perp}(0) \sum_{k=1}^{N} c_k \frac{(1+\alpha^2)\omega_{pr,k}^2 + i\alpha\omega\omega_{pr,k}}{(1+\alpha^2)\omega_{pr,k}^2 - \omega^2 + i2\alpha\omega\omega_{pr,k}} \tag{5.4.9}$$

Here $\omega_{pr,k}$ and c_k denote the precession frequency and depth of the k^{th} energy well. In the case of uniaxial anisotropy Eq. 5.4.9 reduces to the well known expression given in Eq. 5.4.6 with $c_1 = 1$ and the remaining $c_k = 0$.

5.4.3 Results and Discussion

Nonlinear model fitting is used to regress Eqs. 5.4.4, 5.4.5 & 5.4.9 onto the frequency dependent magnetic susceptibility of the 80-530 nm films. The results of the regression are presented in Figure 5.16. The NMinima model accurately fits to the thickness dependent multimodal behaviour of the dynamic magnetic susceptibility of the films with an R-Squared value of 0.99, as illustrated in Figure 5.16. The R-Squared value of 0.99 indicates that the model fits the data with a strong statistical significance. Hence, the Ansatz that the anisotropy energy plane of the thicker films is best described as in-plane uniaxial degraded by superfluous energy wells is justified. Thus, the shape of the internal anisotropy energy plane can be inferred by regressing the model onto the dynamic magnetic susceptibility of the thin films.

More importantly, the frequency position of the multiple FMR peaks did not change with increasing film thickness, rather the amplitude of the peaks was increased. The frequency position of the FMR peak is ultimately determined by the gradient of the energy well. Therefore, the depths of the energy wells (represented by the c_k coefficients in Eq. 5.4.9) increased without changing the gradient of the well. An observed shift in the frequency position of the

resonance peak would indicate a change in the shape of the energy well. The observed reduction in the amplitude and quality factor of the primary FMR peak is caused by a decrease in the barrier height of the primary well. This reduction in the primary FMR peak is known as inhomogeneous broadening [59, 60] and is observed in the dynamic magnetic susceptibility of the amorphous CoZrTaB magnetic thin films (see Fig. 5.16). This is consistent with the depth of the well determining the quality of the resonance peaks through inhomogeneous broadening as the resonance peak will still be centred on the primary precession frequency of the well, even in the event of dispersion of the precession frequency through inhomogeneous broadening. Hence, the amplitude and frequency position of the peaks could be used to draw inference on the underlying physical phenomena causing the existence of the energy wells.

The reduction in the quality factor (ratio of amplitude to width) of the primary resonance peak in the thicker films (see Fig. 5.16) is a consequence of the reduction in the barrier height of the uniaxial anisotropy energy well due to the emergence of the mixed anisotropy. For a small to moderate barrier height ($1 \leq \sigma \leq 5$) there is essentially a dispersion of the precession frequencies of the magnetisation within the anisotropy well. This effect presents itself as inhomogeneous broadening of the primary FMR peak as the effect considerably exceeds the actual damping parameter (α) of the material [59, 60].

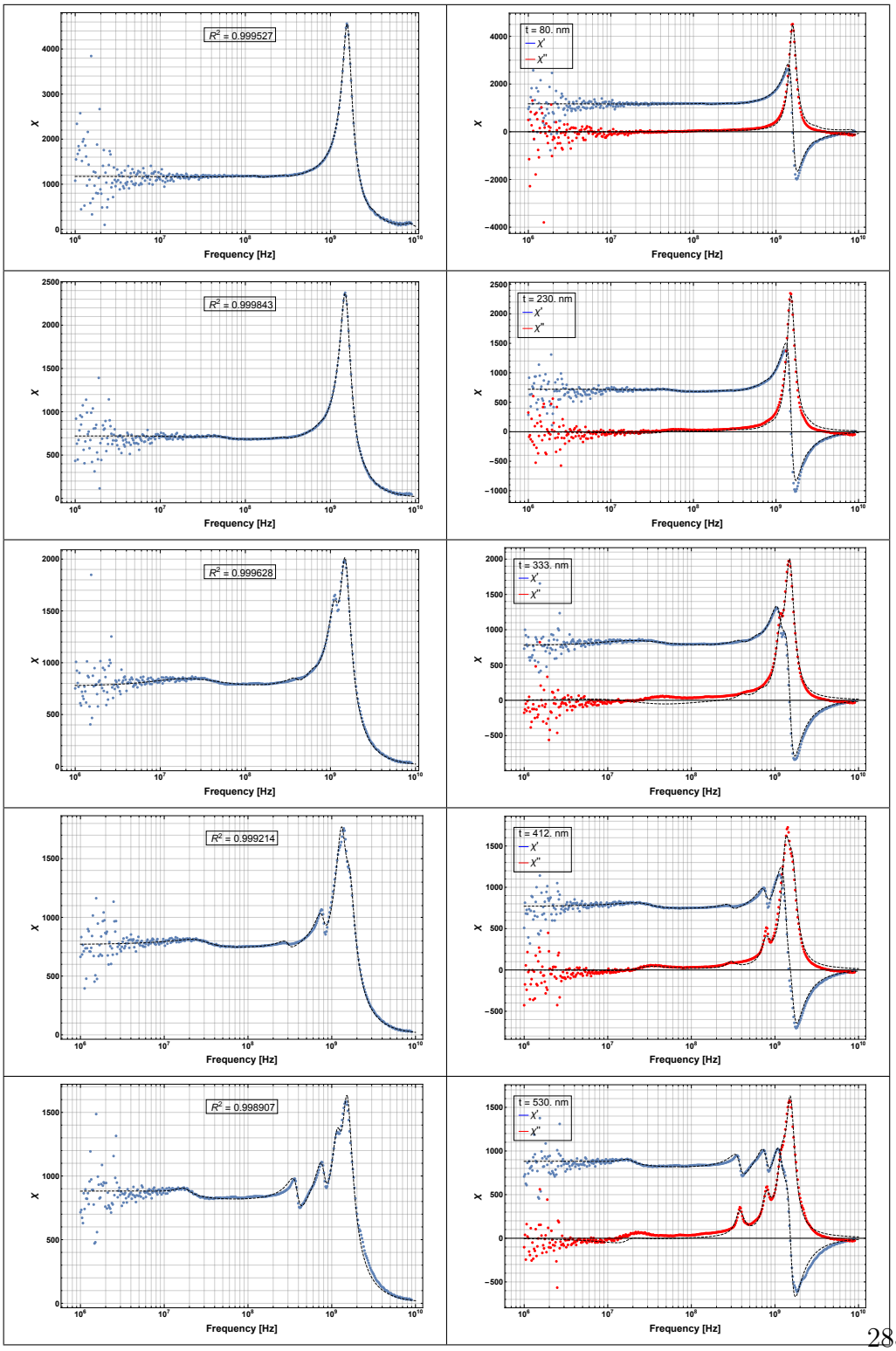

Figure 5.16: Magnetic susceptibility data for amorphous CoZrTaB magnetic thin films spanning thickness 80nm - 530nm; (left) Absolute magnetic susceptibility; (right) Real and imaginary magnetic susceptibility. Dashed lines are the fitted model

Figure 5.17 shows the ratio of c_k coefficients in Eq. 5.4.9 to uniaxial anisotropy plotted for the various films presented in Figure 5.16. It is evident that as the amorphous CoZrTaB films become thicker the anisotropy energy plane is more heavily influenced by additional energy wells within the anisotropy field. This is shown as there is a near linear relationship between increasing film thickness and the amplitude of the c_k coefficients representing the depths of the energy wells. From this graph we can conclude that there is a reduction the barrier height of the in-plane anisotropy caused by the formation of superfluous energy wells with increasing film thickness. The reduction in the amplitude of the anisotropy field is later verified in Fig. 5.19. Importantly, the additional energy wells in the anisotropy energy plane result in a breakdown of the axial symmetry of the anisotropy energy plane. This results in dynamic coupling between the longitudinal and transverse magnetic susceptibilities of the thicker films. Hence, there will be an observed increase in $\chi_{\parallel}$ with increasing film thickness.

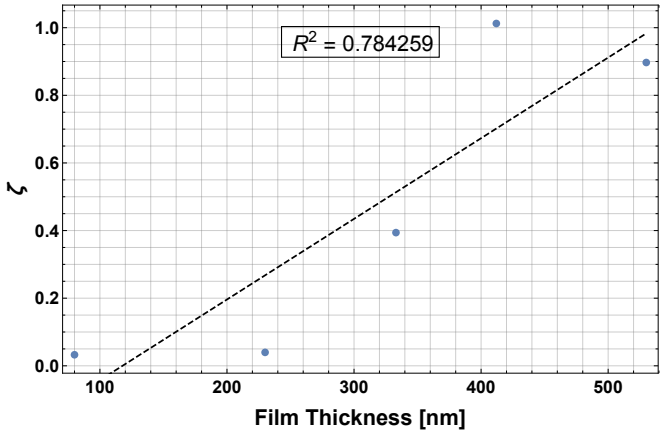

Figure 5.17: ζ is the ratio of the sum of the c_k coefficients (for $k > 1$) to uniaxial anisotropy coefficient (c_1) determined by regressing Eq. 5.4.9 onto the experimental magnetic susceptibility of the amorphous CoZrTaB thin films (see Figure 5.16).

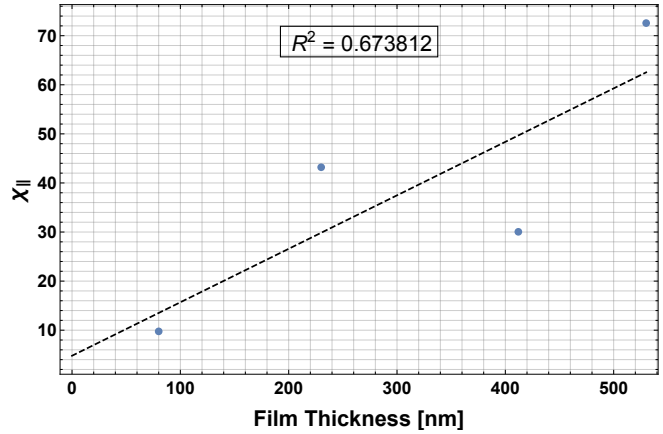

Figure 5.18: Amplitude of the longitudinal magnetic susceptibility in thin films vs film thickness (note the 333nm thick CoZrTaB film is omitted from this plot as the low frequency noise on the magnetic susceptibility measurement resulted in a lower $\chi_{\parallel}$. The effect of the noise is also seen as an error in the modelled the low frequency imaginary component of the magnetic susceptibility of the film).

The amplitude of $\chi_{\parallel}$ versus film thickness is shown in Fig. 5.18. The in-

crease in the longitudinal magnetic susceptibility is responsible for the initial low frequency drop off in the magnetic susceptibility of the films. This drop off occurs between 10-100 MHz (see Fig. 5.16). The low frequency drop in magnetic susceptibility is incredibly detrimental to the performance of the magnetic thin film used in DC-DC power converters. The initial drop is caused by a growth in the imaginary component of the longitudinal magnetic susceptibility and results in a higher loss tangent at lower frequencies.

The breakdown in the uniaxial anisotropy results in greater degrees of freedom in the magnetisation dynamics as the evolution equation for the magnetic thin film is no longer governed by a single state variable and is instead, it is governed by two state variables. The magnetisation dynamics of a thin film with two state variables is governed by the Fokker-Planck Equation [2, 61], Eq. 5.4.10.

$$\frac{\partial W}{\partial t} = k\Delta W + \frac{h^{'}}{\sin\theta}\{\frac{\partial}{\partial\theta}[(\sin\theta\frac{V_{\theta,\phi}}{\partial\theta} + \frac{\partial V_{\theta,\phi}}{\alpha\partial\phi})]W + \frac{\partial}{\partial\phi}[(\frac{1}{\sin\theta}\frac{\partial V_{\theta,\phi}}{\partial\phi} - \frac{\partial V_{\theta,\phi}}{\partial\theta})]W\} \tag{5.4.10}$$

Here $h^{'}$ is Brown's parameter which relates the damping and gyromagnetic moment to the magnetisation saturation; $V_{\theta,\phi}$ is the sum of all the internal anisotropies; and W is the probability distribution function that a magnetic moments orientation lies within an infinitesimally small segment of the unit sphere. Note that k is determined by requiring the steady state distribution

of Eq. 5.4.10 to be Boltzmann.

$$h^{'} = \frac{\alpha\gamma}{(1+\alpha^2)M_s} \tag{5.4.11}$$

$$k = \frac{K_B T h^{'}}{v} \tag{5.4.12}$$

For uniaxial anisotropy the energy term is governed by Eq. 5.4.13.

$$V_\theta = K\sin^2\theta \tag{5.4.13}$$

Hence, for uniaxial anisotropy the $\frac{\partial}{\partial\phi}$ term in Eq. 5.4.10 drops out. Therefore, for uniaxial anisotropy there is no dynamic coupling between the transverse and longitudinal components of the magnetisation dynamics. However, for more complex anisotropies with an azimuthal dependence there will be dynamic coupling between the transverse and longitudinal components of the magnetisation dynamics - resulting in higher material loss.

The magnetisation energy band of the 230 nm and 530 nm films is presented in Fig. 5.19. There is a notable reduction in the amplitude of the anisotropy field within the thicker film. This is consistent with the observed inhomogeneous broadening of the primary FMR peak (shown in Fig. 5.16) caused by the reduction in the barrier height of the in-plane anisotropy energy well (shown in Fig. 5.17). Furthermore, Fig. 5.19 shows clear deviations from in-plane uniaxial anisotropy in the 530nm film caused by additional energy

	Well 1	Well 2	Well 3	Well 4
Angular Position of Well (θ)	10°	$25^\circ \leq \theta \leq 35^\circ$	$160^\circ \leq \theta \leq 165^\circ$	$310^\circ \leq \theta \leq 330^\circ$

Table 5.1: Angular positions of energy minima for 530nm amorphous CoZrTaB magnetic thin film shown in Fig 5.19.

wells with local energy minima. The existence of the additional energy wells in the anisotropy energy plane causes the multimodal behaviour of the dynamic magnetic susceptibility observed in the thicker films. Furthermore, the presence of the additional energy wells also explains the dynamic coupling between the longitudinal and transverse magnetic susceptibility observed in the thicker films. For clarity, the positions of the additional energy minima observed in the 530nm thick film are presented in Table 5.1.

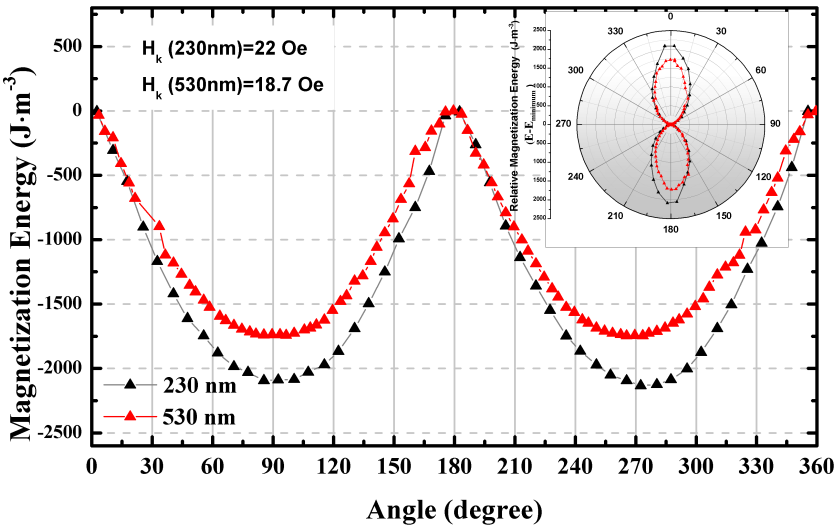

Figure 5.19: In plane anisotropy of 230nm & 530nm amorphous CoZrTaB magnetic thin films (polar plot inset.).

The internal anisotropy of the material can be biased through the application of a DC external field [62–64]. When applied at an oblique angle to the easy axis the bias field breaks the axial symmetry of the anisotropy energy plane. However, applying a DC bias field along the easy axis of the thin film can alter the internal anisotropy energy plane while maintaining axial symmetry. This is important as non-axial symmetry of the anisotropy energy plane causes dynamic coupling between the longitudinal and transverse dynamic magnetic susceptibility. The effect of the DC bias field along the easy axis is shown in Fig. 5.20. Note, in Fig. 5.20 the amplitudes of the multiple resonance peaks are diminished with increasing amplitude of the DC bias field. From the regressed model this suggests that the applied

DC bias field smoothens out the additional energy minima in the internal anisotropy energy plane. Furthermore, the shift in the FMR peak towards higher frequencies is again accounted for by the increased gradient of the internal anisotropy energy plane caused by the biasing field.

Hence, a DC bias field may be used to counter the effect of the thickness dependent multimodal behaviour in the magnetic susceptibility spectrum of amorphous CoZrTaB magnetic thin films via the restoration of uniaxial anisotropy within the film. This is important for DC – DC power converters which utilise amorphous CoZrTaB magnetic thin films (or other materials which exhibit the multimodal behaviour) as the DC bias field can be used to tune the loss within the amorphous thin film and allow for thicker layers of amorphous thin films to be used in the converters.

Moreover, the use of micro-patterning can alter the internal anisotropy energy plane through shape demagnetisation. Therefore, micro-patterning of the amorphous CoZrTaB magnetic thin films can be used to suppress the multimodal behaviour of the dynamic magnetic susceptibility. Indeed, such micro-patterning was successfully used by Yamaguchi et al. [65] to improve the high frequency performance of amorphous CoNbZr magnetic thin films (CoNbZr also exhibits multimodal behaviour). It is clear from the inductance plot [65] that micro-patterning of the thin film along the easy axis stymies the formation of sub FMR resonance peaks by altering the shape anisotropy.

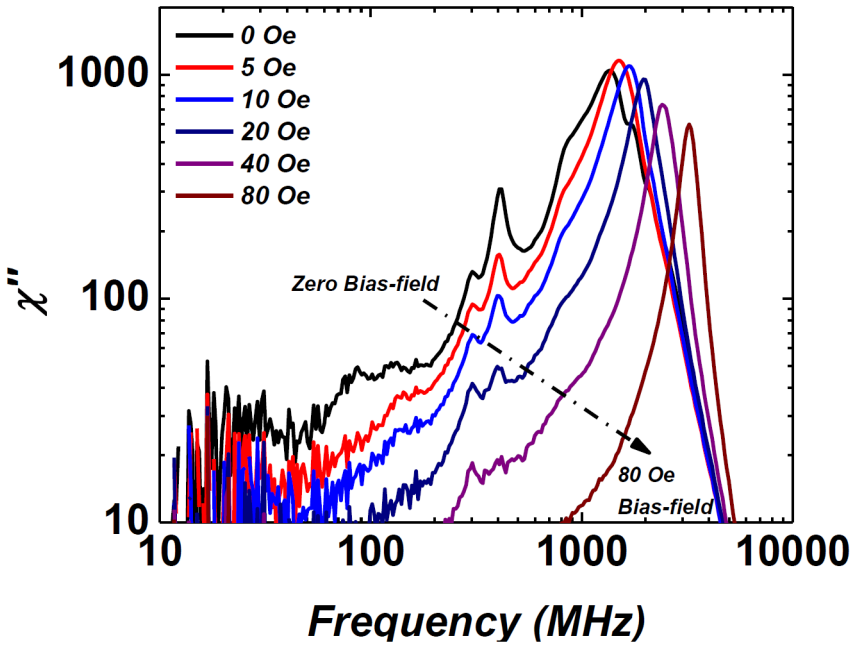

Figure 5.20: Magnetic Susceptibility of 530nm amorphous CoZrTaB magnetic thin film subjected to DC bias field applied along the easy axis.

5.4.4 Conclusion

We have treated the problem of multimodal behaviour in the magnetic susceptibility spectrum of amorphous CoZrTaB magnetic thin films spanning 80nm – 530nm thickness using Brown's continuous diffusion model of magnetic spins. The model was regressed onto the experimental data and achieved R-Squared values above 0.99. The model reproduced the dynamic magnetic susceptibility of the amorphous CoZrTaB magnetic thin films with strong statistical significance. The observed sub FMR multimodal behaviour in the dynamic magnetic susceptibility is attributed to the formation of additional energy wells in the uniaxial anisotropy energy plane of the thin films. We

have shown how the breakdown in the uniaxial anisotropy of the thin films results in dynamic coupling between the transverse ($\chi_\perp$) and longitudinal ($\chi_\parallel$) magnetic susceptibility. The main tractability of this model is that inference can be made to the shape of the internal anisotropy energy plane by regressing the model onto the measured dynamic magnetic susceptibility of the material. From this inference structural properties of the material can be indirectly determined.

Furthermore, the reduction in the main barrier height of the uniaxial anisotropy causes a dispersion of the primary precession frequency resulting in inhomogeneous broadening of the primary FMR peak. We have also shown how the application of an external bias field can be used to diminish the energy minima of the anisotropy field suppressing the multimodal behaviour of the magnetic susceptibility.

5.4.5 Postamble

The role of film thickness in the magnetisation dynamics of thin films was successfully characterised. It was found that increasing film thickness resulted in a higher loss tangent due to dynamic coupling between the transverse and longitudinal reversal modes. This is extremely significant for magnetic thin films utilised as the magnetic passive in PwrSiP applications considering that the surface roughness to thickness ratio (SRT) (see section 5.3) played a key role in determining loss, and that this loss could be minimized by increasing

film thickness. Hence, planarisation of the surface prior to magnetic core deposition, or deposition of the core on a sacrificial layer on Si from which it may later be liberated, is a key technological requirement for the successful integration of thin films for PwrSiP applications.

5.5 Conclusion

This Chapter presented numeric and analytical models developed in order to characterise the magnetisation dynamics of magnetic thin films used in Power Supply in Package applications. The numeric approach used Graphical Processing Units to solve the Landau-Lifshitz-Gilbert equation, and so reduce the simulation runtime by using the superior computational power enabled by the parallel GPU architecture. The fidelity of the magnetisation dynamics predicted by the simulator was verified against mumag Standard Problem 4 solved using the Object Oriented Micromagnetic framework. The simulator was developed in order to treat complex alloy systems comprising many magnetic elements. Hence, it can be later used to optimise magnetic alloy compositions for a unique Power Supply in Package Application. Future work for this simulator entails the verification of the predicted magnetisation dynamics for a given alloy against its real-world counterpart.

Although the numeric approach was initially developed in order to treat the issue of surface roughness in magnetic thin films this problem was ultimately characterised using analytic methods, namely Brown's continuous diffusion of magnetic spins model. The analytic approach was built on the core Ansatz that the surface roughness acted as a source of Additive White Gaussian Noise on the magnetisation dynamics and so shared identical statistical properties on the magnetisation dynamics as those produced by thermal

noise. Hence, Brown's treatment of thermal fluctuations in magnetic particles was extended to treat the problem of surface roughness in magnetic thin films. The core findings of this work were that the films exhibited Dynamic Magnetic Hysteresis effects similar to those predicted by thermal fluctuations i.e., there was a marked tilting and widening of the DMH loops with the noise parameter. Hence it was shown there was a linear correlation between the coercivity of the thin and the surface roughness and a logarithmic correlation between the magnetic susceptibility and the surface roughness. Furthermore, Stochastic Magnetic Resonance of Absorption was observed in the magnetic thin films, which, is a phenomenon directly associated with thermal fluctuations in magnetic particles.

Finally, Brown's diffusion model was further adapted to describe the multimodal behaviour observed in CZTB magnetic thin films spanning thicknesses 80 nm – 530 nm. The multimodal behaviour was shown to be caused by a breakdown in the uniaxial anisotropy of the thin film with increasing film thickness. The reduction in axial symmetry and the emergence of additional energy minima within the anisotropy energy plane was to result in dynamic coupling between the longitudinal and transverse magnetic susceptibility and as the originator of the additional sub FMR resonance peaks observed in the films. Hence, this model shows that the useful film thickness of magnetic thin films used in Power Supply in Package applications is ultimately determined by the ability to induce in plane uniaxial anisotropy. The film

thickness whereat the anisotropy energy no longer retains axial symmetry is the maximum film thickness for ultra-low loss magnetic thin films to be used in Power Supply Applications as the dynamic coupling ultimately increases the loss tangent at lower frequencies due to the low frequency increase of the imaginary component of the magnetic susceptibility.

Bibliography

[1] M. J. Donahue, "Oommf user's guide, version 1.0," tech. rep., 1999.

[2] W. F. Brown Jr, "Thermal fluctuations of a single-domain particle," *Physical Review*, vol. 130, no. 5, p. 1677, 1963.

[3] D. Jordan, G. Wei, Z. Ghaferi, A. Masood, C. O'Mathuna, and P. McCloskey, "Stochastic magnetic resonance of absorption effects of surface morphology in thin film magnetics," *Journal of Magnetism and Magnetic Materials*, vol. 505, p. 166736, 2020.

[4] W. Coffey and Y. P. Kalmykov, *The Langevin equation: with applications to stochastic problems in physics, chemistry and electrical engineering*, vol. 27. World Scientific, 2012.

[5] D. Jordan, P. McCloskey, and G. Wei, "A gpu accelerated micromagnetic simulator for modelling complex magnetic systems," *Journal of Magnetism and Magnetic Materials*, p. 168204, 2021.

[6] B. McMichael, R. Koch, J. Eick, and T. Schrefl, "Mumag standard

problem 4, https://www.ctcms.nist.gov/ rdm/std4/spec4.html," tech. rep.

[7] C. Nvidia, "Cuda," 2008.

[8] R. Zhu, "Grace: A cross-platform micromagnetic simulator on graphics processing units," *SoftwareX*, vol. 3, pp. 27–31, 2015.

[9] G. Booch, D. L. Bryan, and C. G. Petersen, *Software engineering with Ada*, vol. 30608. Addison-Wesley Professional, 1994.

[10] J. M. Coey10, *Magnetism and magnetic materials*. Cambridge university press, 2010.

[11] Y. Nakatani, Y. Uesaka, and N. Hayashi, "Direct solution of the landau-lifshitz-gilbert equation for micromagnetics," *Japanese Journal of Applied Physics*, vol. 28, no. 12R, p. 2485, 1989.

[12] R. Zhu, "Accelerate micromagnetic simulations with gpu programming in matlab," *arXiv preprint arXiv:1501.07293*, 2015.

[13] N. Hayashi, K. Saito, and Y. Nakatani, "Calculation of demagnetizing field distribution based on fast fourier transform of convolution," *Japanese journal of applied physics*, vol. 35, no. 12R, p. 6065, 1996.

[14] R. G. Lyons, *Understanding digital signal processing, 3/E*. Pearson Education India, 2004.

[15] R. Zhu, "Speedup of micromagnetic simulations with c++ amp on graphics processing units," *Computing in Science & Engineering*, vol. 18, no. 4, pp. 53–59, 2015.

[16] M. J. Donahue and D. G. Porter, "Exchange energy formulations for 3d micromagnetics," *Physica B: Condensed Matter*, vol. 343, no. 1-4, pp. 177–183, 2004.

[17] J. Leliaert, M. Dvornik, J. Mulkers, J. De Clercq, M. Milošević, and B. Van Waeyenberge, "Fast micromagnetic simulations on gpu—recent advances made with," *Journal of Physics D: Applied Physics*, vol. 51, no. 12, p. 123002, 2018.

[18] J. Hestness, S. W. Keckler, and D. A. Wood, "Gpu computing pipeline inefficiencies and optimization opportunities in heterogeneous cpu-gpu processors," in *2015 IEEE International Symposium on Workload Characterization*, pp. 87–97, IEEE, 2015.

[19] J. A. Stratton, N. Anssari, C. Rodrigues, I.-J. Sung, N. Obeid, L. Chang, G. D. Liu, and W.-m. Hwu, "Optimization and architecture effects on gpu computing workload performance," in *2012 Innovative Parallel Computing (InPar)*, pp. 1–10, IEEE, 2012.

[20] K. Choo, W. Panlener, and B. Jang, "Understanding and optimizing gpu cache memory performance for compute workloads," in *2014 IEEE*

13th International Symposium on Parallel and Distributed Computing, pp. 189–196, IEEE, 2014.

[21] D. Lustig and M. Martonosi, "Reducing gpu offload latency via fine-grained cpu-gpu synchronization," in *2013 IEEE 19th International Symposium on High Performance Computer Architecture (HPCA)*, pp. 354–365, IEEE, 2013.

[22] "Cuda c best practice guide," 2019.

[23] R. D. McMichael, M. J. Donahue, D. G. Porter, and J. Eicke, "Switching dynamics and critical behavior of standard problem no. 4," *Journal of Applied Physics*, vol. 89, no. 11, pp. 7603–7605, 2001.

[24] R. G. Lyons, *Understanding digital signal processing, 3/E*. Pearson Education India, 2004.

[25] S. G. Brush, "The kinetic theory of gases," *History of Modern Physical Sciences*, vol. 1, 2003.

[26] R. Zwanzig, *Nonequilibrium statistical mechanics*. Oxford University Press, 2001.

[27] W. T. Coffey and Y. P. Kalmykov, "Thermal fluctuations of magnetic nanoparticles: Fifty years after brown," *Journal of Applied Physics*, vol. 112, no. 12, p. 121301, 2012.

[28] Y. P. Kalmykov, S. V. Titov, and W. T. Coffey, "Statistical moment equations for stochastic spin dynamics in phase space: A uniaxial paramagnet subjected to a dc bias field of arbitrary orientation," *Physical Review B*, vol. 86, no. 10, p. 104435, 2012.

[29] R. Kubo, M. Toda, and N. Hashitsume, *Statistical physics II: nonequilibrium statistical mechanics*, vol. 31. Springer Science & Business Media, 2012.

[30] R. F. Greene and H. B. Callen, "On the formalism of thermodynamic fluctuation theory," *Physical Review*, vol. 83, no. 6, p. 1231, 1951.

[31] H. Risken, *Fokker-planck equation*, pp. 63–95. Springer, 1996.

[32] I. Wolfram Research, "Mathematica, version 11.1," 2017.

[33] V. Ignatchenko and R. Gekht, "Dynamic hysteresis of a superparamagnet," *ZHURNAL EKSPERIMENTALNOI I TEORETICHESKOI FIZIKI*, vol. 67, no. 4, pp. 1506–1515, 1974.

[34] J. J. Lu, H. L. Huang, and I. Klik, "Field orientations and sweep rate effects on magnetic switching of stoner wohlfarth particles," *Journal of applied physics*, vol. 76, no. 3, pp. 1726–1732, 1994.

[35] P. Déjardin, Y. P. Kalmykov, B. Kashevsky, H. El Mrabti, I. Poperechny, Y. L. Raikher, and S. Titov, "Effect of a dc bias field on the dynamic hysteresis of single-domain ferromagnetic particles," *Journal of Applied Physics*, vol. 107, no. 7, p. 073914, 2010.

[36] S. V. Titov, P.-M. Déjardin, H. El Mrabti, and Y. P. Kalmykov, "Nonlinear magnetization relaxation of superparamagnetic nanoparticles in superimposed ac and dc magnetic bias fields," *Physical Review B*, vol. 82, no. 10, p. 100413, 2010.

[37] W. Coffey and Y. P. Kalmykov, *The Langevin equation: with applications to stochastic problems in physics, chemistry and electrical engineering*, vol. 27. World Scientific, 2012.

[38] C. W. Gardiner *et al.*, *Handbook of stochastic methods*, vol. 3. springer Berlin, 1985.

[39] W. Coffey and Y. P. Kalmykov, *The Langevin equation: with applications to stochastic problems in physics, chemistry and electrical engineering*, vol. 27. World Scientific, 2012.

[40] Y. L. Raikher, V. Stepanov, and R. Perzynski, "Dynamic hysteresis of a superparamagnetic nanoparticle," *Physica B: Condensed Matter*, vol. 343, no. 1-4, pp. 262–266, 2004.

[41] I. Poperechny, Y. L. Raikher, and V. Stepanov, "Dynamic magnetic hysteresis in single-domain particles with uniaxial anisotropy," *Physical Review B*, vol. 82, no. 17, p. 174423, 2010.

[42] W. Coffey and Y. P. Kalmykov, *The Langevin equation: with applications to stochastic problems in physics, chemistry and electrical engineering*, vol. 27. World Scientific, 2012.

[43] E. Sadykov and A. Isavnin, "Theory of dynamic magnetic susceptibility in uniaxial superparamagnetic particles," 1996.

[44] Y. L. Raikher and V. I. Stepanov, "Stochastic resonance in single-domain particles," *Journal of Physics: Condensed Matter*, vol. 6, no. 22, pp. 4137–4145, 1994.

[45] Y. L. Raikher and V. Stepanov, "Dynamic hysteresis of a superparamagnetic nanoparticle at low-to-intermediate frequencies," *Journal of Magnetism and Magnetic Materials*, vol. 300, no. 1, pp. e311–e314, 2006.

[46] D. Jordan, G. Wei, A. Masood, C. O'Mathuna, and P. McCloskey, "Multimodal behavior of the dynamic magnetic susceptibility spectrum in amorphous cozrtab magnetic thin films," *Journal of Applied Physics*, vol. 128, no. 9, p. 093902, 2020.

[47] J. Stöhr and H. Siegmann, "Magnetism: from fundamentals to nanoscale dynamics. 2006."

[48] Y. P. Kalmykov, W. T. Coffey, B. Ouari, and S. V. Titov, "Damping dependence of the magnetization relaxation time of single-domain ferromagnetic particles," *Journal of magnetism and magnetic materials*, vol. 292, pp. 372–384, 2005.

[49] A. Masood, P. McCloskey, C. Ó. Mathúna, and S. Kulkarni, "Controlling the competing magnetic anisotropy energies in finemet amorphous thin

films with ultra-soft magnetic properties," *AIP Advances*, vol. 7, no. 5, p. 055208, 2017.

[50] P. Sharma, H. Kimura, and A. Inoue, "Magnetic behavior of cosputtered fe-zr amorphous thin films exhibiting perpendicular magnetic anisotropy," *Physical Review B*, vol. 78, no. 13, p. 134414, 2008.

[51] P. Sharma, H. Kimura, A. Inoue, E. Arenholz, and J.-H. Guo, "Temperature and thickness driven spin-reorientation transition in amorphous co-fe-ta-b thin films," *Physical Review B*, vol. 73, no. 5, p. 052401, 2006.

[52] P. Sharma, H. Kimura, and A. Inoue, "Tailoring the magnetic properties of mechanically hardest co–fe–ta–b glassy thin films," *Journal of applied physics*, vol. 101, no. 9, p. 09N502, 2007.

[53] Y. Shimada, M. Shimoda, and O. Kitakami, "Multiple magnetic resonance in amorphous co-nb-zr films with weak perpendicular anisotropy," *Japanese journal of applied physics*, vol. 34, no. 9R, p. 4786, 1995.

[54] F. Schoenstein, P. Aublanc, H. Pagès, S. Queste, V. Barentin, A.-L. Adenot, N. Malléjac, and O. Acher, "Influence of the domain structure on the microwave permeability of soft magnetic films and multilayers," *Journal of magnetism and magnetic materials*, vol. 292, pp. 201–209, 2005.

[55] W. T. Coffey, D. Crothers, J. Dormann, L. Geoghegan, Y. P. Kalmykov, J. Waldron, and A. Wickstead, "Effect of an oblique magnetic field on

the superparamagnetic relaxation time," *Physical Review B*, vol. 52, no. 22, p. 15951, 1995.

[56] A. Masood, P. McCloskey, C. Ó. Mathúna, and S. Kulkarni, "Co-based amorphous thin films on silicon with soft magnetic properties," *AIP Advances*, vol. 8, no. 5, p. 056109, 2018.

[57] Y. P. Kalmykov, W. T. Coffey, and S. V. Titov, "Bimodal approximation for anomalous diffusion in a potential," *Physical Review E*, vol. 69, no. 2, p. 021105, 2004.

[58] L. Landau and E. Lifshitz, "On the theory of the dispersion of magnetic permeability in ferromagnetic bodies," in *Perspectives in Theoretical Physics*, pp. 51–65, Elsevier, 1992.

[59] D. Garanin, V. Ishchenko, and L. Panina, "Dynamics of an ensemble of single-domain magnetic particles," *Teoreticheskaya i Matematicheskaya Fizika*, vol. 82, no. 2, pp. 242–256, 1990.

[60] Y. L. Raikher and V. I. Stepanov, "Intrinsic magnetic resonance in superparamagnetic systems," *Physical Review B*, vol. 51, no. 22, p. 16428, 1995.

[61] I. Klik, "Rotation of magnetization in unison and langevin equations for a large spin," *Journal of statistical physics*, vol. 66, no. 1-2, pp. 635–645, 1992.

[62] W. Coffey, D. Crothers, Y. P. Kalmykov, and S. Titov, "Precessional effects in the linear dynamic susceptibility of uniaxial superparamagnets: Dependence of the ac response on the dissipation parameter," *Physical Review B*, vol. 64, no. 1, p. 012411, 2001.

[63] H. Fukushima, Y. Uesaka, Y. Nakatani, and N. Hayashi, "Switching times of a single-domain particle in a field inclined off the easy axis," *Journal of applied physics*, vol. 101, no. 1, p. 013901, 2007.

[64] L. Geoghegan, W. Coffey, and B. Mulligan, "Differential recurrence relations for non-axially symmetric rotational fokker-planck equations," *Advances in Chemical Physics*, vol. 100, pp. 475–641, 1997.

[65] M. Yamaguchi, K. Suezawa, Y. Takahashi, K. Arai, S. Kikuchi, Y. Shimada, S. Tanabe, and K. Ito, "Magnetic thin-film inductors for rf-integrated circuits," *Journal of Magnetism and Magnetic Materials*, vol. 215, pp. 807–810, 2000.

Chapter 6

Conclusions & Future Work

The purpose of this chapter is to provide a high-level discussion of the key findings of our work, along with a discussion of future work required to address outstanding issues, or limitations, with integrated magnetics in Power Supply in Package (PwrSiP) applications.

6.1 Research Outcomes

The key objective of this thesis was to explore the use integrated magnetics, which had been well demonstrated as the magnetic passive component in Power Supply on Chip (PwrSoC) applications, as the magnetic passive component in PwrSiP applications. In order to support this work an extensive literature review was performed wherein magnetics solutions that existed in package were compared, and benchmarked against those solutions used on

Chip. A key finding from the literature review was the sheer dominance in terms of volume of ferrite materials used in package applications, and the scarcity of thin film magnetics. This indicated that there was a limiting factor to the deployment of thin film magnetic solutions in PwrSiP applications.

This limiting factor was ultimately determined to be caused by the underlying surface conditions of the PCB substrate on which the magnetic thin film would be deposited. This roughness of the underlying substrate resulted in degraded magnetic performance of the thin film. Indeed, the ratio of the surface roughness to the thin films thickness was a key limiting factor in terms of the thin films coercivity, and magnetic susceptibility. In order to treat the issue of surface roughness in thin film magnetics we adapted Brown's diffusion model for magnetic spins subject to thermal noise. The core Ansatz being that surface roughness noise was statistically identical to noise induced by thermal fluctuations i.e., both were sources of Additive White Gaussian Noise.

The work on the effect of surface roughness on the magnetisation dynamics of thin films culminated in a publication in the *Journal of Magnetism and Magnetic Materials*. The research found that the Surface Roughness to Thickness Ratio (SRT) of the magnetic thin film played a key role in the soft magnetic properties of the film, and therefore determined the efficacy of the material used as the magnetic passive component in PwrSiP applications. It

was found that there was a moderate positive linear correlation between the SRT and the magnetic relaxation time of the film. The magnetic relaxation time being the time required by a magnetic film to demagnetise after the removal of an alignment field. Hence it is pivotal for good soft magnetic properties.

Furthermore, this work found that the stochastic influence of the surface roughness on the magnetisation dynamics of the thin film gave rise to a Stochastic Magnetic Resonance of Absorption (SMRA) phenomenon in the thin film. This discovery is in line with the Stochastic Magnetic Resonance (SMR) effects observed in magnetic particles subjected to thermal noise. This justified the core Ansatz of this work in that SRT and thermal noise can be modelled in an analogous manner as they both share identical statistical properties. Recall, both are sources of Additive White Gaussian Noise (AWGN) on the magnetisation dynamics. Hence, it is to be expected that they would share similar phenomenon.

This modelling facilitated the necessary correlations in order to determine the thickness dependent loss of a thin film deposited on a given PCB substrate. Given that the SMRA effects are related to the SRT of the film, the most obvious method to reduce the power absorbed by the film is to deposit a thicker film so that the maximum of the SMRA curve is avoided. As increasing the film thickness was such an obvious way to avoid the maximum of the

SMRA curve the focus of this research turned to investigated the maximum permissible film thickness, and to investigate if there were any deteriorations in the magnetic properties with increased film thickness.

Indeed, we showed that there is a maximum permissible film thickness of thin films used in PwrSiP applications, and that this thickness was not determined by eddy current formations within the film, rather it was the thickness whereat uniaxial anisotropy could no longer be induced. The breakdown in the axial symmetry of the energy anisotropy plane after this critical thickness results in dynamic coupling between the longitudinal and transverse magnetic susceptibility. This is incredibly detrimental to low loss performance as the dynamic coupling gives rise to an increased imaginary component of the dynamic magnetic susceptibility at lower frequencies.

Furthermore, it was shown that the additional energy minima arising due to film thickness can result in additional sub Ferromagnetic Resonance (FMR) resonances. The addition resonances arise when the applied frequency of the AC external field approached the precession frequency of the additional energy wells, $\omega \rightarrow \omega_{pr}$. From this, we were able to show how each energy well, each with a distinct precession frequency, exhibited resonance behaviour at the precession frequency. This is extremely useful as the anistropy potential of the thin film can be modelled from its dynamic magnetic susceptibility.

The breakdown in the axial symmetry is further detrimental to the magnetic performance of the thin film as it gives rise to a low frequency increase in the imaginary component. Hence there is a maximum useful film thickness which is determined by the ability of the process to induce uniaxial in-plane anisotropy during the deposition phase. This work on the multimodal nature of the dynamic magnetic susceptibility of thin films was published in the *Journal of Applied Physics*.

The issue of surface roughness in thin film magnetics was ultimately addressed by developing a release process by which the magnetic thin film could be deposited using Si fabrication techniques and later incorporated into package. This process involved the spinning on of a polymer release layer on the Si substrate on which the magnetic core would be deposited. Application of mechanical stress to the release layer liberated the core, along with the polymer release layer, from the Si substrate. Hence, we were able to deposit smooth magnetic thin films. These films were then later incorporated into package through the use of: 1) wirebonds; 2) a PCB Flip-Chip approach; and 3) fully embedding them in the prepreg layers of the PCB.

The Flip-Chip inductor verified the efficacy of released magnetic thin films integrated into package for PwrSiP applications. Indeed, the Flip-Chip inductor obtained a remarkably high Q-factor through the use of the released magnetic thin film. This, and the novelty of the inductor fabrication pro-

cess, resulted in a body of work the was published in the *IEEE Journal of Emerging and Selected Topics in Power Electronics*, and stands as one of the main accomplishments of our research.

6.2 Challenges & Future Work for Thin Film Magnetics in Power Supply in Package Applications

There are several key challenges still facing integrated thin film magnetics used in power supply in package applications. These challenges are continually updated as the miniaturisation process in electronics continues, and they are as follows: 1) the requirement of a high permeability magnetic material that has constant permeability in the VHF frequency range; 2) the ever increasing current density handling requirements of the magnetic material i.e., a material which does not saturate at low applied fields. This requirement is particularly challenging in light of requirement 1) as the anisotropy field plays crucial role in determining the field at which a magnetic saturates. The higher the anisotropy field, the greater the current handling capabilities, the lower the permeability. Hence there is a near fundamental trade-off between property 1) and property 2); This is a near fundamental trade-off due to property 3) the requirement of a material with inherently high magnetic saturation fields. Snoek's law ultimately sets the useful frequency of the

material as it relates the magnetic saturation field to dynamic magnetic susceptibility and fundamental ferromagnetic resonance frequency. Hence, this law determines the loss of the magnetic material at frequency. Therefore, magnetic materials with higher magnetic saturation fields can use Snoek's law in conjunction with an induced anisotropy field to have simultaneously high permeability, at high frequencies, and at high currents; and finally 4) materials which exhibit high resistivity so required to stymie eddy current formations within the core at high frequencies.

Amorphous soft thin film magnetics simultaneously exhibit the desired magnetic properties 1) – 4) and as such are ideal candidates to be used in future power electronic applications. The lack of long range atomic order in amorphous magnetic materials results in an averaging out of their magnetocrystalline anisotropy and increases resistivity due to reduced electron mobility caused by the lack of a crystal lattice. Hence, they can exhibit ultra-low loss performance at high frequency. However, it is an open challenge today to induce good in-plane uniaxial anisotropy within these materials past a critical films thickness. Hence, this limits useful thickness of the magnetic core.

The use of a multi-layer core structure comprising individual magnetic thins films in which uniaxial anisotropy can be induced to increase the effective thickness of the magnetic core. Such a structure would enable higher den-

sity devices in PwrSiP applications. However, there is an apparent magnetic coupling between the individual magnetic layers which reduces the effective permeability of the stack and increases its loss tangent. This coupling effect was also modelled using Brown's diffusion model and is presented in Appendix A. Therefore, future work is required in order to break coupling between the magnetic layers, and so greatly improve the cores performance in PwrSiP applications.

Further, detailed dielectric materials study is required in order to show the role of the dielectric layer in the magnetisation dynamics of the multilayer stack. The conventional wisdom is that low κ constant (low relative permittivity) materials are desired. However, at this moment in time the multilayer stack that utilises AlN currently exhibits the best magnetic properties. However, an intensive study on the role of the dielectric insulating material in the multilayer core would be of merit.

Finally, preliminary magnetic data obtained from the CZT multilayer core embedded in the prepreg layers of the PCB stack by AT&S shows promise as there was no notable loss in the magnetic performance after embedding. The same is not true for the $Ni_{45}Fe_{55}$ core which showed diminished performance after the embedding. Therefore investigations are needed to understand the diminished performance of the $Ni_{45}Fe_{55}$ core. However, with the successful embedding of the CZT multilayer core the next most obvious step is to actu-

ally design, and create, a fully functional Integrated Voltage Regulator which utilises the integrated magnetic core. This body of work has proved that integrating thin film magnetics into organic substrates for PwrSiP applications is more than just doable, it is beneficial to the converters performance.

6.3 List of Publications

This section of the chapter highlights the novel scientific contributions of this thesis to the body of knowledge in the field of integrated thin film magnetics which have resulted in publications (or that are currently pending consideration for publication) in peer reviewed scientific journals. Each article listed below forms a chapter, or subsection of a chapter, in this thesis.

- S. Kulkarni, D. Li, D. Jordan, N. Wang, C. O'Mathuna, "PCB embedded bondwire inductors with discrete thin-film magnetic core for power supply in package", *IEEE Journal of Emerging and Selected Topics in Power Electronics*, vol 6, pp. 614-620, 2018.

- D. Jordan, G. Wei, Z. Ghaferi, A. Masood, C. O'Mathuna, P. McCloskey, "Stochastic magnetic resonance of absorption effects of surface morphology in thin film magnetics", *Journal of Magnetism and Magnetic Materials*, vol. 505, p. 166736, 2020.

- D. Jordan, G. Wei, A. Masood, C. O'Mathuna, P. McCloskey, "Multimodal Behaviour of the Dynamic Magnetic Susceptibility Spectrum

in Amorphous CoZrTaB Magnetic Thin Films", *Journal of Applied Physics*, vol. 128, no. 9, p. 093902, 2020, doi: 10.1063/5.0013962.

◇ D. Jordan, G. Wei, L. Ye, D. Lordan, P. Podder, A. Masood, K. Rodgers, C. O'Mathuna, P. McCloskey, "High q-factor PCB embedded flip-chip inductors with multi-layer CZTB magnetic sheet for power supply in package (PwRSiP)", *IEEE Journal of Emerging and Selected Topics in Power Electronics*, pp. 1–1, 2020.

◇ D. Jordan, P. McCloskey, G. Wei, "A GPU accelerated micromagnetic simulator for modelling thin film magnetic alloy systems", *Current status "Under Review" for publication in Journal of Magnetism and Magnetic Materials.* October 2019.

6.4 List of Conference Presentations & Proceedings

This section of the thesis enumerates the conferences in which our work was disseminated amongst the scientific community that attended.

◇ D. Jordan, S. Kulkarni, P. McCloskey, A. Masood, C. O'Mathuna, "Influence of anisotropy distributions and exchange interactions on the magnetisation dynamics of amorphous Co-based alloy systems", *Magnetism and Magnetic Materials*, 6th – 10th November 2017, Pittsburgh, USA.

- ◇ D. Jordan, G. Wei, C. O'Mathuna, P. McCloskey, "PCB Embedded Flip-Chip Inductors with Released Multi-Layer CZTB Magnetic Core for Power Supply in Package (PwRSiP)", *Magnetic Frontiers*, 24th - 27th June 2020, Lisbon, Portugal.

- ◇ D. Jordan, P. McCloskey, G. Wei, "A GPU Accelerated Mircomagnetic Simulator for Modelling Complex Magnetic Systems", *Joint European Magnetic Symposia*, 26th – 30th August 2019, Uppsala, Sweden.

Appendix A

Dynamic Coupling of Transverse and Longitudinal Magnetic Susceptibility in Amorphous Multi-Layer CZTB Thin Films

This Appendix further adapts Brown's continuous diffusion model of magnetic spins shown in section 5.4[a] to characterise the dynamic magnetic sus-

[a]Note this appendix could be considered as another sub-section in section 5.4. However, this work was carried out after the work presented in section 5.4 was published in the *Journal of Magnetism and Magnetic Materials*. As I wanted to leave that body of work as close to that published in *JMMM*, this section forms an appendix to that body.

ceptibility in amorphous multilayer CZTB magnetic stacks. Brown's diffusion model is regressed onto experimental data obtained for the amorphous multilayer stack, the fabrication process for which is outlined in sections 3.4.

It is clear from Fig. A.1 the Brown's diffusion accurately describe the magnetisation dynamics of the multilayer stack. Most notable is the diminished primary FMR peaks caused by the magnetic stack. This indicates magnetic coupling through the magnetic dipole-dipole interaction results in a shallowing out of the anisotropy energy minima resulting in inhomogeneous broadening of the FMR peaks due to the dispersion of fundamental resonance frequency. Furthermore, it is evident from the imaginary component of the magnetic susceptibility that there is dynamic coupling between the transverse and longitudinal magnetic susceptibility. Such coupling is detrimental to the magnetic performance of the stack used in Power Supply in Package applications as it results in a higher loss tangent at lower frequencies. Hence, future work is required to magnetically isolate the individual magnetic layers of the core in order to disrupt the dynamic coupling of the magnetic reversal modes.

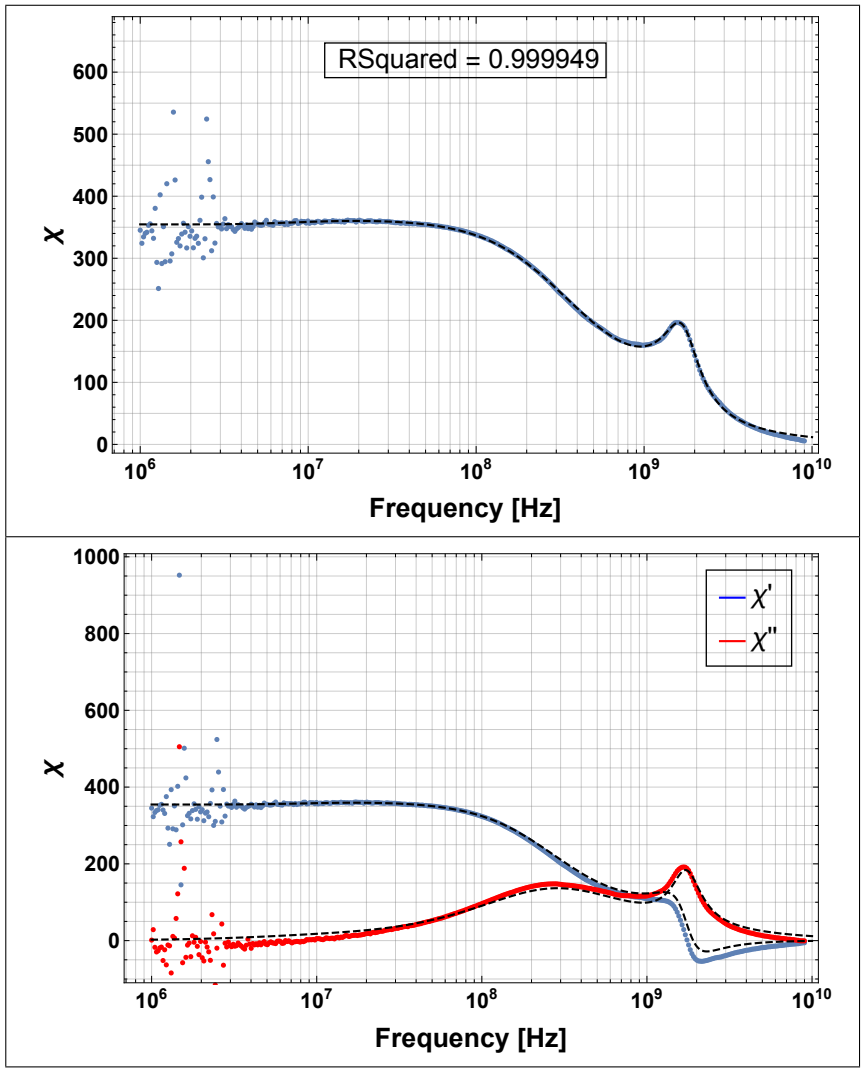

Figure A.1: Magnetic susceptibility data for amorphous multi-layer (16 × 250nm) CZTB stack; (upper) Absolute value of the magnetic susceptibility; (lower) Real and imaginary components of the magnetic susceptibility. Dashed lines are the fitted model